Scuola Internazionale Superiore di Studi Avanzati - Trieste

Astrophysics Sector

A Panchromatic Spectral Population Synthesis Model for Young Star-Burst Galaxies

Thesis submitted for the degree of Doctor of Philosophy in Astrophysics

CANDIDATE

Obi Ikechukwu Anthony

SUPERVISORS

Prof. Alessandro Bressan

Dr. Francesca Perrotta

Dr. Laura Silva

October 2017

SISSA - Via Bonomea 265 - 34136 TRIESTE - ITALY

To my late dad

Abstract

The study of the properties of galaxies to possibly map their formation and evolutionary paths is an active research field both from observational and theoretical point of view. Great observational efforts are continuously devoted to map the spectral energy distribution (SED) of galaxies in the local universe and at high-redshifts over all wavelength range, by surveying the sky with both ground and space-borne instruments. Surveys in different spectral bands have revealed galaxies with drastically different activity levels and energy budgets, symptoms of underlying disparate basic physical properties. It is these basic properties that one aims to uncover in order to get insights on the complex behaviour of mass assembly and recycling in galaxies. The fundamental tools necessary for this task are spectral synthesis models. These models are based on the availability of a complete library of stellar evolution models, that homogeneously cover the range of stellar masses, metallicities, and evolutionary phases that contribute to the integrated SED of a galaxy. From these and a library with a complete coverage of the stellar parameters, the integrated SED of simple stellar populations (SSP) can then be computed. To compare the theoretical SED with the observed one, it is important to account for, at very least, the main processes producing radiation and affecting the radiation path, i.e. stars, ionized gas nebulae for the main recombination lines and continuum emission, core-collapsed supernovae (CCSN) for the non-thermal radio emission, and the interaction between stellar radiation and dust grains in the interstellar medium (ISM).

In this thesis, I focus on a major revision and extension of the SSP models based on the PAdova TRieste Stellar Evolution Code (PARSEC) stellar models. By means of PARSEC, I compute, at five different metallicities (0.0001 - 0.02) and four different IMF upper mass limits (40 - 350$M_{\odot}$) the integrated stellar light, the line and continuum emission (effects of ionized nebulae on this light) and of the non-thermal emission predicted by young SSPs. I then use the new SSP models in combination with the radiative transfer code GRASIL (GRAphites and SILicates) to include the stellar extinction by dust and the ensuing IR emission, therefore providing a panchromatic UV-to radio SED modelling. I calibrate and apply this new model to observations. Thereafter, I carry out a critical investigation of the effect of metallicity, IMF upper mass limit and star formation regime (star bursting versus normal star forming) on star formation rate (SFR) and dust attenuation properties of star forming galaxies. This allowed for the provision of a consistent set of SFR calibrations, that are explicitly dependent on metallicity and IMF upper mass limit and also on the age of the starburst, at wavelengths ranging from UV to radio. Finally, I considered the possible use of the radio slope to identify the the IMF upper mass limit where i showed that the method is well suited for high-redshift objects with a prolonged star formation.

Publications

- **I.A. Obi, A. Bressan, F. Perrotta, L. Silva, O. Vega, Y. Chen, A. Lapi, C. Mancuso, L. Girardi, G.L. Granato, P. Marigo, and A. Slemer**
  Modelling the UV to radio SEDs of nearby star-forming galaxies: new PARSEC SSP for GRASIL,
  2017, submitted to MNRAS
- **Claudia. Mancuso, A. Lapi, I. Prandoni, I. Obi, J. Gonzalez-Nuevo, F. Perrotta, A. Bressan, A. Celotti, L. Danese**
  Galaxy Evolution in the Radio Band: The Role of Star-forming Galaxies and Active Galactic Nuclei,
  2017, ApJ
- **Obi, Ikechukwu Anthony; Bressan, Alessandro; Perrotta, Francesca; Chen, Yang; Marigo, Paola; Slemer, Alessandra**
  Thermal and non-thermal radio emission in young star forming metal poor galaxies,
  2015, IAU General Assembly, Meeting 29, id.2257610

Acknowledgments

First and foremost, I would like to acknowledge and extend my heartfelt gratitude to my supervisors Prof. Alessandro Bressan, Dr. Francesca Perrotta and Dr. Laura Silva for their guidance during the course of my Ph.D study. I am immensely grateful to Prof. Alessandro Bressan for his mentorship and moral support that lead to the completion of this thesis.

My appreciation goes to Riccardo Lancer of the students secretariat for his assistance in administrative matters especially in procuring the yearly residence permit.

To my fellow course mates Guiseppe, Alessandro, Jing and Isabella whom I have alternatively shared the same office with over the years, and to my friends in Trieste, thanks for the memorable and wonderful times together.

Finally, thanks to my mum and siblings for their encouragement and love.

Thank you Trieste for accommodating me.

Contents

Chapter 1

Introduction

Galaxies are very complex objects consisting of billions of stars with different ages, chemical abundances and masses, and of gas and dust in a wide range of phases of the interstellar medium (ISM). Except in our and in some nearby galaxies, it is not possible in all other cases to directly resolve the emission from single stars. Therefore, in order to study the properties and evolution of galaxies, we must rely on the integrated emission of their ensemble of stars and ISM.

The method of building a galactic spectrum through the sum of the spectra of its individual stars is termed stellar population synthesis (SPS, also referred to as Evolutionary PopulationSynthesis) and was pioneered by Tinsley (1972); Searle et al. (1973); Larson & Tinsley (1978). The basic assumption is that the integrated spectrum of a galaxy consists of a superposition of the spectra of simple stellar populations (SSP) of different age and chemical composition. This means that a SSP is a population of stars born at the same time and with the same chemical abundance, with a given initial mass distribution.

Stellar population models have improved significantly in quality over the years as more and more detailed stellar models and techniques for spectral synthesis were developed, as well as an increased volume and quality of observational data have become available as a constraint. Moreover, the combination of the stellar spectral synthesis models with calculations of the interaction with the gas and dust in the interstellar medium has allowed to extend the range of wavelength and resolution covered by the models. In fact, several fundamental quantities related to the properties of galaxies can be retrieved by fitting model spectra to the observed spectra of galaxies, e.g. masses in stars, gas and dust, star formation rates, metallicity and redshifts. Due to the unavoidable uncertainties and degeneracies involved in any model, this possibility is particularly true if data available over the whole observed range are exploited to constrain the models.

1.1 Stellar Population Synthesis Modelling

1.1.1 Historical Overview

The research field on the stellar populations synthesis modelling is relatively old. The HR diagram (Figure 1.1), the relation between the colour and luminosity of stars, was discovered at the beginning of the 20th century. It revealed an orderliness in how stars evolve. Shortly after this discovery, Shapley (1918) demonstrated, with Cepheids, that globular clusters consist of large systems of stars that are few Kpc away from us. It was found afterwards that galaxies such as M31, then regarded as a nebula, were even larger and more distant systems than globular clusters. In 1943, Baade (1944) exploited the opportunity of the blackout caused by the second war to resolve for the first time M31 and its companions into individual stars, revealing that the stellar populations in the bulge of this galaxy are similar to those in the halo of our Galaxy. It was not until about 30 years later that the first set of works (e.g. Whitford 1978; Whitford & Rich 1983; Rich 1988) that focused on deriving information about the stellar contents of galaxy colours led to the realization that the variation of properties along Hubble galaxy classification sequence was strongly connected with star formation in galaxies.

Tinsley (1968), heavily influenced by the ideas about galaxy formation by Eggen et al. (1962), was the first to move from a mere phenomenological recognition of the differences between galaxies, to an actual computation of a galaxy model, able to provide quantitative predictions for stellar populations in galaxies, that could be tested with real observational data. In fact, the basics of the current sophisticated evolutionary stellar population synthesis models date back to a series of paper by Tinsley (Tinsley 1972, 1973, 1980, etc).

1.1.2 Ingredients

Evolutionary tracks and isochrones The first basic ingredient of SPS models are the stellar evolutionary tracks. These provide the evolution of stars of given initial mass and chemical composition on the HR diagram. Isochrones, which specify in the HR diagram the location of stars with a common age and chemical abundance, are constructed from the evolutionary tracks. For tracks that are not well sampled in mass and time, issues may arise in the isochrone construction especially for short and fast evolutionary phases. Therefore it is important for isochrones to span a wide range of age, mass and chemical composition, and at the same time to cover the most important evolutionary phases. Examples of such ischorones are the Padova model (Bertelli et al. 1994; Girardi et al. 2000; Marigo et al. 2008; Bressan et al. 2002; Bertelli et al. 2008; Bressan et al. 2012) and the BaSTI models (Pietrinferni et al. 2004; Cordier et al. 2007). Isochrones that are tailored for very-low-mass stars include the Lyon models (Chabrier & Baraffe 1997; Baraffe et al. 1998; Conroy & van Dokkum 2012a). It can be an difficult task to combine different sets of isochrones, derived from tracks conputed with different assumptions.

Stellar atmosphere models The second basic ingredient needed to model the integrated properties of stellar populations is a library of stellar model atmospheres. These libraries are used to transform the models from the theoretical plane to the observational one. They provide the SED of a star as a

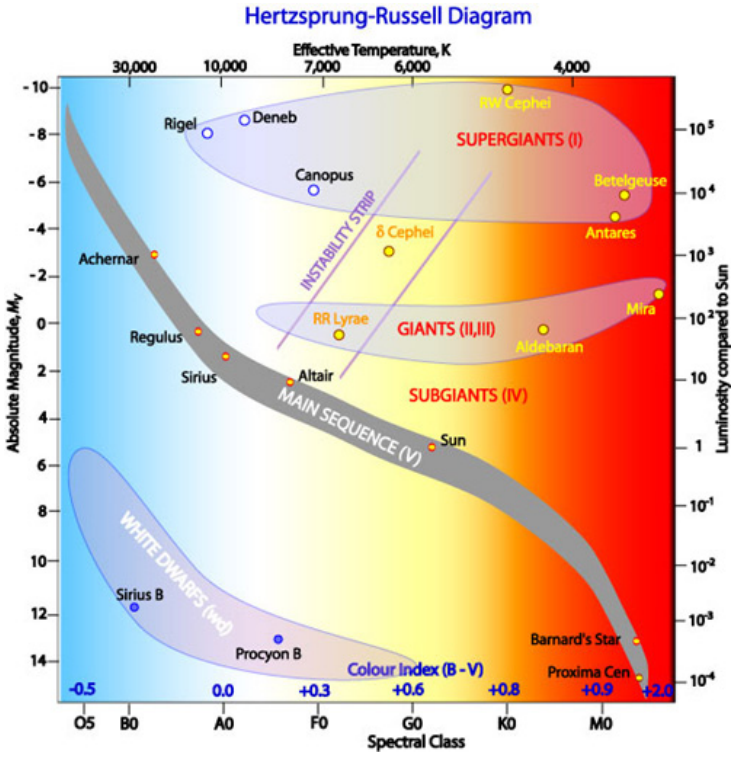

Figure 1.1: The Hertzprung-Russell Diagram. Image credit (http://www.atnf.csiro.au/).

function of it's effective temperature, surface gravitiy and metallicity. Stellar model atmospheres can be fully theoretical (e.g. Kurucz 1992; Hauschildt et al. 1997; Westera et al. 2002; Martins et al. 2005; Lançon et al. 2007; Coelho et al. 2007) or empirical, e.g. ELODIE (Prugniel & Soubiran 2001), TELIB (Le Borgne et al. 2003), Indo-US (Valdes et al. 2004), HST/NGSL (Gregg et al. 2004), MILES (Sánchez-Blázquez et al. 2006; Cenarro et al. 2007), IRTF (Rayner et al. 2009), and the X-shooter library Chen et al. (2011), or both (see the list compiled by D. Montes [1])

Theoretical libraries have the main advantage of covering a larger parameter space at a given spectral resolution (Martins et al. 2005). The main drawback is that the accuracy of the libraries depends on the input atomic and molecular parameters and on the approximations made in the computation of the models. The atomic and molecular line lists can be incomplete particularly at high spectral resolution (Kurucz 2005, 2011). Others drawbacks include for instance difficulties in the modelling the IR emission for stars in the luminosity classes I and II (Lançon et al. 2007).

On the other hand, the main benefit of the empirical libraries is that they are based on real stars and thus do not suffer from issues with line list. Due to the observational limits they are incomplete in their coverage of the parameter space, that is biased towards the compositions of our Galaxy (e.g. Cenarro et al. 2007) and are faced with common observational issues like atmospheric absorption, flux calibration etc. A synthesizing approach aimed at using the strengths of both types of libraries seems to be promising, as will be discussed later in the next Chapter where we dicussed the spectral library adopted in this work.

[1] http://www.ucm.es/info/Astrof/invest/actividad/spectra.html

Initial Mass Function A fundamental ingredient in stellar population models is the stellar Initial Mass Function (IMF), the initial distribution of stellar masses along the zero age main sequence. Since the work of Tinsley (1980), it has been known that the slope α of the IMF at the main-sequence turnoff point determines the rate of luminosity evolution of a passively evolving stellar population. This dependency arises because the giant branch dominates the luminosity for all plausible values of α, and so the IMF determines the rate at which stars turning off the main sequence migrate to the giant branch. A steeper IMF therefore implies that the giant branch is abundantly and quickly populated with time,thereby reducing the natural dimming of the luminosity. At too steep slopes, the slowly evolving dwarfs will dominate the light leading to an almost constant integrated luminosity over time. The IMF is generally obtained by determining the current mass function of stars and correcting it for the evolution of stars. However, this can be done only for stars in or near the solar neighborhood. Salpeter (1955) first described the IMF as a power-law, $dn/dm \propto m^{\alpha}$ where dn is the number of stars in the mass interval m, m + dm, $\alpha = 2.35$. Other studies (Scalo 1986; Kroupa 2001; Chabrier 2003, etc) extended the mass range to higher and lower mass values. All these different IMFs have approximately the same slope down to about 0.6 $M_{\odot}$, and show a similar behaviour of a turnover to a flatter slope at masses smaller than 0.6 $M_{\odot}$, although the exact details are still poorly constrained. It is not clear whether the IMF had the same form over all of cosmic times and in all environments. The low mass end is of particular importance, as $\sim$ 60 - 80 % of the stellar mass density in the Universe is in the form of stars with masses lessthan $0.5M_{\odot}$. Low-mass stars, due to their faintness, provide a negligible contribution to the integrated light of stellar populations.

1.1.3 Computational Methods

As mentioned earlier, SSP model spectra are computed by integrating the spectral contributions from stars along isochrones, and weighting them with the relative fraction of stars at every point along those isochrones. The process of isochrone construction is trivial if the stellar models all have lifetimes that by far exceed the desired isochrone age. All that is required in this case is a simple interpolation within each stellar evolution track to this desired age. The interpolation becomes much harder when we wish to capture the late and short phases of stellar evolution.

In the literature, there are two main methods of interpolation used by current SPS models to compute the spectra of SSPs.

The first method is called isochrone synthesis. It uses the locus of stars with the same age, called an isochrone, in the HR diagram and then integrates the spectra of all stars along the isochrone to compute the total flux. This method was established by Chiosi et al. (1988); Maeder & Meynet (1988) and boosted by the works of Charlot & Bruzual (1991). The majority of stellar population models use this method.

The second uses the fuel consumption theorem approach. This theorem states that the number of stars at each burning stage is proportional to the time it takes to exhaust the amount of hydrogen and helium burnt at that stage. This can be interpreted as the conservation of energy for stellar populations. The main point here is that the luminosity of the post-main sequence stars, which happens to be the most luminous, is directly linked to the fuel available to stars at the turnoff mass (Renzini 1981; Buzzoni

1989; Maraston 1998, 2005), in other words, the fuel is integrated along the evolutionary track. This fuel consumption method is useful for quantifying the contribution of rapid and luminous stellar phases like the tip of the RGB, the AGB and the RGB bump. It is also useful for including in synthetic integrated models those stellar phases for which a complete isochrone may not be available, such as the AGB and the Horizontal Branch.

Numerical experiments have shown that calculations based on the fuel consumption theorem and isochrone synthesis are in agreement with each other Charlot & Bruzual (1991), as long as the mass bin of the mass integration in the isochrone synthesis case is small. Other alternative methods include the use of empirical spectra of star clusters as templates for SSPs (Bica & Alloin 1986) and the method described by Dotter (2016) which is used in the stellar evolution code Modules for Experiments in Stellar Astrophysics (MESA).

Given the library of isochrones, stellar atmosphers and an IMF, the integrated SED of a SSP is obtained as follows:

$$f_{\nu}^{SSP}(t,Z) = \int_{M_{low}}^{M_{up}} \phi(m) f_{\nu}^{*}(m,t,Z) dm \tag{1.1}$$

where $\phi(m)$ is the adopted IMF, $f_{\nu}^{*}(m,t,Z)$ is the SED of a star with initial mass m, age t, and initial metallicity Z. The final step in SPS modelling is to generate the time-dependent stellar spectrum of a galaxy for a given star formation history:

$$f_{\nu}^{gal}(t,Z) = \int_{0}^{t} f_{\nu}^{SSP}(t-t',Z) SFR(t') dt' \tag{1.2}$$

where SFR(t') is the star formation rate at time t' and $f_{\nu}^{SSP}(t-t',Z)$ is the stellar spectrum of a SSP of age $t_{ssp} = t - t'$ and given metallicity Z.

1.1.4 Some relevant uncertainities

Stellar Evolution Some phases of stellar evolution are yet not well understood, both on theoretical and observational grounds, hence they are poorly treated. The most important of these are the thermally pulsing asymptotic giant branch (TP-AGB), horizontal branch (HB), blue stragglers (BSs), post-AGB and Wolf-Rayet phases. These phases are important in SPS due to the high bolometric luminosity they produce relative to that produced on the main-sequence phase.

TP-AGB stars are short-lived, very luminous component of intermediate age populations that tend to be more prominent at low metallicities. The short lifetime and the instability of the pulsations make the modelling of such stars difficult. This instability occurs in stars with initial masses $\leq 5M_{\odot}$ and hence for stellar populations with ages $\geq 10^{8}$yr (Marigo et al. 2008). They can significantly alter the mass-to-light ratio of intermediate age populations, for instance Melbourne et al. (2012) estimated a 17% contribution from the TP-AGB phase to the integrated $1.6\mu m$ near-infrared luminosities of 23 nearby galaxies. Although previously neglected, attention has recently been focused on these stars since it was noticed that the large discrepancies between SSP spectra of different SPS models were due to different

treatment of TP-AGBs in these models (Maraston 2005; Maraston et al. 2006).

The HB consists of old low-mass stars ($M < 1M_{\odot}$) burning helium in their cores, and hydrogen in a shell surrounding the core, at nearly constant bolometric luminosity (Sweigart 1987; Lee et al. 1994). One of the fundamental problems with understanding their morphology is that of the high sensitivity of their temperature to the amount of mass lost. For example, a difference in envelope mass of only 0.04 $M_{\odot}$ can correspond to a temperature increase by a factor of two (Rich et al. 1997), a factor sufficient to explain the morphology of metal-poor systems. Understanding the morphology of the HB from first principles is extremely challenging since there is not yet a theory of mass-loss for evolved stars.

BSs are stars that extend blueward of the main sequence turn-off point. They are prevalent feature of observed globular clusters (e.g. Sandage 1953; Bailyn 1995; Brown et al. 2005). Their origin is still not known, though it is believed to be associated with primordial binary evolution, either through merging or mass transfer (e.g. McCrea 1964; Bailyn 1995; Ferraro et al. 2006). As with HB stars, blue stragglers can affect the interpretation of early-type spectra giving younger average ages. These stars point towards a fundamental limitation of current SSP modelling, in that effects of binary evolution are not included. While the effect of binary evolution is excluded in most SPS models and causes little difference in most cases, in situations where blue stragglers may dominate, binary stellar population models may be more satisfactory. For example, Li & Han (2007) find that including binaries can result in broadband colors bluer by ∼0.05 mag. Xin & Deng (2005) find a contribution by BSs in old open clusters to the B-V color of the integrated cluster as large as ~ 0.2 mag.

The stellar Initial Mass Function (IMF) Though the shape of the IMF is rather well-constrained in the Galactic disk, it is however unclear whether the IMF has had the same shape over all of cosmic times and in all environments. Morever, the IMF is very uncertain in the mass range $0.8 < M_{\odot} < 2M_{\odot}$. For galaxies made up of old stars, this mass range is critical because the main-sequence turnoff is in this case $\sim 1\ M_{\odot}$, and as mentioned earlier, the rate of luminosity evolution for a passively evolving system is strongly related to the logarithmic slope of the IMF at this main-sequence turn off point.

Abundance ratios Abundance ratios of elements in galaxies contain a wealth of information about the way and over which timescale stars were formed. Explosions of supernovae and stellar mass loss cause newly formed atoms to enter the interstellar medium, where they can be used to form new stars, which in turn can again enrich the interstellar medium. The fact that the abundance ratios of galaxies are not always the same as in the solar neighbourhood is established by e.g. the tight relation between [Mg/Fe] and [Fe/H] (e.g. Worthey et al. 1992; Edvardsson et al. 1993). Variations are also seen in the ratio of other α-elements and iron-peak elements as reviewed by Henry & Worthey (1999). Models that study the abundance patterns of galaxies exist only for early-type galaxies with little or no ongoing star formation but currently none for actively star-forming galaxies. This is because of the weaker metal absorption lines of hot young massive stars that dominate the spectra of actively star-forming galaxies, compared to the metal lines of the cooler and older stars. The assumption of solar abundance distribution for stellar isochrones and stellar libraries implies that several features in observed galaxy spectra are not well fit by

the best currently available stellar population models.

1.2 Panchromatic UV to radio SED modelling

The SED of galaxies contains a wealth of combined information, that need to be deciphered in order to recover the quantities necessary to understand their properties. In fact the emerging integrated SED is a complex interplay arising from the radiation emitted by stars distributed across the galaxy and covering a wide range of masses, ages, and compositions, and interacting with the gas and dust in the different phases of the ISM. Going back from the SED to the possible SFRs and masses of the different constituents is well known to be subject to degeneracies. Among these, the age-metallicity and the age-extinction degeneracies are well known to affect any interpretation of UV-optical data alone (Worthey 1994; Arimoto 1996; Worthey 1999; Vazdekis & Arimoto 1999; Vazdekis 2008). This means that different combinations of model parameters are able to reproduce the same data sets.

In order to improve on these problems, and to try to go deeper into the study of galaxy properties, it is important to consider wider spectral ranges, with typically an amount of data much larger than the models parameters. The reason is that different spectral ranges tend to be dominated by different specific emission sources or radiative processes which affect the light as it travels through the ISM. Therefore by analyzing the whole spectral range one can hope to deconvolve all the different information contained in the SED in terms of the SFR history and galaxy evolution in general.

Stellar sources mainly emit in the UV-optical to near IR spectral range, and the SED in this wavelength region is therefore heavily influenced by the star formation history of the galaxy and as a result can be used to study the specific mixture of ages, metallicity and mass distribution of the stellar populations.

UV photons mainly from massive short-lived stars ionize and excite the gas, producing HII regions with emission lines, that are probes of the SFR and the chemistry, energetics and physical state of the ISM where they are produced. These same ionized nebulae are the sites of the production of the free-free emission providing the thermal component of the radio continuum emission from normal galaxies. The non-thermal radio emission is interpreted as synchrotron radiation arising from energetic electrons accelerated in supernova remnant shocks and moving in the galactic magnetic field Condon (e.g. 1992).

The SED from a few μm to the sub-mm (the IR region) is dominated by the interaction of dust grains with stellar radiation. Dust in galaxies, although only a small fraction of the mass of gas ($\sim$ 0.01 in our Galaxy), is a fundamental ingredient prevalent in many environments, such as circumstellar envelopes, supernova remnants, star-forming regions and diffuse clouds. Dust grains absorb and scatter short wavelength stellar radiation (below $\lambda \sim 1\mu$m) with high efficiency and thermally emit the absorbed energy in the IR.

Several panchromatic SED modelling exists in literature, based on different approaches. Some works (e.g. Devriendt et al. 1999; Chary & Elbaz 2001; Dale et al. 2001; Dale & Helou 2002; Galliano et al. 2003; Lagache et al. 2003; da Cunha et al. 2008) have proposed semi-empirical treatments of the SEDs.

The aim of these works is in general to interpret very large samples of data, requiring fast computing

times making use of observationally or physically motivated SEDs. Other works are based on theoretical computations of the radiative transfer in order to have a more general applicability. Within this approach different components and levels of complexity have been considered Rowan-Robinson & Crawford (1989); Silva et al. (1998); Siebenmorgen & Krügel (2007); Groves et al. (2008); Popescu et al. (2000); Gordon et al. (2001); Baes et al. (2003).

In this thesis we have combined our detailed newly computed suite of SSP, for which we have computed also the H recombination lines, the free–free continuum emission and the non -thermal radio emission, with the radiative transfer code GRASIL (Silva et al. 1998; Silva 1999; Granato et al. 2000; Bressan et al. 2002; Silva et al. 2002; Panuzzo et al. 2003; Vega et al. 2005; Silva et al. 2011). This is a relatively realistic and flexible multi-wavelength model, which calculates galactic SEDs by assuming a realistic geometry, the radiative effects of different dusty environments, and the clumping of stars and dust within a more diffuse medium. In this way we can calibrate and interpret the observed UV to radio SED of star forming galaxies. We have concentrated in this work first on the detailed analysis of one archetypal spiral galaxy, M100. This is because of the large available data coverage, that allows to well calibrate the non-thermal radio emission for a galaxy in a stationary situation. We have then studied in detail the SEDs of the single star forming regions in the starburst galaxy NGC6946. These rapidly evolving regions allow us to highlight the contribution of the newly computed free-free emission included in the SSP and to retrieve information on the relations among the different wavelength regions.

1.3 Scheme of the thesis

In Chapter 2 we first provide a thorough review of the PARSEC stellar evolutionary tracks, stellar atmospheric libraries, and stellar isochrone library that are at the base of our SED modelling. The stellar models have been recently updates, with important changes on some basic physical assumptions. Therefore we have computed a SSP library based on this new set of models. In this Chapter we show the continuum SED of the new SSP library, computed for the Kennicutt IMF but with 4 different values of the maximum mass limit.

In Chapter 3 we use our new SSP library together with the photoionization CLOUDY to compute the nebular emission lines and continuum by assuming that young SSPs are the central ionizing source of HII regions. The extincted SED of the SSP is then summed with the output nebular luminosites to provide the new SSP SED library.

In Chapter 4 we discuss how we include in the SSPs also the non-thermal radio emission. The new stellar models for massive stars in PARSEC are characterized by a major revision of the range of masses that undergo core collapse SN. This introduces an important behavior on the age evolution of the shape of the total radio emission. Both the thermal and non-thermal emissions are included in the final SSP SEDs.

In Chapter 5 we combine our new SSP library with GRASIL in order to model the full UV to radio SED

of galaxies, including the reprocessing by dust of the stellar radiation and of the nebular lines. First, we need to calibrate the non-thermal component of the SSP in order to reproduce, for a normal galaxy in steady evolution, the FIR to radio ratio. We have adopted to this aim the archetypal M100 spiral galaxy. We fit the full observed SED separately for the 4 different IMF mass limits.

In Chapter 6 we have analyzed the full SED of several single star forming regions observed within the starburst galaxy NGC6946. These non steady regions allow us to highlight the importance of our thermal radio emission modelling in combination with the other spectral regions, and also to discuss the dependence of the best fits on the IMF mass limits.

In Chapter 7 we discuss the relations between SFR and luminosity in different bands, by showing the necessity of different assumptions when dealing with galaxies in steady evolution or in a fast starburst phase. Also we show explicitly the dependences on the different IMF mass limits.

In Chapter 8 are the summary and conclusions.

Chapter 2

Panchromatic spectra of simple stellar populations

The modelling of the spectral energy distribution (SED) of star forming regions and galaxies with the spectral synthesis technique, is based on the availability of a spectral library of simple stellar populations (SSP), i.e. of single generation star clusters whose integrated SED depends on age, initial metallicity and initial mass function (IMF) of the constituent stars. Therefore, in order to compute a reliable SSP library covering a large range of the parameters, the required ingredients are detailed models of stellar evolutionary tracks and of stellar photospheres. Our stellar tracks are computed with the stellar evolution code *PARSEC*, the *P*adova T*R*ieste *S*tellar *E*volution *C*ode (Bressan et al. 2012). In this chapter we review the properties of *PARSEC*, with particular emphasis on the most recent and major updates, and of our reference stellar spectral library (Chen et al. 2015). After a biref review of the method of the isochrones synthesis commonly used to translate the stellar tracks to single generation stars of given age and metallicity, I describe the new set of simple stellar population (SSP) spectra I have calculated for the present work.

2.1 New evolutionary tracks with PARSEC

The Padova repository of stellar evolutionary tracks and isochrones is a widely used database that allows the astronomical community to obtain predictions of observational properties of stars. It has been updated continuously by several authors during the last two decades, and *PARSEC* is the most recent version of the stellar evolution code used to compute these tracks. In particular the new models of massive stars computed with *PARSEC* (Tang et al. 2014; Chen et al. 2015) supersede the old ones that were computed more than twenty years ago. The code is fully described by Bressan et al. (2012) but for the sake of convenience, we synthesize below the major changes.

- All the major physical processes have been revisited and, where necessary, updated with the most recent prescriptions. This concern the equation of state, for which we adopt the *FREE-EOS* CODE (Irwin

2012), the radiative opacities, which now take into account the new molecular opacities computed with the *ÆSOPUS* code (Marigo & Aringer 2009) and the nuclear reaction rates that are now taken form the *JINA REACLIB* database (Cyburt et al. 2010). Besides changing the input sources we have also refined the interpolation schemes and, for example, the constitutive equations of the stellar structure can now be computed following the variations of the global internal metallicity caused by different mixing processes.

- The code accounts for microscopic atomic diffusion. This is important not only for the modelling of the old stellar populations but also to obtain an accurate calibration of the mixing length parameter from the observed Sun. We refer in particular to the ability of reproducing not only the surface quantities like luminosity, effective temperature and radius, but also quantities derived from helioseismology like the internal run of the density and sound speed velocity profiles and the position of the bottom of the convective envelope. The calibration, that is a necessary step after the changes in constitutive and structure equations, has allowed a robust determination of the mixing length parameter. It is important to recall here that a major variation in recent years is concerned with the partition of the heavy elements of the Sun. The reference solar metallicity value has changed from about Z=0.018 (Grevesse & Sauval 1998) to Z=0.012 (Asplund et al. 2005) and more recently has risen again to $Z = 0.01524$ (Caffau et al. 2011), our adopted solar reference value, or to Z=0.0134 (Asplund et al. 2009). We recall that these values do not refer to the initial solar metallicity but to the current solar metallicity, and that the initial solar metallicity, as well as the intial He content of the Sun, must be derived by the aforementioned calibration process.

- The pre-main sequence phase (PMS) has been also implemented and the tracks begin as homogeneous contracting spheres with central temperature T$\sim 10^5$ K. The PMS phase is computed at constant mass but it can be also computed accounting for accretion. In the domain of low and very low mass stars the location of the Zero Age Main Sequence is poorly defined. In general below an initial mass of M$\sim$0.6 $M_\odot$ the models show radii that are progressively too small with respect to observations, at decreasing initial mass. This is common to all models of very low mas stars when an attempt to compare with observed radii has been made. The average relative difference in radius around M$\sim$0.2 $M_\odot$ is of about 5%. The physical reason of this discrepancy is not yet known. However Chen et al. (2014) have eliminated the discrepancy by considering a small shift in the relation providing the temperature at a given optical depth obtained by stellar atmosphere models.

- The models adopted here (the published models) end their evolution at the beginning of either the thermally pulsing phase or of the central carbon burning. The AGB phase is added to the evolutionary tracks using the *COLIBRI* AGB models (Marigo et al. 2013). The *COLIBRI* code contains a fast numerical method to compute the AGB evolution of a star of any mass and composition, once the initial conditions of a model entering such phase are provided. In our case these conditions are provided by the first thermal pulses computed by *PARSEC*. The main advantage of the *COLIBRI* code is that, because of its rapidity and flexibility, it allows a rapid but wide exploration of the effects of the main physical processes accompanying the AGB evolution. Among others we recall, efficiency of the third dredge up

and of the mass-loss rate. The efficiency of the hot bottom burning is instead an output of the models. In this respect it is worth noting that only this code is able to follow the AGB evolution with molecular opacities that are simultaneously recomputed at varying chemical composition as caused, for example, by the variation of carbon, nitrogen and oxygen abundances due to the eventual third dredge up and hot-bottom burning processes. We note that the most recent version of *PARSEC* follows massive star evolution up to the beginning of the central oxygen burning but we have not considered it here because the results are preliminary.

- The mass loss process in massive stars has been profoundly revised (Tang et al. 2014; Chen et al. 2015). Mass loss in massive stars is considered only for masses above $12 M_{\odot}$. The algorithm used for the new sets of massive star models has been obtained by combining several prescriptions found in literature for the different spectral types. In the Blue Super Giant (BSG) phases ($T_{\rm eff} \geq$ 12000 K) *PARSEC* adopts the relations of Vink et al. (2000, 2001). In the red supergiant phases ($T_{\rm eff} <$ 12000 K) the relations provided by de Jager et al. (1988) are used while, in the Wolf-Rayet (WR) phases, the formalism by Nugis & Lamers (2000) is adopted. We have also included in our formalism the explicit dependence of the mass-loss rates on the ratio of the stellar luminosity to the corresponding Eddington luminosity, Γ, as described by Vink et al. (2011) for O stars of solar metallicity and by Gräfener & Hamann (2008) for WR stars of different metallicity. In brief, both authors find that the mass-loss rates are strongly enhanced when the stars approach the Eddington limit and, in particular, while all formulations show a dependence of the mass loss rate on the metallicity (generally $\dot{M} \sim Z^{-0.8}$), this dependence becomes much shallower when the stars approach the Eddington limit. It is worth noticing that, by including this dependence for the mass-loss rates, the models are able to reproduce the observed Humphreys-Davidson limit (Humphreys & Davidson 1979), observed at near solar metallicity (Chen et al. 2015).

- Finally, the new grids of stellar evolutionary tracks have a larger mass resolution and have a significantly broader range in both initial mass, from M=0.1 $M_{\odot}$ to M=350 $M_{\odot}$, and metallicity, from Z=0.0001 to Z=0.07. The models have been published only for the solar partition of heavy elements, though models with different partitions have been computed for sake of comparison. New sets with non solar partition are under calculation and will be soon published.

We note that the effects of rotation on stellar evolution (Huang & Struve 1954; Meynet & Maeder 1997; Maeder et al. 2000; Maeder & Meynet 2003; Leitherer et al. 2014; Aerts 2015) are not included in the published models though they are currently being included in *PARSEC*. Another effect that is not yet included in the models is that of the interaction caused by binarity (de Mink 2010; de Mink et al. 2013; Zhang et al. 2004, 2005) .

As an example and for illustration purposes, we show in Figure 2.1 some of these evolutionary tracks for four different metallicities (Z = 0.0001, 0.004, 0.02 and 0.06) and for stellar masses ranging from 12 $M_{\odot}$ to 350 $M_{\odot}$.

A preliminary comparison of the new models with observed colour-magnitude diagrams (CMD) of star-forming regions in three selected nearby low metallicity dwarf irregular galaxies (Sextans A, WLM and NCG6822) was performed by Tang et al. (2014). The new models were also already used to construct

ultraviolet, optical and NIR integrated spectra and emission line properties of galaxies by Gutkin et al. (2016).

The full set of new evolutionary tracks and the corresponding isochrones can be found in `http://people.sissa.it/~sbressan/parsec.html` and `http://stev.oapd.inaf.it/cgi-bin/cmd`, respectively. In the next section, we will focus on how to compute the integrated spectra from the evolutionary tracks.

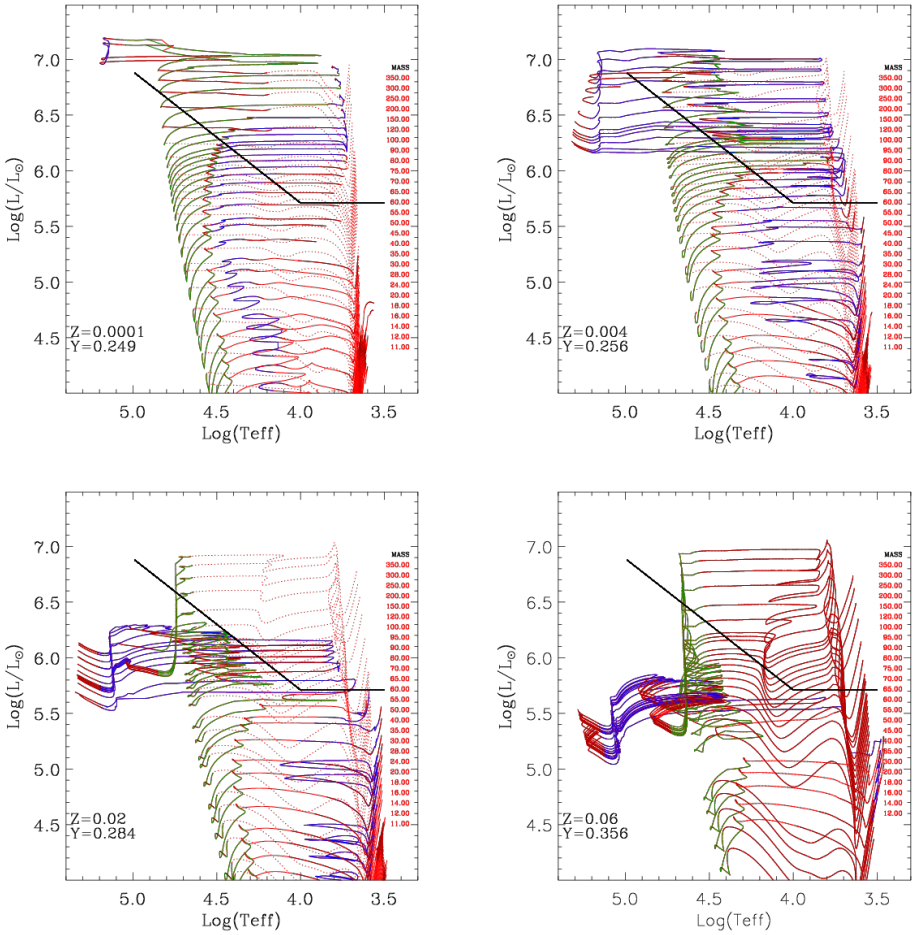

Figure 2.1: New PARSEC evolutionary tracks (V1.2s version) for four different metallicities (Z = 0.0001,0.004,0.02 and 0.06) and for stellar masses ranging from 12 $M_{\odot}$ to 350 $M_{\odot}$. The central hydrogen burning phase is indicated in blue, the central helium burning phase in green and the expansion/contraction phases in red. The black line represents the Humphreys & Davidson (1979) limit, which marks the region of the HR diagram where there are no observed supergiant stars at near solar-metallicity due to the enhanced mass-loss in this region.

2.2 From stellar tracks to isochrones

The integrated spectrum of a SSP of a given age is a weighted sum of the spectra of all the stars of that SSP at the selected age (see Equation 2.1 below). It is therefore necessary to first obtain, from the database of stellar tracks that represent all the possible evolutionary phases of a star of any mass,

chemical composition and age, the locus of the models with constant age and metallicity, which is simply called the "isochrone" that corresponds to the SSP.

Considering only a given metallicity, the evolutionary tracks represent loci of constant initial mass and varying age, while isochrones represent loci of constant age and varying initial mass. There are several methods described in literature by which one may generate an isochrone starting from a set of evolutionary tracks (Chiosi et al. 1988; Maeder & Meynet 1988; Buzzoni 1989; Charlot & Bruzual 1991; Maraston 1998, 2005)

This is not a trivial step as it may in principle appear mainly because evolutionary tracks contains important phases that have greatly different lifetimes. It is possible to show (Buzzoni 1989; Renzini & Fusi Pecci 1988) that the important quantity that must be preserved in modelling the advanced evolutionary phase is neither time nor luminosity but the product of the two. Short lived (i.e. relatively less populated) luminous phases in the HR diagram may contribute to the total integrated spectra as long lived (i.e. well populated) less luminous phases. Thus a well behaved isochrone must account for all the contributing evolutionary phases of the interested tracks, even the shortest if these are relatively important in the integrated spectra. The basic algorithm consists in constructing a class of so called auxiliary tracks obtained by interpolation from the ones explicitly calculated with stellar evolution models. Here the difficulty is to select the better interpolation scheme and one is guided by the consideration that, at the end, stars (of similar metallicity and mass) that occupy nearby position in the HR diagram have also similar spectra. Thus the better scheme is the one that allows a smooth transition in any region of the HR diagram, between tracks of different mass. In short one efficient scheme must be able to generate auxiliary tracks of any mass within the allowed range, preserving the morphology of the base tracks. This is commonly done by dividing the tracks in pieces of 'equivalent' evolutionary phases and by generating a new independent variable that describes the evolutionary phase of the track of a given mass. This will be the independent variable that will be used to interpolate new auxiliary tracks from the base tracks. For example, the total life time of an auxiliary track of a given mass will be interpolated from the last value of the phase variables of the bracketing tracks of the initial database. In this way the evolution of an auxiliary mass can be fully reconstructed from two bracketing original tracks. The method involves a careful selection of evolutionary phases and a careful dealing of discontinuous evolutionary phases, such as the transition between stars with He flash ignition and those slightly more massive that ignite central Helium in a non electron-degenerate core. Similarly another transition is present between stars that evolve through the AGB phase and stars that instead are able to ignite Carbon in the center. An example of isochrones obtained with this procedure is shown in Figure 2.2.

2.3 The Stellar Spectral Library

Stellar atmospheric libraries are used to transform the stellar tracks and isochrones from the theoretical quantities to the observational ones, i.e. from luminosities and effective temperatures to magnitudes and spectra.

Our adopted spectral library is based on the work by Chen et al. (2015), who homogenised different

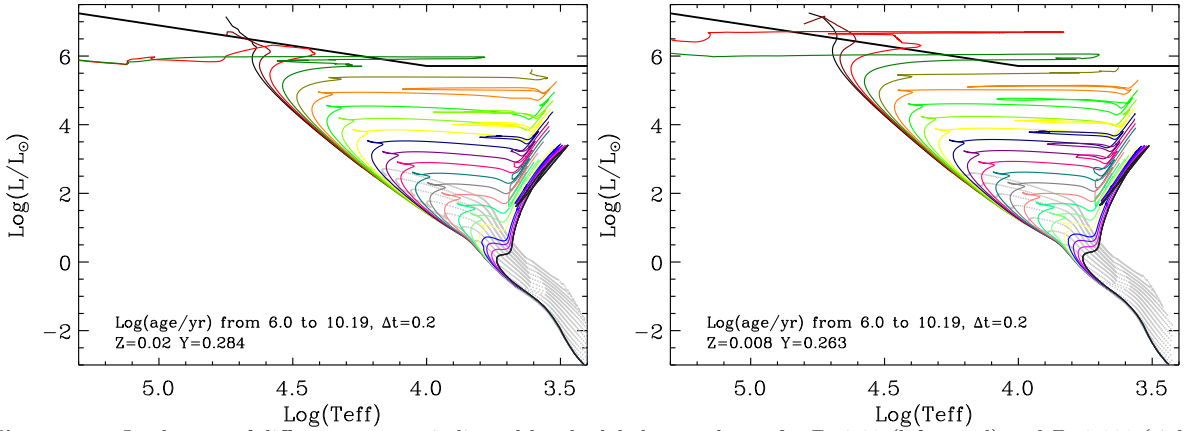

Figure 2.2: Isochrones of different ages, as indicated by the labels, are shown for Z=0.02 (left panel) and Z=0.008 (right panel). Note that at young ages intermediate and low mass stars are still on the pre-main sequence (grey dots). The Humphreys-Davidson limit is also drawn as in figure 2.1.

sets of existing stellar atmosphere libraries for both cool and hot stars, as outlined in the following. Chen et al. (2015) used the *ATLAS9* models (Kurucz 1993; Castelli & Kurucz 2004), for intermediate and low mass stars with photospheric temperatures between 6000 K and 19000 K, the public code WM-Basic for temperatures between 19000 K and 60000 K. For the coolest stars, Teff $<$ 4500 K they adopt the Phoenix models (Allard et al. 1997).

For hot massive stars were mass-loss may be so strong to affect the outcoming energy flux distribution, Chen et al. (2015) generated new atmosphere models with the *WM-BASIC* code Pauldrach et al. (1986), that accounts also for the effects of radiation driven wind. For Wolf Rayet stars, where the winds may be even stronger they adopted the new models of the Potsdam group (see e.g. Sander et al. 2015).

The above models have been generated with different codes by different authors. In particular, the different sets of libraries have different metallicities and they have been homogenized by means of a suitable interpolation, on a common grid of metallicities, the one adopted by the *PARSEC* models (Girardi et al. 2002; Chen et al. 2014, 2015). These libraries have already been used by Chen et al. (2014, 2015) to compute magnitude and colours for the individual stars and their ability to reproduce the colour-magnitude diagrams of star clusters of different ages and metallicities has already been tested (e.g. Tang et al. 2016; Rubele et al. 2015; Tang et al. 2014).

As an example, Figure 2.3 from Chen et al. (2015), shows the different spectral libraries used in the different regions of th HR diagram. The tracks show the evolution of selected stellar models and the vertical lines represents the limits adopted for the different atmosphere sets. In the case of stars, the libraries are used to derive the corresponding magnitudes but the same process is also adopted for constructing the integrated spectrum with the only difference being that, instead of evolutionary tracks, we deal with isochrones in the HR diagram.

2.4 The Initial Mass Function

The integrated spectrum (flux emitted per unit frequency), f_ν^{ssp}, of SSPs of age t, and metallicity Z is obtained as the sum of the spectra of individual stars along the isochrone, weighted by the initial mass

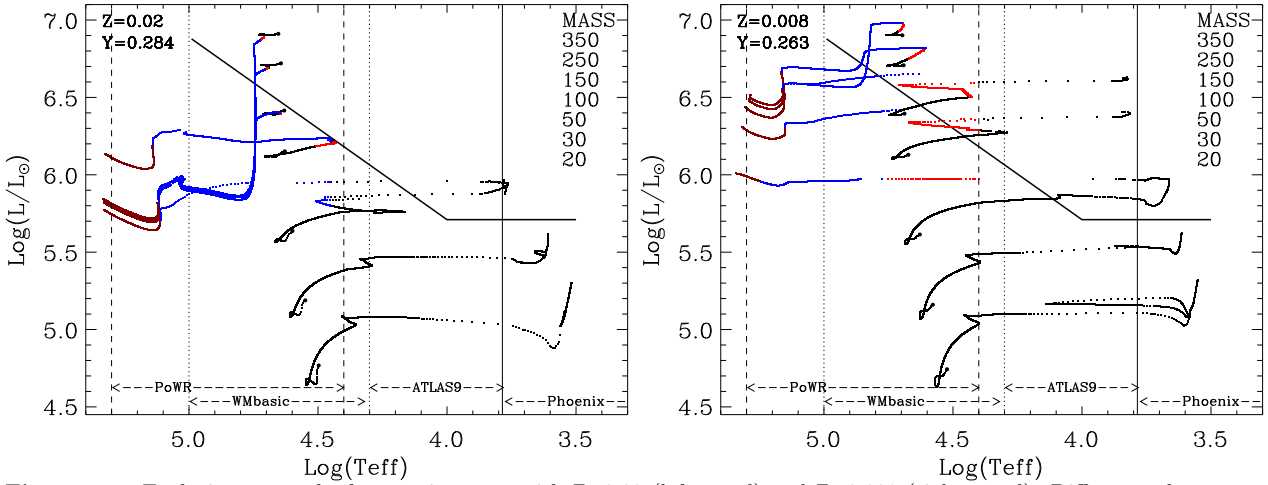

Figure 2.3: Evolutionary tracks for massive stars with Z=0.02 (left panel) and Z=0.008 (right panel). Different colours represent different evolutionary stages: black for stages precedent of WR phases, red for models using PoWR WNL-H50 ($Z = 0.02$) or WNL-H40 ($Z = 0.008$), blue for WN models, and brown for WC models. The over-plotted vertical lines delimit the coverages of different atmosphere models as indicated in the plots. The Humphreys-Davidson limit is also drawn as in figure 2.1.

function:

$$f_\nu^{SSP}(t, Z) = \int_{M_{low}}^{M_{up}} f_\nu(m, t, Z)\phi(m)dm \tag{2.1}$$

where m is the initial mass of the star and $dN = \phi(m)dm$ represents the number of stars with initial mass between m and $m+dm$, with a normalization constant that generally refers to one solar mass initially formed. The isochrone locus is not explicitly shown in the above integral, but the function $f_\nu(m, t, Z)$ is actually $f_\nu(g(m, t, Z), T_{eff}(m, t, Z), L(m, t, Z))$ with g -surface gravity-, T_{eff} -effective temperature- and L -stellar luminosity- describing the locus of the isochrone of age t and metallicity Z as a function of m, in the HR diagram.

As already anticipated, the integration 2.1 requires the use of one or more sets of stellar atmosphere libraries that provide f_ν over a wide parameter space in log g, T_{eff} and Z. With this so called 'isochrone synthesis' method we obtain the integrated spectral energy distribution of SSPs. The integrated spectra only account for the effects of stars, i.e. they only contain continuum and absorpton features characteristic of stellar atmospheres. For the most massive stars the atmosphere may also contain emission line features that forms in the expanding wind.

As for the IMF, in this work we have adopted a simple two-slope power law (Kennicutt 1983):

$$dn/dm \propto m^{-\alpha} \tag{2.2}$$

with the slope $\alpha = 1.4$ in the mass interval 0.1 $M_\odot$ - 1 $M_\odot$ and $\alpha = 2.35$ for ≥ 1 $M_\odot$. This law has been selected for its simplicity, especially in performing analytic calculations and checks and because, at the same time, it seems more realistic than the other very simple number distribution, the Salpeter (Salpeter 1955) one. Indeed the number of massive stars predicted per unit mass by this IMF is very similar to that obtained with the Chabrier one (Chabrier 2003), as shown in Table 2.1.

Table 2.1: Relative massive stars fractions for different IMF, this work (KEN), Chabrier (Chabrier 2003) (CHA) and the Salpeter (Salpeter 1955) (SAL). The $MassNormalization$ is the total mass in solar masses of the IMF without a normalization constant. M is the mass integral and N is the number integral.

M_{UP}	40 $M_\odot$	80 $M_\odot$	120 $M_\odot$	350 $M_\odot$
$Normalization$				
KEN	3.3195	3.4888	3.5703	3.7374
CHA	0.0754	0.0794	0.0813	0.0855
SAL	5.6107	5.7800	5.8615	6.0286
$M > 1\ M_\odot/M_{Tot}$				
KEN	0.6240	0.6423	0.6504	0.6661
CHA	0.5665	0.5882	0.5981	0.6177
SAL	0.3692	0.3877	0.3962	0.4129
$M > 10\ M_\odot/M_{Tot}$				
KEN	0.1478	0.1891	0.2077	0.2431
CHA	0.1443	0.1870	0.2067	0.2454
SAL	0.0874	0.1142	0.1265	0.1507
$N > 1\ M_\odot/M_{Tot}$				
KEN	0.2216	0.2117	0.2071	0.1981
CHA	0.1937	0.1849	0.1807	0.1722
SAL	0.1311	0.1278	0.1262	0.1228
$N > 1\ M_\odot/N_{KEN}$				
CHA	0.8741	0.8734	0.8725	0.8690
SAL	0.5916	0.6036	0.6091	0.6199
$N > 10\ M_\odot/M_{Tot}$				
KEN	0.0084	0.0089	0.0089	0.0088
CHA	0.0082	0.0087	0.0087	0.0085
SAL	0.0050	0.0054	0.0054	0.0054
$N > 10\ M_\odot/N_{KEN}$				
CHA	0.9693	0.9737	0.9747	0.9736
SAL	0.5916	0.6036	0.6091	0.6199

As can be seen from Table 2.1, the number of stars more massive than M=1 $M_\odot$ in the Chabrier initial mass function is about 14% smaller than that obtained with our IMF (Kennicutt (1983)two power law). However, since the slope of the IMF in the massive star regime we have adopted is $dn/dm \propto m^{-2.35}$, slightly steeper than the formal exponent of the Chabrier IMF (-2.30 ± 0.3), the fraction of massive stars ($M \geq 10\ M_\odot$) is very similar in the two aforementioned IMF distributions (last but one row in Table 2.1). Thus at a given star formation rate the number of massive stars in our adopted IMF is about 3% larger that that obtained with the Chabrier IMF. This implies that a slightly lower SFR ($\sim$3%) is needed to produce the same luminosity in young SSPs, with our IMF. If one adopts the Chabrier IMF, the relations derived between the SFR and the luminosity (in any band, if they are due to massive stars) must be rescaled by dividing the required SFRs by the factors shown in the last but one row in Table 2.1.

For comparison we see that the Salpeter (Salpeter 1955) IMF yields significantly less massive stars ($\approx$60%) than our IMF. The comparison with results obtained with a Salpeter IMF must take into acccount that this IMF implies a significantly lower number of massive stars.

2.5 Integrated photospheric spectra of SSP

We have considered five values of the initial metallicity Z=0.0005, Z=0.001, Z=0.004, Z=0.008 and Z=0.02 and we have considered four different values of the upper mass limit, M_{up}, of 40, 80, 120 and 350 $M_\odot$. As an example, we show in Figure 2.4 , the synthesised spectra of SSP at ages of t = 2, 5 and 40 Myr and for three values of initial metallicities, Z = 0.02, 0.004 and 0.0001.

The effect of assuming different M_{up} values, at fixed total initial mass, is more pronounced at an age of 2 Myr. At 5 Myr, when stars with masses of 120 $M_\odot$ and 350 $M_\odot$ have already left the main sequence or already died out, the spectra of SSP with upper mass limits of 80 ,120 and 350 $M_\odot$ are superimposed, while those of 40 $M_\odot$ remains distinct. At 40 Myr the spectra are almost independent of M_{up}, though the spectrum of the SSP with larger M_{up} has a lower luminosity, because of the higher mass budget stored in massive stars. We already note from this figure that the effects of M_{up} on the number of ionizing photons disappears at ages larger than about 5 Myr, as discussed below.

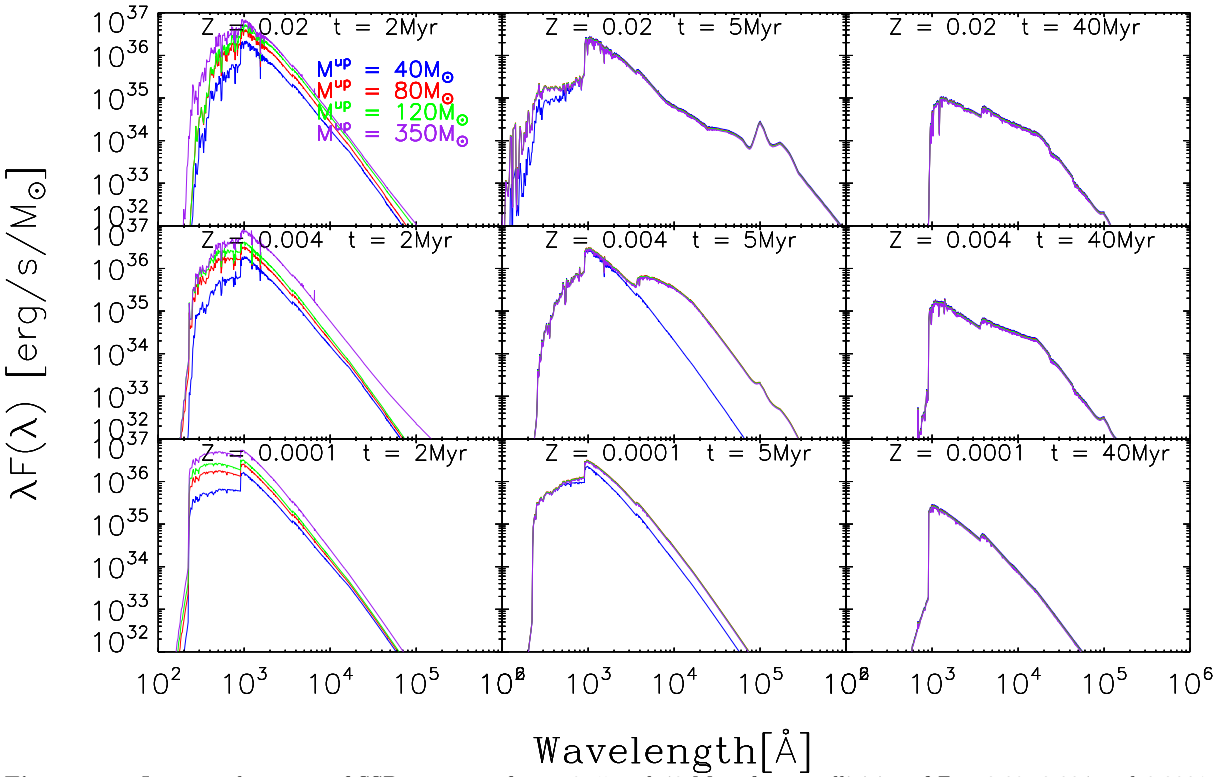

Figure 2.4: Integrated spectra of SSPs at ages of t = 2, 5 and 40 Myr, for metallicities of Z = 0.02, 0.004 and 0.0001, as indicated in the different panels. Different values of M_{up}=40, 80, 120 and 350 $M_{\odot}$ are indicated by the solid blue, red, green and purple lines respectively.

Chapter 3

Nebular Emission

Stellar populations may contain stars with sufficiently high effective temperatures that the emitted radiation is able to ionize part or all of the surrounding interstellar medium. Examples of such stars may be the hot post-AGB stars, whose temperature may even reach a few 10^5K, and whose most known example of ionized environment are the planetary nebulae (PN), or the massive hot stars stars ionizing the so called HII regions. The latter stars are actually the most important producers of stellar ionizing radiation in star forming galaxies, while the former objects may be important producers of stellar ionizing radiation in passively evolving galaxies. Furthermore it is important to recall that, while the previous examples are characteristic of single stellar evolution, other stars may reach these high surface temperatures because of the stripping of the external envelope by the action of a binary companion. In this chapter we will analyze and model how the integrated spectra of stellar populations are modified by the presence of a surrounding ionized ISM, with particular emphasis on the case of young stellar population which contains HII regions. For this purpose we will briefly review in this chapter the problem of 'nebular emission' which refers to the study of the conditions and the results of the presence of ionizing radiation inside a region of the ISM. Since there are in literature textbooks[1] and specific papers on the subject (Bowen 1928; Rubin 1968b; Osterbrock 1989; Condon & Ransom 2016), here I will only briefly summarize the main processes at work and I will instead concentrate on how I have computed the line and continuum emission of our SSP with the photoionisation code CLOUDY (Ferland 1996; Ferland et al. 2013)[2]

3.1 HII Regions: General overview

Two main processes govern the physics of HII regions. One is the balance between the photoionization rate induced by the stellar radiation field and the spontaneous recombination between electrons and ions. In a stationary case the surrounding gas may reach the so called photoionization equilibrium where the two rates exactly balance each other. At the same time there is a thermal balance between heating and cooling processes, because free electrons tend to heat the surrounding medium while other processes

[1] e.g. http://www.cv.nrao.edu/course/astr534/HIIRegions.html
[2] http://www.nublado.org

like the escape of line radiation from the region tend to cool it. Additional processes may also occur and modify this simple picture like when one include hydrodynamic processes like shocks generated by outflows and winds from the embedded stars.

In the case of a spherically symmetric pure hydrogen nebula one may write, at a given radius r from the central ionising source, the rate of photoionisations per unit volume as

$$n_{H^0} \int_{\nu_0}^{\infty} \frac{4\pi J_\nu(r)}{h\nu} a_\nu d\nu \tag{3.1}$$

where n_{H^0} is the density of neutral hydrogen atoms in cm^{-3}, ν_0 is the cutoff frequency (13.6 eV or 3.29 PHz), J_ν is the mean radiation intensity (erg cm^{-2} s^{-1} Hz^{-1} sr^{-1}) and a_ν is the photoionisation cross section (cm^2).

On the other hand, the rate of recombinations per unit volume is given by

$$n_e \; n_p \; \alpha(H^0, T) \tag{3.2}$$

where n_e and n_p are the electron and proton densities (cm^{-3}) respectively, $\alpha(H^0, T)$ is the rate coefficient for recombination (cm^{-3} s^{-1}). If we assume that the radiation field J$_\nu$ arises entirely from a single ionising central source and ignore contributions that come from the diffuse radiation inside the nebula, we then have

$$4\pi J_\nu(r) = \frac{L_\nu}{4\pi r^2} \tag{3.3}$$

The photoionisation equilibrium condition is found by balancing the local photoionization and recombinations rates given above

$$\xi n_H \int_{\nu_0}^{\infty} \frac{L_\nu}{4\pi r^2} \frac{a_\nu}{h\nu} d\nu = (1-\xi)^2 n_H^2 \alpha(H^0, T) \tag{3.4}$$

where ξ is the hydrogen neutral fraction which relates the densities of electrons, protons and neutral hydrogen such that $n_e = n_p = (1-\xi) n_H$ ($\xi = 0$ implies fully ionised and $\xi = 1$ fully neutral).

Assuming an average value for the photoionisation cross section a_ν, we see that the left hand side of Equation 3.4 contains the quantity

$$Q(H) = \int_{\nu_0}^{\infty} \frac{L_\nu}{h\nu} d\nu \tag{3.5}$$

which represents the number of Hydrogen ionizing photons emitted by the central source per unit time. This quantity, which will be discussed in more detail in a following section, is one of the fundamental parameters regulating the properties of the ionized regions.

To proceed further one needs to analyze the thermal equilibrium between heating and cooling processes. For this purpose one needs to consider the details of the heating and cooling mechanisms. As for the heating processes the main mechanism is the energy input by photoionization, i.e. the kinetic energy of photoelectrons that is thermalized in the surrounding ISM. As for the cooling processes the main ones are the energy loss by recombinations, by emission of free-free radiation, and by line radiation from collisionally excited ions of heavy elements (C,N,O, Ne, S etc.) which give rise to important emission lines. Finally there is the line radiation loss by the collisionally excited neutral Hydrogen in the foundamental

level that, in spite of the very small abundance of neutral hydrogen atoms in an ionized nebula, is an important source of emission, the so called two photon emission.

The calculation of the emitted spectrum from a volume element of the ionized nebula depends on the local thermodynamical conditions that are determined by all the above processes and by the characteristics of the nebula like its element abundance, ion density and ionization photon flux denisty, $Q(H)/4\pi r^2$.

All these quantities are taken into account by the photoionization codes existing in literature. In the next section I will discuss the parameters I have adopted with the code CLOUDY, to obtain the emitted spectrum of the HII regions.

3.2 Overview of the photoionisation code CLOUDY

Photoionization codes are indispensable tools used to describe the properties of gas irradiated by an ionizing source. Most of the existing photoionization codes are static and treat gas in thermal equilibrium and ionization balance. The main differences between these photoionization codes are mainly (a) in the assumed geometry (plane-parallel or spherical geometry or 3D); (b) time-dependent versus static cases; (c) accounting for hydrodynamical effects; (d) adopted atomic data (mainly concerning the data sources).

In this work, I use the photoionisation code CLOUDY (Ferland 1996; Ferland et al. 2013)[3] to compute nebular emission from HII regions. Other widely used photoionisation codes are Mocassin (Ercolano et al. 2003), Mappings (Sutherland & Dopita 1993) and XStar (Kallman 1999).

CLOUDY can compute the emitted spectrum of an ionized region over a wide range of physical conditions. In our case, in order to compute the synthetic spectrum emerging from gas ionized by young stars, we have to specify the following main input parameters.

- The shape of the incident ionizing continuum. In the context of this work it is the spectrum of the ionising star clusters, represented by our SSP spectra, for different ages and for the metallicities corresponding to the evolutionary tracks discussed before.
- The chemical composition.
- The geometry of the gas. Different geometries may be adopted for the gas distribution around the central source, as shown in Figure 3.1.
- The total hydrogen density of the gas, n_H.

The input parameters I have adopted are discussed in more detail in Section 3.2.2. After the incident continuum and initial conditions are specified, CLOUDY computes the thermal, ionization and chemical structure of the ionized cloud and the emergent spectrum (including nebular absorption and emission) by simultaneously solving the equations of thermal and statistical equilibrium, the equations that balance ionization-neutralization processes, and the heating-cooling processes. The continuum computed by CLOUDY is composed of several components: the diffuse continuum emitted by the gas and grain within the nebula, the reflected continuum (which is only computed for an open geometry in CLOUDY) emitted

[3] http://www.nublado.org

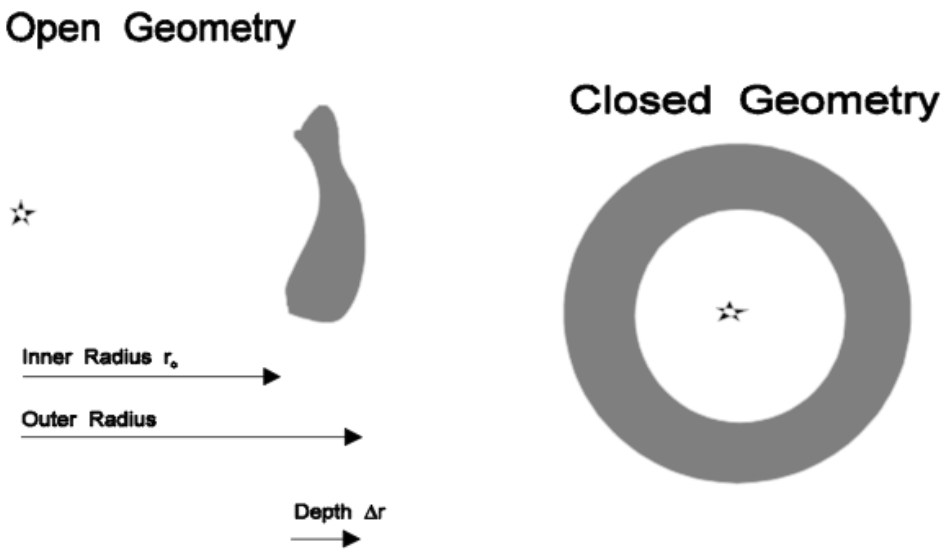

Figure 3.1: The two limiting geometries, open and close geometry, that can be assumed for the HII region. The grey area represents nebular gas. (Picture Credit: Hazy/CLOUDY)

from the illuminated face of the cloud towards the central source, and the transmitted continuum which is the net continuum emerging from the shielded face of the the cloud. The latter continuum includes both the attenuated incident continuum and the transferred diffuse continuum. These various continua are illustrated in Figure 3.2.

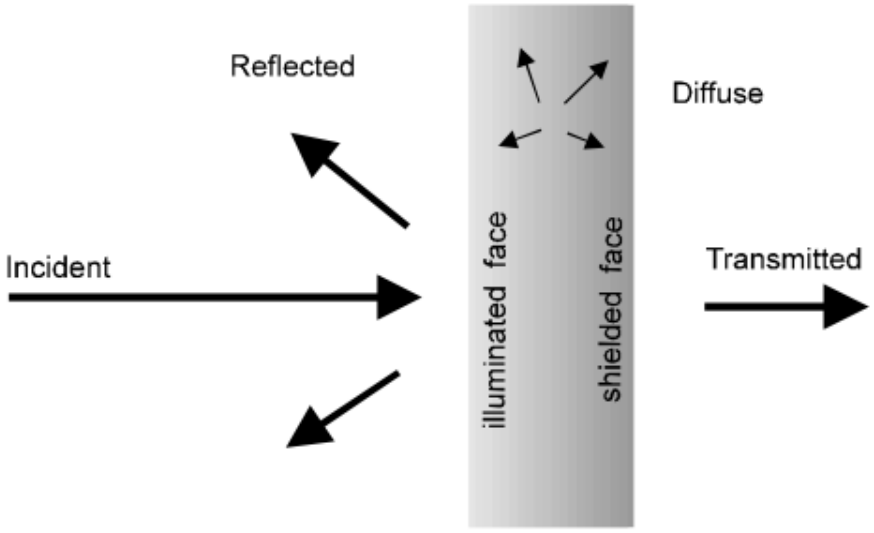

Figure 3.2: Illustration of the several continua involved in CLOUDYs computation of the line intensities. (Picture Credit: Hazy/CLOUDY)

3.2.1 Ionizing photon luminosities

The shape of the incident continua supplied to CLOUDY are derived from the integrated spectra of the SSP, some of which have been already shown in Figure 2.4. From these spectra it is simple to determine the ionizing photon luminosities Q(H) of our young SSP. As already specified before, we are not interested here in ionized nebulae associated with post-AGB stars of intermediate and old stellar populations. While important for the studies of their parent populations, the ionizing photon luminosities of these regions are generally much lower than those typical of HII regions. In star forming galaxies, the main producers of ionizing photons are O-B main sequence stars and Wolf Rayet stars. Thus the number of these photons is critically dependent on the shape of the initial mass function in the domain of massive stars. While CLOUDY internally computes the corresponding ionizing photons luminosities, we show in this section how these luminosities depend on the stellar population parameters like age, metallicity and IMF. We thus obtain the Hydrogen ionizing photons production rate Q(H), in s^{-1}, as a simple integral of the SSP spectra computed in Section 2.5:

$$Q(H) = \int_{\nu_H}^{\infty} \frac{f_\nu}{h\nu} d\nu \tag{3.6}$$

where $h\nu$ is the photon energy and ν_H is the photoionisation threshold frequency ($h\nu_H$ ~13.6 ev corresponding to $\sim$ 912 $\mathring{A}$) for HI.

Figure 3.3 shows the time evolution of the rate of ionizing photons emitted per unit solar mass of the SSP, for selected SSPs. We plot the results obtained with different upper mass limits (M_{up}) and metallicities. From this figure we may appreciate the role of age, metallicity and upper mass limit of the IMF on the ionizing photon rate Q(H). For a given Z and M_{up}, Q(H) generally increases to a maximum value at increasing time and then, once a threshold age is reached, it rapidly decreases to negligible values. At fixed M_{up}, both the maximum value of Q(H) and the threshold age decrease, at increasing metallicity. In general after 6–7 Myr the ionization photon luminosity is about one order of magnitude lower than its peak value, the decrease being more rapid at increasing metallicity. We recall that the lifetime of a 20 $M_\odot$ star of solar metallicity is $\sim$ 10 Myr. Thus we can say that when the turn-off mass of a star cluster goes below this value, the cluster is no more a source of ionizing photons. Of course it is important to stress that this is the result of single stellar evolution. Recent calculations that include the effects of binary accretion and spoiling show that this age limit becomes less sharp. In these circumstances a significant number of ionizing photons (quite hard indeed because they correspond to compact hot stars) may be produced up to ages $\sim$ 100 Myr (see e.g. Eldridge et al. 2015). We also see that, in general, for fixed M_{up}, Q(H) increases at decreasing metallicity. The above dependencies of Q(H) on age and metallicities are easily explained by recalling that, at lower Z the stellar Main Sequence becomes hotter so that also the H burning lifetime in the temperature range for an efficient production of ionizing photons also increases. We also note some spikes in the production rates. These are due to the advanced phases, where the stars may become very hot and compact when they expose at the surface the inner nuclear processed layers because of the mass-loss suffered during the evolution. In these phases the ionizing spectra become also harder, i.e. they are capable of producing high ionization elements, as thoroughly discussed in e.g. Leitherer et al. (1999). When these hot stars begin to dominate the ionizing region of the integrated

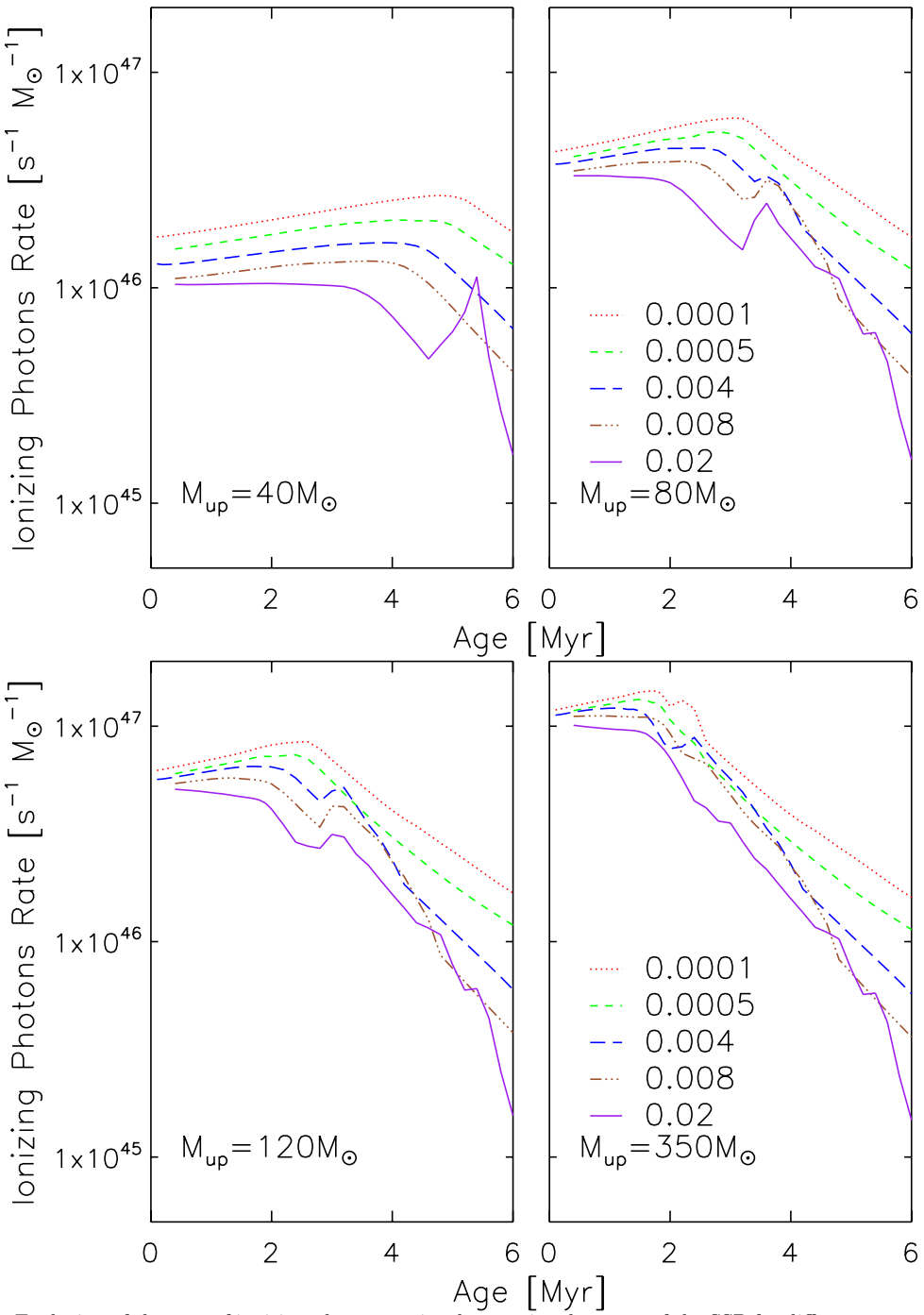

Figure 3.3: Evolution of the rate of ionising photons emitted per unit solar mass of the SSP for different upper mass limits and metallicities. Different line styles correspond to different metallicities as illustrated in the plot.

spectra of the SSP the simple and monotonic behaviour described before is of course no longer valid.

As expected, the effect of M_{up} is strong. A star cluster with M_{up} of 350 $M_{\odot}$ produces more than about seven times the ionizing photons produced by a cluster with a M_{up} of 40 $M_{\odot}$, at constant total mass. Moreover, the age to attain the maximum Q(H) becomes younger at increasing upper mass limit. For $M_{up} = 40M_{\odot}$ the threshold age is between 3.5 Myr (for Z=0.02) and 5 Myr (for Z=0.0001). For $M_{up} = 80M_{\odot}$ it is between 2 Myr and 3 Myr (for the same metallicity range); for $M_{up} = 120M_{\odot}$ it is between 1.8 Myr and 2.5 Myr (for the same metallicity range); for $M_{up} = 350M_{\odot}$ it is between 1.5 Myr and 2 Myr (for the same metallicity range). This reflects the larger relative weight of more massive stars in the ionizing photon budget.

The incident ionizing continuum is actually fully specified once the geometry of the cloud is provided and, in particular, by the inner radius of the cloud. This parameter together with other important ones are discussed in the next section.

3.2.2 Parameters of the HII region model

Having specified the luminosities and spectral shapes of the central ionizing sources, I now need to consider the parameters of the surrounding gas. As for the geometry I use a closed plane parallel configuration: the region is modelled as a thin shell placed at a distance of R_H=15 pc from the central ionizing source. With this parameter the incident ionizing continuum is fully specified. The density of the nebula is assumed to be constant with $n_H = 100cm^{-3}$. I do not consider effects of clumpiness, i.e. I assume a filling factor of unity. The chemical composition is identical to the initial composition assumed in our evolutionary tracks. I do not take into account possible variations due to the nuclear processing and ejection of the elements (self enrichment) in the life times of the star clusters. I also account for dust depletion of the elements but not for dust effects (absoption and re-emission) within the ionized nebula. As mentioned earlier, dust could absorb a fraction of the ionizing photons and thus, to a first approximation, the main effect would be a corresponding decrease of the intensities of the recombination lines and of the free-free emission.

In the calculation of the synthetic spectrum I assume Case B recombination (Osterbrock 1989). We note at this point that our goal is not that of performing a detailed analysis of the dependence of a large ensemble of emission lines on the critical parameters of the HII nebulae, for the determinations of element abundances or for using them as diagnostics of the ISM conditions (Osterbrock 1989). Instead we aim at obtaining a robust estimate of the intensities of the main recombination lines and of the nebular continuum emission which will be used to improve the diagnostic capabilities of our population synthesis code, in particular as estimators of the star formation rates or as diagnostics of the attenuation by the ISM. Since the nebula is assumed to be radiation bounded it is optically thick to the hydrogen ionizing continuum. In this case the intensity of recombination lines depends mostly on the luminosity of the ionizing continuum, with relatively little dependence on the properties of the nebula. This is not so for the prediction of the intensities of collisionally excited lines, for which one should consider a wider and more specific set of initial parameters (see e.g. Panuzzo et al. 2003; Wofford et al. 2016). Nevertheless for the sake of preliminary comparisons we have included (but not used in our subsequent calculations)

Line Name	$\lambda(\mathring{A})$	$\lambda(\mathring{A})$
Lyα	1216.00	1216
Lyβ	1025.00	1025
Hα	6563.10	6563
Hβ	4861.10	4861
Hγ	4340.10	4340
Hδ	4102.10	4102
Hϵ	3970.00	3970
Hζ	3889.00	3889
Hη	3835.00	3835
Hθ	3798.00	3798
Paα	18750.10	18752
Paδ	10050.10	10050
Brα	40520.00	40515
Brβ	26250.00	26254
Brγ	21660.10	21657
Brδ	19450.10	19447
Pfα	74580.00	74585
[NII]	6584.10	6584
[OII]	3727.10	3728.5
[OIII]	5007.00	5007
[OIII]	4959.00	4959
[SII]	6731.00	6731
[SII]	6717.00	6716
[SIII]	9532.00	9532
[SIII]	9069.00	9069

Table 3.1: Lines (recombination lines and the main collisionally excited lines) considered and added to our modelled SEDs in this work.

also collisionally excited lines. The full list of recombination lines and the main collisionally excited lines considered here is provided in Table 3.1.

3.2.3 SSP with Emission Lines

After running CLOUDY I have obtained the intensities of recombination lines as a function of the age of the SSP for five different values of the metallicity, Z = 0.0001, Z = 0.0005, Z = 0.004, Z = 0.008, Z = 0.008, Z = 0.02 and for different values of M_{up}. I also obtain the intensities of some collisionally excited lines, that of the nebular continuum and the electron temperatures (T_e) of the HII regions.

Here we describe how we combine the results of CLOUDY with the integrated spectra of the SSP to obtain the integrated spectra with nebular emission. We first select only a sub-sample of the emission lines computed by CLOUDY, as detailed in Table 3.1. CLOUDY also provides the "transmitted stellar continuum" flux in the outward direction, i.e. the fraction of the flux that has not been absorbed by the ions in the medium of the HII region. This is essentially all the incident flux above the Hydrogen ionization limit, also because, as we have already stated we do not include at this level effects of dust in our CLOUDY calculations. Separately, CLOUDY also provides the "diffuse continuum emission" flux by the nebula, in the outward direction. By adding these two components we obtain the "continuum flux" after the interaction of the source radiation field with the ISM of the surrounding nebula. This is

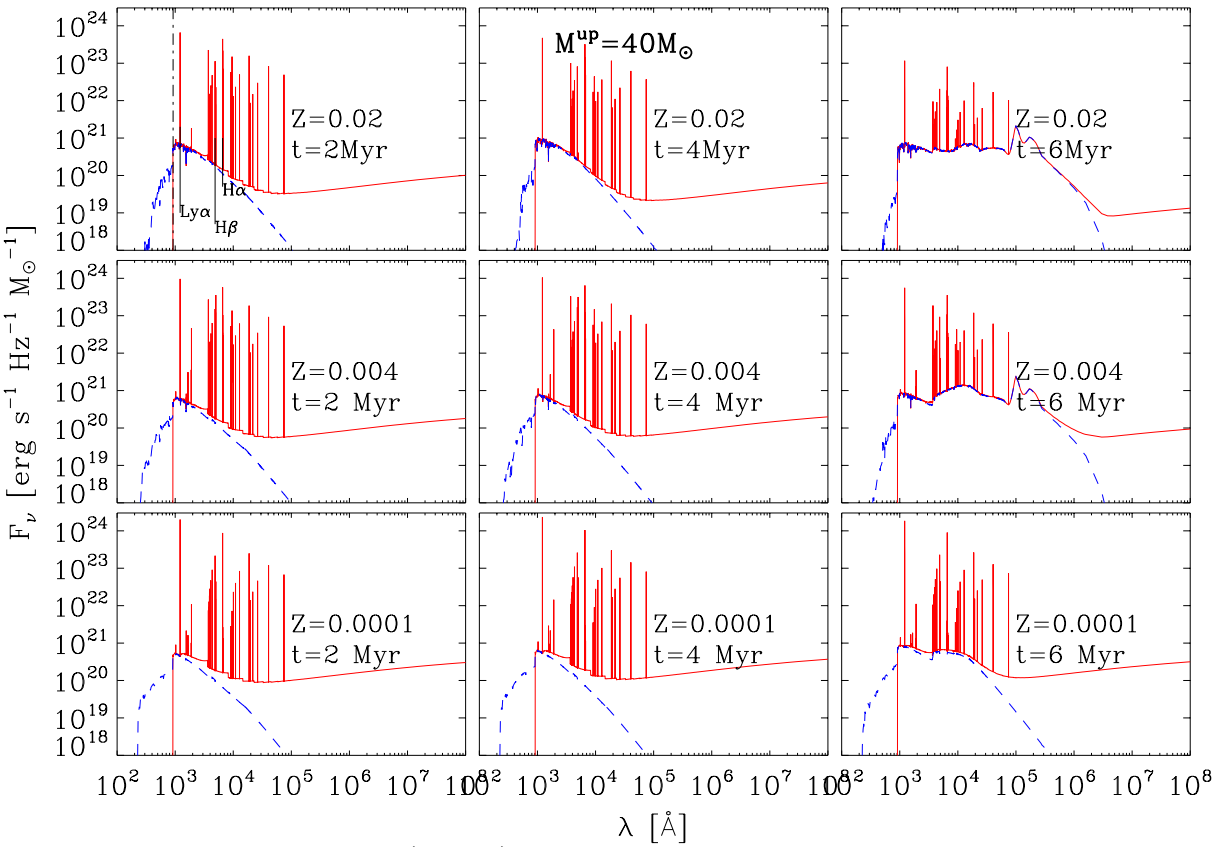

Figure 3.4: Integrated spectra of SSPs (solid red) after inclusion of nebular emission for the case of $M_{up} = 40$ at ages of t =2, 4 and 6 Myr, for metallicities of Z = 0.02, 0.004 and 0.0001, as indicated in the different panels. The dashed blue lines refer to the original spectrum emitted by the star clusters. The dot-dashed vertical line in top-left plot with Z = 0.02 and t = 2 Myr indicates the Hydrogen ionisation potential at 921 A. To the left of this line are hydrogen ionising fluxes and to the right are non-ionising fluxes. We have also labelled the three emission lines Hα, Hβ and Lymanα in the same plot.

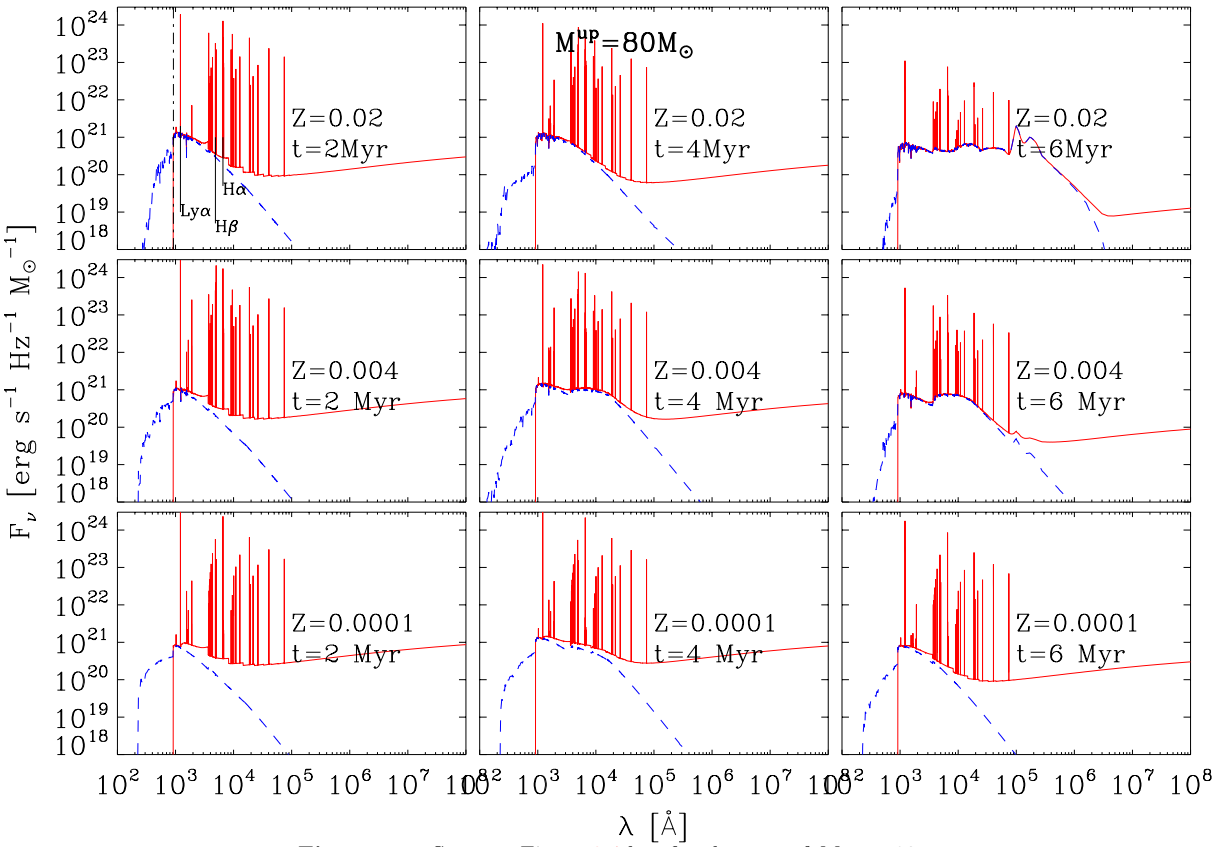

Figure 3.5: Same as Figure 3.4 but for the case of $M_{up} = 80$

the shape of the continuum flux that will reach the observer if all subsequent absorption and emission processes by the neutral ISM are neglected. We need now to add the lines to these spectra. For this purpose we sum the line intensities provided by CLOUDY to the above continua, by assuming a gaussian profile broad enough to allow us to measure their intensities as if they were real observed spectra. At this stage the SSP spectra are the sum of the original integrated stellar photospheric light strongly absorbed in its H-ionising part, of the continuum nebular emission and of the individual emission lines. These SSP spectra are all normalized to one solar mass of initially formed stars so that they can easily be convolved with a star formation history to provide a galaxy spectrum with emission lines.

The new integrated spectra with nebular emission included are shown in Figure 3.4 to 3.7. In the different panels of the figures, the blue dashed lines represent the emitted integrated spectra of the star clusters while the red solid lines are the composite spectra that exit from the ionized nebulae. The wavelength domain extends from the FUV to the radio regime. Apart from the presence of the emission lines, the most noticeable difference with respect to the original SSPs is the presence of the continuum emission that extends up to the radio wavelengths. This is the contribution of the so called free-free radio emission and it will be thoroughly discussed in the next chapter devoted to the radio emission emitted by young stellar populations.

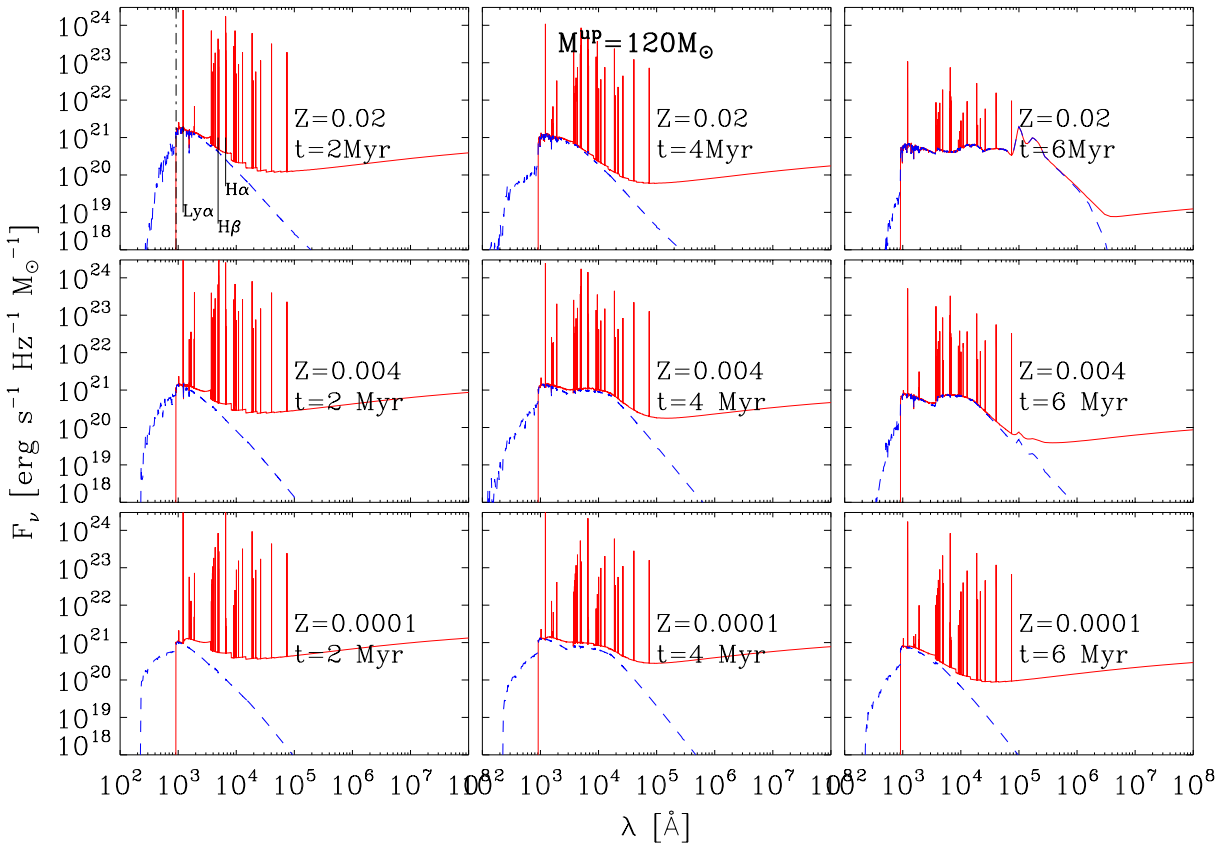

Figure 3.6: Same as Figure 3.4 but for the case of $M_{up} = 120$

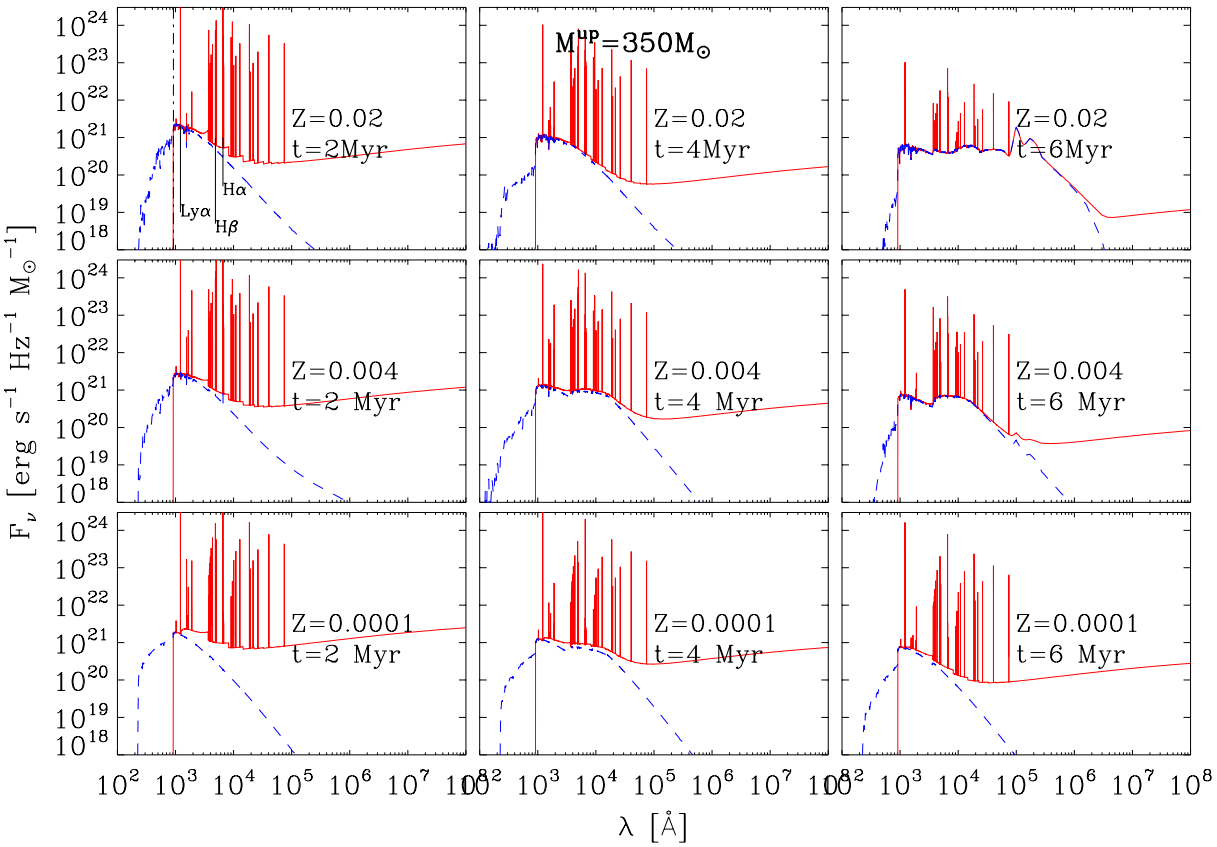

Figure 3.7: Same as Figure 3.4 but for the case of $M_{up} = 350$

Chapter 4

Radio Emission from Star Forming Regions

In the previous section, we discussed how the integrated photospheric emission of a young stellar population is modified by the presence of the surrounding interstellar gas that may be ionized by radiation emitted by the most massive stars. We have seen that the gas is responsible of characteristic emission lines and of continuum emission. In particular free-free continuum from ionized HII regions is an important source of emission associated with the massive star populations, at radio frequencies. In the hypothesis that the surrounding gas is ionization bounded, the intensities of such component is so tightly related to the massive stellar population that it can be used as a robust star formation indicator. However at radio frequencies another component associated with young massive stars is observed, and must be taken into account for a correct modelling of the spectral energy distribution of galaxies at these frequencies. This component is due to non-thermal emission believed to be synchrotron radiation associated with the exploding core collapse supernovae (CCSN). More specifically it originates from the interaction of relativistic electrons produced in the shocked ejecta of a core-collapse supernova with the ambient magnetic field (Condon 1992). Since the discovery of a tight correlation between radio emission and star formation, radio emission from star forming galaxies has been the subject of many studies (van der Kruit 1971, 1973; Rickard & Harvey 1984; Helou et al. 1985; Condon et al. 1991; Bressan et al. 2002). In this chapter I present a discussion of these two important components associated with the young massive stellar populations, following the paper by Bressan et al. (2002, hereafter B02). I will show that the advent of updated evolutionary tracks, the dependence on the upper limit of the IMF and the new advances in the theory of supernova explosions, call for a re-visitation of the correlation with the SFR and, in particular, for a revision of the relations provided by B02.

4.1 Thermal radio emission

At radio frequencies a tight relation between the free-free emission of a star forming galaxy and its star formation rate is observed. The nature of this relation has been explained by Rubin (1968a) who first derived a theoretical relation between the luminosity of free-free emission of the HII regions and the corresponding rate of ionising photons. Using the equation for the free-free emission derived by Oster (1961) in the form suggested by Mezger & Henderson (1967), Rubin (1968a) derived the following relation between the specific luminosity of free-free emission $L_{\rm ff}(\nu)$ of an ionization-bounded HII region and the rate of ionising photons Q(H)

$$\frac{L_{\rm ff}}{\rm erg\,s^{-1}\,Hz^{-1}} = \frac{1}{6.3\times\ 10^{25}}\left(\frac{\rm T_e}{10^4\,\rm K}\right)^{0.45}\left(\frac{\nu}{\rm GHz}\right)^{-0.1}\left(\frac{\rm Q(H)}{\rm s^{-1}}\right) \tag{4.1}$$

In the right hand side of Equation 4.1, $\rm T_e$ is the gas electron temperature (more precisely the density square weighted volume average of $\rm T_e$), ν the frequency of the emitted radiation and $Q(H)$ the number of Hydrogen ionizing photons emitted per unit time by the ionizing source. Since the latter term depends on the number of ionizing massive stars present in a given stellar population and the lifetime of these stars is relatively short, then it is expected that $L_{\rm ff}$ correlates with the star formation rate.

The tiny dependence of the free-free radio luminosity from the frequency shown in equation 4.1, can be appreciated in the first two columns of Figures 3.4 to 3.7, which correspond to ages where nebular emission is significant. Actually the figures show that the frequency dependence is not exactly $\nu^{-0.1}$. This due to the fact that in equation 4.1, Rubin (1968a) used the approximation of the free-free velocity averaged Gaunt factor by Mezger & Henderson (1967).

If this explicit dependence on the Gaunt factor is retained, equation 4.1 writes:

$$L_{\rm ff} = \frac{\rm Q(H)}{C_1}\left(\frac{\rm T_e}{10^4\,\rm K}\right)^{0.3}\rm G_{ost}(\nu, T_e) \tag{4.2}$$

with $C_1 = \sqrt{3}/\pi \times 6.86 \times 10^{26}$ and

$$\rm G_{ost}(\nu, T_e) = \ln\left[4.955\times 10^{-2}\left(\frac{\nu}{\rm GHz}\right)^{-1}\right] + 1.5\,\ln\left(\frac{\rm T_e}{\rm K}\right) \tag{4.3}$$

Other equivalent but more recent approximations of the velocity averaged Gaunt factors may be found in literature (e.g. Draine 2011; Mancuso et al. 2016)

With Equation 4.1 it is easy to derive the free-free luminosity of a young simple stellar population at any radio frequency. For this purpose it would be enough to obtain the ionizing photon luminosity, Q(H), from the integral in Equation 3.6. However, as shown by Equation 4.1, $L_{\rm ff}$ has a non negligible dependence from the electronic temperature. In the case of the SSP spectra with nebular emission presented in the previous Chapter, the value of $\rm T_e$ results from the solution of the HII model equation but, in order to allow the use of the 4.1 for other purposes, we discuss in the next section a useful simple approximation in terms of metallicity and upper limit of the IMF.

4.1.1 Electron Temperature

In literature, the electron temperature of gas in equation 4.1, T_e, is usually assumed to have a constant value (10^4K). However T_e is the result of the balance between the various processes that regulate the interior structure of the ionized nebula, already discussed in the previous Chapter and, in fact, it may change by a significant factor by changing the metallicity of the nebula or the age of the ionizing star cluster. Here I use the HII models calculated as described in Chapter 3 to quantitatively asses the temperature dependence on the main parameters of the models. In Fig 4.1, we show the evolution of the

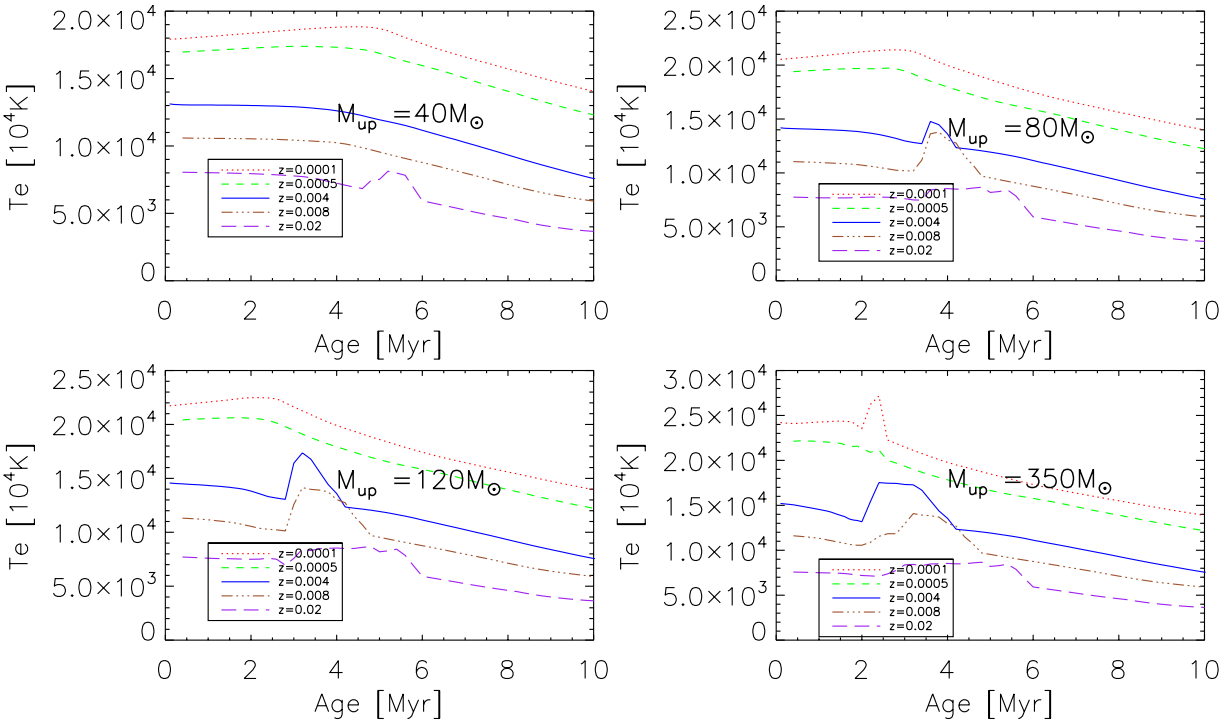

Figure 4.1: Evolution of electron temperature T_e (obtained from *CLOUDY*) with age (for ages $\leq$ 10 *Myr*) for different upper mass limits and metallicities which are indicated by the different line styles.

T_e of our models, for the four values of M_{up} adopted in this work. We select only ages $\leq$ 10 *Myr* because, as already said, at older ages the ionizing photon flux becomes negligible with respect to that provided by the young SSP. The figure clearly shows that T_e is a strong function of the metallicity, decreasing by more than a factor of two from the lower to the higher metallicity values considered here. There is also a certain dependence on the age but this is very mild for ages younger than 6 Myr, that is the limit after which the ionization photon luminosity drops considerably. There is also a certain dependence on M_{up} because, the higher it is, the higher is the ionizing photon luminosity and so the heating source. However the dependence on M_{up} becomes less pronounced at increasing metallicity, likely because of the larger cooling efficiency. Finally we note that the presence of Wolf Rayet stars gives rise to peaks in T_e, because the corresponding ionizing spectra are harder and so the average kinetic energy of the electrons is higher. With these caveats in mind we have collected in Table 4.1 the values of the electron temperature T_e averaged over the first 6 Myr, for different values of metallicity and M_{up}. These values are plotted

Table 4.1: Electron temperature (T_e) for different metallicities (Z) and upper mass limits.

M_{up}	350	120	80	40
Z		$\frac{T_e}{K}$		
0.0001	24210.0	21730.0	20530.0	17920.0
0.0005	22090.0	20350.0	19330.0	16940.0
0.0040	15210.0	14570.0	14180.0	13120.0
0.0080	11640.0	11370.0	11110.0	10640.0
0.0200	7663.0	7768.0	7795.0	8081.0

in Figure 4.2 to show the variation of the time averaged T_e with the metallicity of the HII region, for different values of M_{up}. We see that T_e increases by almost a factor of three at decreasing metallicity, from about $Z_\odot$ to about $Z_\odot/100$. For comparison purposes, we also plot in the figure an average of the empirical fits obtained by López-Sánchez et al. (2012) (black solid line) with the *MAPPINGS III* code (Sutherland & Dopita 1993). We transformed the metallicity values provided by López-Sánchez et al. (2012) ($x = 12 + \log(O/H)$) to our absolute metallicity Z, by adopting the solar Oxygen abundance given by Asplund et al. (2009), $x_\odot = 12 + \log(O/H)_\odot = 8.69 \pm 0.05$ and $Z_\odot = 0.0134$, thus obtaining $x = 8.69 + 12 + \log(Z/0.0134)$. The vertical dot-dashed line marks the solar metallicity value by Asplund et al. (2009).

The values shown in Table 4.1 and plotted in Figure 4.2 are fitted by a multiple regression relation between T_e, M_{up} and Z. The fitting relation, which holds within about 10% of the T_e values given in Table 4.1 is provided by the following equation:

$$\begin{aligned} \mathrm{Log}\,(T_e) \;=\; & 3.890 - 0.4802\ \mathrm{Log}\left(\frac{Z}{0.02}\right) - \ 0.1747\ \mathrm{Log}\left(\frac{Z}{0.02}\right)^2 - \ 0.0205\ \mathrm{Log}\left(\frac{Z}{0.02}\right)^3 \\ & + 0.062\ \mathrm{Log}\left(\frac{M_{up}}{120}\right)\ \mathrm{Log}\left(\frac{Z}{0.02}\right) \end{aligned} \tag{4.4}$$

As shown in Figure 4.2 the major dependence in Equation 4.4 is from the metallicity term. Though the exponent of the metallicity dependence is small, the dependence is not negligible since the metallicity may change by orders of magnitude. The upper mass limit of the IMF has instead a much lower impact on the electronic temperature and, actually this dependence could have been neglected, as previously discussed. Because of that, the relation provided by Equation 4.4 can be used with confidence almost independently of the adopted IMF.

4.1.2 Free-Free Emission from Young Stellar Populations

We may use equation 4.4 within equation 4.1, to obtain the free-free luminosity of a young SSP of any metallicity from its ionizing photon luminosity. Figure 4.3 shows the time variation of the 33 GHz and 1.4 GHz free-free luminosities of our simple stellar populations. This figure strictly mimics the evolution of the rate of ionising photons emitted by SSPs shown in Figure 3.3. As in the case of the rate of ionizing photons, the free-free luminosity rises to a peak within the first few Myr and then immediately drop to negligible values, following the decay of the ionizing photons. We see from Figure 4.3 that the free-free

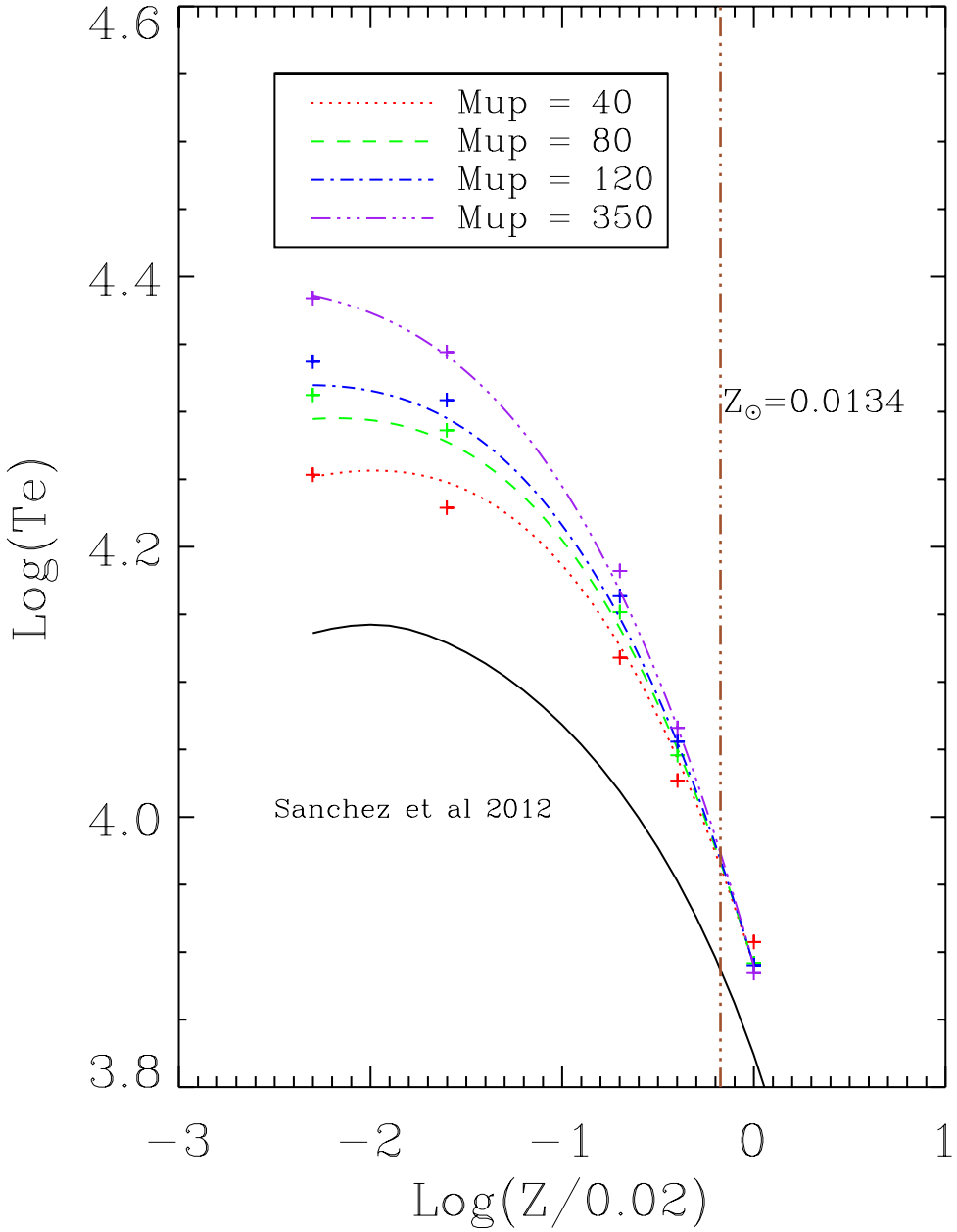

Figure 4.2: Plot of electron temperature T_e averaged over the first 6 Myr against metallicity Z for different values of M_{up} as indicated by the labels. The plus symbols are the models obtained with *CLOUDY*) while the corresponding curves are obtained by the multivariate best fit represented by Equation 4.4 for M_{up} = 40, 80, 120 and 350, respectively. The vertical dot-dashed line indicates the metallicity at Z = 0.0134 which we adopted in this work as the solar metallicity. The average of the empirical fits derived by López-Sánchez et al. (2012) for high-ionization OIII and for low-ionization OII zones is shown by the solid black line.

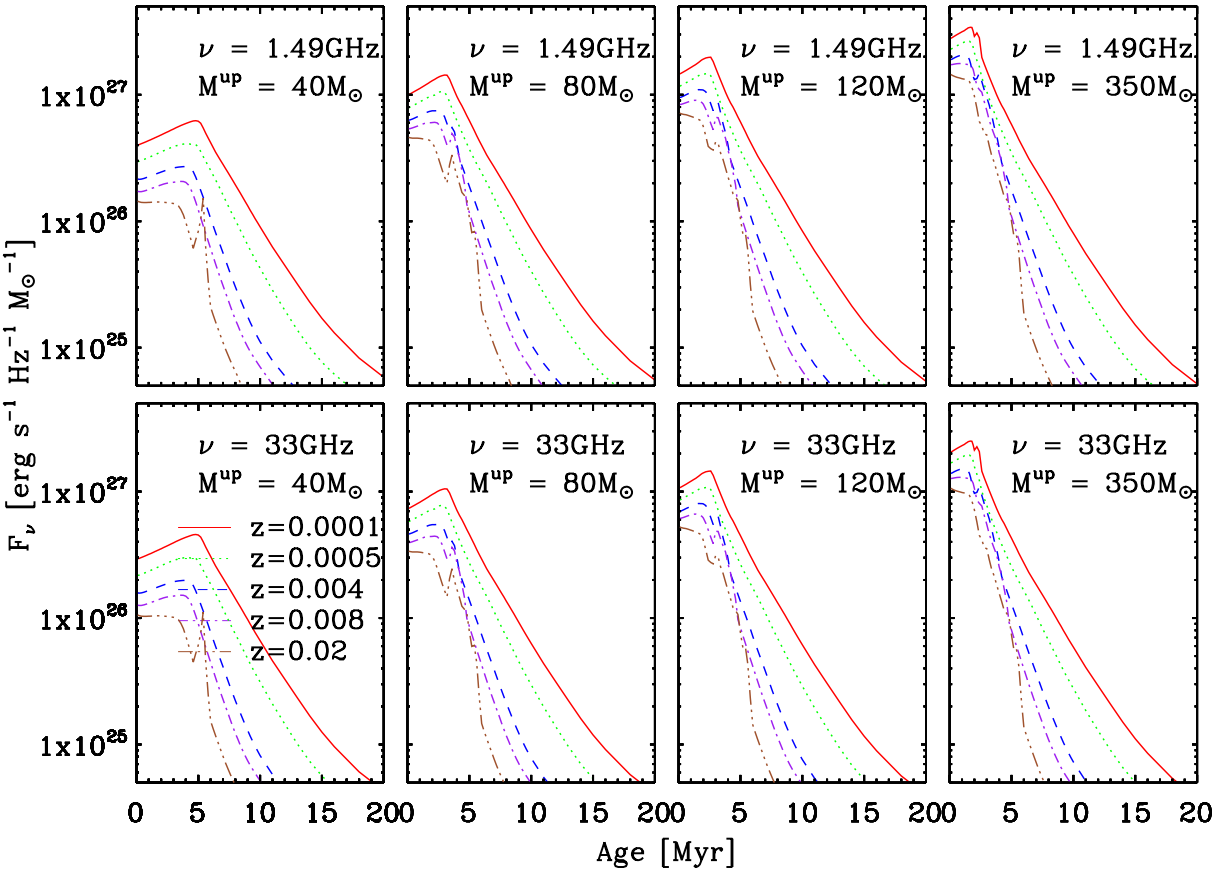

Figure 4.3: Variation of the thermal radio emission luminosity with age, for different metallicities and different IMF upper mass limits. The upper panels refer to the frequency $\nu = 1.49$GHz and the lower panels to $\nu = 33$GHz, respectively.

radio luminosity is an indicator of the presence of very young massive stars. Actually the thermal radio emission probes the same ages probed by the emission lines, because they have the same origin. However while the latter may suffer from significant absorption by a dusty ISM, at radio frequencies if the medium is not too dense, the emitted radiation is unaffected by attenuation.

4.2 Non-Thermal radio emission

At radio frequencies another emission component associated with young massive stars is observed, and must be taken into account for a correct modelling of the spectral energy distribution of galaxies at these frequencies. This component is believed to be synchrotron radiation associated with the exploding core collapse supernovae (CCSN). More specifically it originates from the interaction of relativistic electrons produced in the shocked ejecta of a core-collapse supernova with the ambient magnetic field (Condon 1992). The characteristic spectral slope of non-thermal radio emission is higher than that of thermal emission so that, at frequencies below a tens of GHz, in general it dominates the spectral emission of star forming galaxies. Given this tight link with the CCSNe, in the spectral synthesis models the intensity of non-thermal emission is set proportional to the CCSN rate, ν_{CCSN}, and the absolute value is calibrated with observations at a particular frequency. The emission at other frequencies is then scaled according to the observed slope of the synchrotron emission (Condon 1992). Among the observational evidence supporting the above interpretation of the non-thermal radio emission in star forming galaxies is the far infrared (FIR)-radio correlation that was mentioned earlier. For all types of star forming galaxies it is observed that the radio emission at 1.4 GHz, where the non-thermal component generally dominates, is tightly correlated with the emission in the FIR. At at 1.4 GHz the correlation is expressed by the following ratio ($q_{1.4}$) derived from IRAS and radio observations (Helou et al. 1985):

$$q_{1.4} = \log \frac{\mathrm{F_{FIR}}/(3.75 \times 10^{12}\ \mathrm{Hz})}{\mathrm{F}_\nu(1.49\ \mathrm{GHz})/(\mathrm{W\ m^{-2}\ Hz^{-1}})} \approx 2.35 \pm 0.2 \tag{4.5}$$

where $F_{\mathrm{FIR}} = 1.26 \times 10^{-14}(2.58 S_{60\mu m} + S_{100\mu m})\mathrm{Wm^{-2}}$ (Young et al. 1989), $S_{60\mu m}$ and $S_{100\mu m}$ are IRAS flux densities in Jy.

B02 derived the following theoretical relation between NT radio emission L^{NT} and the CCSN rate:

$$\frac{L_{NT}/\frac{\nu_{CCSN}}{yr^{-1}}}{10^{30} erg\ s^{-1}\ Hz^{-1}} = E^{SNR}_{1.49}(\frac{\nu}{1.49})^{-0.5} + E^{NT}_{1.49}(\frac{\nu}{1.49})^{-\alpha} \tag{4.6}$$

where $E^{SNR}_{1.49}$ is the average non thermal radio luminosity per young Supernova Remnant (SNR) and $E^{NT}_{1.49}$ is the average injected energy in relativistic electrons per CCSN event. They also estimated that, the contribution of young SNRs could be well represented by a power low index -0.5 but also that at 1.49GHz the contribution from young SNRs is $E^{SNR} \approx 0.06 E^{NT}$ and thus it is negligible with respect to $E^{NT}_{1.49}$. Equation 4.6 can thus simply be written to a good approximation as

$$\frac{L_{NT}}{10^{30} erg\ s^{-1}\ Hz^{-1}} = E^{NT}_{1.49}(\frac{\nu}{1.49})^{-\alpha} \times \frac{\nu_{CCSN}}{yr^{-1}} \tag{4.7}$$

For the Galaxy, B02 adopted $L^{NT} = 6.1 \times 10^{21}$ W Hz^{-1} (Berkhuijsen 1984) at 0.4GHz and $\nu_{CCSN} = 0.015\ yr^{-1}$. In order to reproduce the observed average slope of the NT radio emission in normal spiral galaxies between 8.5 GHz and 1.49 GHz ($\sim$0.8) they have adopted $\alpha = -\frac{d\ \log S_\nu}{d\ \log \nu}$=0.9. With this slope for non-thermal radio emission , they obtain $E^{NT}_{1.49} = 1.38$. After the slope α is defined and the quantity $E^{NT}_{1.49}$ is calibrated, the non-thermal radio luminosity of any young SSP is obtained by inserting in Equation 4.7 the corresponding value of ν_{CCSN}.

To model the non thermal radio emission in star forming galaxies it is thus important to predict CCSN supernova rates of young populations. If all the massive stars were ending their lives as exploding supernovae, as assumed by B02, then the CCSN rate would be nothing but the rate of dying stars. The latter, in turn, is nothing but the time derivative of the total number of massive stars in a given SSP, $\delta n/\delta t$. This quantity can be easily obtained from stellar isochrones either numerically or by considering that it may be expressed as

$$\delta n/\delta t = \delta n/\delta m \times \delta m/\delta t \tag{4.8}$$

where $\delta n/\delta m$ is the value of the IMF corresponding to the current dying mass and $\delta m/\delta t$ is the evolution of the dying mass with age and can be derived by differentiating the mass-age relation of evolutionary tracks.

As already said this is true if one assumes that all massive stars die producing an exploding supernova. There have been recently large efforts to understand the final phases of massive stars, in particular after the first detection of gravitational wave emission from merging black holes in binary systems (Abbott et al. 2016). On one side, there has been growing evidence that the efficiency of the mass loss rates in massive stars have been overestimated by significant factors in the past, leading to pre-supernova masses significantly smaller to those predicted by the most recent calculations. On the other one, most recent works on CCSN explosion have shown that the assumption that the final fate of the massive stars is regulated entirely by the Carbon-Oxygen core mass at the end of central He burning, as the sole parameter driving the kind of explosion as believed in the past, is not more true and likely a more complicated relation with the initial mass must be taken into account. In parallel there has been a significant effort to model the evolution of stars in the mass range around the transition between Asymptotic Giant Branch (AGB) stars and massive stars, between 6 $M_\odot$ and 10 $M_\odot$. It has been shown that these stars, while igniting Carbon in a non degenerate core thus skipping the AGB phase, they end their life as Super-AGB with electron degenerate Oxygen-Neon-Magnesium cores, and thus they do not explode as CCSN (e.g., Siess 2007; Hurley et al. 2000).

All these aspects may significantly modify the range of masses that may produce exploding CCSN events and that may consequently contribute to the non-thermal radio emission in star forming galaxies. In the next section I will discuss how I have revisited the non-thermal radio emission model by including all these new pieces of information.

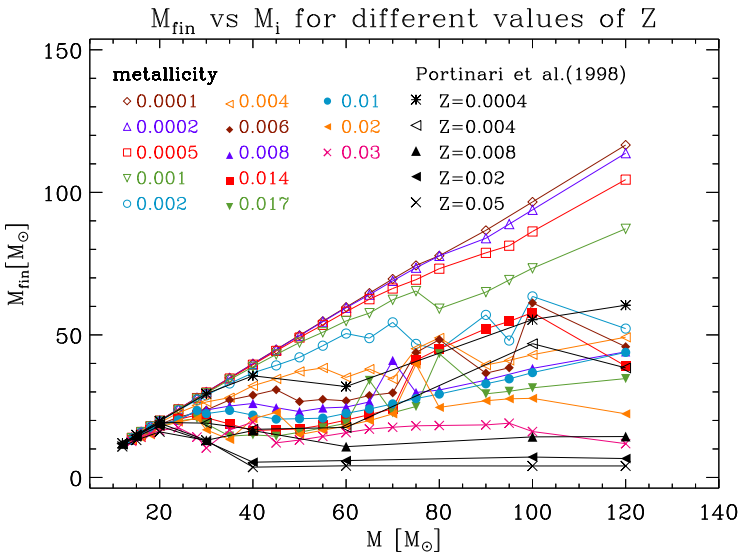

Figure 4.4: Comparison of the final mass before the explosion between the new PARSEC and the old PADOVA evolutionary tracks of massive stars (from Slemer et al. (2017))

4.2.1 Which Supernovae Feed Non-Thermal Radio Emission ?

The final fate of stars primarily depends on their initial mass M_i and metallicity Z_i. The conditions for a star to proceed through all nuclear stages up to silicon burning with consequent formation of an iron core are that carbon burning in the centre is ignited in non-degenerate conditions, and that an oxygen-neon core is built up with a mass larger than $\simeq 1.37\,M_\odot$(Nomoto 1984). We call the corresponding minimum initial mass that fulfull these requirements M_{mas}. The detailed analysis of Siess (2007) shows that M_{mas} is related to a minimum mass of the He-exhausted (CO) core formed at the end of the He-burning phase, $M_{He}^{mas} \simeq 1.246 \pm 0.015\,M_\odot$ for stellar models with convective overshoot, with a relatively small dependence on the initial metallicity. Using this criterion for the PARSEC tracks, Slemer et al. (2017)) find that M_{mas} is an increasing function of the metallicity, ranging from $M_{mas} \simeq 6\,M_\odot$ at $Z_i = 0.0001$ to $M_{mas} \simeq 8\,M_\odot$ at $Z_i = 0.02$. This is thus the initial mass of the least massive star that must be assumed in the calculations.

Concerning the final fate of these massive stars, we first remind that not all these stars die with an exploding supernova. Detailed evolutionary calculations including the latest stages of massive stars show that, depending on the mass of H-exausted core at the end of pre-supernova phase, M_{He}, massive stars can be divided in two main broad groups (Heger & Woosley 2002; Heger et al. 2003; Nomoto et al. 2013) *Core Collapse Supernovae (CCSN)*: stars that develop $M_{He} \leq 40\,M_\odot$. These objects form an iron core before ending the evolution as supernova explosion or collapsing into a black hole. They have initial masses in the range from M_{mas} to $100\,M_\odot$, depending on the adopted mass loss rates. However the occurrence or not of the explosion, and the corresponding kind of remnant (neutron star or black hole), crucially depend on the structure just prior to the core collapse.

Very Massive Object (VMO): stars that have $M_{He} \geq 40\,M_{\odot}$ may explode before forming the iron core. This class comprises three sub-groups. The pulsation pair instability supernovae (PPISN), with $40\,M_{\odot} \leq M_{He} \leq 65\,M_{\odot}$, corresponding to initial masses in the interval $100\,M_{\odot} \leq M_i \leq 140\,M_{\odot}$. The pair-instability supernovae (PISN), with $65\,M_{\odot} \leq M_{He} \leq 133\,M_{\odot}$ and $140\,M_{\odot} \leq M_i \leq 260\,M_{\odot}$. The stars with $M_{He} \geq 65\,M_{\odot}$ which proceed directly to a massive black hole, without producing ejecta.

In the following section I will analyze in detail the different final fates of massive stars belonging to the various groups, focusing on the nature (SN, BH) and mass of their remnants.

The link between the late evolutionary stages of massive stars and their final fates and remnants, neutron stars (NS) or black holes (BH), is still poorly constrained. The type of remnant finally produced is a critical parameter for estimating its contribution to non-thermal radio emission. If it is a BH, it is likely that the external envelope also collapses, thus leaving behind neither significant ashes for a typical SN light curve nor relativistic electrons. These events are termed *Failed SN* (O'Connor & Ott 2011) because they will likely remain undetected in optical-NIR surveys. Indeed the existence of a class of failed SN could solve the so called *Red Supergiant* (RSG) and *SN rate* problems at once. The first problem concerns the lack of SNII detections with RSG precursors more massive than about 20M⊙ (Smartt 2009). The second one concerns the mismatch between the observed cosmic SN rate and the rate expected from the cosmic star formation history, which is about a factor of two larger (Horiuchi et al. 2011).

The first important parameter that affects the final evolution of the massive stars is the mass-loss rate. To highlight this important point and to stress the need of a revision of the whole radio model by B02 we show in Figure 4.4 the differences between the final masses before the explosion predicted by the new PARSEC models and by the previous Padova models. We see from the figure that, e.g. at Z=0.02, due to the lower mass-loss rates adopted, the PARSEC final masses can be even a factor of three more massive than those predicted by the old Padova models. Thus the differences in the mass loss rates are the prime cause of the differences in the final phases.

Concerning the explosion phase, some recent works in the attempt to characterize the parameters of successful and failed supernovae have yielded some structural parameters of the pre-SN stars, such as the *compactness* parameter, that can be utilized in predicting the fate of SNe (eg. Ertl et al. 2015; Sukhbold & Woosley 2014; Ugliano et al. 2012; Janka 2012; O'Connor & Ott 2011). Using these parameters, Spera et al. (2015); Spera & Mapelli (2017); Slemer et al. (2017) were able to characterize the final fate of *PARSEC* massive stars for the different criteria adopted for successful CCSN explosion.

The reader can refer to Figures 6 to 11 of Spera et al. (2015) for the mass spectrum the compact remanants obtained with PARSEC models as a function of M_{ZAMS} for different metallicities and SN recipes. Here we limit the discussion to the range of exploding CCSNe and to failed SNe, as calculated by Spera et al. (2015). Figure 4.5 shows the results of adopting the so called compactness parameter (O'Connor & Ott 2011) while Figure 4.6 shows the results obtained with the M_4 parameter of Ertl et al. (2015). In both plots the horizontal axis is the initial mass while the vertical axis refers to the value of the adopted parameter. The white bars refer to models in which the explosion energy is enough to eject the external layers producing a visible SN. The filled bars refers to models where the explosion is not able to eject the external mantle and the stars thus collapses to a black hole. We remind here that in the SN

models of Fryer et al. (2012) a one-parameteric monotonic relation (the CO core mass at the explosion) appeared to be enough to distinguish SN explosion from failed SN. On the contrary, as can be seen in Figures 4.5 and 4.6, in the new models there is a range of initial masses (23 $M_\odot \geq M_{ZAMS} \geq 28\ M_\odot$, in the figures) where the final fate is uncertain. Using both criteria, when M_{ZAMS} is larger than 30 $M_\odot$ the Core Collapse model fail to explode as Supernovae.

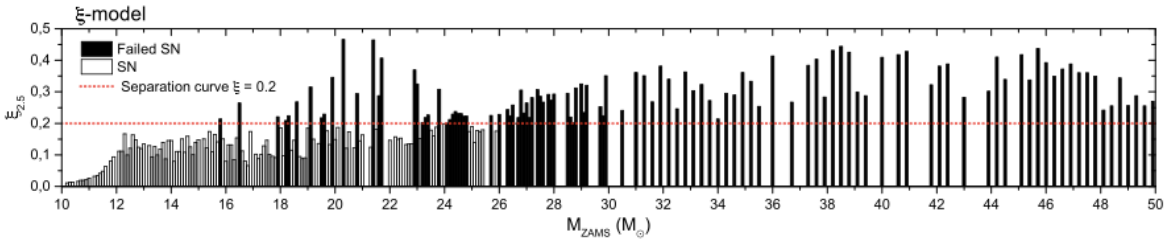

Figure 4.5: Value of compactness parameter at the innermost $2.5M_\odot$, $\epsilon_{2.5}$, as a function of M_{ZAMS}, for the PARSEC models evolved up to the Fe-core infall using MESA. Black bars indicate non-exploding models (failed SNe) while white bars refer to exploding models (SNe). The dotted line $\epsilon_{2.5} = 0.2$ is the threshold we chose to distinguish between SNe and failed SNe according to Horiuchi et al. (2014). The simulation grid goes from $M_{ZAMS} = 10.0M_\odot$ up to $M_{ZAMS} = 30.0\ M_\odot$ with steps of $0.1M_\odot$, and from $M_{ZAMS} = 30.0M_\odot$ to $M_{ZAMS} = 50.0\ M_\odot$ with steps of 0.3 $M_\odot$. Some models in the grid are not shown in the results because of numerical convergence issues.

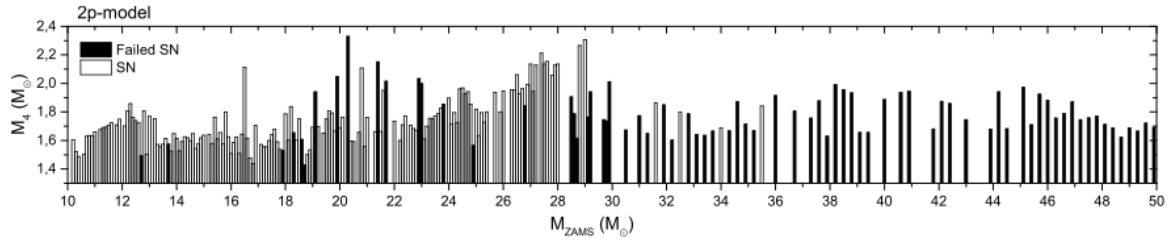

Figure 4.6: Same as Figure 4.5 but here we show the parameter M_4 of the model by Ertl et al. (2015) as a function of M_{ZAMS}. M_4 represents the baryonic mass of the proto-compact object following the SN explosion event. In this case, to distinguish between SNe and failed SNe, we used the linear function $y_{sep}(\mathrm{x}) = 0.283\mathrm{x} + 0.0430$ which corresponds to the calibration w18.0 of Ertl et al. (2015).

4.2.2 Implementing Non thermal Radio Emission in Simple Stellar Populations

In the previous section we have seen that the most recent PARSEC models of massive star evolution coupled with the most recent explosion criteria indicate that the final collapse produces a CCSN if the initial mass of the star is below $M = 30\mathrm{M}_\odot$. Stars more massive than this either undergo a failed SN event ore will enter the pair instability phase. The progenitors undergoing pair-instability SNe (Woosley 2017) either collapse to a BH or are completely destroyed by a strong instability without producing relativistic electrons, similarly to what we assumed for SNIa. Thus in any case, stars more massive than $M = 30\mathrm{M}_\odot$ will not produce a CCSN supernova which is thought to produce the observed synchrotron radiation.

As shown by B02, non-thermal radio emission can be included in the integrated spectra of SSP using Equation 4.7 and the constant $E^{NT}_{1.49}$. The rate of CCSN, ν_{CCSN}, in Equation 4.7 is calculated by means of Equation 4.8, taking into account that stars with initial mass above about $M = 30\mathrm{M}_\odot$ do not contribute

to non-thermal radio emission. For this purpose while making the integrated spectra of SSP I compute numerically the two terms entering Equation 4.8. Starting from the youngest isochrone, corresponding to the higher initial mass, we know for each age the dying mass, m_d, if the age is large enough. If $m_d > 30M_\odot$ we set the non thermal emission to zero. In the other case and as long as $m_d > M_{mas}$ we compute $\delta n/\delta m_d$, the IMF, and the term $\delta m_d/\delta t$ by numerical differentiating m_d with respect to the age of the isochrones. The variation of the quantity $\delta n/\delta t$ so computed is shown in Figure 4.7 for the case of $M_{up} = 120\ M_\odot$ and for different metallicities, as indicated by the different line colors. We see that $\delta n/\delta t$ is a decreasing function of the age of the stellar population. We remind that $\delta n/\delta t$ is the product of two terms that have an opposite behaviour with age. The first term on the right hand side of Equation 4.8 corresponds to the IMF value of the turn-off mass and it increases at increasing age (decreasing turn-off mass). The second term on the right hand side is well approximated by the rate of evolution of the turn-off mass (which is very similar to the mass of the dying star along the isochrone) and it is strongly decreasing with increasing age (decreasing turn-off mass) because of the age-mass relation. For the adopted shape of the IMF, the product is dominated by the lengthening of the stellar lifetimes as the initial mass decreases. The net effect is that the dying rate decreases by a factor of about two as the turn-off mass decreases from the more massive stars to the lower limit of massive stars.

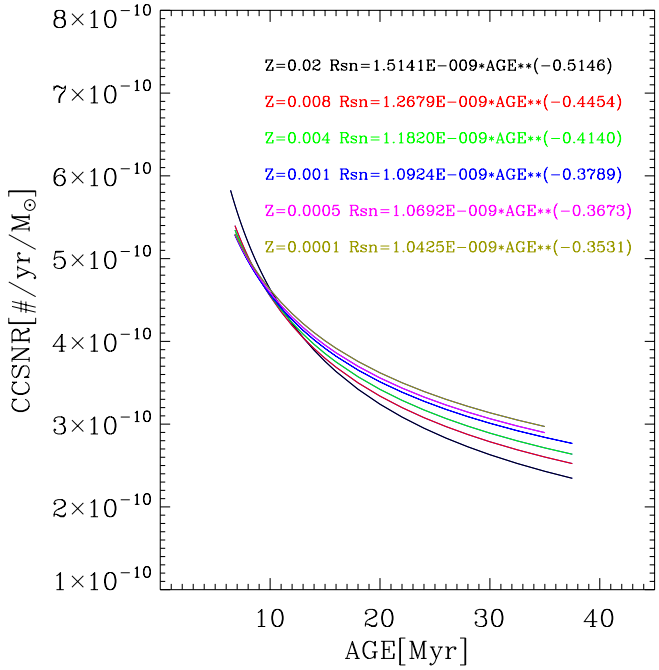

Figure 4.7: Evolution of dying rate of massive stars, $\delta n/\delta t$, with age obtained for our SSPs with $M_{up} = 120$

In Figures 4.8 and 4.9 we show the time evolution of the non-thermal radio emissions of our SSP at two frequencies, 1.49GHz and 33GHz respectively, and for different upper mass limits and metallicities. In the same Figures we also show for sake of comparison, the free-free radio emission, discussed in the previous section. We note that introducing the distinction between SN and failed SN has a twofold effect. First the expected effective SN rate should be smaller, as underlined by the cosmic SN rate

problem discussed above. At first glance this could affect the calibration constant, E^{NT}. However this constant is empirically derived and so it should already account for the *true observed* SN rate and for the *true observed* non-thermal luminosity. The second effect is that the new scheme introduces a larger delay between free-free radio emission and non-thermal radio emission. If all stars more massive than $M = 8M_{\odot}$ explode, then the first SN appears after about 3 Myr, the life-time of the more massive stars. Instead if stars more massive than M = 30 $M_{\odot}$ fail to explode, non-thermal radio emission begins to appear at an age of $\sim$ 7 Myr which, by coincidence, is also the age at which free-free emission abruptly fades down. We note that non-thermal radio emission is not sensitive to the upper mass limit of the IMF, as long as it is larger than the assumed threshold for failed SN, M = 30 $M_{\odot}$. We finally see that SSP are source of non-thermal emission up to about 35–38 Myr, depending on the metallicity.

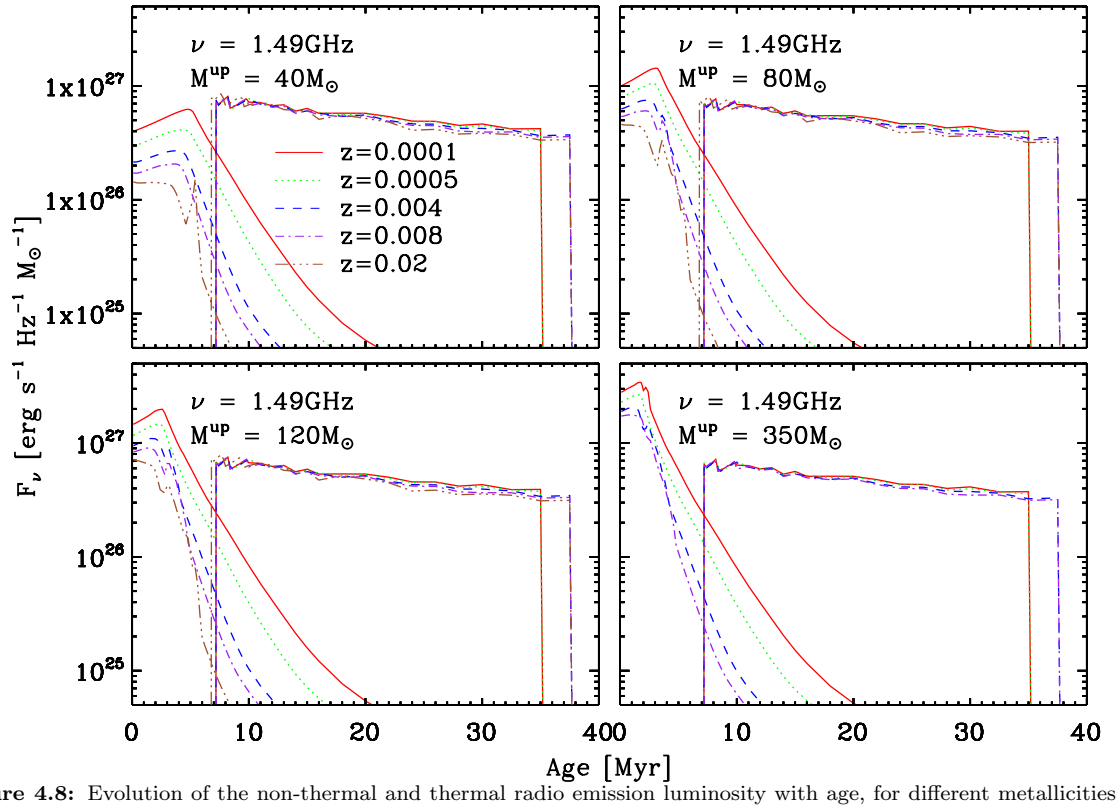

Figure 4.8: Evolution of the non-thermal and thermal radio emission luminosity with age, for different metallicities and different IMF upper mass limits, for frequency ν = 1.49 GHz.

At this stage the SSP include the stellar component, the HII component, both emission lines and nebular continuum including the thermal radio emission, and the non-thermal radio component. Examples of the resulting SSPs are shown in Figures 4.10 to 4.13. The only missing component is now dust in the ISM which, however, has a very important role because dust absorption and re-emission may significantly modify the shape of the SED.

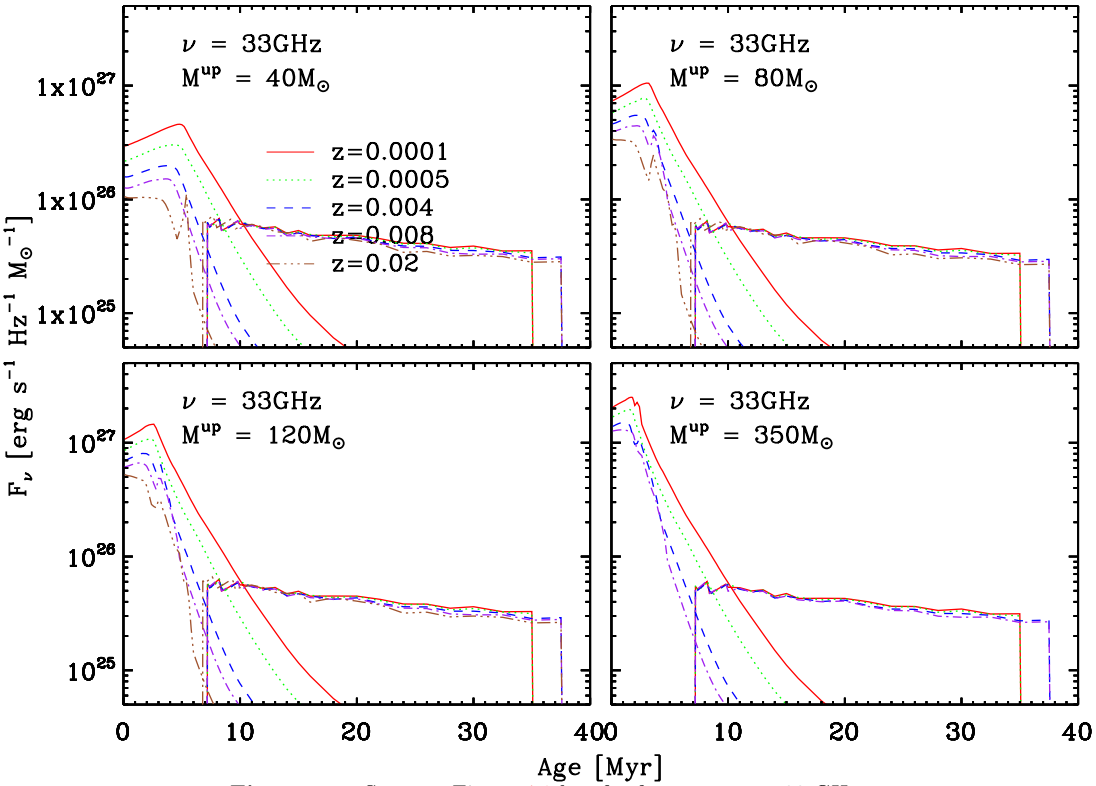

Figure 4.9: Same as Figure 4.8 but for frequency $\nu = 33$ GHz.

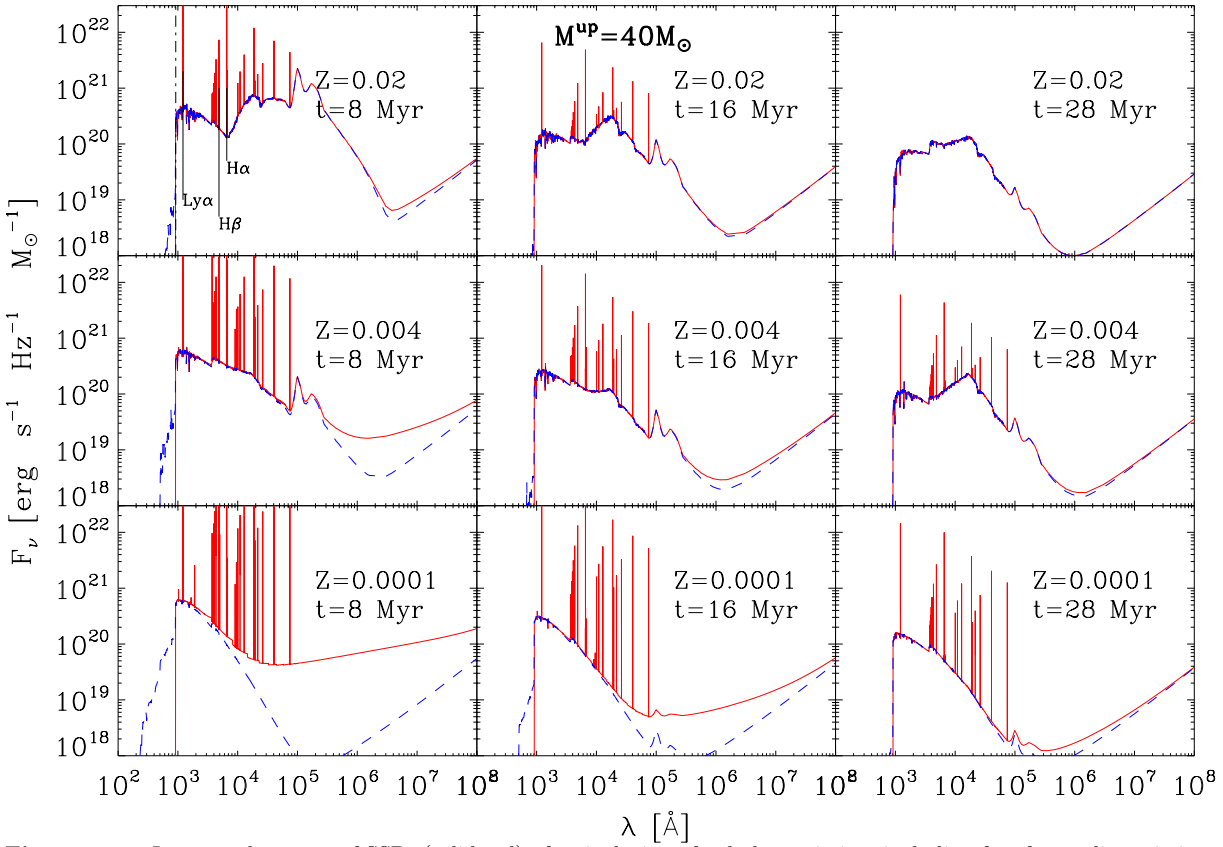

Figure 4.10: Integrated spectra of SSPs (solid red) after inclusion of nebular emission, including free-free radio emission, and non-thermal radio-emission, at ages of t = 8, 16, and 28 Myr, for M_{up} = 40 and Z = 0.02, 0.004 and 0.0001, as indicated in the different panels. The dashed blue lines refer to the original spectrum emitted by the star clusters. The dot-dashed vertical line in the top left plot indicates the Hydrogen ionisation potential at 921 $\AA$.

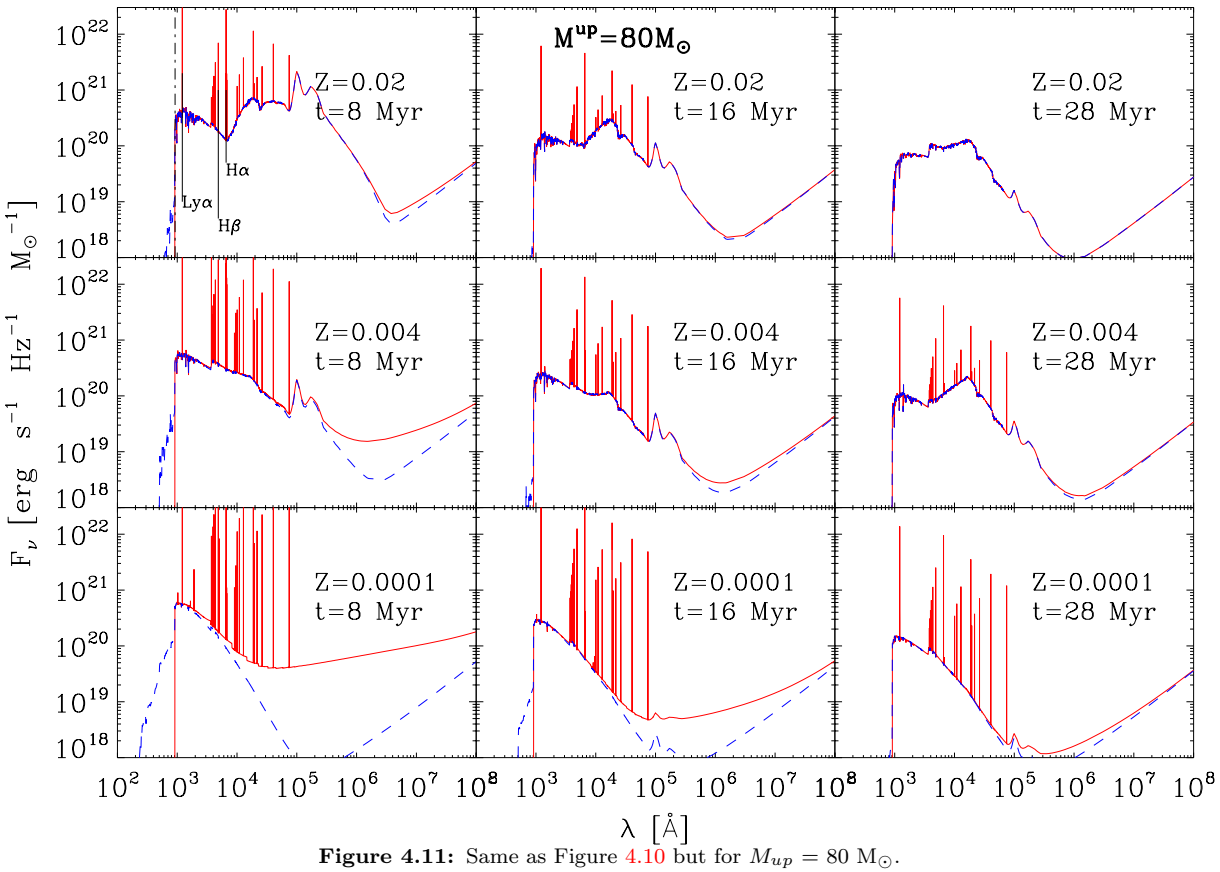

Figure 4.11: Same as Figure 4.10 but for $M_{up} = 80$ M$_\odot$.

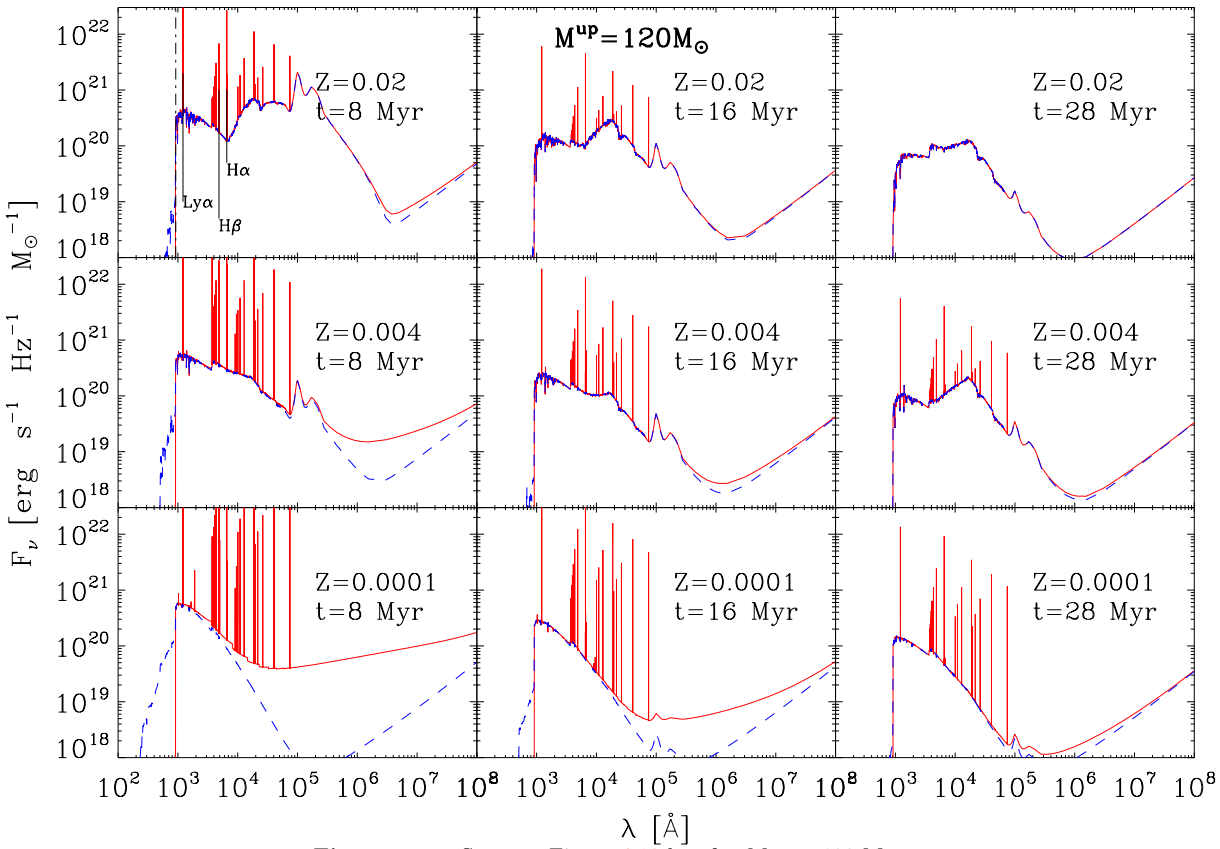

Figure 4.12: Same as Figure 4.10 but for $M_{up} = 120$ M$_\odot$.

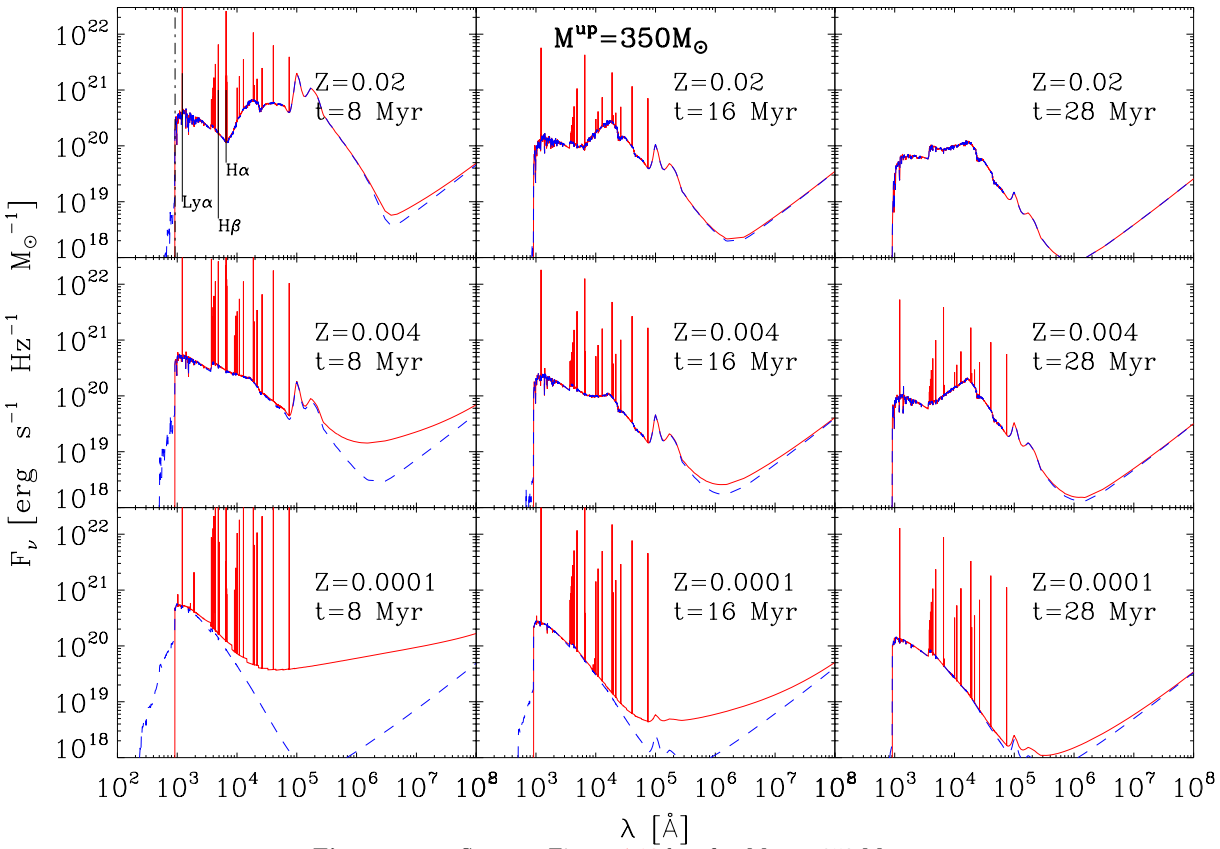

Figure 4.13: Same as Figure 4.10 but for M_{up} = 350 $M_{\odot}$.

Chapter 5

Population synthesis with Dust

The modelling of the spectral energy distribution of a stellar system is not complete if it does not account for dust absorption and re-emission. It is known that dust is an ubiquitous component of the ISM and that, because of its optical properties, it may strongly affect the SED emitted by the stars. This is particularly true for galaxies that host star forming regions, because it is known that the star formation process is triggered by the cold gas that, in typical conditions, contains significant amounts of dust. In stellar population synthesis models the effect of dust on the UV - optical stellar light is often described by suitable extinction laws. Determining the shape and strength of the extinction law is one of the more difficult task in astrophysics and there is strong evidence that this law could be different in different environments. Among the many papers on this subject we recall a few that are basic building blocks in many population synthesis tools, like those of Cardelli et al. (1989) and Calzetti et al. (2000). More recently an important difference has been recognized to exist between the individual extinction laws, generally referring to the attenuation of a single object by the intervening dust along the line-of-sight, and the internal attenuation of a whole galaxy, that is a combination of all these extinction laws and the relative distribution of stars and gas within the galaxy. In the first case the extinction depends only on the dust properties, like the optical properties of grains, their size distribution and their fractional weights with respect to the atom density. In the second case the geometrical and even temporal properties of the stellar populations also enter the game and introduce a further complication in the models. Usually, simple attenuation laws that are often adopted in the literature do not account for the differential dust and star geometries (disks, bulges, dust lanes e.t.c.). Even more critical is that it is still not well known at what level an internal attenuation law derived for a given galaxy is affected by the spatial and age distribution of its components. Associated to this problem is the fact that in the last few decades a new window was opened in the region where dust is strongly emitting, the mid and far infrared, and that, to make a census of the stellar populations content one has to really perform a careful balance of the energy seen in the different spectral regions: what is absorbed at certain wavelengths must be found in some other spectral regions.

In this work I will use the a spectral synthesis code GRASIL (Silva et al. 1998; Granato et al. 2000; Vega et al. 2005; Silva et al. 2011) to model the spectral energy distribution of a stellar system in presence

of dust. After a brief summary on how GRASIL works, i.e. how it combines and modifies the input SSP spectra, I will describe how the output spectral distribution depends on some basic parameters used to perform a sound modelling of the stars and dust properties. Then I will use a template galaxy, M100, which is has a very well sampled panchromatic spectral energy distribution, to test how the new SSP perform. In particular we will use this galaxy to check the calibration of the non-thermal radio emission which is one effect to which we devoted a detailed analysis.

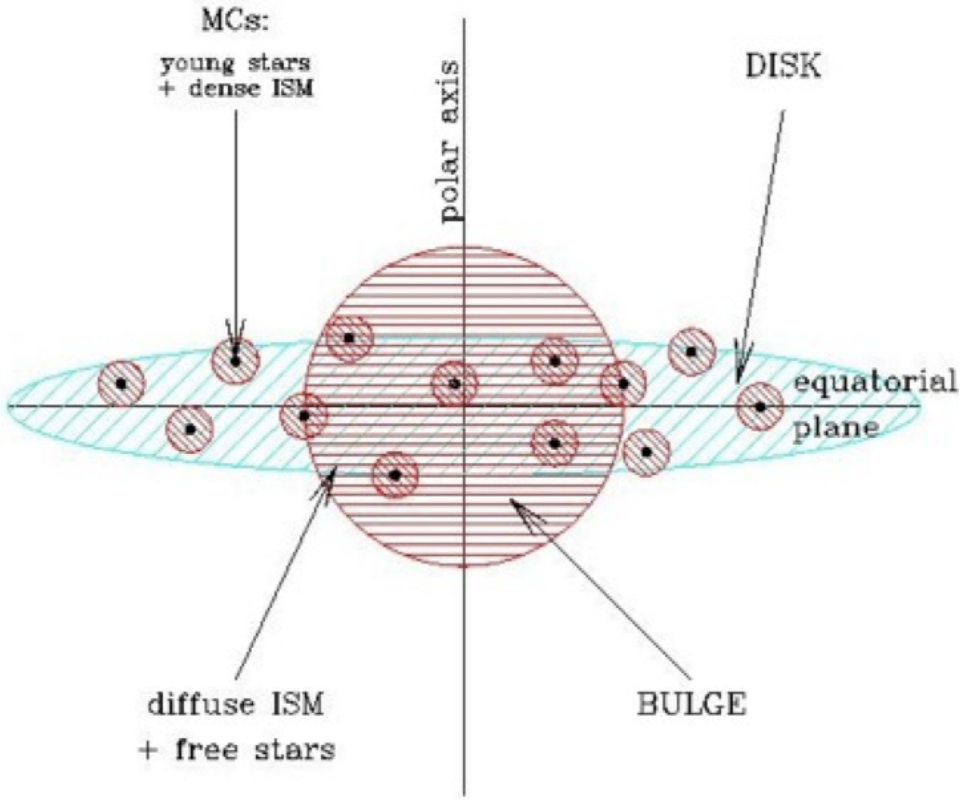

Figure 5.1: GRASIL pictorial representation of a galaxy

5.1 Summary of Grasil

I have used the new suite of SSPs described in the previous Chapters as an input to the spectral synthesis and radiative transfer model GRASIL (Silva et al. 1998; Granato et al. 2000; Vega et al. 2005; Silva et al. 2011). By providing an input star formation history (SFH) and a SSP library, GRASIL calculates the UV-to-submm SED resulting from the interaction of the stellar radiation and associated nebular emission, with the dust in the ISM. I provide here a summary of its main features and refer to the original papers for details.

For the input SFH, I use here CHE_EVO (Silva 1999), a standard one-zone open box chemical evolution code (e.g. Arimoto & Yoshii 1987; Matteucci & Tornambe 1987; Matteucci & Francois 1989; Koeppen & Arimoto 1990; Andrews et al. 2017) that computes the evolution of the SFR, and of the mass and metallicity of the gas as a function of the galaxy age. The gas from which stars form, with total mass

M_{inf}, has an infall rate given by an exponential function of time with an e-folding time τ_{inf}. The SFR is expressed as a function of the mass of gas, to which, if required, an exponential term can be superimposed to represent a starburst:

$$SFR(t) = \nu_{sch} M_{gas}(t) + f_b(t, M_b, \tau_b). \tag{5.1}$$

The first term on the right hand side is a Schmidt-type law with efficiency ν_{sch} in Gyr^{-1}. The second is an analytical term given by

$$f_b(t, M_b, \tau_b) = M_b \times \exp(-(t - t_0)/\tau_b), \tag{5.2}$$

where M_b is the mass of gas converted into stars by the burst that started at the galaxy age t_0, and τ_b is the e-folding time of the burst.

The SED is then computed for a given SFH and galaxy age t_{gal}. In absence of a dusty ISM, the pure stellar SED of a galaxy is straightforwardly obtained by summing up the SFR-weighted SED of each SSP of the appropriate age and metallicity, as defined by the SFH of Equation 5.1:

$$F_\nu(t_{gal}) = \int_0^{t_{gal}} f_\nu^{ssp}(t_{gal} - t, Z(t))\, SFR(t)\, dt \tag{5.3}$$

In order to model the UV-to-submm SED of galaxies, we use GRASIL to calculate the radiative transfer of stellar radiation through the dust in the ISM. The main features of GRASIL are as follows:

- the total mass of gas M_{gas} at age t_{gal} is subdivided in a dense phase, with fraction f_{mol}, and in a diffuse phase, as sketched in Figure 5.1. The amount of dust is set by the dust-to-gas mass ratio δ. This can be set either proportional to the gas metallicity (e.g. Issa et al. 1990; Lisenfeld & Ferrara 1998; Inoue 2003; Calura et al. 2017) or to a fixed value (e.g. Edmunds 2001). Since we are dealing here with fits to local objects, we have fixed $\delta = 0.010$ i.e. close to the value of the Milky Way (which, for e.g., varies from 0.0056 (Draine et al. 2007) , 0.0063 (Zubko et al. 2004) to 0.0083 (Li & Draine 2001), all with typical uncertainties of about 10%.

- the dense phase represents optically thick star-forming molecular clouds (MCs). Here, the individual MCs are assumed to have the same mass. Typical observed range of mass M_{mc} and radius r_{mc} of the clouds are $\approx 10^5 - 10^6 M_\odot$ and $10 - 50$ pc respectively. Stars are supposed to be born within MCs, and to escape in a timescale t_{esc}. This is represented by linearly decreasing with age the fraction ($f(t_{gal})$) of the SSP energy radiated inside the cloud

$$f(t_{gal}) = \begin{array}{ll} 1 & t_{gal} < t_{esc} \\ x & t_{esc} < t_{gal} < 2t_{esc} \\ 0 & 2t_{esc} < t_{esc} \end{array} \tag{5.4}$$

where $x = (2t_{esc} - t_{gal})/t_{esc}$. The time dependence of $f(t_{gal})$ on t_{esc} mimics an age-selective extinction whereby younger stars that spend more time in the relatively denser clouds suffer more attenuation

than the older ones in the diffuse ISM. But it may also represent the possibility that, due to holes in the surrounding medium, radiation from the younger stars may escape from the MCs. This age-selective extinction is a distinctive feature of GRASIL. The newly born stars are represented as central point sources of spherically symmetric MCs with optical depth $\tau_\lambda^{mc} \propto M_{mc}/r_{mc}^2$. The effective parameter is therefore the optical depth of the MC, that can be changed through r_{mc} or M_{mc}. The light emitted from MCs and from more evolved stars interacts with the diffuse (cirrus) phase.

- Stars and dust are distributed in a galaxy with either a spherical symmetry, or a disk shape, or a combination of the two. The adopted spatial distributions are a King profile for spherical symmetry (with scale radii r_{star} and r_{diff} respectively for stars and diffuse dust), and a double exponential along the radial and vertical directions for the disk geometry (with scale radii rd_{star}, rd_{diff}, $zdstar$, zd_{diff}).

- As for the properties of the dust, GRASIL adopts a mixture of graphite and silicate spherical grains, with optical properties by Laor & Draine (1993) and with a power-law size distribution:

$$\frac{dn_i}{da} = \begin{cases} A_i\, n_H\, a^{\beta_1} & \text{if } \mathrm{a_b} < \mathrm{a} < \mathrm{a_{max}} \\ A_i\, n_H\, a_b^{\beta_1-\beta_2} a^{\beta_2} & \text{if } \mathrm{a_{min}} < \mathrm{a} < \mathrm{a_b} \end{cases} \tag{5.5}$$

  where a is the radius of an individual grain whose shape is assumed to be spherical. The default choice for the parameters of the size distribution is set so to reproduce the average dust extinction and emission in the MW (Draine & Lee 1984; Silva et al. 1998): $a_{min} = 8$ Å, $a_{max} = 0.25$ μm, $a_b = 50$ Å, $\beta_1 = -3.5$, $\beta_2 = -4.0$ and $A_g = 10^{-25.22} cm^{2.5}/H$ for graphite, and $a_{min} = 50$ Å, $a_{max} = 0.25$ μm, $a_b = 50$ Å, $\beta = -3.5$, and $A_s = 10^{-25.11} cm^{2.5}/H$ for silicates. Beside that, GRASIL includes very small grains and and Polycyclic Aromatic Hydrocarbons (PAH) molecules.

  It is important to stress here that GRASIL does not adopt an attenuation curve. Starting from this mixture, that defines a fixed extinction law, the attenuation curve resulting from GRASIL may be different from galaxy to galaxy, depending on the geometrical distribution of dust and stars, on the relative importance of the molecular cloud and cirrus components and on the escape time from molecular clouds of young stars. This is important to interpret for instance the amount of extinction suffered by nebular lines with respect to the underlying continuum (Panuzzo et al. (2007) and as will be shown later for the star bursting regions studied in this work, or the shape of the Calzetti et al. (2000) attenuation curve measured for starburst galaxies (e.g. Granato et al. 2000; Panuzzo et al. 2007).

- At each point within the galaxy and for each grain type the appropriate temperature is computed, either the equilibrium temperature for big grains or a probability temperature distribution for small grains and PAHs. The radiative transfer of starlight through dust is computed along the required line of sight to get the resulting SED.

In addition to the dust in the dense and diffuse ISM accounted for by GRASIL, another dusty environment is directly accounted for in the SSPs, i.e. the dusty envelopes around AGB stars (Bressan et al. 1998). The same recipe has been used also for red supergiant stars. The modelling of dust reprocess-

ing and of the radio and nebular emission included in the SSP, allow to consider the full UV to radio continuum and line data of galaxies.

Escape of ionizing photons

In this work I have also introduced the possibility that a fraction of Ly-continuum photons escapes from the galaxies into the intergalactic medium. Gaps in the distribution of the ISM, possibly caused by SN explosions and stellar winds may allow the leakage of photons (Bergvall et al. 2006; Borthakur et al. 2014; Izotov et al. 2016, e.g.). This subject is particularly relevant at high redshifts, to investigate the sources of the reionization of the Inter-Galactic Medium (IGM). However, since from the analysis of the reionization of the IGM by primeval galaxies it emerges that this fraction should not be larger than 10%, I have not considered this effect in the present work (Iwata et al. 2009; Vanzella et al. 2010; Robertson et al. 2010; Nestor et al. 2013; Heckman et al. 2011; Alexandroff et al. 2015; Sharma et al. 2016).

5.2 Effects of GRASIL main parameters on the SED

GRASIL is a physically sound tool to interpret the pancromatic spectral energy distribution of galaxies. Starting from individual emitting SSP with known age and metallicity it tries to follow in detail the main modifications induced by the presence of a dusty medium. As discussed in Section 5.1, there are a number of parameters that must be used to define the complex environments observed in galaxies and this is the drawback of abandoning simple population synthesis models. Actually the parameters provided by the fit of the observed spectral energy distribution should drive us toward a deeper understanding of the underlying physical processes at work. It is thus important to summarize the main parameters that will be used in this work and to see which are the effects of varying them in a simulation. We illustrate this in Figures 5.2 to 5.4. The top panel of Figure 5.2 gives the base starburst model. In this base model, we have fixed the chemical evolution parameters and adopted an upper mass limit $M_{up} = 120$ and a spherical geometry. We show the effects on the SED of different values of t_{sb}, the age at which the starburst is observed; t_{esc}, the escape time scale of young stars from their MCs; r_{mc} , the radius of the MCs, r_{star}/r_{diff}, the scale radius ratio of star to diffuse dust distribution.

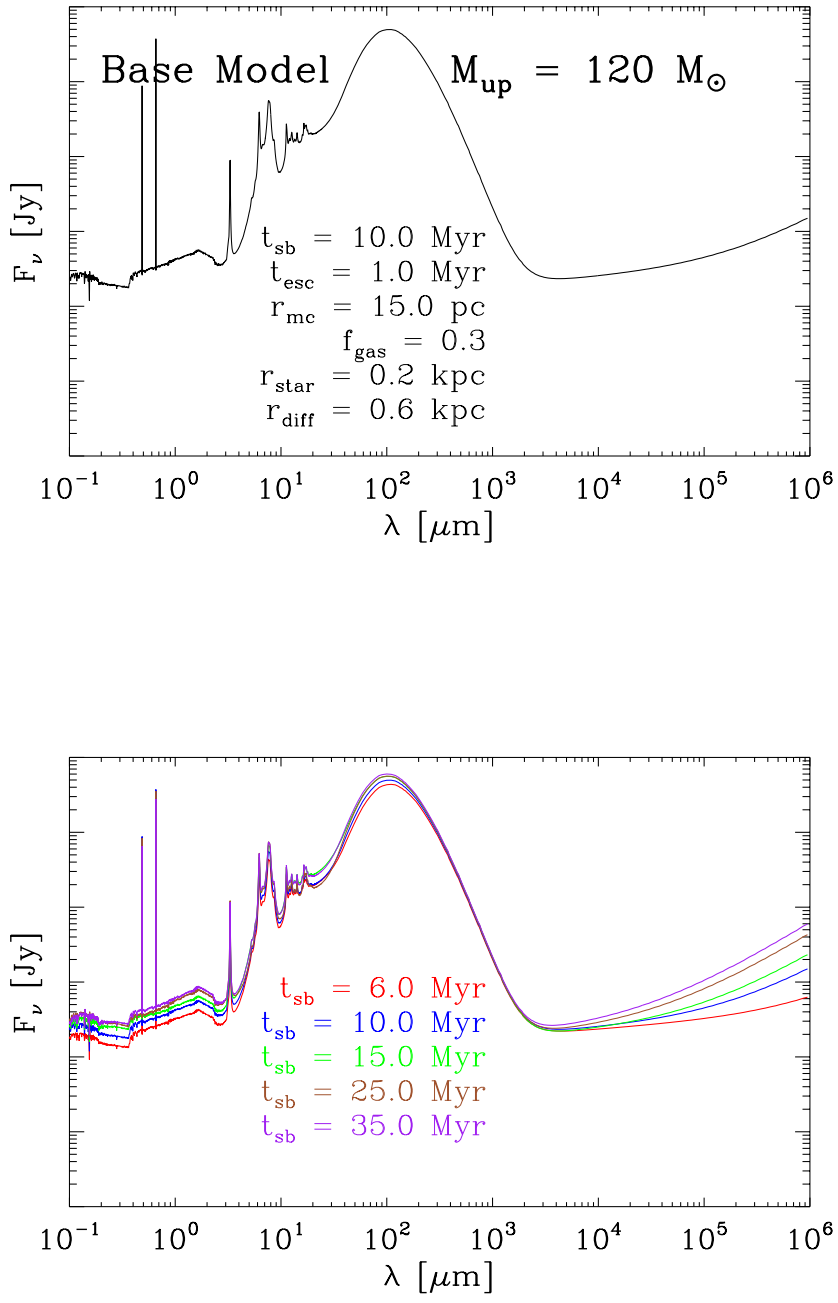

Figure 5.2: Effect of varying the main parameteres in GRASIL. Upper panel: the reference starburst model. Lower panel: varying the age of the burst.

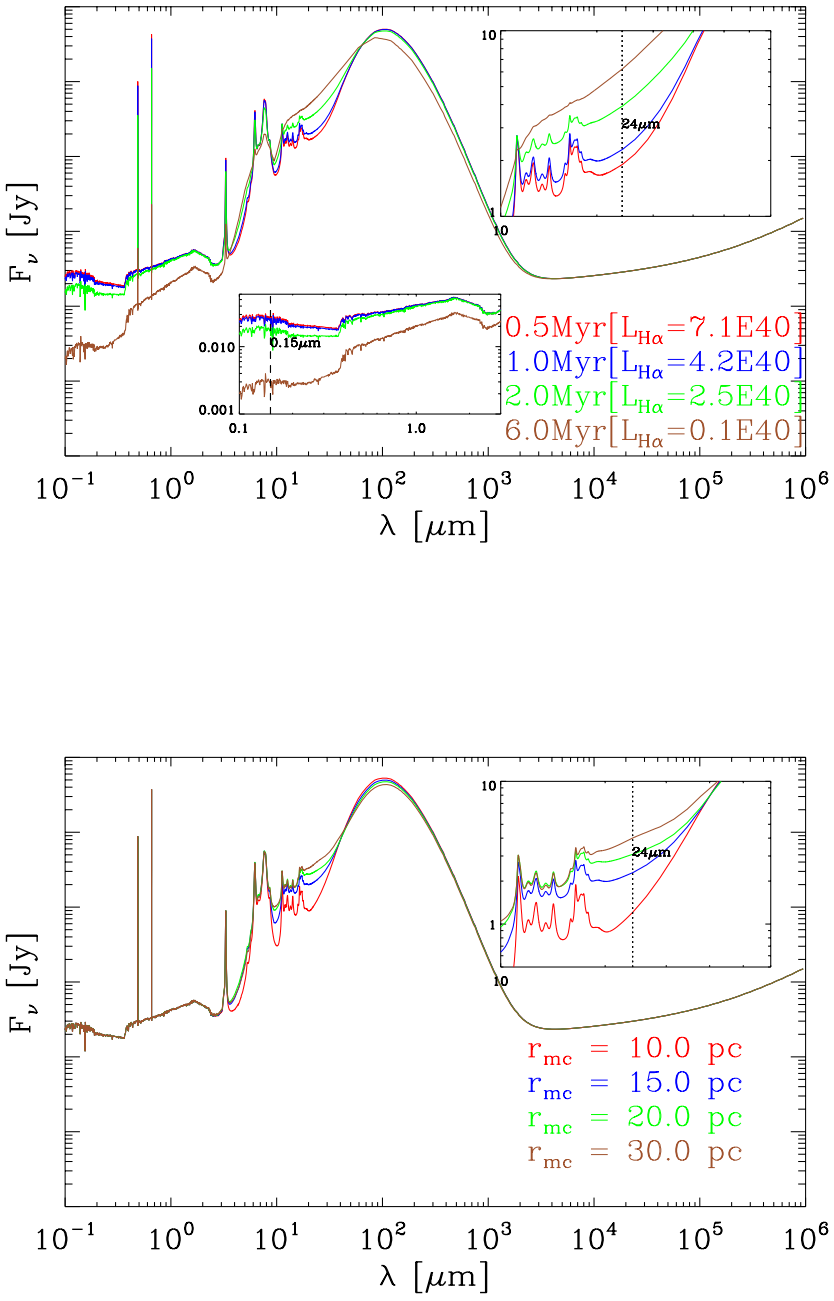

Figure 5.3: Upper panel: varying the escape time of young stars from their birth cloud. We have reported in parenthesis the predicted Hα luminosity in erg s^{-1} so to illustrate better it's variation with t_{esc}. Lower panel: varying the radius of the molecular clouds r_{mc}, i.e. their optical depth $\tau^{mc} \propto M_{mc}/r^2_{mc}$.

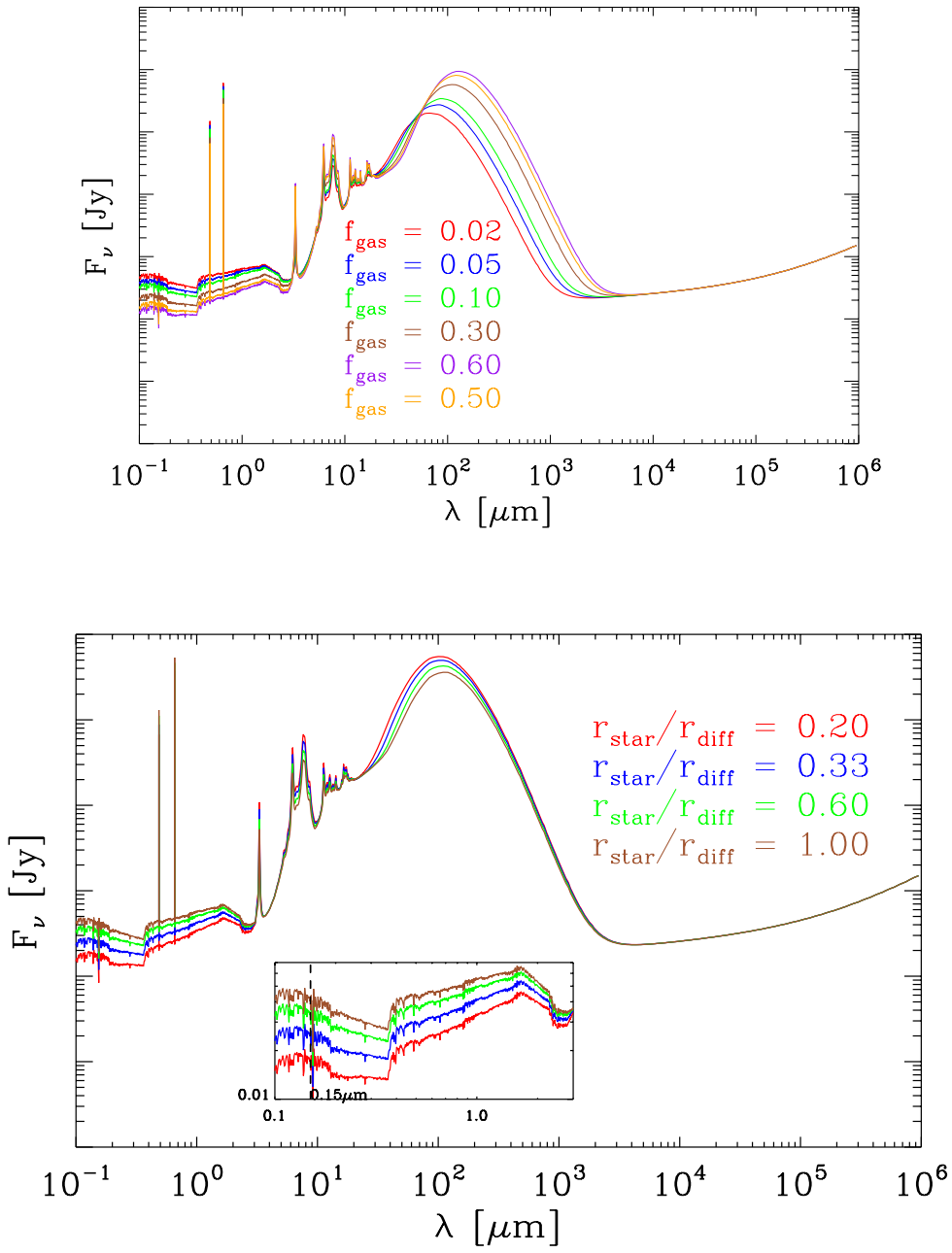

Figure 5.4: Upper panel: varying the mass fraction of total gas mass at the current time, i.e. the total mass of dust. Lower panel: varying the ratio r_{star}/r_{diff} of the core radius for the star distribution to the core radius for the diffuse dust distribution.

The age of the burst affects significantly the radio wavelength region of the SED (Figure 5.2). This is expected as the thermal and non-thermal radio emissions have different timescales, with the non-thermal radio emission starting late at about 7 Myr after the burst. The rise in radio emission after this age is mainly due to the contribution of the non-thermal radio emission. As shown in Figure 5.2, the predicted radio flux increases by a factor of ~ 5 and the UV flux by a factor of ~ 2 as the burst age is increased from 3 to 20 Myr.

The escape time of young stars from their birth clouds t_{esc} mainly affects the MIR region. The longer the young stars are embedded in these clouds, the more the dust in the clouds gets heated by their emission. This results in a higher predicted $24\mu m$ flux (vertical dotted line) which is very sensitive to the dust temperature. To illustrate clearly and quantitatively the effect of t_{esc} on the MIR and FUV regions, we have inserted in the top right and bottom left part of Figure 5.3 an enlarged view of the SED in these wavelength regions. As can be noted, an escape time of 6 Myr will produce a $24\mu m$ flux that is about two times larger than that produced with an escape time of 1 Myr (note that the SED is observed at 6 Myr after the start of burst in both cases). A reverse effect is observed in the predicted UV fluxes at 0.15μm and 0.22μm (vertical dashed lines in the botton left inset) because the shorter the escape time, the more the number of young stars (higher FUV flux) that have escaped the MC at a given time. The change in the UV flux becomes less pronounced as we move redward of 0.15μm. More interesting is the significant variation in our model's Hα flux as we gradually go from an escape time of 0.5 to 6 Myr. We have added to the t_{esc} labels the Hα flux (enclosed in parenthesis) in units of erg s^{-1} in order to show clearly these variations. Shorter escape times produce a higher Hα flux because of the much lower attenuation of the Hα line that is produced in HII regions in the cirrus. We remind that the ionising photons responsible for the latter line are both those that are produced by stars already in the cirrus and those that are produced in the MC and have escaped from it.

In Figure 5.3, we show the effect of varying the radius of the MC. Since we fixed M_{mc} to a value of 10^6 M$_\odot$, and the MC optical depth is given by $\tau^{mc} \propto M_{mc}/r^2_{mc}$, a change in r_{mc} implies a corresponding modification of the opacity of the clouds. Therefore stars, as well as the recombination lines in a MC with a shorter radius will suffer more dust attenuation because of a higher τ^{mc}.

In Figure 5.4 we show the effect of increasing the amount of gas in the model galaxy. Since we adopt a constant dust to gas mass ratio δ, this corresponds to increasing the total amount of dust of the same factors as the gas. The increased opacity of the MC and cirrus implies a larger reprocessing of stellar radiation to the IR, and also a redistribution of this energy to increasingly longer wavelength.

The last parameter we considered is the scale radius of the distribution of stars in the diffuse medium. We remind that for spherical symmetry we adopt a King profile with core scale radii r_{star} and r_{diff}.

In the lower panel of Figure 5.4 we show the effects of varying the relative distribution of stars and diffuse dust. We have assumed a diffuse dust distribution with r_{diff}=0.6 Kpc and different values of r_{star}, as indicated by the labels in the Figure. This simulates the transition from a dust screen like geometry, with all the stars concentrated in the central region and the dust acting as a slab, to a uniform distribution between dust and stars (e.g. Calzetti et al. 1994) In the bottom of the figure there is an enlarged view of the UV–optical region where the effects are more significant. As can be noted in the

figure, the model's FUV at 0.15μm changes by a factor of ~ 2 when r_{star}/r_{diff} changes by a factor of 5. The mass fraction of gas in molecular clouds is also a parameter that can be varied. However its effects are significant only at the extreme values (near zero or near unity) because it affects the presence of the molecular and the diffuse component, respectively.

We present in Table 5.1 a summary of the GRASIL parameters discussed above and of the spectral regions mostly affected by their variation. These are the main parameters we have considered in the fits performed in subsequent sections. If required to improve the fit, there is the possibility to change the slope, β, of the sub-mm emission of dust grains from its default value of 2 (Draine & Lee 1984; Draine et al. 2007). While it is conceivable that the intrinsic dust properties of single star forming regions may be different from the average properties of the Milky Way (e.g. Calzetti et al. 1994; Panuzzo et al. 2007), we have tried to always use the default value β=2.

Table 5.1: Effects of varying the main parameters of the GRASIL code (as shown in Figures 5.2 to 5.4).

Parameter	Values	Mainly affected SED region	Figure	Unit
t_{sb}	6 10 15 25 35	Radio slope, FUV	5.2	Myr
t_{esc}	0.5 1.0 2.0 6.0	UV, Mid-Infrared	5.3	Myr
r_{mc}	10 15 20 30	Mid-Infrared	5.3	pc
f_{gas}	0.02 0.05 0.1 0.3 0.5 0.6	UV, Far-Infrared	5.4	
$r_{c,*}/r_{c,diff}$	0.23 0.33 0.63 1.00	UV	5.4	

5.2.1 Performing the SED fitting

The SED fitting is performed considering the continuum emission and the Hα intensity. We searched the best fit separately for the different SSP sets with different M_{up} values. For this purpose we minimized the merit function

$$\mathrm{M} = \sqrt{\sum_i \left(\frac{F_{obs}(i) - F_{mod}(i)}{F_{obs}(i)} \right)^2} \tag{5.6}$$

where, $F_{mod}(i)$ and $F_{obs}(i)$ are the model flux values and the observed fluxes, respectively. This function allows us to focus on the best reproduction of some specific bands, independently of the real error, to check the performance of the model. For example, this is a useful indicator of the response of the models to changes in the main parameters and can be a useful guide for the fitting procedure. We also computed the standard χ^2 function

$$\chi^2 = \frac{1}{N} \sum_{i=1}^{N} \left(\frac{F_{mod}(i) - F_{obs}(i)}{Err(i)} \right)^2 \tag{5.7}$$

where $Err(i)$ are the observational errors respectively and N is the number of photometric points (including Hα) of the observed SEDs. The values of the χ^2 function generally agreed with the merit function M.

An important point to be kept in mind is that the number of varied parameters is always smaller than the number of available photometric data points.

5.3 Calibration of the non-thermal radio model

Besides describing how we use the GRASI code, this chapter is also meant to discuss the calibration of the non thermal radio emission. The SSP SEDs were already extended to the radio domain by Bressan et al. (2002) (hereafter B02) using for the non-thermal radio emission, the simple recipe by Condon & Yin (1990) which relates the non-thermal radio emission to the typeII SN rate.

The calibration by B02 yields a value of $E^{NT}_{1.49}$=1.38 for the proportionality parameter in Equation 4.7. As we have seen before, since the rate of CCSN is proportional to the SFR rate, this parameter is of fundamental importance for a panchromatic SED, because it sets the relative proportion between the FIR emission and non-thermal radio emission in a star forming galaxy. Generally these two parameters are fitted separately or by assuming a fixed proportion between the two luminosities. The latter approximation is suggested by the observational evidence coming from the FIR-radio correlation already mentioned in Section 4.2.

We recall that at 1.4 GHz the correlation is expressed by the ratio in Equation 4.5, with mean value $q_{1.4} \approx 2.35 \pm 0.2$.

However B02 have also noted that there are deviations from this ratio that may be explained with variations of internal conditions. The most important one is the effect of the age of a starburst. In the case of a very young starburst the radio emission may be dominated by thermal emission. In this case the slope of the radio emission is flatter and the $q_{1.4}$ value is higher than the average value, because an important component, the one due to CCSN, is lacking. This properties has already been used to fix or confirm the presence of very young populations in some star forming galaxies (e.g. Rosa-González et al. 2007; Thomson et al. 2014)

It is thus fundamental to check the value of the $E^{NT}_{1.49}$ parameter in a star forming galaxy, and more generally if the radio emission obtained with this value provides a q parameter consistent with the FIR/Radio correlation

For this reason we test the new SSP models with GRASIL on a well studied galaxy, M100, as discussed in the next section.

5.3.1 The SED of M100 as a template of spiral galaxies

The spiral galaxy M100 was selected from the Spitzer Nearby Galaxies Survey (SINGS) (Kennicutt et al. 2003), a collection of 75 nearby galaxies with a rich data coverage from the far-UV to the radio, because it is one of the best sampled objects, including the intensities of main emission lines. The resulting best-fit SED that will be presented in the next section (and those of subsequent galaxies that will be studied in this work) will provide the opportunity to check, for the first time in *GRASIL*, the consistency of the SED continuum and emission lines fitting.

For the chemical evolution model we adopt the parameters of the chemical evolution code *CHE_EVO* given by Silva et al. (1998) who was able to well-reproduce M100. They are infall time scale t_{inf} = 3.0 Gyr, efficiency of the Schmidt star formation law ν_{sch} = 0.75 Gyr^{-1}, and the total infall mass m_{inf} = 2 × 10^{11} $M_{\odot}$. Figure 5.5 shows the SFH and gas mass history resulting from the adopted chemical

evolution parameters. The SFH is indicated by the solid black line and the gas mass history by the dotted purple line.

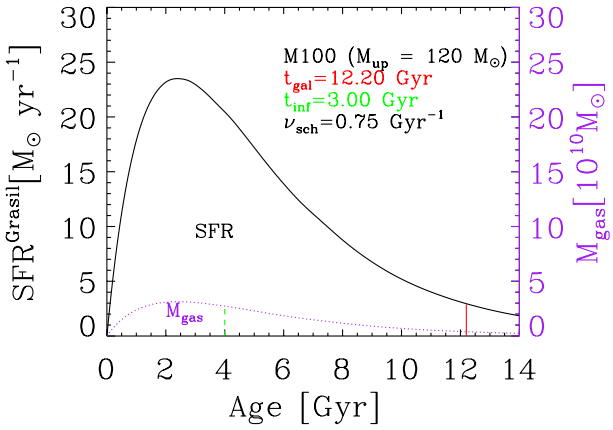

Figure 5.5: Star formation and gas mass history of M100 adopted in our *CHE-EVO* model. The model parameters are labelled: galaxy's age t_{gal}(the vertical solid red line), infall time t_{inf}(the vertical dashed green line) and schmidt-law efficiency ν_{sch}. These parameters were adopted by Silva et al. (1998) based on constraints to reproduce the observed final mass of M100. The SFH is indicated by the solid black line and the gas mass history by the dotted purple line.

To perform the SED fit, we consider several time steps t_{gal} along the chemical evolution of the galaxy for which we built a library of SED models with different GRASIL parameters. We note that since the observed SED refers to the whole galaxy, the derived parameters correspond to a luminosity average of the physical properties, as commonly obtained by this kind of fitting process. We also investigate the effect of changing the upper mass limit of the IMF, $M_{up} = 40,\ 80, 120$ and $350 M_{\odot}$, on some physical quantities derived from our best-fit SED, in particular the SFR.

In addition to t_{gal}, the *GRASIL* parameters we have varied are the escape time t_{esc}, the MC radius r_{mc} in order to modify the optical depth of molecular clouds, and the amount of gas given as the fraction, f_{gas}, of the total mass of the galaxy.

We present and discuss these best-fits in the next section.

5.3.2 Results

Our *GRASIL* best-fit SEDs of M100 for $M_{up} = 40, 80, 120$ and $350 M_{\odot}$, are shown in the Figures 5.6, 5.7, 5.8 and 5.9 respectively, while the corresponding best fit parameters are summarised in Table 5.2.

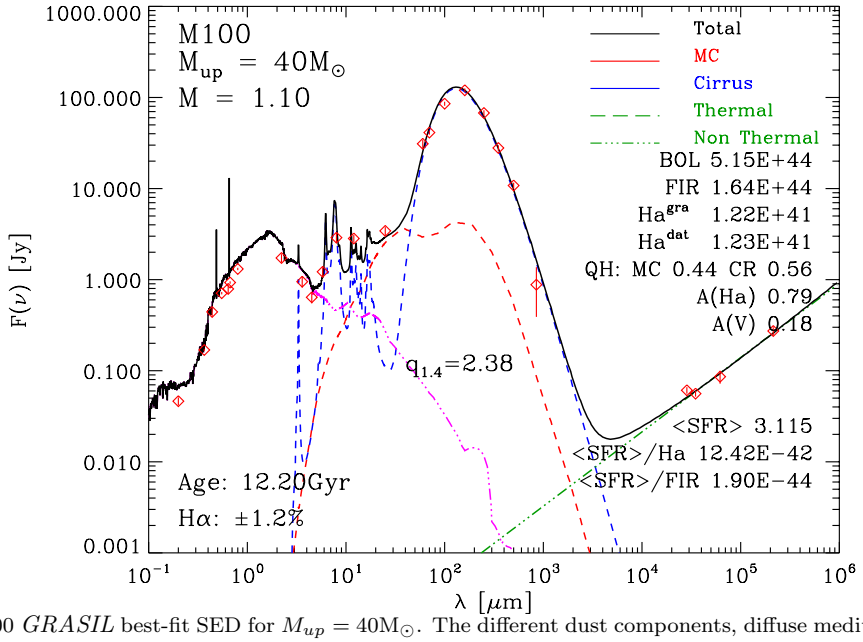

Figure 5.6: M100 *GRASIL* best-fit SED for $M_{up} = 40M_\odot$. The different dust components, diffuse medium and molecular clouds are represented by the dashed blue and red lines respectively. The thermal and non thermal radio components are represented by the green dashed and dot-dashed dotted lines as shown in the Figure. The thermal component can be seen to be negligible for this M_{up}. The age of the galaxy is given in the bottom left side of the plot. Other quantities labelled are described in the text.

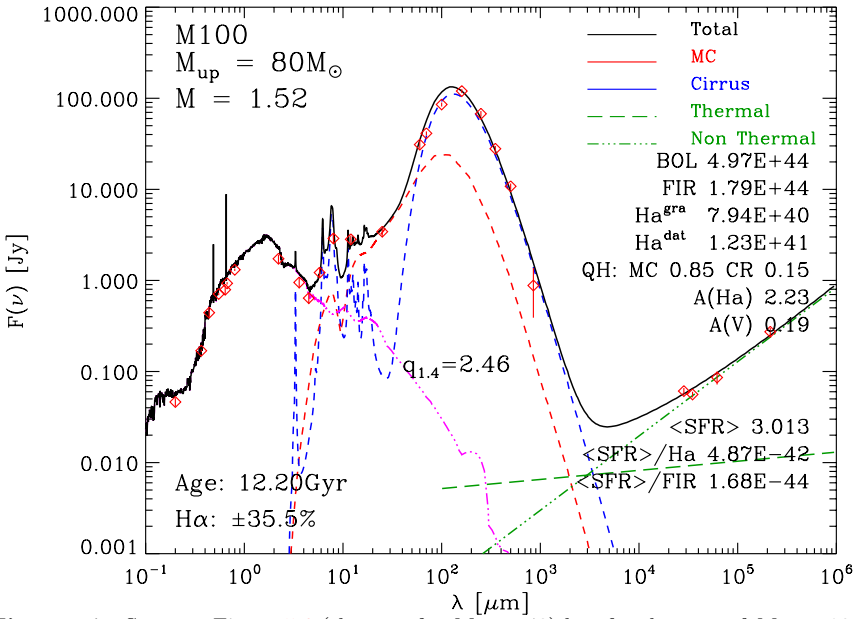

Figure 5.7: Same as Figure 5.6 (the case for $M_{up} = 40$) but for the case of $M_{up} = 80$.

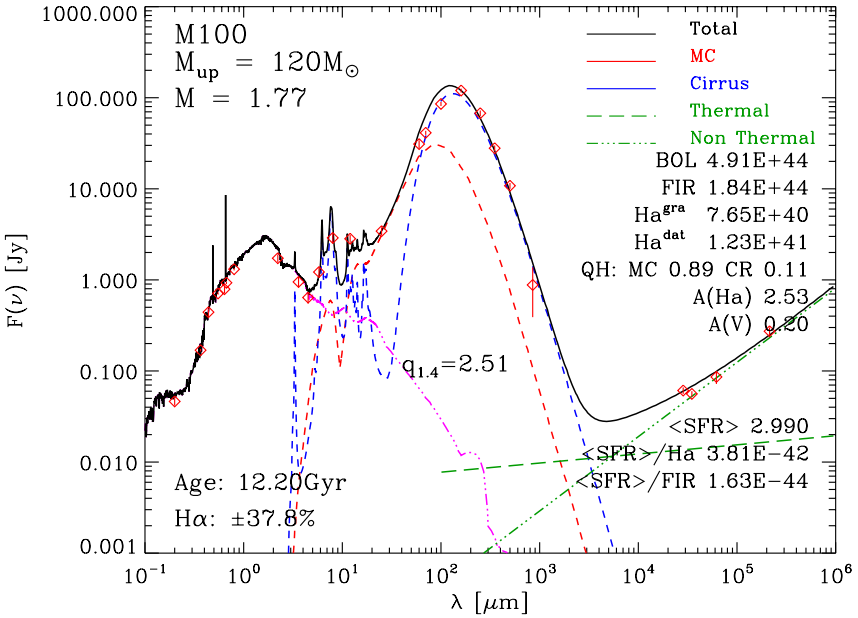

Figure 5.8: Same as Figure 5.6 but for the case of $M_{up} = 120$.

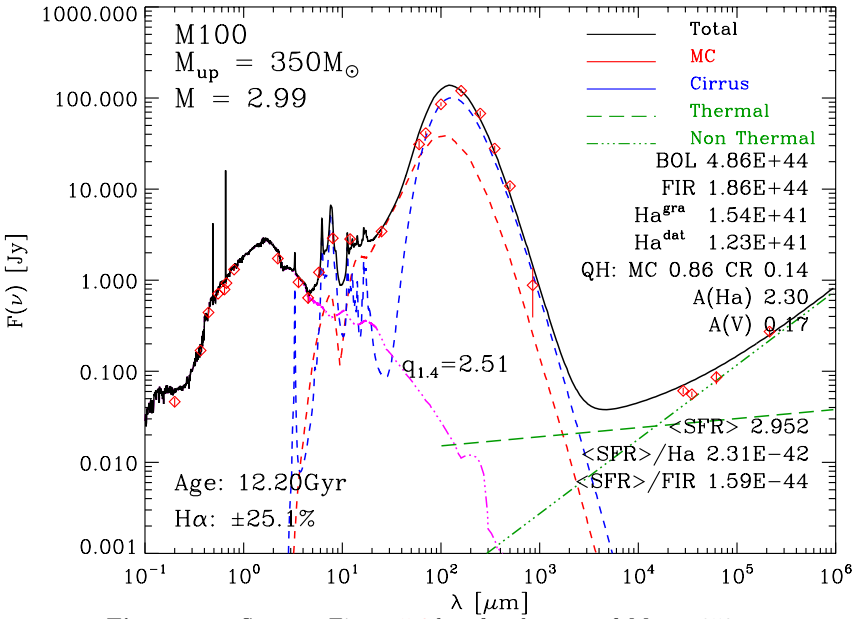

Figure 5.9: Same as Figure 5.6 but for the case of $M_{up} = 350$.

M_{up}	t_{gal} (Gyr)	t_{esc} (Myr)	r_{mc} (pc)	f_{gas}	f_{mc}	β
40	12.2	1.5	27.0	0.05	0.10	2.0
80	12.2	3.0	13.0	0.05	0.10	2.0
120	12.2	3.0	11.0	0.05	0.06	2.0
350	12.2	2.0	11.0	0.05	0.20	2.0

Table 5.2: *GRASIL* best fit parameters (for upper mass limits of 40, 80, 120 and 350) for the modelled SED of M100.

The different dust components in diffuse medium (cirrus) and molecular clouds in the figures are indicated by the blue and red dashed lines, respectively. The thermal and non-thermal radio emission components are indicated by the green dashed and dashed dotted lines, respectively. The thermal component can be seen to be negligible for the case of $M_{up} = 40\mathrm{M}_{\odot}$.

The labels in the plots refer to some important quantities derived from our best fits: the bolometric luminosity from UV to radio (BOL), the total IR luminosity from 3 - 1000 μm (FIR), the predicted transmitted (i.e. not the intrinsic one) H_{α} luminosity (Ha^{gra}), the observed H_{α} luminosity (Ha^{dat}), the H_{α} attenuation A(Hα), the attenuation in the V(0.55μm) band A(V), the SFR averaged over the last 100 Myr ($<$ SFR $>$), the q-parameter as defined by Equation 4.5 ($q_{1.4}$), the coefficients of the SFR/H_{α} and SFR/IR calibrations ($<$ SFR/Ha $>$ and $<$ SFR/FIR $>$ respectively). The merit function M labelled on the top left is given in Equation 5.6. A summary of other important quantities derived from our best fit is provided in Tables 5.3 and 5.4.

We now examine the best fits models obtained with different values of M_{up}. The best fit obtained with $M_{up} = 40\ \mathrm{M}_{\odot}$ reproduces very well the radio, the far and mid infrared spectral regions. This model provides a q ratio $q = 2.38$ which is very similar to the average value provided by the FIR-Radio correlation ($q_{1.4} = 2.35 \pm 0.15$). The model also reproduces fairly well the near infrared and optical spectral region but it overestimate the UV flux. The Hα line intensity is almost perfectly reproduced (within 1.2%).

The best fit obtained with $M_{up} = 80\ \mathrm{M}_{\odot}$ also provides a fairly good fit to the observed SED of M100. However we note a slight excess in the FIR, at 100μm and a slight defect at 1.4GHz. Both discrepancies combine to produce a slightly higher value for the ratio q, $q_{1.4} = 2.46$, which however is still within the allowed values. A further fine tuning of the fitting to eliminate these two small discrepancies will decrease the q ratio toward the average one given by the FIR$-$radio correlation. We note that the UV flux is quite well reproduced by the best fit while the intensity of the Hα emission is about 35% lower than the observed one.

The case computed with $M_{up} = 120\ \mathrm{M}_{\odot}$, is very similar to the best fit obtained with $M_{up} = 80\ \mathrm{M}_{\odot}$. here the excess in the FIR is a bit larger than in the case of $M_{up} = 80\ \mathrm{M}_{\odot}$. Apart from the fact that the overall fit is excellent and as in the previous case, a fine tuning of the parameters aimed at decreasing the FIR excess will provide a q ratio that is in better agreement with the one resulting from the FIR$-$radio correlation.

Finally the case computed with $M_{up} = 350\ \mathrm{M}_{\odot}$, while also providing an overall acceptable fit, it shows an evident excess of ionizing photons. On one side the slope of the radio emission is flatter than that

expected from the observed data since the 1.4 GHz emission is underestimated and all other radio fluxes are overestimated. The UV flux is also overestimated and the predicted Hα emission is larger than the observed one, though within the 25%. The excess thermal emission produced adopting M_{up} = 350 $M_\odot$ is the strongest indication that this upper mass limit is not realistic for M100.

We note that all the best fit models produce a more or less evident excess flux in the UV region. This discrepancy could be cured by increasing the escape time of young stars in their parent clouds but this will lead to a larger absorption by the MCs. Such larger absorption from MCs will increase the predicted 24 μm flux above the observed one. Note that at 24 μm the cirrus component has a pronounced minimum and its contribution to the overall MIR emission is only a small fraction of the total. Thus, the 24 μm flux, being dominated by the MC emission, is indeed a strong diagnostic for the amount of light reprocessed by the MC component.

Thus a fine tuning of all the other parameters will be necessary to remove the small discrepancies that still remain between the best fit models and the observed data at least in the cases with M_{up} = 80 $M_\odot$ and M_{up} = 120 $M_\odot$.

The important result obtained from the best fit models of M100 is that we may fix the ratio between the CCSN-rate and the non thermal radio emission, the constant $E_{1.49}^{NT}$ in equation Equation 4.7.

All the best fit models have been computed by assuming $E_{1.49}^{NT} = 1.944$, thus the new calibration for the factor $E_{1.49}^{NT}$ is

$$E_{1.49}^{NT}(\text{Thiswork}) = 1.944 = \text{E}_{1.49}^{\text{NT}}(\text{B02}) \times 1.4 \tag{5.8}$$

The newly obtained $E_{1.49}^{NT}$ constant is thus about a factor of 1.4 larger than the value obtained by B02 using the previous radio model.

We finally note that the predicted average SFR resulting from the panchromatic fit of M100 is only slightly affected by the adoption of a different value of M_{up}. By increasing M_{up} from 40 to 120 $M_\odot$ the average SFR decreases by about 6%.

Having calibrated the non-thermal component of the total radio emission in this section, we proceed in the next section to check if the other component, the thermal radio emission, can be well reproduced in star forming HII regions (while using the non thermal radio calibration value so obtained).

Table 5.3: GRASIL Best-fit model luminosities for M100

(1)	(2) (17)	(3)	(4)	(5)	(6)	(7)	(8)	(9)	(10)	(11)	(12)	(13)	(14)	(15)	(16)
ID	M_{up}	BOL	FUV_i	FUV_t	24	70	FIR	FIR_H	33	8.5	4.9	1.4	q	MC	CIR
	$M_\odot$	10^{42}	10^{41}	10^{41}	10^{41}	10^{41}	10^{42}	10^{-11}	10^{26}	10^{26}	10^{26}	10^{26}			
M100	40	514.11	625.50	371.00	106.00	598.00	164.00	220.00	68.5()	180.0()	276.0()	772.0()	2.38	13.0	87.0
M100	80	497.22	678.60	311.00	133.00	724.00	179.00	259.00	89.5(31)	196.0(15)	286.0(10)	747.0(4)	2.46	32.0	68.0
M100	120	490.67	700.23	298.00	120.00	821.00	184.00	289.00	99.6(41)	204.0(21)	293.0(15)	742.0(7)	2.51	35.0	65.0
M100	350	486.91	728.89	336.00	129.00	831.00	186.00	292.00	131.0(59)	235.0(35)	320.0(27)	750.0(13)	2.51	39.0	61.0

Col.(1): ID. Col.(2-4): bolometric and FUV (at 0.16 μm) luminosities. ^{i} and ^{t} indicates intrinsic and attenuated transmitted luminosities respectively. Cols.(5 and 6): luminosities at 24 μm and 70 μm. Col.(7): total (3-1000 μm)IR luminosity. Col.(8): FIR flux in ergs s^{-1} cm^{-2} in the 40 - 120 μm interval derived using the 60 and 120 μm fluxes (Helou et al. 1988) and used in the calculation of $q_{1.4}$ that is given in Column 13. Cols.(9-12): radio luminosities at and 33, 8.5, 4.9 and 1.4 GHz Enclosed in parenthesis is the fraction in per cent of the thermal radio component to the total radio emission. Col.(13): q-parameter as defined by Equation 4.5. Cols.(14 and 15) are the MC and cirrus contribution (in per cent) to the total IR (Col.7) luminosity respectively. The bolometric, FUV and infrared luminosities are in erg s^{-1} while all radio luminosities are in erg s^{-1} Hz^{-1}. The corresponding SFR calibrations at these luminosities are given in Table 6.4.

Table 5.4: GRASIL Best-fit derived SFRs and their calibrations at various bands for M100

(1) ID	(2) M_{up} $M_\odot$	(3) $< SFR >$	(4) $C(BOL)$ 10^{-44}	(5) $C(FUV)$ 10^{-43}	(6) $C(24)$ 10^{-43}	(7) $C(70)$ 10^{-43}	(8) $C(FIR)$ 10^{-44}	(9) $C(33)$ 10^{-28}	(10) $C(8.5)$ 10^{-28}	(11) $C(4.9)$ 10^{-28}	(12) C(1.4) 10^{-28}	(13) t
M100	40	3.12	0.61	0.50	2.94	0.52	1.90	4.55	1.73	1.13	0.40	12.2
M100	80	3.01	0.61	0.44	2.27	0.42	1.68	3.36	1.54	1.05	0.40	12.2
M100	120	2.99	0.61	0.43	2.49	0.36	1.63	3.00	1.46	1.02	0.40	12.2
M100	350	2.95	0.61	0.40	2.29	0.36	1.59	2.26	1.26	0.92	0.39	12.2
Literature												
				0.44[a]	2.46[d]	0.97[g]	4.55[b]	6.53[a]	2.0[e]	1.4[e]	0.64[a]	
					4.80[h]	0.92[h]	3.88[a]	0.62[e]				
							0.58[f]	3.99[h]				

Col.(1): ID. Col.(2): average SFR (in $M_\odot\ yr^{-1}$) derived by considering the last 100 Myr time interval for the normal star-forming galaxy M100 and the age of the burst in the star-forming regions of NGC 6946 Cols.(3-11): SFR calibrations obtained using the above averaged SFR and the luminosities (intrinsic value for FUV) given in Table 5.3. Col.(12): age of the galaxy in Gyr for M100 or the age of the burst in Myr, for NGC 6946 extranuclear regions. The last row in each of the four panels (with ID, $< NGC\ 6946 >$) gives the median values of all quantities given for NGC 6946 star-bursting regions. The values of the SFR calibrations given in the fifth panel were taken from the literature. The superscript on these values indicates the reference as described below: [a]Murphy et al. (2011), [b]Kennicutt (1998), [c]Calzetti et al. (2007), [d]Zhu et al. (2008), [e]Schmitt et al. (2006b), [f]Li et al. (2010), [g]Lawton et al. (2010), [h]Panuzzo et al. (2003). These authors adopted different IMF and evolutionary synthesis models.

Chapter 6

Modelling the SED of star-bursting regions

6.1 Introduction

In the previous chapter, I used the observed SED of the galaxy M100 as a template to check the performance of our models and, in particular, we used the best fit model to calibrate the constant $E_{NT}^{1.4}$ of the non-thermal radio emission model. In M100 the radio emission is dominated by the non-thermal component, the free-free emission becomes apparent only at frequencies significantly lower than 1.4 GHz. We have also seen that it is possible to fit fairly well the SED of M100 with four different values of the upper mass limit of the IMF, M_{up}=40 $M_\odot$, 80 $M_\odot$, 120 $M_\odot$ and 350 $M_\odot$.

With M_{up}=350 $M_\odot$ the models predict an excess of ionizing photons which appear more clearly in an excess of free-free emission with respect to the observed data. This cannot be cured by increasing the attenuation because at the frequencies where free-free emission is important, it is negligible. Moreover neither free-free absorption can be invoked because, given its strong dependence on the frequency ($\propto \nu^{-2.1}$) it should almost completely absorb the non-thermal emission component.

However neither the model with M_{up}=120 $M_\odot$ is acceptable because, though being able to reproduce perfectly the panchromatic broad band SED of the galaxy, it severely underestimate the predicted Hα luminosity. The best fit, within the acceptable uncertainties of the data, is provided by the models adopting M_{up}=40 $M_\odot$ and M_{up}=80 $M_\odot$. The former is favoured by the better match with the Hα luminosity while the latter produces a better match with the observed UV emission. In any case the SED of M100 is typical of a normal star forming spiral where the observed average star formation rate seems to change slowly with time, as opposed to the case of a star-burst galaxy, where the star formation rate may be dominated by a recent episode of enhanced intensity. In the latter case we would expect a larger relative contribution of the free-free component with respect to the former case simply because the average age of the star-burst could be younger and thus, as seen in previous chapters, the thermal component is more evident. It would be extremely interesting to test the performance of our models

against a star-burtsting galaxy because it would provide the opportunity of measuring the SFR from independent spectral windows and at least the two are related to the same physical process occurring in the presence of a population of massive stars, the flux of ionizing photons.

For this purpose I examined the literature seeking for suited candidates with well sampled SEDs allowing a panchromatic analysis that includes also at least one recombination emission line. We have found that the best workbench for our models is the galaxy NGC6946, the so called *Fireworks Galaxy*. This well studied face-on galaxy, located at a distance of 6.8 Mpc, is dominated by very young star-burst regions. These regions have been extensively studied and what is interesting is that they show relatively large thermal over non-thermal emission ratios (e.g. Murphy et al. 2010). Furthermore, Murphy et al. (2010) observed these regions (Figure 6.1) at 1.4, 1.5, 1.7, 4.9, 8.5 and 33 GHz and complemented their full SEDs with existing data from the UV to the submm range. For eight observed regions, Murphy et al. (2010) estimated an average 33 GHz thermal component of $\approx$ 85% of the total, while for one region (named extra-nuclear region 4), this percentage was found to be significantly lower, $\approx$ 42 %, likely because of the presence of a so-called anomalous dust emission component which suppresses the thermal component. Particularly interesting for our purpose is that Murphy et al. (2010) also provide the intensity of the Hα emission for each region, that can be directly compared to the predictions of a panchromatic synthesis tool.

In the following sections we will present the best fit models of the SEDs of these regions and discuss the obtained results.

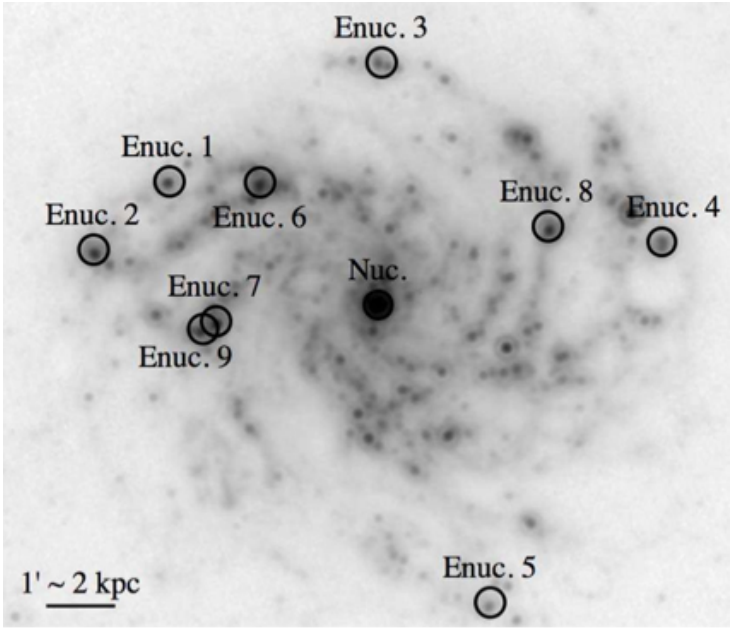

Figure 6.1: NGC 6946 10 star forming regions observed by Murphy et al. (2010). The extra-nuclear regions are indicated by the terms "Enuc.1" through "Enuc.9". We did not consider the nuclear region (indicated by "Nuc") in our analysis.

6.2 The SED model library

A complete GRASIL model requires a specification of the star formation history and corresponding metal enrichment, to calculate the integrated light of the underlying SSPs, and a set of parameters more specific to GRASIL radiation transfer calculations, as described in the previous Chapter.

To fit the data we have thus first constructed a large library of SED models taking into account the variations of the main parameters, as specified below.

Concerning the adopted star formation rate we note that, for the analysis of the SEDs, we make use of the data not corrected for the local background emission of the galaxy, though Murphy et al. (2011) also provide an estimate of this background. We thus adopt a chemical evolution model composed of a star-burst event superimposed to a quiescent star forming disk. This choice allows us to obtain results that are independent of the subtraction performed by Murphy et al. (2011) and eventually compare our results with their estimates. For purposes of clarity we show in Figure 6.2 a plot of the star formation history used for one of the extra-nuclear regions, region 3. The corresponding chemical evolution model parameters are labelled in the left side of this figure. The ongoing starburst has formally an exponentially

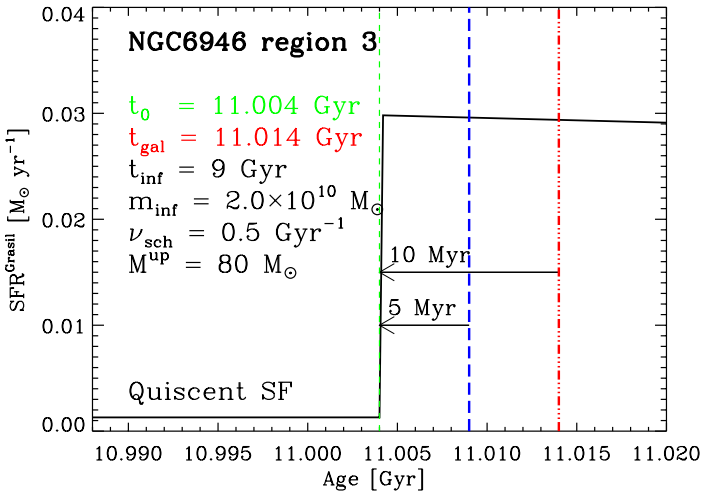

Figure 6.2: Star formation history of one of the NGC6946 extranuclear regions, NGC6946 region 3 for $M_{up} = 80 M_{\odot}$ case. The red dotted-dashed line indicates the time (t_{gal}= 11.014 Gyr) at which the best-fit SED of this region was observed, t_{sb}= 10 Myr after the burst of star formation started at t_0= 11.004 Gyr (green short dashed line). We included an observation time of 11.009 Gyr (blue long dashed line) which corresponds to 5 Myr after the burst started only to illustrate that we do not expect any contribution to the non-thermal emission from the starburst at this age according to our radio model in Figures 4.8 and 4.9. At burst ages between $\sim$ 7 Myr and 30 Myr, we expect a contribution to the non-thermal radio emission also from the starburst.

declining SFR that begins at $t_0 = t_{gal} - t_{sb}$, where t_{sb} is the age of the starburst and $t_{gal} = 11.014$ Gyr is the age at which the region was observed for our best fit SED. It is not important to use the actual age of the galaxy as the regions are dominated by the starburst. On the contrary the age of the starburst is very important because, for exactly the same reason, the age is one of the parameters that modify the

Table 6.1: Parameters varied in the GRASIL model library.

Parameter	N	Range	
M_{UP}	4	40 – 350	$M_\odot$
t_{sb}	7	6 –18	Myr
t_{esc}	4	0.3 – 2.0	Myr
f_{gas}	7	0.05 – 0.6	
f_{mol}	4	0.1 – 0.6	
r_{mc}	3	12 – 20	pc
r_{diff}	4	0.3 – 1.0	Kpc
r_{star}	2	0.5× r_{diff}, 1× r_{diff}	
β	1	2.0	

slope at radio frequencies and, actually, it is one of the derived parameters. The SFR example shown in Figure 6.2 have observation times of t_{gal}=11.009 (long dashed blue line) and 11.014 (red dotted-dashed line) Gyr corresponding to burst ages of 5 and 10 Myr respectively.

As shown in Figures 4.8 and 4.9, in the first case we are not expecting any contribution to the non-thermal emission from the starburst while, in the second case since the age is larger than 7 Myr we expect a contribution to the non-thermal radio emission also from the starburst. Thus any age between t_{sb}= 7 Myr and 30Myr can provide SEDs with different percentages of thermal vs non-thermal radio emission. We note that with this choice we can mimic possible different contributions of non thermal emission from the underlying disk. Concerning the gas and most recent star metallicities, we note that the regions are located in the outskirts of the galaxy and, for this reason we adopt a chemical composition of Z = 0.008 (Pilyugin et al. 2014), i.e. about 0.5−0.6 solar depending on the adopted solar abundance value. This has been done for all the regions independently of their location but, unless our estimate of the metallicity is not grossly in error, this choice will not impact our results. Furthermore we note that we do not consider any auto-enrichment due to the ongoing starburst. We also note that the decline of the SFR within the few initial tens of Myr is not strong and the results would not be significantly different if a constant SFR is adopted.

We now consider the parameters we have used in the library of GRASIL models. We first consider the geometry. We have already specified that GRASIL may work with three option for the geometry, a spherical symmetric distribution with a King profile a disk geometry with a given orientation, or a mix of the two. Since the galaxy is face-on and the regions have a typical size of 0.8 Kpc, the best option with which to model their SEDs is a spherical symmetric distribution with a King profile for both the stars and dust. This geometry is assumed for all the models in our library.

The other parameters varied in the library have been selected after an initial exploratory run and are the following. The upper mass limit of the IMF M_{up}, which affects the underlying SSPs libraries; the starburst age t_{sb}; the escape time of young stars from their birth clouds t_{esc}; the total gas fraction f_{gas}; the fraction of the gas in molecular clouds f_{mol}; the optical depth of molecular clouds at $1\mu m$, τ_1 (represented by r_{mc} since the mass of individual molecular clouds is fixed at $10^6 M_\odot$); the core radii for diffuse dust r_{diff} and stars r_{star} King profile distributions; the submm dust emissivity index β. Their values are shown in Table 6.1

In total the number of combinations considering all the parameters and their adopted values cor-

responds to 75264 models. However in the exploratory run we have seen that there are some evident correlations between some parameters. For example the models with M_{up}=350M$_\odot$ produce much more ionizing photons than those that adopt M_{up}=40M$_\odot$. This implies that, at a given age, the radio slope of the models adopting the former M_{up} is flatter than that computed with M_{up}=40M$_\odot$. This can be balanced by an older star-burst age in models with M_{up}=350M$_\odot$ so that, since the model must fit the data, there is a correlation between the value of M_{up} and the star-burst age, in the sense that low values of M_{up} coupled with old star-burst age produce model dominated by non-thermal emission which are excluded by the observations. This helped to reduce the number of independent models to about 30000.

As in the case of the M100 SED, to select these best-fit models we use the merit function shown in Equation 5.6. We separately constructed the merit functions for the different sets of models with different M$_{up}$ We now note that in computing the merit functions we decided to exclude two of the observed bands. One is the flux near 8 μm which is dominated by the strong PAH emission features at 7.7 and 8.6 μm. This flux is strongly dependent on the assumption concerning the abundance of such components. For example Vega et al. (2008) had to suppress the PAH emission from the molecular cloud component in order to reproduce the SEDs of Ultra Luminous Infrared Galaxies (ULIRGS). This assumption was justified by the fact that near strong radiation sources there seem to be a depletion of the PAH carriers. But it is not known if this assumption is still valid in the star forming regions that we are analysing.

The second assumption arises from the difficulty we encountered in fitting the UV broad band values at once. We find that it is almost impossible to fit the far UV (at 0.15 μm) and near UV (at 0.23 μm) fluxes and, at the same time, the Hα flux with a single star-burst model. The attenuation resulting from the observed ratio of the UV fluxes would be so high to suppress almost entirely the Hα emission. On the other hand we have seen that while the far UV flux is tightly linked with the recent star burst activity, the near UV flux (at 0.23 μm) may depend also on the underlying older disk component, that we have not subtracted from the observed fluxes. This is the only component we have in the SED that is sensitive to intermediate age populations and a match of this band would have forced us to compute many other disk models, that is not what we are looking for in the present study. Thus we decided to fit the near UV band by adding a single SSP representative of the average underlying intermediate age disk population. The adopted SSP is clearly shown in all the plots presented below. Alternatively we could have omitted this band from the fits.

In the sections that will follow up we present the fits of the individual star bursting regions of NGC 6946 and discuss their characteristics. The parameters of the best fit SEDs are shown in Table 6.2.

6.3 Fitting the SEDs of the individual NGC6946 regions

Here we present and discuss our best-fit SEDs of the star bursting regions of NGC 6946 modeled with GRASIL. For all regions the observed IR SED can be fairly well reproduced by using either of the IMF upper mass limits. We discuss separately the regions as follows.

Region 1 In the four panels of Figure 6.3 we show the best-fit SEDs for the extranuclear region 1 for M_{up} = 40, 80, 120 and 350 respectively. Each panel separately contains two plots. In the upper plot we show the observed photometric data points, represented by the red diamonds, and the corresponding models while, in the lower one, we show the relative residuals between the data and the model, $(F_{obs}-F_{mod})/F_{obs}$, indicated by red squares. We have added in the bottom left of the SED plot the age of the burst and the value of the residual for the Hα luminosity, in percentage. We remind that the models are normalized to the data at 100 μm. The dashed lines in the residual plot indicate the region where our model reproduces the observed data within 20 percent while the solid line represents the zero of the residuals. The best fit model (solid black line) is decomposed in its different components. Starting from the right side of the SED plot we first recognise the non thermal radio emission component (green three-dot-dashed line). Below the non thermal component we see the free-free emission (green long dashed line) that runs much flatter. At decreasing wavelengths the latter overcomes the synchrotron emission and becomes the dominant component at around λ=10 mm. At even shorter wavelengths we see the rapidly rising emission from the diffuse cirrus (blue short dashed line) and, just below it, the molecular cloud component (red short dashed line). The infrared peak is dominated by the cirrus component which, however, being cooler than the molecular cloud component fades more rapidly in the mid -infrared spectral region. At 24 μm the molecular cloud component is warm enough to dominate the emission from dust. However immediately short-ward the PAH emission from the cirrus competes with the emission from molecular clouds and gives rise to the typical emission bands seen in star forming regions. The 8μm band is entirely dominated by the emission from PAHs. Nevertheless we stress that the combined PAH and cirrus continuum dust emission form a hole around 24 μm where the molecular cloud contributes up to 90% of the whole flux. This is an important window to estimate the escape time from molecular clouds and, of course, the flux at this wavelength is strictly related with the far UV flux and with the Hα emission because they arise from the more massive stars which constitute the more dust embedded population. At even shorter wavelengths, in the near infrared (NIR) the intermediate age population begins to appear (brown dot-dashed line), together with the population of red supergiant stars (magenta triple dashed line in the NIR). These populations host dust enshrouded stars, Asymptotic Giant Branch or red supergiant stars. In both cases we see the peaks of the silicate emission of their dusty envelopes which are modelled during the construction of the integrated SSP spectra. The intermediate age component is the main continuum stellar component up to the ultraviolet region, where the contribution of the absorbed star-burst becomes the most important one. However we note the two prominent emission lines, Hα and Hβ on top of the stellar continuum that, together with the other emission lines calculated but not shown in these plots, are the signature of the massive stars population at optical wavelengths. As already discussed before it is impossible to reproduce both the far and near UV fluxes with the absorbed star-burst. The required attenuation would be too high and incompatible with the observed Hα luminosity. Just short-ward of the near-UV the intermediate population contribution drops leaving the absorbed star-burst as the only component in the far-UV spectrum.

The extranuclear region N 1 is well fitted by a young ongoing star-burst with age between 8 Myr and 16 Myr depending on the adopted upper mass limit of the IMF. The age of the burst in the best

fit model is shown in the lower left region of the SED plot. Other important quantities are indicated in the plot. Starting from the upper right we list the bolometric luminosity of the region (BOL), obtained by integrating the SED of the the model after accounting for the distance of NGC 6946. We then show the infrared emission (FIR), computed in the same way but from 3 μm to 1000μm. We then show the predicted trasmitted luminosity in the Hα line (Ha^{gra}), i.e. after absorption by dust, and the observed one (Ha^{dat}). Then we show the value of the attenuation in the Hα line, estimated from the ratio of the transmitted and the intrinsic model luminosities, and the attenuation in the visual band, estimated in the same way. All these quantities refer to the star-burst alone and they do not include the contribution from the intermediate age population, which is added only for plotting purposes. In the bottom right side of the figure we list the average star formation rate derived from the best fit model, ($< SFR >$). This is computed as the integral of the star formation rate of the model during the burst and up to its current age, divided by the current age of the burst. Then we list the ratio between the average star formation rate and the $H\alpha$ luminosity and that with respect to the FIR luminosity. These quantities indicate the calibration ratios between SFR and luminosity, for the FIR and for Hα. We finally provide the ratio $q_{1.4}$, between FIR and radio emission computed following equation 4.5.

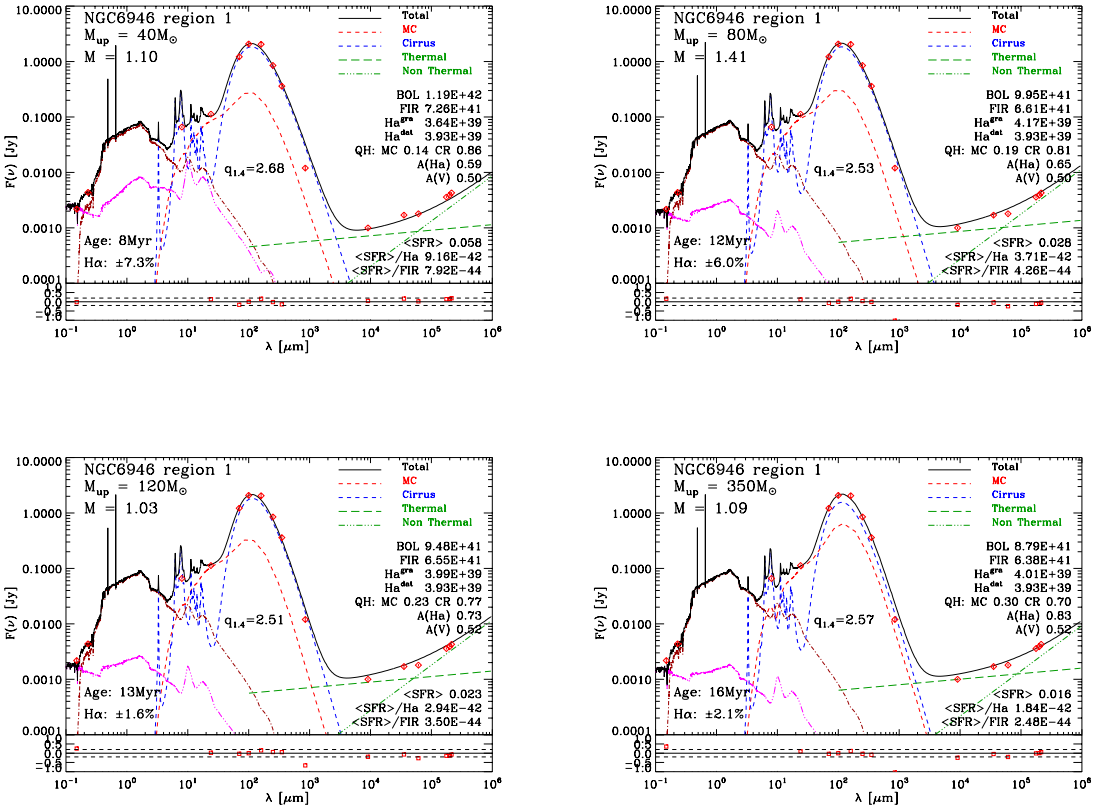

Figure 6.3: *GRASIL* best fit SEDs for the extra-nuclear Region 1 of NGC6946 (red diamonds) for different M_{up} as labelled in the different panels. The lower plots in each panel report the relative differences between data and best fit model, with the dashed lines highlighting the ±20% residuals. See text for more details.

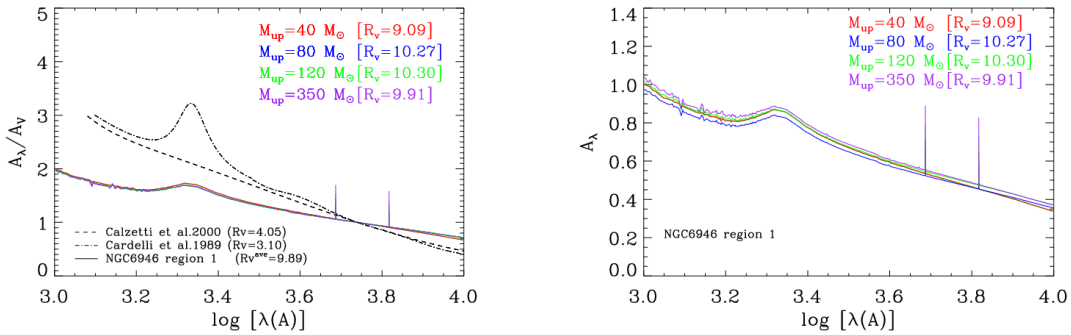

Figure 6.4: Attenuation curves for the extra-region Region 1 of NGC6946. The different colors refer to the different values of M_{up} in the best fit models. The attenuation curves of Calzetti et al. (2000) and Cardelli et al. (1989) (dashed and dot-dashed lines respectively) are also shown, for comparison. We can note the significant difference in the attenuation of the two recombination lines $H\alpha$ and $H\beta$ compared to the underlying continuum.

The SED of Region 1 is characterised by a quite flat radio-slope and a q ratio which is higher than that of normal spiral galaxies (q=2.35) by about 0.2 dex, indicating a FIR to radio emission ratio about 60% higher. A flatter radio slope and a higher q ratio is expected in young starburst (Terlevich et al. 1991; Bressan et al. 2002; Rosa-González et al. 2007; Thomson et al. 2014). We see from Figure 6.3 that fairly good fits to the SED of Region 1 can be obtained for a quite broad range of values of M_{up}, from M_{up}=40 $M_\odot$ to M_{up}=350 $M_\odot$. Since increasing M_{up} at a fixed age has the effect of increasing the number of ionizing photons, it is expected that, to fit the radio slope a progressively older age must be used in order to counterbalance the increasing strength of the free-free radio emission with respect to the synchrotron component. Moreover, increasing M_{up} at a fixed age produces a more luminous model and, in order to be able to fit the same FIR and radio data, which both depend strongly on the SFR, the derived SFR must decrease at increasing M_{up}. The average SFR obtained by increasing M_{up} from 40 $M_\odot$ to 350 $M_\odot$ decreases from ∼0.058 $M_\odot$/yr to 0.016 $M_\odot$, i.e. a factor of almost 4. However, going from M_{up} 40 $M_\odot$ to 80 $M_\odot$, the average SFR already decreases by a factor of 2. It can also be noted, from the labels reported in Figure 6.3, that as we go from low to high M_{up}, while the attenuation in the visual band is almost the same, A(V)∼0.50, that of the $H\alpha$ flux increases from A(Hα)∼0.59 to A(Hα)∼0.83. Since the observed Hα flux is well matched in all cases, within 7% as shown in the label in the bottom left side of the panels, it means that the combination of the upper mass limit of the IMF and the SFR required by the panchromatic fit, results in a flux of ionizing photons that is about 25% higher in the case of the higher M_{up} than in the case of the lower one.

The best fit parameters resulting from the best fits with different values of M_{up} are listed in Table 6.2. Here we note that the escape time from molecular clouds is less than 1 Myr. The typical radius of molecular clouds is ∼20 pc, apart from the case with M_{up}=350 $M_\odot$ which requires a smaller radius. We remind that this helps in lowering the emission at 24μm, as shown in Figure 5.3. This wavelength region is dominated by the molecular cloud component and it is also very sensitive to the escape time. The fit with M_{up}=350 $M_\odot$ requires also a lower escape time (0.3 Myr instead of 0.5 Myr of the other regions) and this is likely due to the need to match the Hα emission. We note however that the far-UV flux is under-reproduced by the model, in spite of it having the lowest escape time in all the library. Changing it to zero, i.e. eliminating the molecular component would not help in increasing the far-UV flux because 0.3 Myr is already a very small value. Also, the model with M_{up}=350 $M_\odot$ shows a mismatch of the radio emission at 33 GHz indicating that there is an excess of ionizing photons. This introduces us to the question of whether it is possible to discriminate between the different values of M_{up} from the best fit SEDs. What we may conclude from these fits is that while they are all very good within the errors, there is a preference for the model with M_{up}=80 $M_\odot$ because it is the one that better reproduces the observed panchromatic SED and at the same time the observed Hα luminosity

To illustrate better the attenuations for the different upper mass limits, we show in the left and right panels of Figure 6.4 the relative (A_λ/A_V) and total (A_λ) attenuation curves respectively, for the different values of M_{up} =40, 80, 120 and 350 $M_\odot$ (red, blue, green and purple solid lines respectively). In the relative attenuation curve plot, we have also added for comparison purposes the attenuation curves of Calzetti et al. (2000) and Cardelli et al. (1989) (dashed and dot-dashed lines respectively).

We first note that the relative attenuation is very similar for the different M_{up} cases, in spite of the different properties of the models. The attenuation is characterised by a high value of the ratio R_V=A(V)/E(B-V). It is quite flat with a R_V ∼10. We remind that the attenuation in our models arises from the effect of two components. A uniform dust screen with high optical depth, our dense molecular clouds, mainly affecting very young stellar populations with age ∼ t_{esc} and, as a function of time, also the ages between t_{esc} and 2× t_{esc}. The second component, is the so called "internal dust" component (see Calzetti et al. 1994), because molecular clouds and escaped stars are embedded in a less dense diffuse medium that can absorb and also scatter the light. It has been clearly shown by Calzetti et al. (1994) that neither of the two components can by themselves reproduce the observed behaviour of attenuation in star-burst galaxies. However a more complex situation, like such described here, including also an age-dependent effect, can reproduce very well the observed emission of our star forming regions. We are not claiming here that these are the "attenuation laws" because, for such a claim a better analysis of the UV region would have been needed, for example to check the strength of the UV bump, and this will be done in a future work. However, as a matter of fact, we are able to reproduce the far-UV attenuation, the attenuation in the Hα line, the emission in the Mid and Far-infrared and the intensity and slope of the emission at radio frequencies which, being not affected by internal extinction are powerful indicators of the star formation rate.

Region 2 The Results for region 2 are shown in Figure 6.5. The format of the figure is identical to that of Figure 6.3 and the GRASIL parameters of the best fit models for the different values of M_{up} are listed in Table 6.2. Region 2 appears to be characterized by a SFR which is about twice that of Region 1. As in the previous case, at increasing M_{up}, the age of the starburst is increasing. Even in this case the data can be fairly well fitted with all the four value of M_{up}. The best model are those obtained with M_{up}=80 $M_\odot$ and M_{up}=120 $M_\odot$ but very good fits can also be found for the other values of M_{up}. The relative attenuation curves for this region are shown in Figure 6.6. They are characterized by R_V ∼5.5, a value which is more similar to the the one we have found for M100 and also more similar to the value found by Calzetti et al. (2000). Why such a difference with respect to the attenuation derived in Region 1. Looking to Table 6.2 we see that in Region 2 the fraction of gas in molecular clouds (f_{mol}) is definitely higher than in Region 1. This evidently enhance the contribution from the uniform dust screen. Another important difference is the larger core radius of the star and diffuse dust spatial distributions, which are about twice or more the ones used in Region 1.

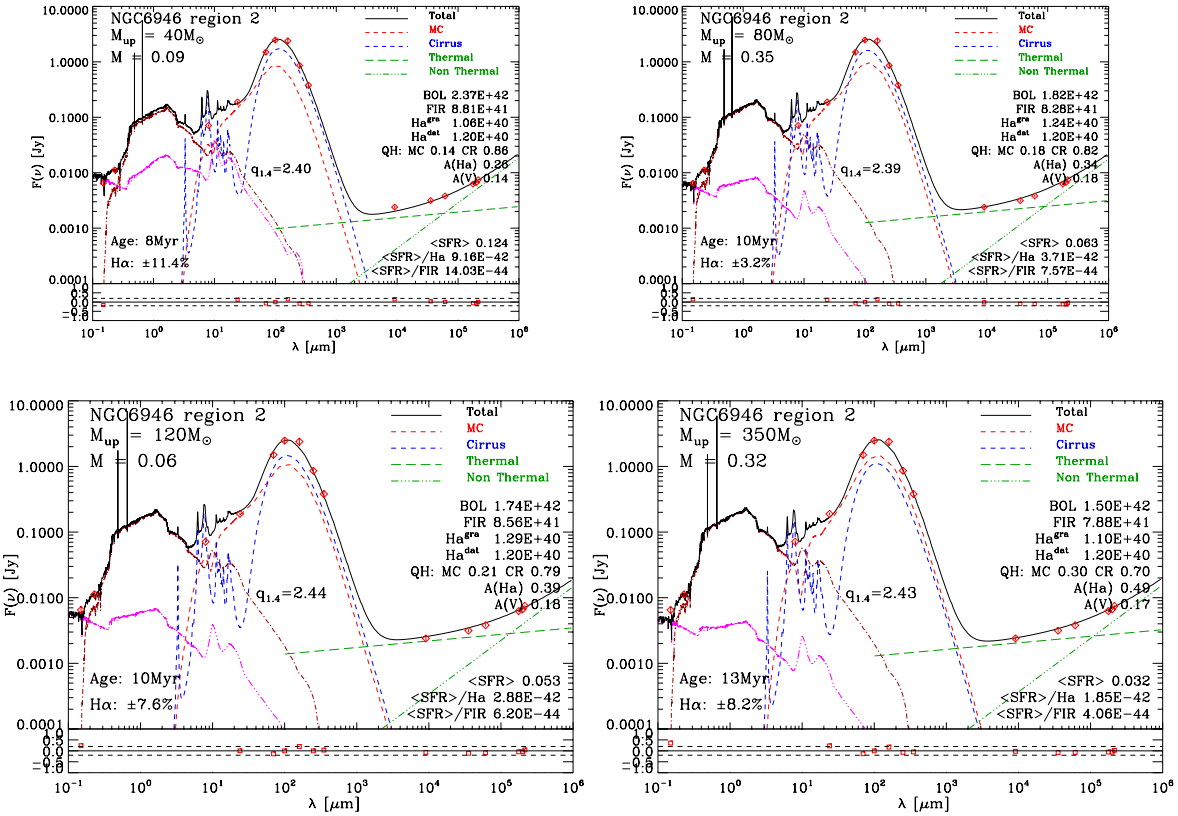

Figure 6.5: *GRASIL* best fit SEDs for the extra-nuclear Region 2 of NGC6946 (red diamonds) for different M_{up} as labelled in the different panels. The lower plots in each panel report the releative differences between data and best fit model. See text for more details.

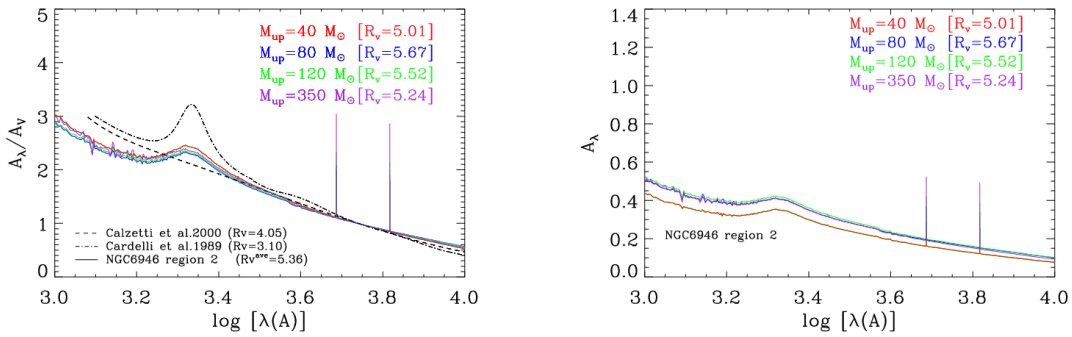

Figure 6.6: Attenuation curves for the extra-region Region 2. The different colors refer to the different values of M_{up} in the best fit models. The attenuation curves of Calzetti et al. (2000) and Cardelli et al. (1989) (dashed and dot-dashed lines respectively) are also shown, for comparison.

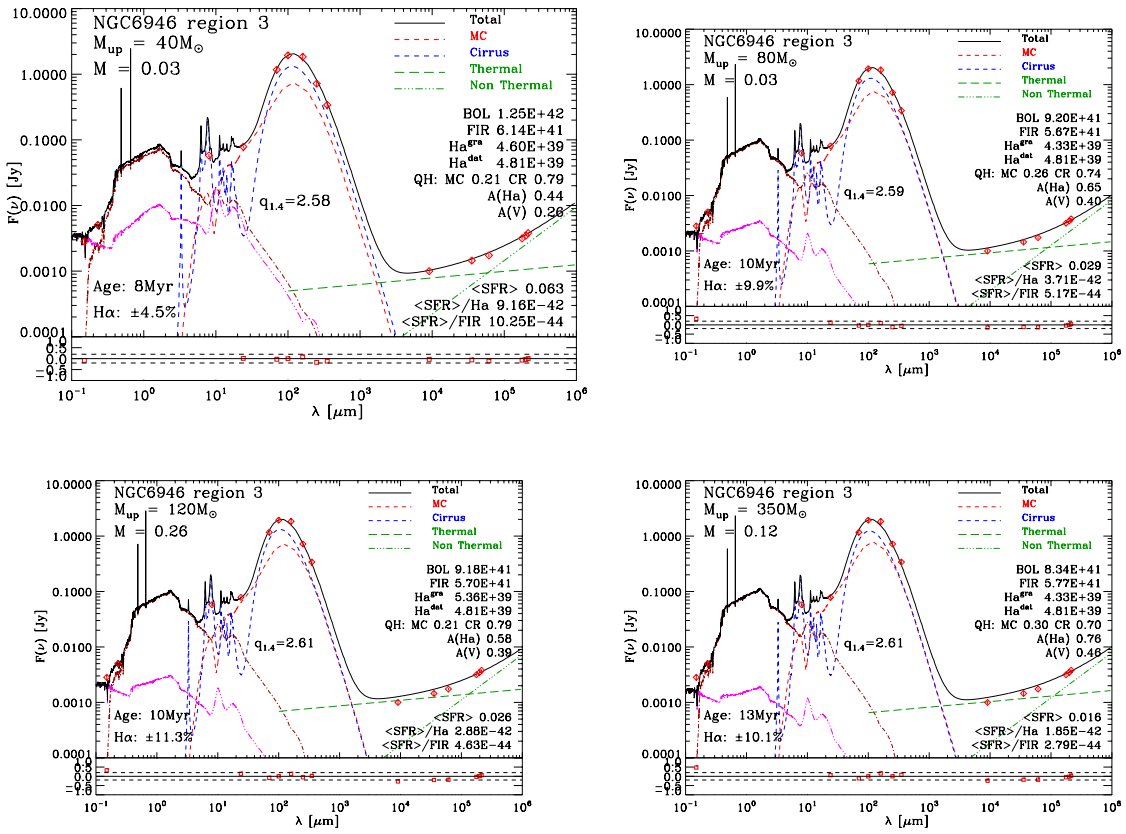

Figure 6.7: *GRASIL* best fit SEDs for the extra-nuclear Region 3 of NGC6946 (red diamonds) for different M_{up} as labelled in the different panels. The lower plots in each panel report the releative differences between data and best fit model. See text for more details.

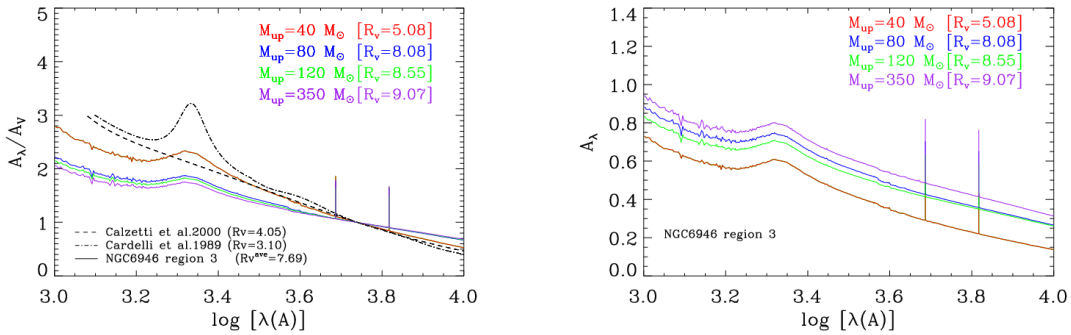

Figure 6.8: Attenuation curves for the extra-region Region 3. The different colors refer to the different values of M_{up} in the best fit models. The attenuation curves of Calzetti et al. (2000) and Cardelli et al. (1989) (dashed and dot-dashed lines respectively) are also shown, for comparison.

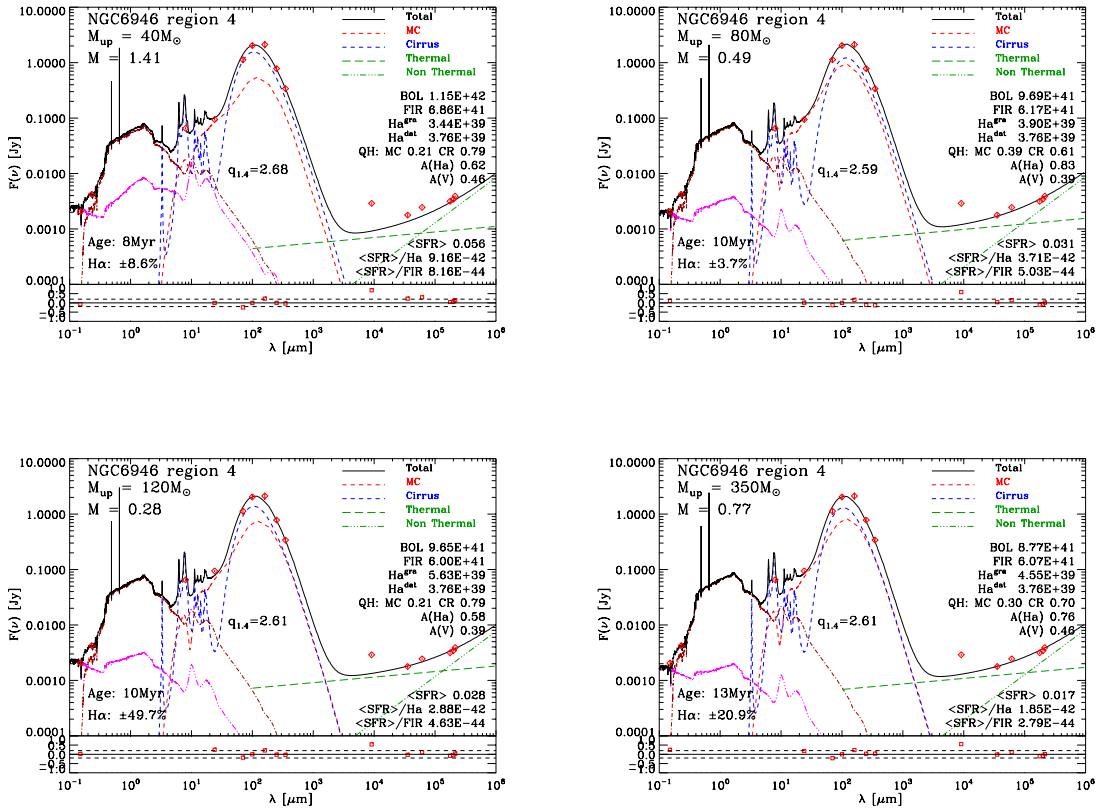

Figure 6.9: *GRASIL* best fit SEDs for the extra-nuclear Region 4 of NGC6946 (red diamonds) for different M_{up} as labelled in the different panels. The lower plots in each panel report the releative differences between data and best fit model. See text for more details.

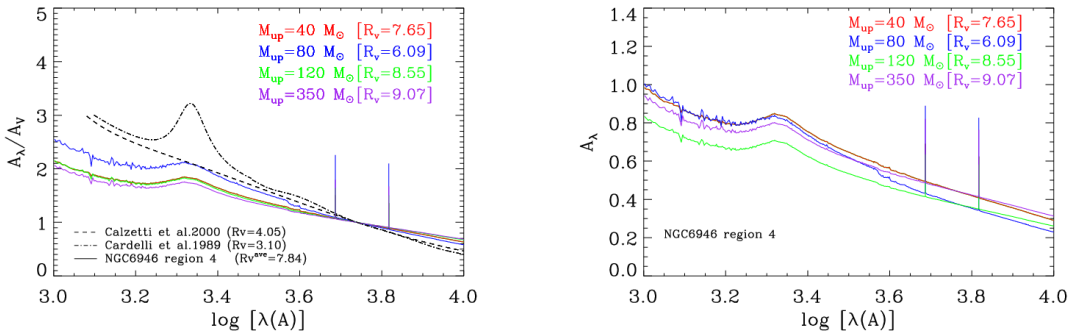

Figure 6.10: Attenuation curves for the extra-region Region 4. The different colors refer to the different values of M_{up} in the best fit models. The attenuation curves of Calzetti et al. (2000) and Cardelli et al. (1989) (dashed and dot-dashed lines respectively) are also shown, for comparison.

Region 3 The fits of the SED of Region 3 are shown in Figure 6.7 adopting the same format of the previous similar figures. In Region 3 the derived SFR is almost identical to that of Region 1. The fit obtained with M_{up}=40 $M_\odot$ is definitely the best one. In all the other cases the far-UV flux is underestimated and the Hα flux is either underestimated (M_{up}=80 $M_\odot$ and M_{up}=350 $M_\odot$) or overestimated (M_{up}=120 $M_\odot$). Given the wide range of parameters adopted in building our library of spectral models, this could be a case where one could say that the upper mass limit cannot be largely above M_{up}=40 $M_\odot$. Here we note that the attenuation curve of the model with M_{up}=40 $M_\odot$, shown in Figure 6.8, has R_V ∼5, while the models computed with the other values of M_{up} show R_V ∼8.5. From Table 6.2 we see that Region 3 has a relatively high fraction of gas in molecular clouds (f_{mol}), like Region 2, and that, the best model, has a diffuse distribution with stars more concentrated than the gas and an escape time t_{esc} from molecular clouds of 1 Myr. This again may increase the relative weight of the dust screen configuration for what concern the attenuation.

Region 4 The fits of SED of Region 4 are shown in Figure 6.9 adopting the same format of the previous similar figures. Region 4 shows a 33GHz flux that significantly deviates from the values at lower radio frequencies. The region can be fitted by models with any M_{up} value though the best model appears to be the one with M_{up}=80 $M_\odot$. The other models either do not match some observations in the radio (excluding the 33GHz one) or they severely over-reproduce the observed H_α flux, by 50% for M_{up}=120 $M_\odot$ and 21% for M_{up}=350 $M_\odot$. Again the attenuation curve of the best model (Figure 6.10) is the one with the lowest value of R_V (∼6). The model for the other values of M_{up} require R_V greater than 7.7.

Region 5 The fits to the SED of Region 5 are shown in Figure 6.11 adopting the same format of the previous similar figures. Region 5 can be fitted only by adopting a value of M_{up}=80 $M_\odot$. The best fit is very good and reproduces the observed panchromatic SED, including the Hα flux, with a very good accuracy. On the contrary, adopting M_{up}=40 $M_\odot$ we obtain a best model that under-reproduces the Hα flux and the radio emission and, by adopting M_{up}=120 $M_\odot$ or M_{up}=350 $M_\odot$, besides under-reproducing the Hα and radio emission we also under-estimate the far-UV emission. Interestingly the best fit model with M_{up}=80 $M_\odot$ adopts β=2.0, while the other models need β=1.8 to fit the FIR data. Even in this case the attenuation curve of the best model (Figure 6.12) has one of the lowest values of R_V (∼7). We note that the other model that reproduces the far-UV, with M_{up}=40 $M_\odot$ has the lowest R_V (∼6.6).

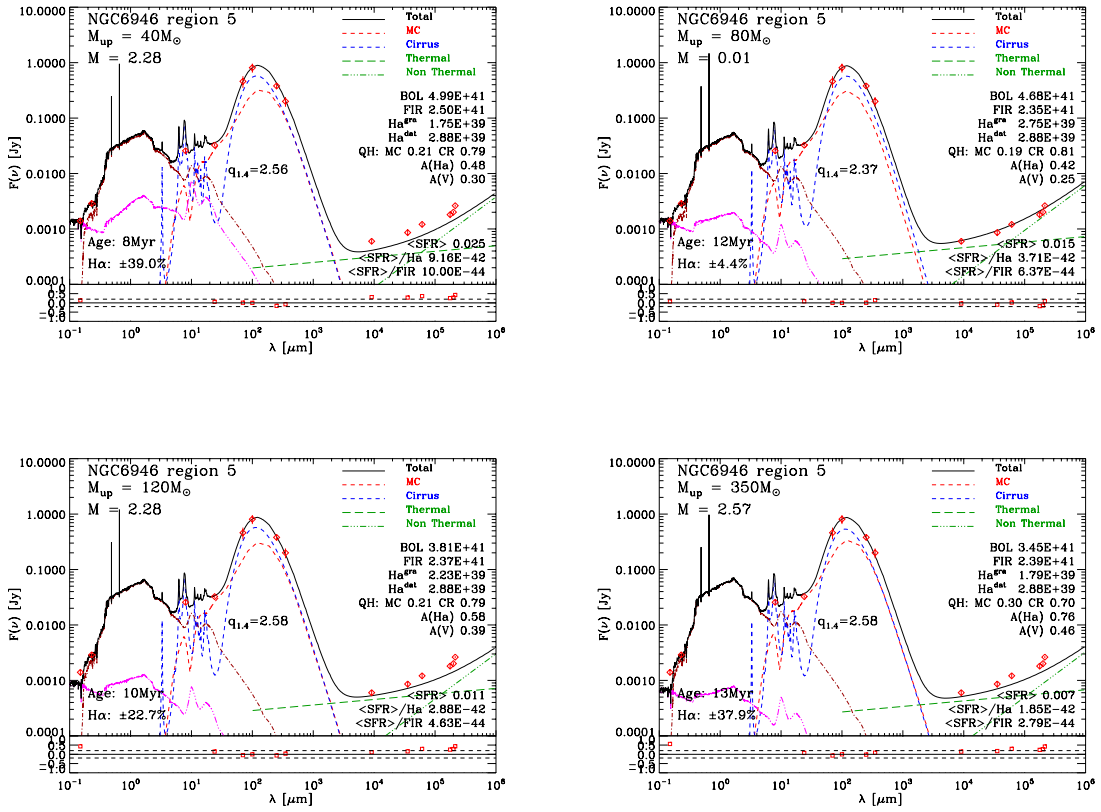

Figure 6.11: *GRASIL* best fit SEDs for the extra-nuclear Region 5 of NGC6946 (red diamonds) for different M_{up} as labelled in the different panels. The lower plots in each panel report the releative differences between data and best fit model. See text for more details.

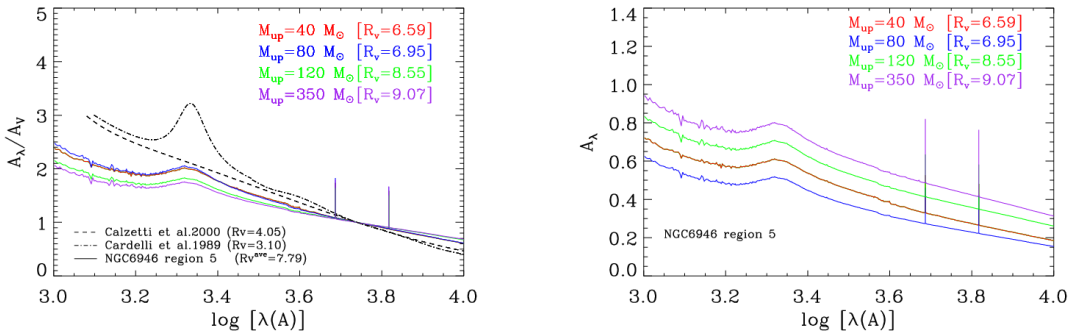

Figure 6.12: Attenuation curves for the extra-region Region 5. The different colors refer to the different values of M_{up} in the best fit models. The attenuation curves of Calzetti et al. (2000) and Cardelli et al. (1989) (dashed and dot-dashed lines respectively) are also shown, for comparison.

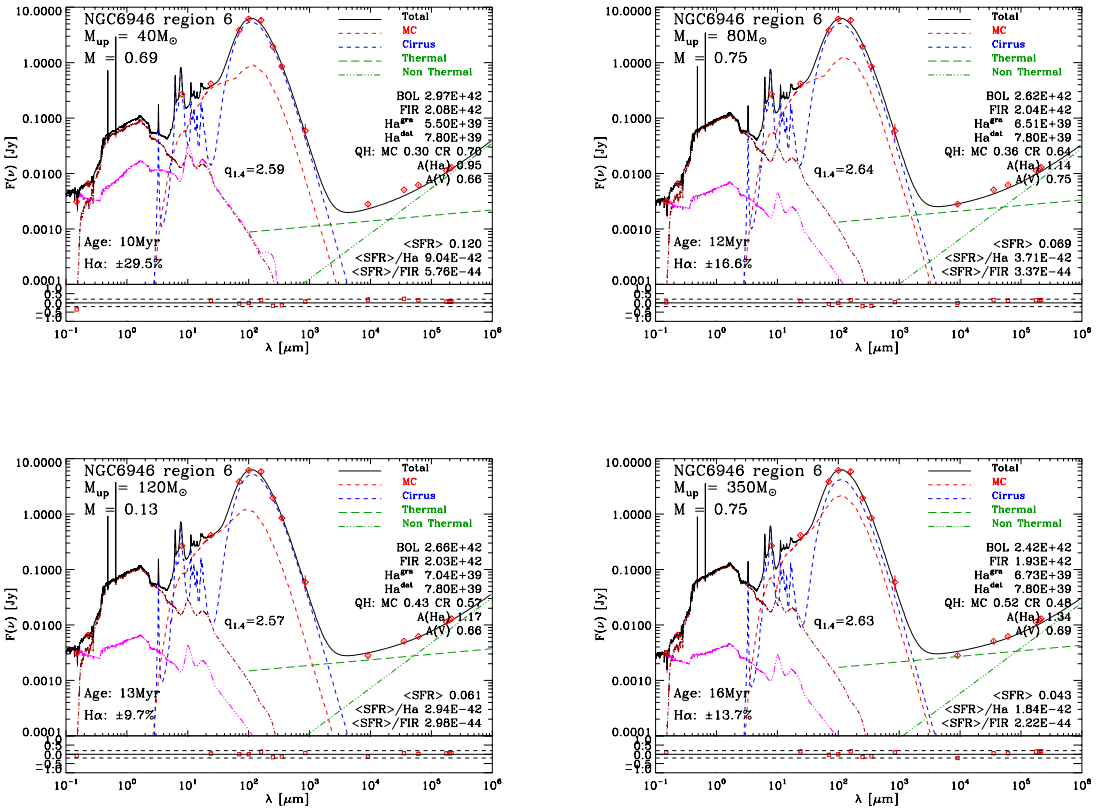

Figure 6.13: *GRASIL* best fit SEDs for the extra-nuclear Region 6 of NGC6946 (red diamonds) for different M_{up} as labelled in the different panels. The lower plots in each panel report the releative differences between data and best fit model. See text for more details.

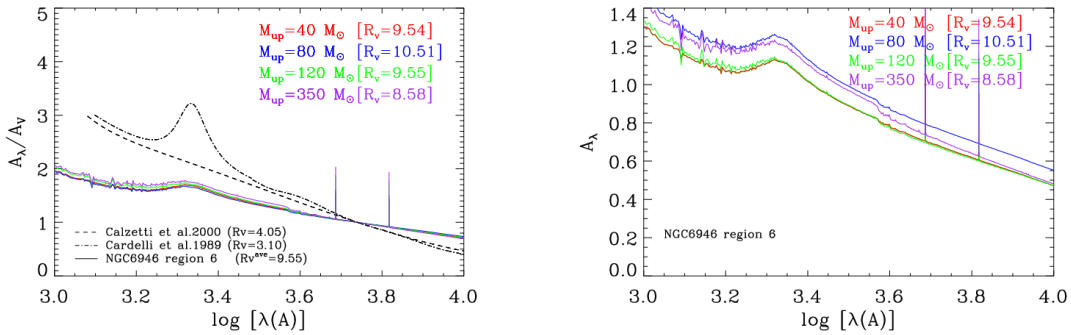

Figure 6.14: Attenuation curves for the extra-region Region 6. The different colors refer to the different values of M_{up} in the best fit models. The attenuation curves of Calzetti et al. (2000) and Cardelli et al. (1989) (dashed and dot-dashed lines respectively) are also shown, for comparison.

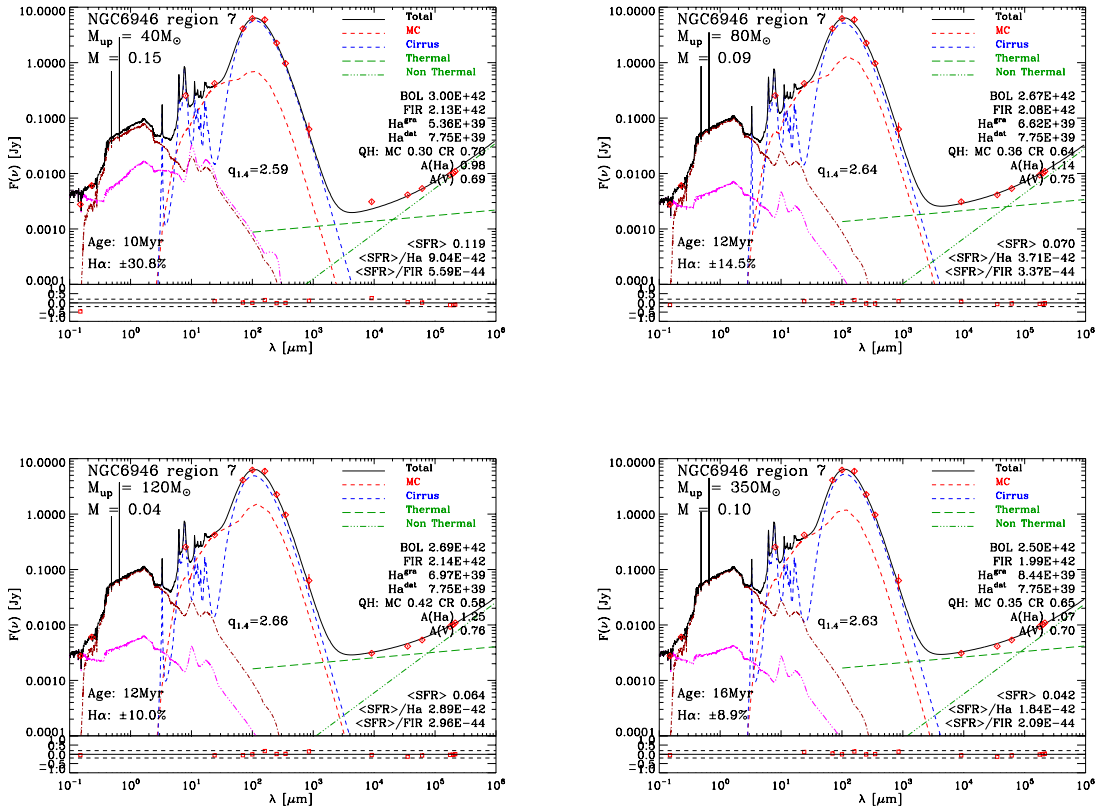

Figure 6.15: *GRASIL* best fit SEDs for the extra-nuclear Region 7 of NGC6946 (red diamonds) for different M_{up} as labelled in the different panels. The lower plots in each panel report the releative differences between data and best fit model. See text for more details.

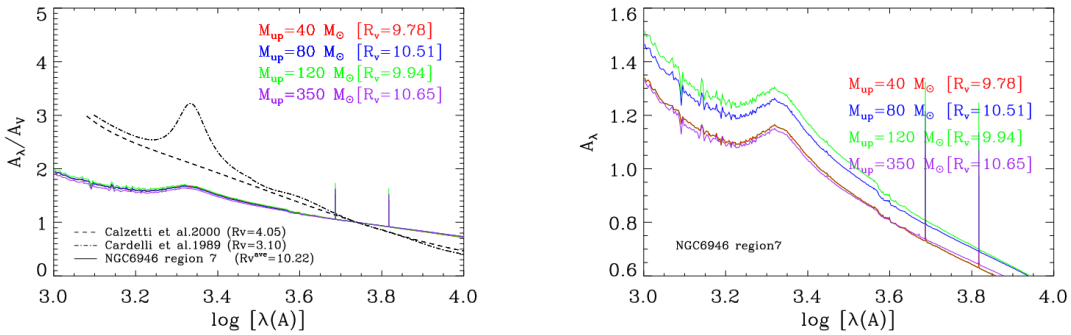

Figure 6.16: Attenuation curves for the extra-region Region 7. The different colors refer to the different values of M_{up} in the best fit models. The attenuation curves of Calzetti et al. (2000) and Cardelli et al. (1989) (dashed and dot-dashed lines respectively) are also shown, for comparison.

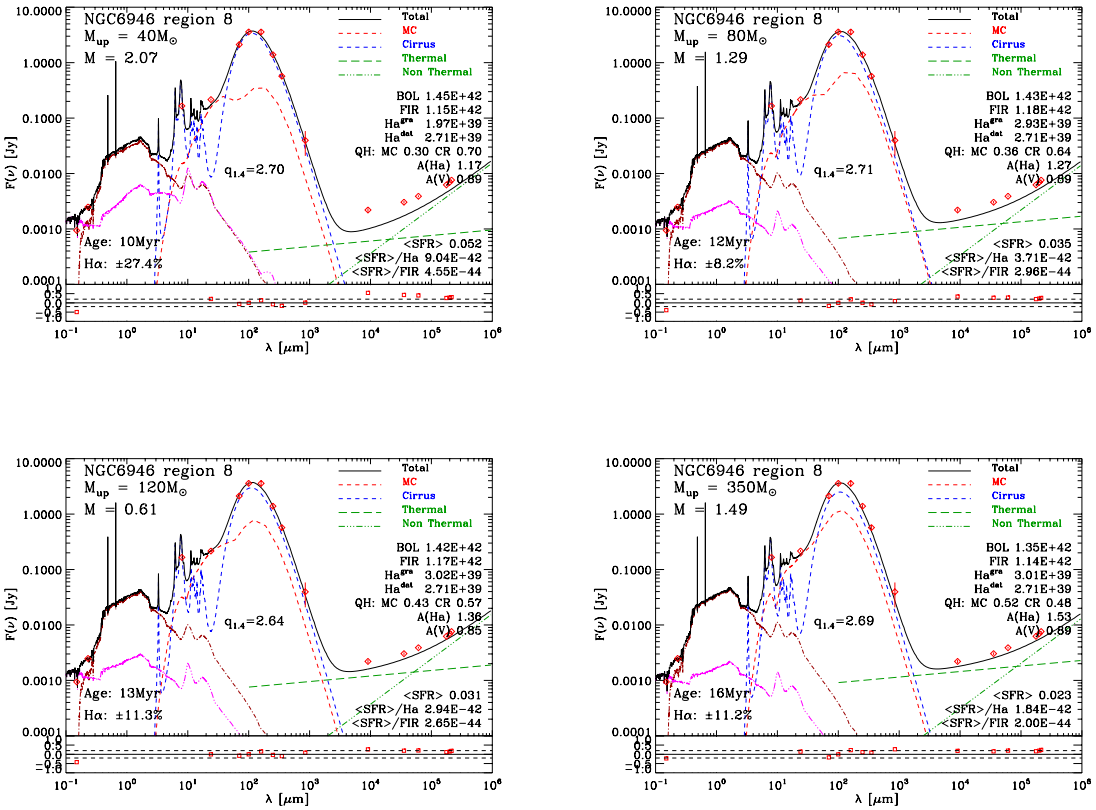

Figure 6.17: *GRASIL* best fit SEDs for the extra-nuclear Region 8 of NGC6946 (red diamonds) for different M_{up} as labelled in the different panels. The lower plots in each panel report the releative differences between data and best fit model. See text for more details.

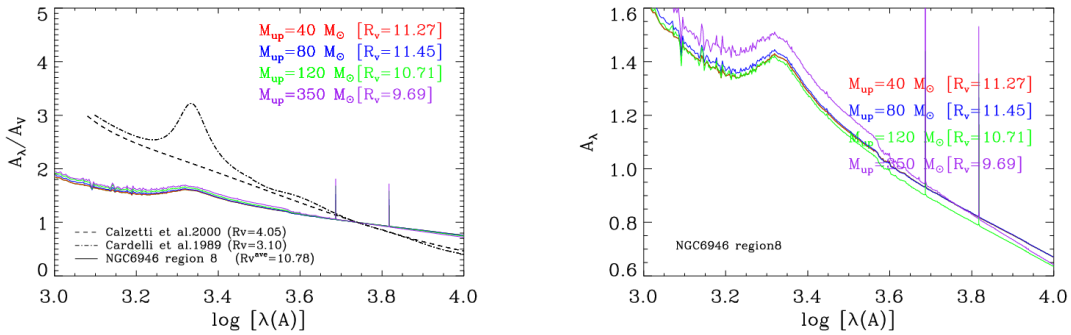

Figure 6.18: Attenuation curves for the extra-region Region 8. The different colors refer to the different values of M_{up} in the best fit models. The attenuation curves of Calzetti et al. (2000) and Cardelli et al. (1989) (dashed and dot-dashed lines respectively) are also shown, for comparison.

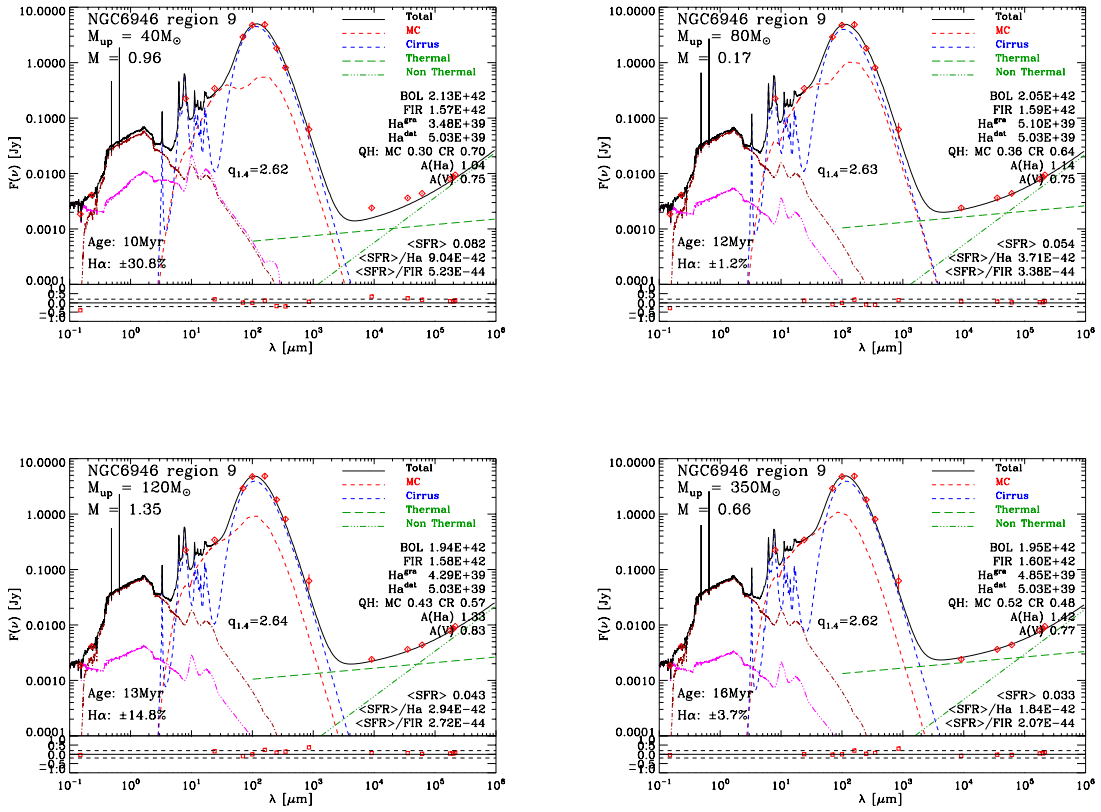

Figure 6.19: *GRASIL* best fit SEDs for the extra-nuclear Region 9 of NGC6946 (red diamonds) for different M_{up} as labelled in the different panels. The lower plots in each panel report the releative differences between data and best fit model. See text for more details.

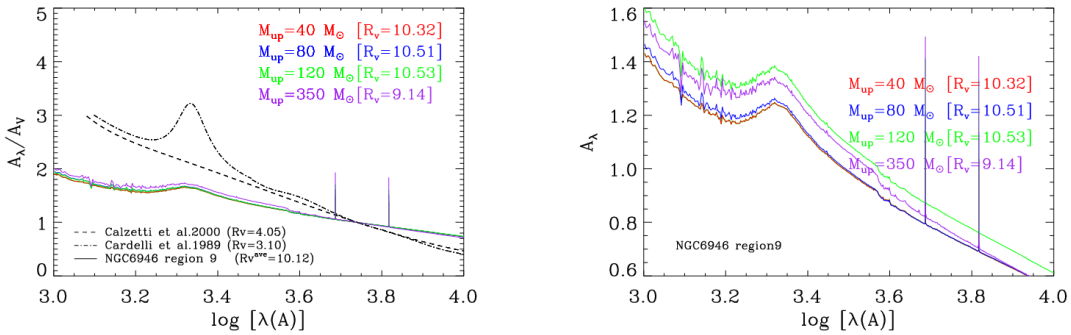

Figure 6.20: Attenuation curves for the extra-region Region 9. The different colors refer to the different values of M_{up} in the best fit models. The attenuation curves of Calzetti et al. (2000) and Cardelli et al. (1989) (dashed and dot-dashed lines respectively) are also shown, for comparison.

Region 6 The fits to the SED of Region 6 are shown in Figure 6.13 where we adopt the same format of the previous similar figures. For this region the best fit model is that obtained with M_{up}=120 $M_\odot$. The fit is very good though the Hα flux is underestimated by 10%. Fairly good fits may also be obtained from the models with M_{up}=80 $M_\odot$ and M_{up}=350 $M_\odot$. However the former under-estimates the Hα flux by the 17% and the latter by the 14%. The model with M_{up}=40 $M_\odot$, besides under-estimating the Hα flux by the 30%, significantly over-estimates the far-UV flux. The attenuation curves obtained for this region, shown in Figure 6.14 are very similar to those obtained for region 1, with R_V values in the range 9 to 10.

Region 7 The SED of Region 7, shown in Figure 6.15 where we adopt the same format of the previous similar figures, is very similar to that of region 6. The star formation rates derived by the fitting process are almost identical. Even in this case the best fit is obtained with models that adopt M_{up}=120 $M_\odot$, but a very good fit, with a slightly better residual in the Hα flux, can be obtained with M_{up}=350 $M_\odot$. The best fit model with M_{up}=80 $M_\odot$ sligthly under-estimates the Hα flux ($\sim$14%), while the best model with M_{up}=40 $M_\odot$, besides under-estimating the Hα flux by 30%, significantly over-estimates the far-UV flux. Note that the discrepancies of the latter model as well as the similar ones in the same model of Region 6, cannot be easily cured. If we wish to reproduce the UV flux we need to increase the attenuation but, doing so we decrease even further the predicted Hα flux. The opposite is also true if we wish to match the Hα flux. This shows how powerful a population synthesis tool is where the emission in all the bands is linked by realistic physical processes. As far as the attenuation curves are concerned, they are very similar to those derived for Region 6 with $R_V \sim 10$ (Figure 6.16)

Region 8 For Region 8, whose SED is shown in Figure 6.17 we cannot find a satisfactory model from our library. The estimated SFR is similar to that in Regions 1, 3 and 4 but none of our models can reproduce the observed SED. All the best fit models over-estimate the observed far-UV flux and, at the same time, they under-estimate the radio fluxes. The two best models are those obtained with M_{up}=120 $M_\odot$ and with M_{up}=350 $M_\odot$. Both models over-estimate the Hα flux by about 11%. Work is in progress to understand the reason of this failure.

Region 9 The fits of the SED of Region 9 are shown in Figure 6.19 where we adopt the same format of the previous similar figures. The star formation rate derived for this region is only 50% larger than that derived for Region 8 but, for this region we are able to find very good models in our library. The best fit models are for M_{up}=120 $M_\odot$ and for M_{up}=350 $M_\odot$. In the latter case the fit is almost perfect, with a defect of Hα emission of the 3% while, in the former case the Hα emission is under-estimated by the 14%. The model that best reproduces the Hα flux (within 1%) is the model computed with M_{up}=80 $M_\odot$, but this model slightly over reproduces the far-UV flux. The best fit model with M_{up}=40 $M_\odot$ shows a low flux in Hα ($\sim$31%) and at 33GHz, and it significantly over-estimate the far-UV flux. Also in this case an upper mass limit of M_{up}=40 $M_\odot$ can be excluded while all the other values could be acceptable. As far as the attenuation is concerned, we see form Figure 6.20 that it runs very flat with R_V up to 11. The lowest value of R_V ($\sim$9) is obtained in the best fit model, i.e. the one with M_{up}=350 $M_\odot$.

Table 6.2: *GRASIL* best fit parameters (for upper mass limits of 40, 80, 120 and 350) for the modelled SEDs of NGC6956 SF regions.

M_{up}	ID	t_{sb}	t_{esc}	r_{cloud}	f_{mol}	f_{gas}	β	r_{star}	r_{diff}
40	NGC6946 Region 1	8.0	0.5	20.0	0.1	0.05	1.5	0.15	0.3
80	NGC6946 Region 1	12.0	0.5	20.0	0.1	0.2	1.8	0.3	0.3
120	NGC6946 Region 1	14.0	0.5	20.0	0.1	0.4	2.0	0.4	0.4
350	NGC6946 Region 1	16.0	0.3	15.0	0.4	0.6	1.9	0.4	0.4
40	NGC6946 Region 2	8.0	0.5	15.0	0.2	0.1	2.0	0.8	0.8
80	NGC6946 Region 2	10.0	0.5	15.0	0.4	0.2	2.0	0.8	0.8
120	NGC6946 Region 2	10.0	0.5	15.0	0.4	0.2	2.0	0.8	0.8
350	NGC6946 Region 2	14.0	0.5	12.0	0.6	0.4	2.0	1.0	1.0
40	NGC6946 Region 3	8.0	1.0	12.0	0.4	0.2	2.0	0.5	1.0
80	NGC6946 Region 3	10.0	1.0	12.0	0.6	0.4	2.0	0.4	0.4
120	NGC6946 Region 3	10.0	0.5	12.0	0.6	0.4	2.0	0.4	0.4
350	NGC6946 Region 3	14.0	0.5	12.0	0.6	0.6	2.0	0.4	0.4
40	NGC6946 Region 4	8.0	1.0	15.0	0.4	0.1	1.8	0.2	0.4
80	NGC6946 Region 4	10.0	1.2	12.0	0.4	0.4	2.0	0.5	1.0
120	NGC6946 Region 4	10.0	0.5	12.0	0.6	0.4	2.0	0.4	0.4
350	NGC6946 Region 4	14.0	0.5	12.0	0.6	0.6	2.0	0.4	0.4
40	NGC6946 Region 5	8.0	1.0	12.0	0.6	0.2	1.8	0.4	0.4
80	NGC6946 Region 5	12.0	0.5	12.0	0.4	0.4	2.0	0.8	0.8
120	NGC6946 Region 5	10.0	0.3	12.0	0.6	0.4	1.8	0.4	0.4
350	NGC6946 Region 5	14.0	0.5	12.0	0.6	0.6	1.8	0.4	0.4
40	NGC6946 Region 6	10.0	1.2	22.0	0.2	0.2	2.0	0.2	0.4
80	NGC6946 Region 6	12.0	1.2	20.0	0.4	0.4	2.0	0.2	0.4
120	NGC6946 Region 6	14.0	1.2	20.0	0.1	0.4	2.0	0.3	0.3
350	NGC6946 Region 6	16.0	1.2	15.0	0.4	0.6	2.0	0.3	0.3
40	NGC6946 Region 7	10.0	1.2	25.0	0.1	0.2	2.0	0.2	0.4
80	NGC6946 Region 7	12.0	1.2	20.0	0.4	0.4	2.0	0.2	0.4
120	NGC6946 Region 7	12.0	1.2	20.0	0.4	0.4	2.0	0.2	0.4
350	NGC6946 Region 7	16.0	1.0	20.0	0.2	0.6	2.0	0.3	0.3
40	NGC6946 Region 8	10.0	1.2	25.0	0.4	0.4	2.0	0.15	0.3
80	NGC6946 Region 8	12.0	1.2	20.0	0.6	0.6	2.0	0.15	0.3
120	NGC6946 Region 8	14.0	1.2	20.0	0.4	0.6	2.0	0.2	0.4
350	NGC6946 Region 8	16.0	1.2	15.0	0.4	0.6	2.0	0.2	0.4
40	NGC6946 Region 9	10.0	1.2	25.0	0.4	0.4	2.0	0.2	0.4
80	NGC6946 Region 9	12.0	1.2	20.0	0.6	0.6	2.0	0.2	0.4
120	NGC6946 Region 9	14.0	1.2	20.0	0.2	0.4	2.0	0.2	0.4
350	NGC6946 Region 9	16.0	1.2	20.0	0.1	0.6	2.0	0.3	0.3

Table 6.3: GRASIL Best-fit model luminosities

(1) ID	(2) BOL 10^{42}	(3) FUV_i 10^{41}	(4) FUV_t 10^{41}	(5) 24 10^{41}	(6) 70 10^{41}	(7) FIR 10^{42}	(8) FIR_H 10^{-11}	(9) 33 10^{26}	(10) 8.5 10^{26}	(11) 4.9 10^{26}	(12) 1.4 10^{26}	(13) q	(14) MC	(15) CIR
M_{up} = 40														
M100	514.11	625.50	371.00	106.00	598.00	164.00	220.00	68.5()	180.0()	276.0()	772.0()	2.38	13.0	87.0
NGC6946_1	1.19	4.68	2.19	0.67	3.36	0.73	5.93	0.5(79)	0.8(59)	1.0(49)	1.9(28)	2.68	25.0	75.0
NGC6946_2	2.37	10.0	7.37	1.14	3.8	0.88	6.79	1.1(79)	1.7(59)	2.1(49)	4.1(28)	2.4	46.0	54.0
NGC6946_3	1.25	5.08	3.01	0.54	2.86	0.61	5.16	0.6(79)	0.8(59)	1.1(49)	2.1(28)	2.58	40.0	60.0
NGC6946_4	1.15	4.52	2.16	0.66	3.33	0.69	5.87	0.5(79)	0.8(59)	0.9(49)	1.9(28)	2.68	32.0	68.0
NGC6946_5	0.5	2.02	1.19	0.21	1.08	0.25	2.0	0.2(79)	0.3(59)	0.4(49)	0.8(28)	2.56	39.0	61.0
NGC6946_6	2.98	11.11	4.14	2.54	9.49	2.08	16.8	1.3(64)	2.2(40)	2.9(31)	6.6(16)	2.59	28.0	72.0
NGC6946_7	3.0	11.02	4.01	2.65	9.57	2.13	16.9	1.3(64)	2.2(40)	2.9(31)	6.6(16)	2.59	27.0	73.0
NGC6946_8	1.46	4.81	1.39	1.18	5.33	1.15	9.5	0.6(64)	1.0(40)	1.3(31)	2.9(16)	2.7	21.0	79.0
NGC6946_9	2.13	7.59	2.57	1.92	6.8	1.57	12.3	0.9(64)	1.5(40)	2.0(31)	4.6(16)	2.62	25.0	75.0
M_{up} = 80														
M100	497.22	678.60	311.00	133.00	724.00	179.00	259.00	89.5(31)	196.0(15)	286.0(10)	747.0(4)	2.46	32.0	68.0
NGC6946_1	1.0	3.74	1.81	0.68	3.08	0.66	5.47	0.6(77)	1.0(56)	1.2(47)	2.5(26)	2.53	28.0	72.0
NGC6946_2	1.82	7.78	5.45	1.16	3.83	0.83	6.83	1.3(84)	1.9(66)	2.3(57)	4.3(35)	2.39	48.0	52.0
NGC6946_3	0.92	3.59	1.89	0.48	2.88	0.57	5.15	0.6(84)	0.9(66)	1.1(57)	2.0(35)	2.59	40.0	60.0
NGC6946_4	0.97	3.84	1.83	0.65	3.01	0.62	5.47	0.7(84)	0.9(66)	1.2(57)	2.1(35)	2.59	50.0	50.0
NGC6946_5	0.47	2.0	1.28	0.21	1.09	0.24	2.0	0.3(77)	0.5(56)	0.7(47)	1.3(26)	2.37	41.0	59.0
NGC6946_6	2.62	9.21	3.03	2.61	9.71	2.04	17.2	1.6(77)	2.4(56)	3.0(47)	6.0(26)	2.64	32.0	68.0
NGC6946_7	2.67	9.35	3.08	2.66	9.88	2.08	17.5	1.6(77)	2.4(56)	3.1(47)	6.2(26)	2.64	32.0	68.0
NGC6946_8	1.44	4.67	1.31	1.32	5.85	1.18	10.3	0.8(77)	1.2(56)	1.5(47)	3.1(26)	2.71	27.0	73.0
NGC6946_9	2.04	7.21	2.37	2.11	7.45	1.59	13.2	1.2(77)	1.9(56)	2.4(47)	4.7(26)	2.63	32.0	68.0
M_{up} = 120														
M100	490.67	700.23	298.00	120.00	821.00	184.00	289.00	99.6(41)	204.0(21)	293.0(15)	742.0(7)	2.51	35.0	65.0
NGC6946_1	0.95	3.5	1.63	0.76	2.98	0.66	5.33	0.7(78)	1.0(57)	1.3(47)	2.5(26)	2.51	31.0	69.0
NGC6946_2	1.74	7.13	4.93	1.31	4.04	0.86	7.17	1.4(87)	1.9(72)	2.3(64)	4.0(42)	2.44	54.0	46.0
NGC6946_3	0.92	3.48	1.91	0.47	3.01	0.57	5.32	0.7(87)	1.0(72)	1.1(64)	2.0(42)	2.61	38.0	62.0
NGC6946_4	0.97	3.75	2.01	0.49	3.16	0.6	5.6	0.7(87)	1.0(72)	1.2(64)	2.1(42)	2.61	38.0	62.0
NGC6946_5	0.38	1.47	0.79	0.19	1.14	0.24	2.07	0.3(87)	0.4(72)	0.5(64)	0.8(42)	2.58	38.0	62.0
NGC6946_6	2.65	9.27	3.36	2.75	9.1	2.03	16.3	1.7(78)	2.6(57)	3.3(47)	6.7(26)	2.57	37.0	63.0
NGC6946_7	2.69	9.24	2.9	3.07	10.2	2.14	17.9	1.8(82)	2.5(63)	3.1(54)	6.0(32)	2.66	37.0	63.0
NGC6946_8	1.42	4.71	1.35	1.49	5.42	1.17	9.67	0.9(78)	1.3(57)	1.7(47)	3.4(26)	2.64	32.0	68.0
NGC6946_9	1.94	6.53	1.93	1.98	7.59	1.58	13.4	1.2(78)	1.9(57)	2.4(47)	4.7(26)	2.64	33.0	67.0
M_{up} = 350														
M100	486.91	728.89	336.00	129.00	831.00	186.00	292.00	131.0(59)	235.0(35)	320.0(27)	750.0(13)	2.51	39.0	61.0
NGC6946_1	0.88	3.1	1.41	0.7	2.99	0.64	5.39	0.7(83)	1.0(65)	1.2(56)	2.2(34)	2.57	39.0	61.0
NGC6946_2	1.5	6.03	4.2	1.01	4.02	0.79	7.19	1.4(86)	1.9(69)	2.2(60)	4.0(38)	2.43	62.0	38.0
NGC6946_3	0.83	3.0	1.5	0.51	3.08	0.58	5.44	0.7(86)	0.9(69)	1.1(60)	2.0(38)	2.61	42.0	58.0
NGC6946_4	0.88	3.19	1.58	0.54	3.24	0.61	5.73	0.7(86)	1.0(69)	1.2(60)	2.1(38)	2.61	42.0	58.0
NGC6946_5	0.35	1.31	0.62	0.21	1.16	0.24	2.11	0.3(86)	0.4(69)	0.5(60)	0.8(38)	2.58	42.0	58.0
NGC6946_6	2.42	8.33	2.78	2.43	9.4	1.93	16.7	1.9(83)	2.6(65)	3.2(56)	6.0(34)	2.63	45.0	55.0
NGC6946_7	2.5	8.14	2.94	2.55	9.28	1.99	16.5	1.8(83)	2.6(65)	3.1(56)	5.8(34)	2.63	34.0	66.0
NGC6946_8	1.35	4.46	1.16	1.28	5.86	1.14	10.3	1.0(83)	1.4(65)	1.7(56)	3.2(34)	2.69	40.0	60.0
NGC6946_9	1.95	6.4	1.96	2.36	7.03	1.6	12.6	1.4(83)	2.0(65)	2.5(56)	4.6(34)	2.62	42.0	58.0

Col.(1): ID. Col.(2-4): bolometric and FUV (at 0.16 μm) luminosities. ^{i} and ^{t} indicates intrinsic and attenuated transmitted luminosities respectively. Cols.(5 and 6): luminosities at 24 μm and 70 μm. Col.(7): total (3-1000 μm)IR luminosity. Col.(8): FIR flux in ergs s^{-1} cm^{-2} in the 40 - 120 μm interval derived using the 60 and 120 μm fluxes (Helou et al. 1988) and used in the calculation of $q_{1.4}$ that is given in Column 13. Cols.(9-12): radio luminosities at and 33, 8.5, 4.9 and 1.4 GHz Enclosed in parenthesis is the fraction in per cent of the thermal radio component to the total radio emission. Col.(13): q-parameter as defined by Equation 4.5. Cols.(14 and 15) are the MC and cirrus contribution (in per cent) to the total IR (Col.7) luminosity respectively. The bolometric, FUV and infrared luminosities are in erg s^{-1} while all radio luminosities are in erg s^{-1} Hz^{-1}. The corresponding SFR calibrations at these luminosities are given in Table 6.4.

Table 6.4: GRASIL Best-fit derived SFRs and their calibrations at various bands

(1) ID 10^0	(2) $< SFR >$	(3) $C(BOL)$ 10^{-44}	(4) $C(FUV)$ 10^{-43}	(5) $C(24)$ 10^{-43}	(6) $C(70)$ 10^{-43}	(7) $C(FIR)$ 10^{-44}	(8) $C(33)$ 10^{-28}	(9) $C(8.5)$ 10^{-28}	(10) $C(4.9)$ 10^{-28}	(11) C(1.4) 10^{-28}	(12) t
$M_{up} = 40$											
M100	3.12	0.61	0.50	2.94	0.52	1.90	4.55	1.73	1.13	0.40	12.2
NGC6946_1	0.06	4.86	1.24	8.67	1.73	7.92	11.0	7.44	5.94	3.02	8.0
NGC6946_2	0.12	5.22	1.24	10.88	3.26	14.0	11.1	7.44	5.94	3.02	8.0
NGC6946_3	0.06	5.05	1.24	11.73	2.2	10.2	11.1	7.44	5.94	3.02	8.0
NGC6946_4	0.06	4.86	1.24	8.52	1.68	8.16	11.0	7.44	5.94	3.02	8.0
NGC6946_5	0.03	5.02	1.24	11.79	2.31	10.0	11.0	7.44	5.94	3.02	8.0
NGC6946_6	0.12	4.03	1.08	4.72	1.26	5.76	9.39	5.46	4.08	1.8	10.0
NGC6946_7	0.12	3.97	1.08	4.49	1.24	5.59	9.39	5.46	4.08	1.8	10.0
NGC6946_8	0.05	3.56	1.08	4.41	0.98	4.55	9.37	5.46	4.08	1.8	10.0
NGC6946_9	0.08	3.85	1.08	4.27	1.21	5.23	9.38	5.46	4.08	1.8	10.0
$< NGC6946 >$	0.06	4.86	1.24	8.52	1.68	7.92	11.00	7.44	5.94	3.02	8.00
$M_{up} = 80$											
M100	3.01	0.61	0.44	2.27	0.42	1.68	3.36	1.54	1.05	0.40	12.2
NGC6946_1	0.03	2.81	0.75	4.09	0.91	4.26	4.39	2.89	2.29	1.14	12.0
NGC6946_2	0.1	5.76	1.35	9.05	2.74	12.6	7.82	5.51	4.52	2.45	10.0
NGC6946_3	0.03	3.15	0.81	6.04	1.01	5.17	4.68	3.3	2.71	1.47	10.0
NGC6946_4	0.03	3.2	0.81	4.78	1.03	5.03	4.68	3.3	2.71	1.47	10.0
NGC6946_5	0.01	3.21	0.75	7.28	1.38	6.37	4.4	2.89	2.29	1.14	12.0
NGC6946_6	0.07	2.63	0.75	2.64	0.71	3.37	4.4	2.89	2.29	1.14	12.0
NGC6946_7	0.07	2.62	0.75	2.63	0.71	3.37	4.4	2.89	2.29	1.14	12.0
NGC6946_8	0.04	2.44	0.75	2.65	0.6	2.96	4.39	2.89	2.29	1.14	12.0
NGC6946_9	0.05	2.64	0.75	2.56	0.72	3.38	4.39	2.89	2.29	1.14	12.0
$< NGC6946 >$	0.04	2.81	0.75	4.09	0.91	4.26	4.4	2.89	2.29	1.14	12.0
$M_{up} = 120$											
M100	2.99	0.61	0.43	2.49	0.36	1.63	3.00	1.46	1.02	0.40	12.2
NGC6946_1	0.02	2.43	0.66	3.03	0.77	3.5	3.49	2.31	1.82	0.91	14.0
NGC6946_2	0.09	5.0	1.22	6.64	2.15	10.1	6.13	4.51	3.79	2.19	10.0
NGC6946_3	0.03	2.83	0.75	5.57	0.86	4.63	3.76	2.77	2.32	1.34	10.0
NGC6946_4	0.03	2.9	0.75	5.7	0.89	4.63	3.76	2.77	2.32	1.34	10.0
NGC6946_5	0.01	2.88	0.75	5.76	0.96	4.63	3.74	2.77	2.32	1.34	10.0
NGC6946_6	0.06	2.3	0.66	2.22	0.67	2.98	3.49	2.31	1.82	0.91	14.0
NGC6946_7	0.06	2.38	0.69	2.08	0.63	2.96	3.59	2.49	2.02	1.07	12.0
NGC6946_8	0.03	2.18	0.66	2.08	0.57	2.65	3.49	2.31	1.82	0.91	14.0
NGC6946_9	0.04	2.21	0.66	2.17	0.57	2.72	3.49	2.31	1.82	0.91	14.0
$< NGC6946 >$	0.03	2.43	0.69	3.03	0.77	3.5	3.59	2.49	2.02	1.07	12.0
$M_{up} = 350$											
M100	2.95	0.61	0.40	2.29	0.36	1.59	2.26	1.26	0.92	0.39	12.2
NGC6946_1	0.02	1.82	0.52	2.29	0.54	2.48	2.31	1.63	1.33	0.71	16.0
NGC6946_2	0.05	3.34	0.83	4.95	1.24	6.33	3.69	2.67	2.22	1.24	14.0
NGC6946_3	0.02	1.92	0.53	3.14	0.52	2.79	2.37	1.71	1.42	0.8	14.0
NGC6946_4	0.02	1.94	0.53	3.17	0.52	2.79	2.37	1.71	1.42	0.8	14.0
NGC6946_5	0.01	2.03	0.53	3.37	0.6	2.79	2.36	1.71	1.42	0.8	14.0
NGC6946_6	0.04	1.77	0.52	1.77	0.46	2.22	2.32	1.63	1.33	0.71	16.0
NGC6946_7	0.04	1.68	0.52	1.65	0.45	2.09	2.32	1.63	1.33	0.71	16.0
NGC6946_8	0.02	1.7	0.52	1.8	0.39	2.0	2.32	1.63	1.33	0.71	16.0
NGC6946_9	0.03	1.69	0.52	1.4	0.47	2.07	2.32	1.63	1.33	0.71	16.0
$< NGC6946 >$	0.02	1.82	0.52	2.29	0.52	2.48	2.32	1.63	1.33	0.71	16.0
Literature											
			0.44^a	2.46^d	0.97^g	4.55^b	6.53^a	2.0^e	1.4^e	0.64^a	
				4.80^h	0.92^h	3.88^a	0.62^e				
						0.58^f	3.99^h				

Col.(1): ID. Col.(2): average SFR (in $M_\odot\ yr^{-1}$) derived by considering the last 100 Myr time interval for the normal star-forming galaxy M100 and the age of the burst in the star-forming regions of NGC 6946 Cols.(3-11): SFR calibrations obtained using the above averaged SFR and the luminosities (intrinsic value for FUV) given in Table 6.3. Col.(12): age of the galaxy in Gyr for M100 or the age of the burst in Myr, for NGC 6946 extranuclear regions. The last row in each of the four panels (with ID, $< NGC\ 6946 >$) gives the median values of all quantities given for NGC 6946 star-bursting regions. The values of the SFR calibrations given in the fifth panel were taken from the literature. The superscript on these values indicates the reference as described below: [a]Murphy et al. (2011), [b]Kennicutt (1998), [c]Calzetti et al. (2007), [d]Zhu et al. (2008), [e]Schmitt et al. (2006b), [f]Li et al. (2010), [g]Lawton et al. (2010), [h]Panuzzo et al. (2003). These authors adopted different IMF and evolutionary synthesis models.

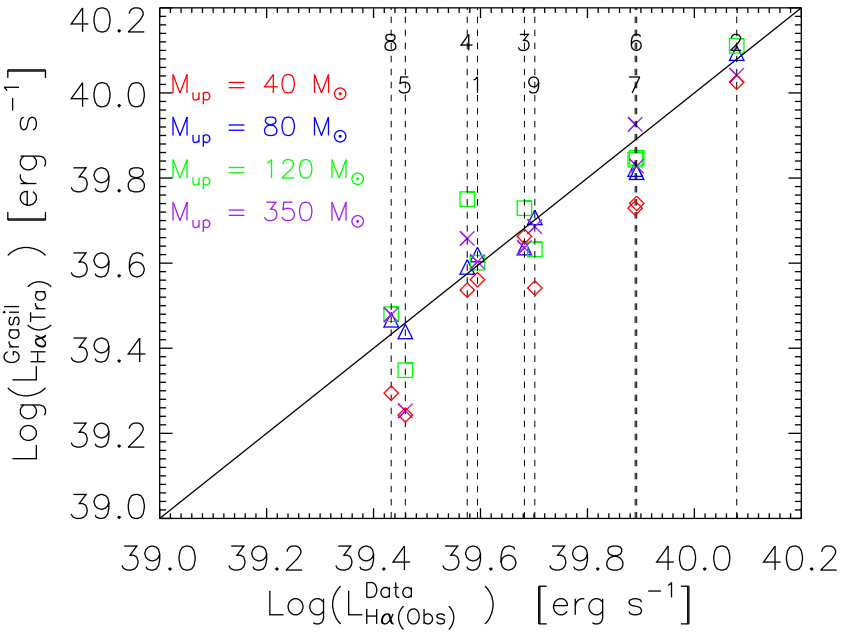

Figure 6.21: Comparisons between our model's transmitted intensities of the Hα emission lines with the observed ones, for M_{UP}=40 $M_\odot$ (red diamonds), M_{UP}=80 $M_\odot$ (blue triangles), M_{UP}=120 $M_\odot$ (green squares) and M_{UP}=350 $M_\odot$ (purple crosses) cases. The nine extra-nuclear star-bursting regions of NGC 6946 are indicated by the numbers 1 to 9. The solid line indicates the one-to-one correlation.

6.4 Summary of bestfit SEDs

We present in Table 6.3 the luminosities of the best fit models in selected photometric bands, from the UV to radio wavelengths. Results obtained for increasing values of M_{up} are shown in different sections of the table. The FIR luminosity in column 11 was obtained by integrating the IR spectral luminosity from 3μm to 1000μm. We also show the value of the q parameter $q_{1.4}$ and the relative contribution to the 3–1000μm FIR luminosity by the molecular clouds component and by the cirrus component. Finally, in the columns of radio luminosities, we enclose in parenthesis the fractional contribution of the thermal radio component to the total radio emission, as derived from the models. As the non-thermal radio emission starts about 7Myr after the beginning of the burst of star formation, we have the opportunity to perform an accurate decomposition of the radio flux into thermal and non thermal components, at different radio frequencies.

The q ratio A common characteristics of the star-burst regions with respect to M100, is a high value of q. In general, the value of $q_{1.4}$ is found to lie between 2.5 and 2.7. This is about 0.2 dex larger than the value observed in normal star forming galaxies ($q_{1.4}$ = 2.35) implying that, in these star forming regions, the ratio between radio and FIR luminosity is about a factor 1.6 lower than in normal star forming galaxies. The estimated young starburst ages support the notion that this is due to a lack of non-thermal radio emission as predicted by the original models by B02. This is also evident from the radio slope which is found to be flatter than the value observed in normal star forming galaxies ($-\delta ln(F_\nu)/\delta ln(\nu)$ = 0.8). It is worth reminding here that we adopted the calibration ($E^{NT}_{1.49}$) of non-

thermal radio luminosity obtained from the fits to M100. The selected star forming regions in NGC6946 did not yet reach a stationary equilibrium for non-thermal radio emission and not only their radio slopes appear flatter but also their $q_{1.4}$ are higher than that of normal star forming galaxies (Bressan et al. 2002).

The second thing that we note by inspecting Table 6.3 is that the value of the $q_{1.4}$ does not significantly depend on the upper limit of the IMF, because the panchromatic fit imposes that both the radio luminosity and the FIR luminosity be fitted at once. Indeed we see from the FIR and the bolometric (BOL) luminosities that, while the FIR/BOL ratio may change significantly from region to region, it does not change noticeably with M_{up}, for the same region. In order to be able to reproduce the ratio q and the slope of the radio emission, the panchromatic fit imposes a solution with a different age, larger for larger M_{up}, in order to counter-balance the larger importance of free-free component for higher M_{up} values. We recall that the non-thermal component is not affected by M_{up} as long as it is larger than the threshold mass for exploding supernovae which is around $30M_{\odot}$ Thus while, in principle, the different dependence of some SFR indicators from M_{up} could have been used to try to determine the upper mass limit of the IMF, this is rendered more challenging by the presence of a certain degeneracy with the age of the burst. This problem will be discussed in more detail in a following section.

The FIR to Bolometric luminosity ratio Another common characteristics of the star forming regions we have analyzed is that the ratio between the FIR and the bolometric luminosity shows significant variation in the sample. In these circumstances the far-Infrared is no more a robust indicator of the star formation rate. This is true also for other FIR indicators generally used as tracers of the star formation activity, like the luminosity at 24 μm or in other infrared bands. In Table 6.4 we have collected the estimated ratios of the SFR and the luminosities in different bands, including the FIR. We see, for example, that the quantity C(FIR)=SFR/L(FIR), in Column 7 of the table, shows a variation among the different sources of even a factor of two. This is due to the variation of the ratio between the SFR and the bolometric luminosity (Column 3), that shows the same variation. This is clearly in contrast with what happens in the more obscured sources where it is found that the ratio SFR/L(FIR) is a more robust star formation indicator. This point will be discussed in more detail in the next chapter, that will be devoted to the analysis of the star formation indicators. In contrast, the ratios between the SFR and the radio luminosity is a more stable SFR indicator because this is tightly linked to the number of massive stars. We will discuss in more detail in the next chapter the relations between the SFR and the luminosities in different spectral regions, the so called "SFR indicators", obtained from our best fit models and, in more generality, from our starburst models.

The emission lines Concerning the emission lines, we compare in Figure 6.21 the predicted intensities of the Hα emission lines (the transmitted luminosities of the best fit models) with the observed values, for the different cases of M_{up}, as shown by the different symbols and colours. The solid line in the figure indicates the one-to-one correlation. After looking at this figure we may say that, in general, the observed values may be fairly well reproduced by the panchromatic fits obtained with any value of M_{up},

from 40 $M_\odot$ to 350 $M_\odot$. We stress here that we are working with panchromatic SEDS because they are tightly constrained by the observed data. For example, by increasing M_{up} we increase the flux of ionizing photons and thus we not only increase the Hα luminosity but also the UV and the free-free emission. The latter is transmitted essentially unattenuated at radio wavelengths and the new model must account for it by readjusting the SFR which, in turn, has an impact on all other luminosities. The only exception is constituted by region ♯5, for which only the case with M_{up}=80 is able to provide a fit within 10%. The cases where the models with M_{up}=40 $M_\odot$ are not able to produce reasonable fits are those of regions ♯5, ♯6, ♯7, ♯8, ♯9. All the models with M_{up}=80 $M_\odot$ are able to produce reasonable fits. There is one case, region ♯4, where the models with M_{up}=120 $M_\odot$ do not provide a good fit and the models with M_{up}=350 $M_\odot$ provide a poor fit only in the case of region ♯4. It is important, at this stage, to remind that these conclusions should be taken with care because the current SSP adopted do not account for binary evolution. Indeed it has been shown recently that binary evolution can produce more ionizing photons at later stages than single star evolution, because binary interaction may cause the loss of the entire envelope of a companion star that then becomes a source of ionizing photons (Wofford et al. 2016).

The β parameter While we have listed the slope of the dust emissivity curve, β, as a free parameter in Table 6.1, we see from Table 6.2 that this parameter is different from the standard value (β=2, Draine & Lee (1984); Draine et al. (2007)) only in few cases. In region ♯5 the models with M_{up} different from 80 $M_\odot$ need a value of β=1.8, which produces a shallower decline of the dust emission at wavelengths larger than 100μm. However we note that these models are not able to provide a good fit of the Hα line (Figure 6.21), and the one that is able to match the panchromatic SED and the Hα line luminosity, with M_{up}=80 $M_\odot$, requires β=2. The other case requiring β=1.8 is region ♯4 with M_{up}=40 $M_\odot$. The model provides a good fit to the panchromatic SED and the Hα line luminosity. But again the best fit to the panchromatic SED and the Hα line luminosity is provided by a model with M_{up}=80 $M_\odot$ and β=2. Finally in the fits of region ♯1 the models with M_{up}=350 $M_\odot$ require β=1.9, M_{up}=120 $M_\odot$ require β=2.0, the ones with M_{up}=80 $M_\odot$ require β=1.8 and the ones with M_{up}=40 $M_\odot$ require β=1.5. In all the M_{up} cases Region ♯1 is fitted very well by the models. However by looking at Figure 6.21 we see that the models with β=2 and with β=1.9, besides providing a good fit to the observed SED, almost match exactly the observed Hα luminosity. We note that, without a distribution of grain sizes, one is often led to fit the FIR-sub-millimetric SED with a modified black-body which adopts an index β different from the standard one. GRASIL provide theoretical SEDs that are the result of a superposition of many blackbodies at different temperatures, regulated by the energy balance of the individual grains. This characteristics eliminates in many cases the need of a lower β exponent. Our fits suggest that β=2 should be the preferred value and that, when a value different than that is required, it is perhaps the result of a wrong set of parameters used to determine the best fit. It is important to stress here that the slope of the dust emissivity curve, affecting the location of the peak of FIR emission, is one of the parameters that strongly affects the accuracy of the photometric redshifts determination based on FIR broad band measurements. Determining whether β should be kept as a constant or not is thus of a certain importance.

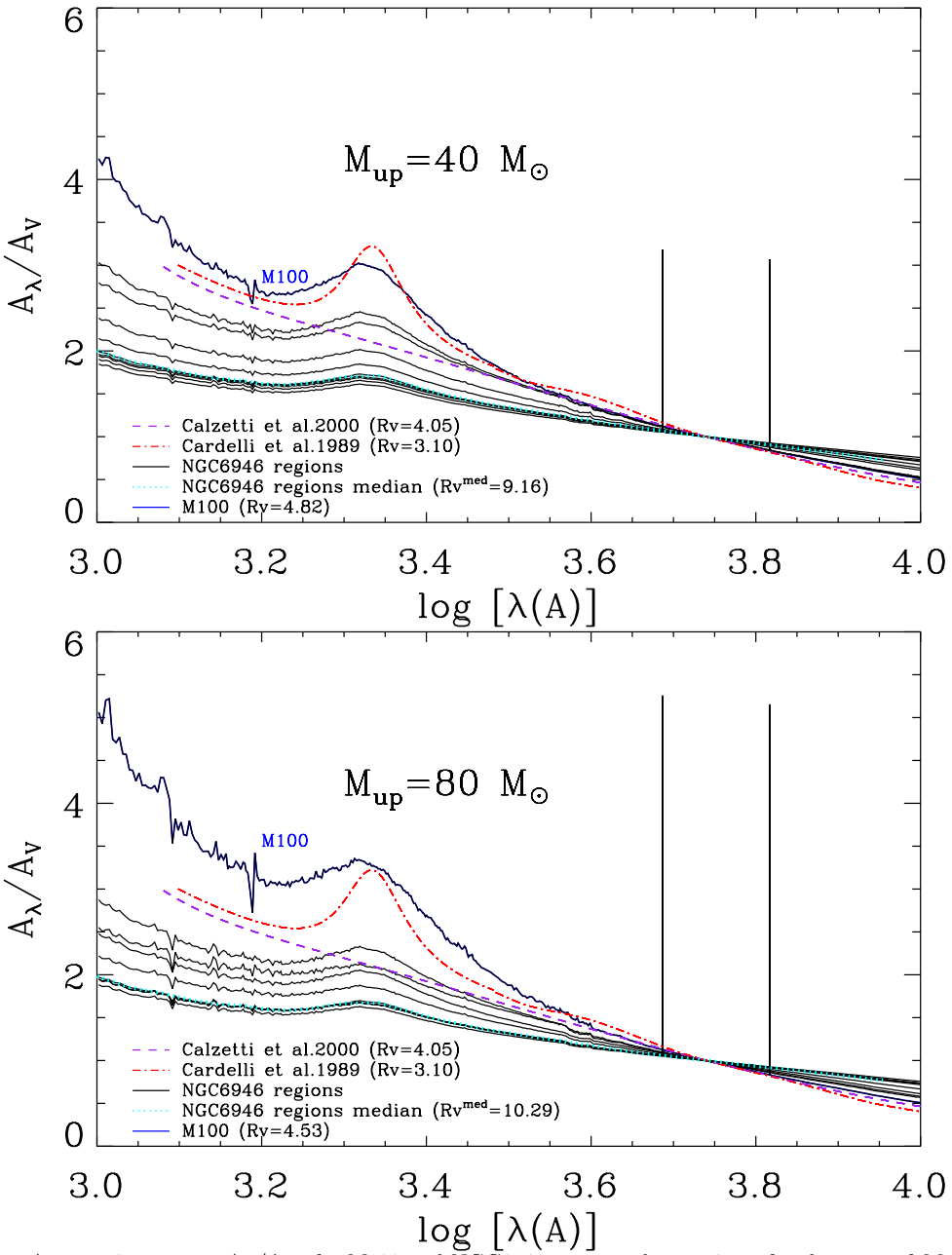

Figure 6.22: Attenuation curves, A_λ/A_V, for M100 and NGC6946 extra-nuclear regions, for the cases of $M_{up} = 40$ (top panel) and $M_{up} = 80$ (bottom panel). The black solid lines are the attenuation curves of the nine regions of NGC6946 while the dotted cyan line represents the median of these curves. The median value of ,$\tilde{R}_V$ for the star-forming regions are also given in the labels. The blue solid lines are the attenuations curves of M100. For comparison purposes, we added the attenuation curves of Calzetti et al. (2000) (purple dashed line) and Cardelli et al. (1989) (red dashed-dotted line) The latter attenuation seems to agree very well with that of M100 at wavelengths above $\sim$ 4000A.

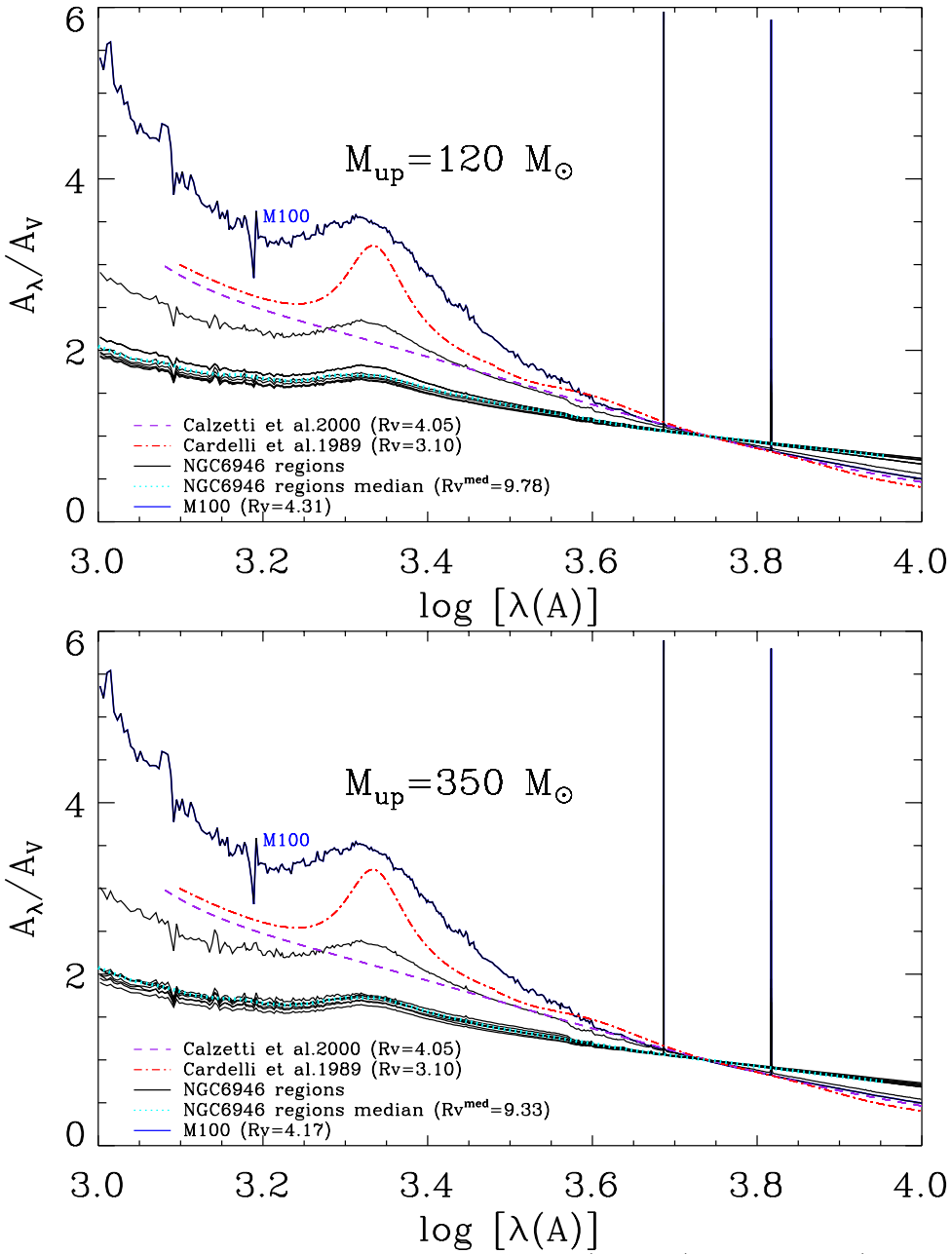

Figure 6.23: Same as Figure 6.22 but for the cases of $M_{up} = 120$ (top panel) and $M_{up} = 350$ (bottom panel).

6.5 Dust attenuation Properties

The light emission from star forming regions is not heavily absorbed by dust. In general the attenuation in the visual band, A(V), of our regions is between 0.5 and 1. It has been already shown in Silva et al. (1998) and Granato et al. (2000) that attenuation is the result of the interplay between the extinction properties of dust grains and the distribution between dust and stars in space and in time. Further discussion can also be found in Charlot & Fall (2000) and Panuzzo et al. (2003). The best fit models give us the opportunity to investigate the properties of the attenuation curves of the galaxies studied here, in particular their dependence on the galaxy type, i.e. starburst vs. normal regime, and also to investigate on the effects of using different parameters in the analysis, such as changing the M_{up} in the IMF. To this purpose, we show in Figures 6.22 the attenuation curves, A_λ/A_V, of M100 (blue solid line) and of the NGC6946 extra-nuclear regions (black solid lines), for the two cases of M_{up}=40 $M_\odot$ and M_{up}=80 $M_\odot$ The other two cases of M_{up}=120 $M_\odot$ and M_{up}=350 $M_\odot$ are shown in Figure 6.23. The attenuation curves are derived by the ratio between the transmitted flux and the intrinsic one, as a function of the wavelength. For comparison purposes, we also plot the attenuation curves of Calzetti et al. (2000) (purple dashed lines) and of Cardelli et al. (1989) (red dot-dashed lines).

The attenuation curves of the individual regions together with R_V=A_V/E(B-V) have been already shown in Figures 6.3 to 6.19. Here we show the median values of the attenuation and R_V=A_V/E(B-V) for the star-bursting regions, for M100 and for the attenuation curves of Calzetti et al. (2000) and Cardelli et al. (1989). The attenuation at Hα, Hβ, in the FUV (0.16μm) and NUV (0.20μm), in the B-band(0.45μm) and V-band(0.55μm), are shown in Columns (2) to (7) of Table 6.5. Column (8) gives the optical depth of the molecular cloud at 1μm derived from *GRASIL* and Column (9) provides the R_V ratio. In Column (10)we show the value of the escape time of young stars from the molecular clouds, t_{esc}. Several points can be noted by inspection of Table 6.5 especially regarding the regime of star formation, that is, normal star-forming galaxy versus star-bursting. First of all, we see that, while in the normal galaxy M100, the attenuation in the lines is significantly higher than that in the surrounding continuum, by a factor of 4 on average, this is not true for the star bursting regions where this factor is not greater than 1.3. The fact that the attenuation in the lines is significantly higher than that in the surrounding continuum is well known and it is a manifestation that young stars are more dust enshrouded than older stars (Calzetti et al. 1994; Silva et al. 1998; Charlot & Fall 2000; Panuzzo et al. 2003). However, in the case of the star-bursting regions the underlying continuum is essentially produced by the same stellar populations, with a small contribution from the older populations, so that the attenuation in the lines is not much different from that in the continuum. To get more insights from the models we compare the characteristic R values in the lines and in the nearby continuum. We find that, for M100, $R_{H\alpha}$=$A_{H\alpha}$/($A_{H\beta}$-$A_{H\alpha}$) is much larger than the value obtained in the corresponding interpolated underlying continuum regions ($R_{65} = A_{65}/(A_{48} - A_{65})$). For example, for M100, $R_{H\alpha}$=16(10) while R_{65}=4(4), for M_{up}=40(120)$M_\odot$. In the star-burst regions, $R_{H\alpha}$ and R_{65} have similar values between 6 and 10. The high values so determined for $R_{H\alpha}$ would suggest a high neutral absorption in these objects but this is not the case because we have not modified the grain size distribution which, by default in

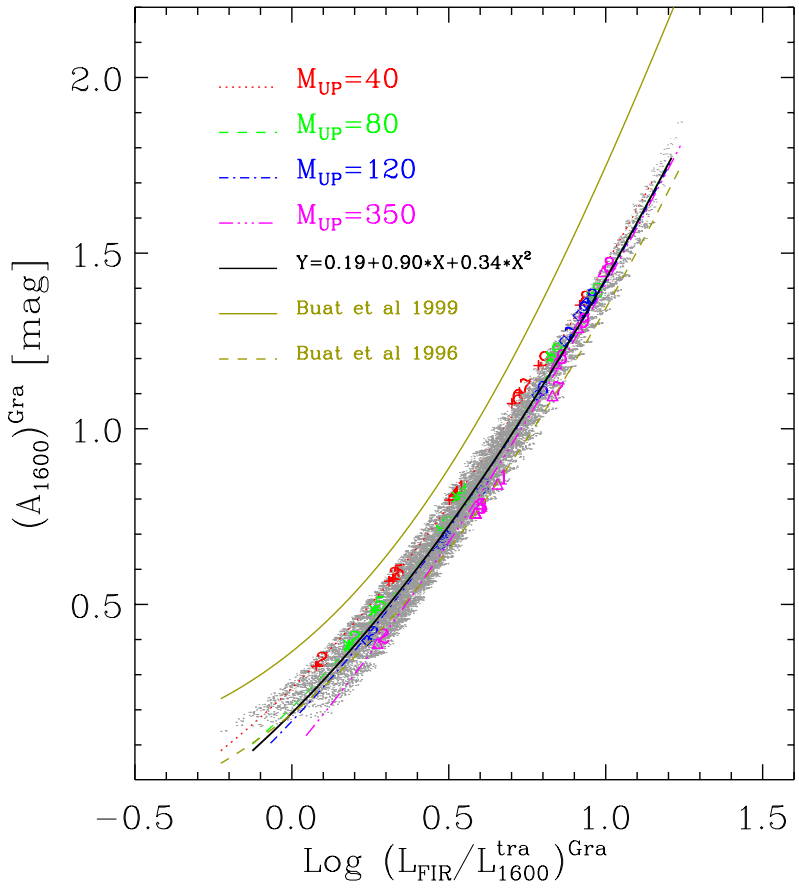

Figure 6.24: Plot of attenuation at 1600 $\AA$ against the ratio L_{FIR}/L_{1600} for our library of star-burst models (grey points). L_{FIR} is the 3 μm−1000 μm infrared luminosity. We provide polynomial fits for the different upper mass limits: red dotted, green dashed, blue dotted-dashed and purple triple dotted-dashed lines for $M_{up} = 40, 80, 120$ and 350 respectively. We over plotted on the models, with the same colour code and for the different upper mass limits, the same quantities extracted from our best-fit models (the plus, asterisk, diamond and triangle symbols correspond to $M_{up} = 40, 80, 120$ and 350 respectively). A_{1600}, L_{FIR} and L_{1600} are respectively as given in column 4 of Table 6.5, columns 7 and 4 of Table 6.3. The solid and dashed gold lines represent the relation given by Buat et al. (1999) and Buat & Xu (1996) respectively while the the solid black line represents a multiple regression (for all M_{up}) fit for our models as given in the relation in the label and by Equation 6.1. The latter authors used the 60 and 100μm in computing L_{FIR} between 40 - 120 μm but we converted this luminosity to the one obtained by integrating from 8 -1000 μm using our models average ratio (2.1) of the two different luminosities.

Table 6.5: GRASIL Best-fit derived quantities related to dust attenuation

ID	$A_{H\alpha}$	$A_{H\beta}$	A_{FUV}	A_{NUV}	A_B	A_V	τ_1	R_V	t_{esc}
(1)	(2)	(3)	(4)	(5)	(6)	(7)	(8)	(9)	(10)
$M_{up} = 40$									
M100	0.79	0.85	0.57	0.62	0.22	0.18	6.58	4.31	1.50
NGC6946_1	0.59	0.66	0.81	0.85	0.56	0.5	12.0	9.09	0.5
NGC6946_2	0.26	0.28	0.32	0.34	0.17	0.14	21.33	5.01	0.5
NGC6946_3	0.43	0.49	0.57	0.6	0.31	0.26	33.33	5.08	1.0
NGC6946_4	0.62	0.69	0.8	0.83	0.52	0.46	21.33	7.65	1.0
NGC6946_5	0.48	0.53	0.57	0.6	0.35	0.3	33.33	6.59	1.0
NGC6946_6	0.95	1.03	1.07	1.11	0.73	0.66	9.91	9.54	1.2
NGC6946_7	0.98	1.05	1.1	1.14	0.76	0.69	7.68	9.78	1.2
NGC6946_8	1.17	1.25	1.35	1.4	0.96	0.89	7.68	11.27	1.2
NGC6946_9	1.04	1.12	1.18	1.23	0.82	0.75	7.68	10.32	1.2
$M_{up} = 80$									
M100	2.23	2.31	0.85	0.87	0.24	0.19	28.39	3.65	3.00
NGC6946_1	0.65	0.71	0.79	0.82	0.54	0.49	12.0	10.27	0.5
NGC6946_2	0.34	0.37	0.38	0.4	0.21	0.18	21.33	5.67	0.5
NGC6946_3	0.65	0.7	0.71	0.73	0.45	0.4	33.33	8.08	1.0
NGC6946_4	0.83	0.89	0.81	0.82	0.46	0.39	33.33	6.09	1.2
NGC6946_5	0.42	0.46	0.48	0.51	0.29	0.25	33.33	6.95	0.5
NGC6946_6	1.14	1.22	1.2	1.24	0.82	0.75	12.0	10.51	1.2
NGC6946_7	1.14	1.22	1.2	1.24	0.82	0.75	12.0	10.51	1.2
NGC6946_8	1.27	1.35	1.38	1.42	0.96	0.89	12.0	11.45	1.2
NGC6946_9	1.14	1.22	1.2	1.24	0.82	0.75	12.0	10.51	1.2
$M_{up} = 120$									
M100	2.53	2.61	0.93	0.97	0.26	0.20	39.66	3.56	3.00
NGC6946_1	0.73	0.79	0.82	0.86	0.57	0.52	12.0	10.29	0.5
NGC6946_2	0.39	0.42	0.4	0.41	0.21	0.18	21.33	5.52	0.5
NGC6946_3	0.58	0.64	0.67	0.69	0.43	0.39	33.33	8.55	0.5
NGC6946_4	0.58	0.64	0.67	0.69	0.43	0.39	33.33	8.55	0.5
NGC6946_5	0.58	0.64	0.67	0.69	0.43	0.39	33.33	8.55	0.3
NGC6946_6	1.17	1.24	1.1	1.13	0.73	0.66	12.0	9.55	1.2
NGC6946_7	1.25	1.33	1.25	1.29	0.84	0.76	12.0	9.95	1.2
NGC6946_8	1.36	1.44	1.36	1.4	0.94	0.85	12.0	10.71	1.2
NGC6946_9	1.33	1.41	1.32	1.36	0.91	0.83	12.0	10.53	1.2
$M_{up} = 350$									
M100	2.30	2.36	0.84	0.87	0.22	0.17	39.66	3.52	2.00
NGC6946_1	0.83	0.89	0.84	0.87	0.58	0.52	21.33	9.91	0.3
NGC6946_2	0.49	0.52	0.39	0.4	0.2	0.17	33.33	5.24	0.5
NGC6946_3	0.76	0.82	0.76	0.79	0.51	0.46	33.33	9.07	0.5
NGC6946_4	0.76	0.82	0.76	0.79	0.51	0.46	33.33	9.07	0.5
NGC6946_5	0.76	0.82	0.76	0.79	0.51	0.46	33.33	9.07	0.5
NGC6946_6	1.34	1.41	1.19	1.22	0.77	0.69	21.33	8.58	1.2
NGC6946_7	1.07	1.14	1.09	1.13	0.77	0.7	12.0	10.65	1.0
NGC6946_8	1.53	1.62	1.45	1.49	0.98	0.89	21.33	9.69	1.2
NGC6946_9	1.42	1.5	1.29	1.32	0.86	0.77	12.0	9.14	1.2

Col.(1) :ID. Cols.(2 - 7) give the attenuations in Hα, Hβ, FUV (0.16μm), NUV (0.20 μm), B-band(0.45 μm) and V-band(0.55 μm) They were derived using the ratio of the intrinsic unattenuated and attenuated (observed) fluxes. Col.(8): optical depth of the molecular cloud at 1 μm. Col.(9): R_V. Col.(10): escape time of young stars from their birth cloud in Myr.

GRASIL is the one of the Galactic ISM. We also see that in M100, R_{65} in the continuum, has a value of ∼3, compatible with the common extinction laws provided in literature (Calzetti et al. 2000; Cardelli et al. 1989). Instead this effect is due to the fact that the attenuation within molecular clouds is so high (see the values of $\tau_{1\mu m}$ in Table 6.5) that the emission of young stars is almost completely absorbed, until they escape from the clouds. This effect, that mimics a neutral absorption, is enhanced for the emission lines because they are generated only by stars younger than about 6 Myr, so that the fraction of line flux absorbed by molecular clouds with respect to the total one, is even higher. Adopting a t_{esc} larger than 7 Myr will erase line emission in our model, irrespective of the galaxy types considered here.

Since in starburst galaxies the un-attenuated luminosity is essentially produced by the massive star population which are the primary contributors to the UV light it is customary to use empirical relation to correct the observed UV luminosity from attenuation. In Figure 6.24 we plot the transmitted far−UV flux against the ratio, IRX, between the FIR and the transmitted far−UV flux of all our starburst models (gray dots). These should correspond to observed quantities and then the relation could be used to correct the FUV flux for attenuation in objects with a mild dust absorption. From all the models we get the following relation

$$A_{1600} = 0.19 + 0.90 \log\left(\frac{L_{FIR}}{L^{tra}_{1600}}\right) + 0.34 \log\left(\frac{L_{FIR}}{L^{tra}_{1600}}\right)^2 \tag{6.1}$$

that it is plotted as a solid black line in the figure. In this relation, A_{1600} is the attenuation at $\lambda = 1600$ Å. The transmitted luminosity L_{1600} (at λ=1600 Å) = $\nu \times L_\nu = \lambda \times L_\lambda$ and L_{FIR} is the 3 μm−1000 μm infrared luminosity. The other curves are fits of the models with different values of M_{up} as indicated by the corresponding colour codes and line styles (red dotted, green dashed, blue dot-dashed and purple triple-dot dashed lines for M_{up} = 40, 80, 120 and 350 respectively).

6.6 Testing the Upper Mass Tail of the IMF

In general our best fit models are able to reproduce the observed values of luminosity with an accuracy of about 10%. An important question, introduced in the previous section, is whether it is possible to discriminate between the different values of M_{up} from the SEDs of the galaxies. We note here that the question does not concern only M_{up} but, in more generality, the relative mass distribution of massive stars. Indeed an increase of the weight of the massive stars relative to the lower mass stars can be obtained either by increasing the upper mass limit, or by decreasing the slope of the upper tail of the mass distribution, or by just increasing the lower mass limit of the distribution. In all the three cases we will produce an increase of the relative weight of the massive stars, a so called top heavy IMF. By converse, acting in the opposite direction one may obtain a bottom heavy IMF, i.e. a mass distribution where the low mass stars have a relatively higher weight than in the *standard* IMF. If we consider these variations at constant total mass, a top heavy IMF will produce more light and more metal enrichment per unit mass while a bottom heavy IMF will reduce both the light emitted and the metals ejected per unti mass. Whether the IMF is a universal distribution or not is one of the challenging problems of the astrophysics that remains still unsolved. There are different opinions in literature.

- Bottom Heavy IMF.

  From observations of the strengths of gravity sensitive narrow band integrated indices in local ellipticals, van Dokkum & Conroy (2012) and Conroy & van Dokkum (2012b), conclude that the IMF in such galaxies must be definitely bottom heavy, i.e. dominated by the low mass stars.

- Top Heavy IMF.

  On the contrary, a recent investigation of the isotopic abundances of CNO elements in starburst galaxies (Romano et al. 2017) find strong evidence that the low O^{16}/O^{18} abundance ratios observed in starburst galaxies cannot be produced without assuming a top heavy IMF. In the same direction there are also some indirect studies that, in order to reproduce the observed high luminosities, postulate that the IMF during the starburst phase must be top heavy (e.g. Lacey et al. 2016). The analysis performed by Romano et al. (2017) is particularly relevant because it includes recent determinations of isotopic abundances in high redshift star-bursting galaxies performed with ALMA. Among the analysed galaxies there is a group of sub-millimetre galaxies characterized by high star formation rates that are thought to be the precursors of the local ellipticals and thus this conclusion may be in clear contradiction to that reached by van Dokkum & Conroy (2012) and Conroy & van Dokkum (2012b).

- Standard IMF.

  A support for a, let us say, *normal* Chabrier (2003) IMF, comes from the simple considerations that, one one side we know that elliptical galaxies are among the most metal rich objects in the local universe, which would be difficult to explain with a constant bottom heavy IMF. On the other hand, we know that elliptical galaxies contain more than the 50% of all the formed visible star in the local universe, a fact that would be difficult to explain if their progenitors were forming stars with a top heavy IMF. The latter argument can now be directly tested at high redshifts by comparing the mass derived distributions with the star formation derived distributions. These different distributions show that at any epoch (redshift) the stellar mass distribution is consistent with the integral of the SFR estimated at earlier epochs (redshifts) assuming a Chabrier (2003) IMF (Lapi et al. 2017b,a; Mancuso et al. 2017).

The latter however is a statistical argument and if both Conroy & van Dokkum (2012b) and Romano et al. (2017) inferences are correct then a possible explanation could be that the IMF changes with time from a top heavy one (perhaps in the burst phase or in an early phase) to a bottom heavy one (perhaps in a quiescent phase or in a later phase).

Thus it will be extremely important to have an independent observable that may discriminate between a top-heavy and bottom-heavy IMF. In this respect, an important conclusion resulting from our previous analysis is that some features of the SEDs should indeed depend from the adopted values of M_{up}. For example we find that the relative number of massive stars in the different ranges responsible for the thermal and non thermal radio emission may affect the radio slope of the SED. Thus, in principle, the radio slope could be used to try to determine the upper mass limit of the IMF. However, in practice, when we look at the fits of the individual star forming regions of NGC6946, we do not see a clear indication concerning the value of M_{up}. For any region we obtain very good fits for almost all the vales of M_{up} and we cannot exclude that, in the cases where a very good fit has not been found, this is due to a

restricted range of the adopted parameters, in spite of the wide range that we have explored. Should we abandon this method ?. The answer comes from the inspection of Figure 6.25, where we plot the time evolution of the 33GHz−1.4GHz radio-emission slope, $\delta ln(F_\nu)/\delta ln(\nu)$, in our starburst models for different metallicities, Z=0.001, 0.004, 0.008 and 0.02. From the figure we note that the slope starts very flat and it becomes steeper as the age of the starburst increases. This behaviour has been already described and it is due to the lack of non-thermal emission in the first ∼7 Myr of evolution and to the rising of the non-thermal contribution as the models become older than this age threshold. At the beginning, i.e. for ages younger than about 20 Myr, there is a strong degeneracy between the value of M_{up} and the age of the burst, in the sense that the same slope may be reproduced by models with larger values of M_{up} and larger ages. This is exactly the age range of our star-bursting regions and this age-M_{up} degeneracy renders impossible to disentangle the two effects.

Our starburst regions have ages of less than ∼ 20 Myr and thus occupy a region in the different panels of Figure 6.25 where models of different M_{up} can be found. We see from the figure that the same slope may be reached by models with increasing M_{up}, by increasing their age. Thus as long as the age is less than ∼ 30 Myr it is impossible to determine the value of M_{up} using the slope of the radio emission.

However, when the age becomes larger than a few tens of Myr, the slope approaches a constant value that depends only on M_{up}. This represent the stationary status where the relative number of stars of different age remains constant, because the flow of stars in and out from the phases that produce thermal and non thermal radio photons has reached a constant value. In order to detect the effect of M_{up} we should look at starbursts with continuous SFR for time periods larger than ∼ 30 Myr, for which the radio slope is constant and depends significantly from M_{up}. It could be difficult to find in the local Universe regions of constant star formations with ages larger than this value because, in general, the gas consumption time-scales are shorter than a few tens of Myr, exactly as in our star bursting regions (e.g. Papovich et al. 2016a). Instead this condition could be fulfilled by high redshift galaxies where the gas consumption timescales are found to be much longer than those observed in local systems (e.g. Tacconi et al. 2008; Papovich et al. 2016a). Models of early galaxy evolution indicates that constant star formation rates can be sustained for periods of time much longer than those found in local starbursts and in some case as long as the formation history of the galaxy (e.g. Mancuso et al. 2017; Lapi et al. 2017a; Mancuso et al. 2016). If so, the radio slope of early star forming galaxies could may serve as a strong probe of their IMF.

The radio slope of a sample of about 50 sub-millimetre galaxies has been recently measured by Thomson et al. (2014). Their slopes are shown in in Figure 6.26 taken from Thomson et al. (2014) paper. The vertical axis reports the rest-frame radio slope between 1.4 GHz and 610 MHz while the horizontal axis is the q ratio. The distribution of the radio slope of individual sources is shown as a gray histogram in the vertical axis. The authors find the average slope $< \alpha >= -0.79 \pm 0.06$ with a typical standard deviation for the individual objects of $\sigma = 0.15$. We note that the distribution is quite broad with slopes steeper than $\alpha = -1.0$. However this average value is very similar to the synchrotron slope found in local star forming galaxies. A similar results has been also found by Ibar et al. (2010). In figure 6.27 we show the radio slope of our star-burst models between 4.9 GHz and 1.4 GHz (left panel). This should already

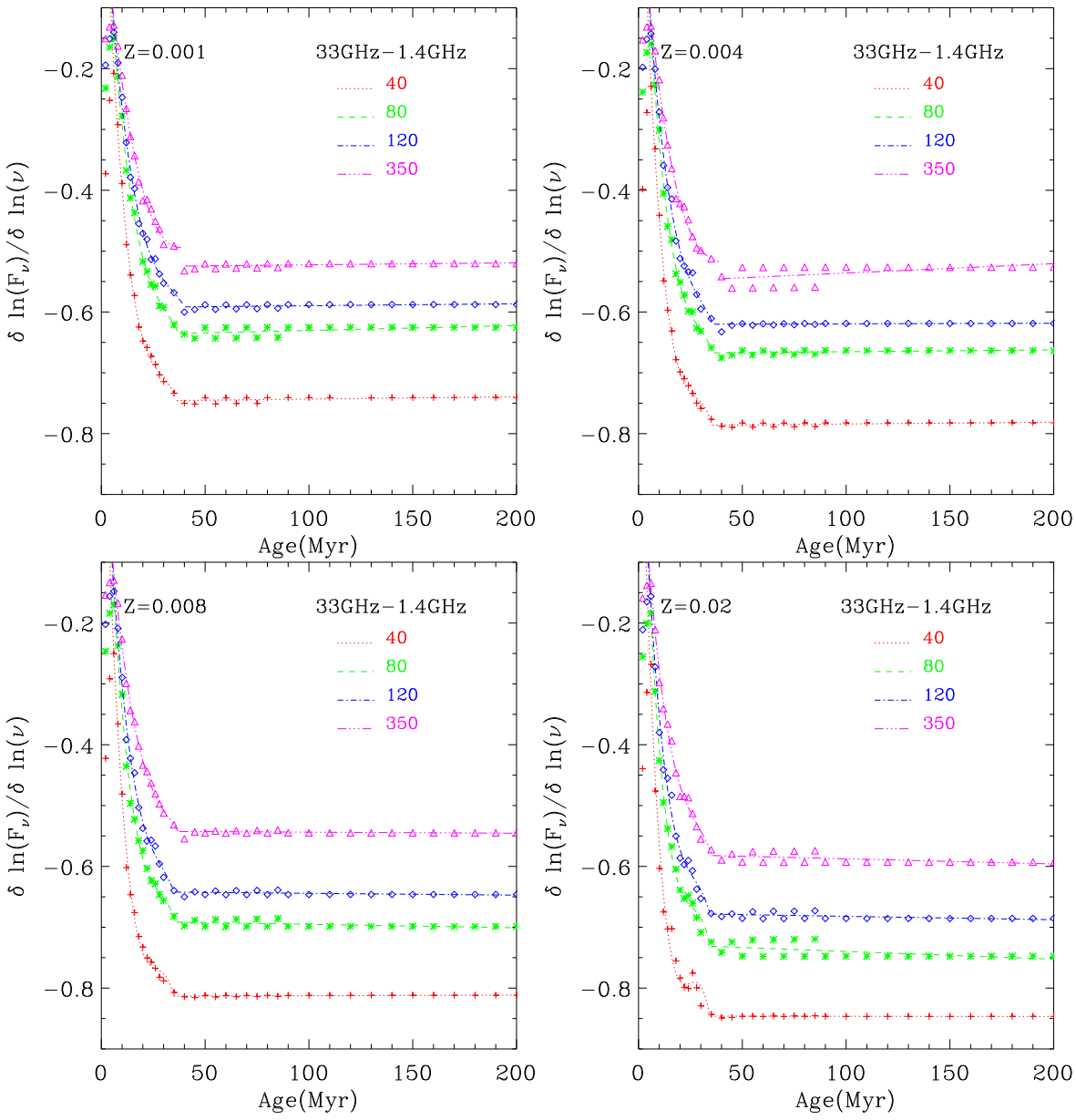

Figure 6.25: Time evolution of the 33GHz−1.4GHz radio-emission slope, $-\delta(ln(F_\nu)/\delta ln(\nu)$, in our starburst models.

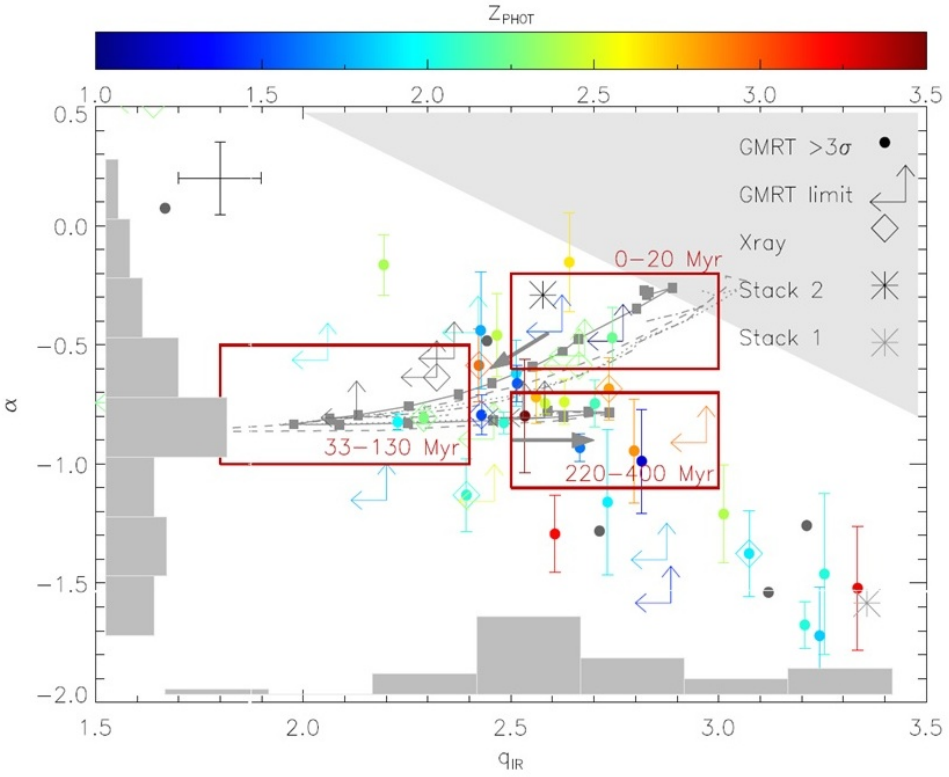

Figure 6.26: Radio-slope vs q for a sample of sub-millimetre galaxies (from (Thomson et al. 2014). The vertical axis reports the rest-frame radio slope between 1.4 GHz and 610 MHz while the horizontal axis is the q ratio. The distribution of the radio slopes is shown as a histogram in the vertical axis. The authors find that $< \alpha >= -0.79 \pm 0.06$. The typical standard deviation of the individual objects is $\sigma(\alpha) = 0.15$, as shown in the upper left corner.

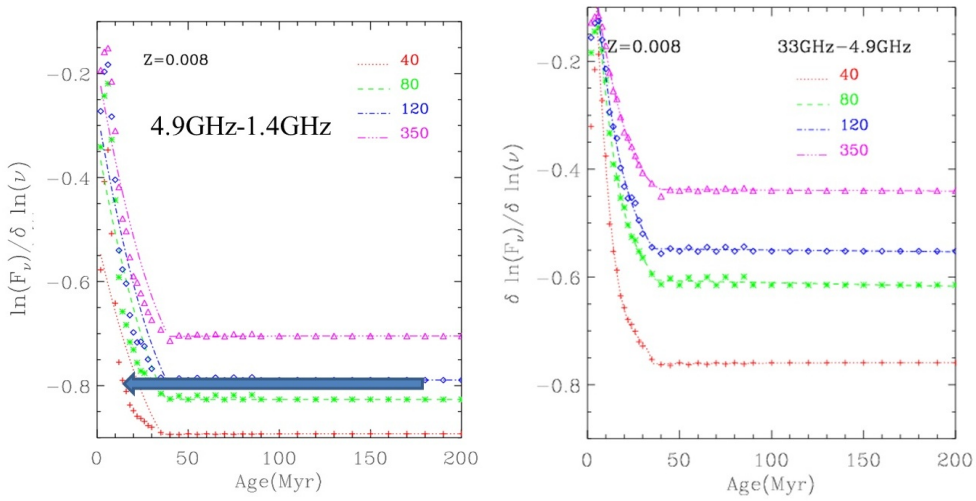

Figure 6.27: Radio-slope of starburst models at different frequencies, $\alpha_{4.9\ GHz-1.4\ GHz}$ and $\alpha_{33\ GHz-4.9\ GHz}$. The arrow in the left panel indicates the average value found by Thomson et al. (2014). Note the larger range of the $\alpha_{33\ GHz-4.9\ GHz}$ slope caused by the larger sensitivity of the rest frame 33 GHz band to free-free emission.

be very similar to the radio slope between 1.4 GHz and 610 MHz, because in both frequency ranges synchrotron radiation should dominate the radio emission. The average value found by Thomson et al. (2014) is indicated by the arrow in the left panel of the figure. This value is consistent with our adopted IMF with upper mass limit between 120 $M_\odot$ and 80 $M_\odot$. This IMf has almost the same relative number of massive stars as the Chabrier (2003) IMF (see Table 6.6). This very preliminary direct measurement of the IMF slope in the range of massive stars seems to suggest that a normal IMF should be preferred on average for the observed high redshift star forming galaxies.

To show the ability of the models to detect the signatures of different IMF types (in the domain of massive stars) we have run very simple simulations where starburst models are assigned an age uniformly distributed from zero to a maximum age. However we have used a higher rest frame upper frequency limit (33GHz), more sensitive to the free-free emission, to give the slope a larger sensitivity to the upper mass limit, as shown in the right panel of Figure 6.28. After applying to the radio slope $\alpha = \delta ln(F_\nu)/\delta ln(\nu)$ a relative error drawn from a gaussian distribution with a conservative standard deviation $\sigma(\alpha)$=0.1, we construct the histogram of the distribution. The results are shown in three different panels for three different values of the maximum ages of the starbursts, representing the time-scales of the constant star formation episodes, T_{MAX}= 50 Myr, 100 Myr and 200 Myr. For each histogram we have used 500 objects. It is evident from the figure that the four different values of M_{up} give rise to different family of models with the slope that peaks at different values. At an age of 50 Myr the separation of the different families is already well apparent. The effect becomes more pronounced as the maximum age of the starburst increases. This age represents the duty cycle of the star-burst, i.e. the period over which the galaxy is actively forming stars with almost constant SFR. Similar plots could have been done for different star formation histories but, in the case of high redshift star forming galaxies, the assumption of a constant SFR over such timescales is a fair hypothesis (e.g. Papovich et al. 2016b). There is a clear correlation of the peak of the slope distribution with M_{up} which is explained by the constant proportions reached by

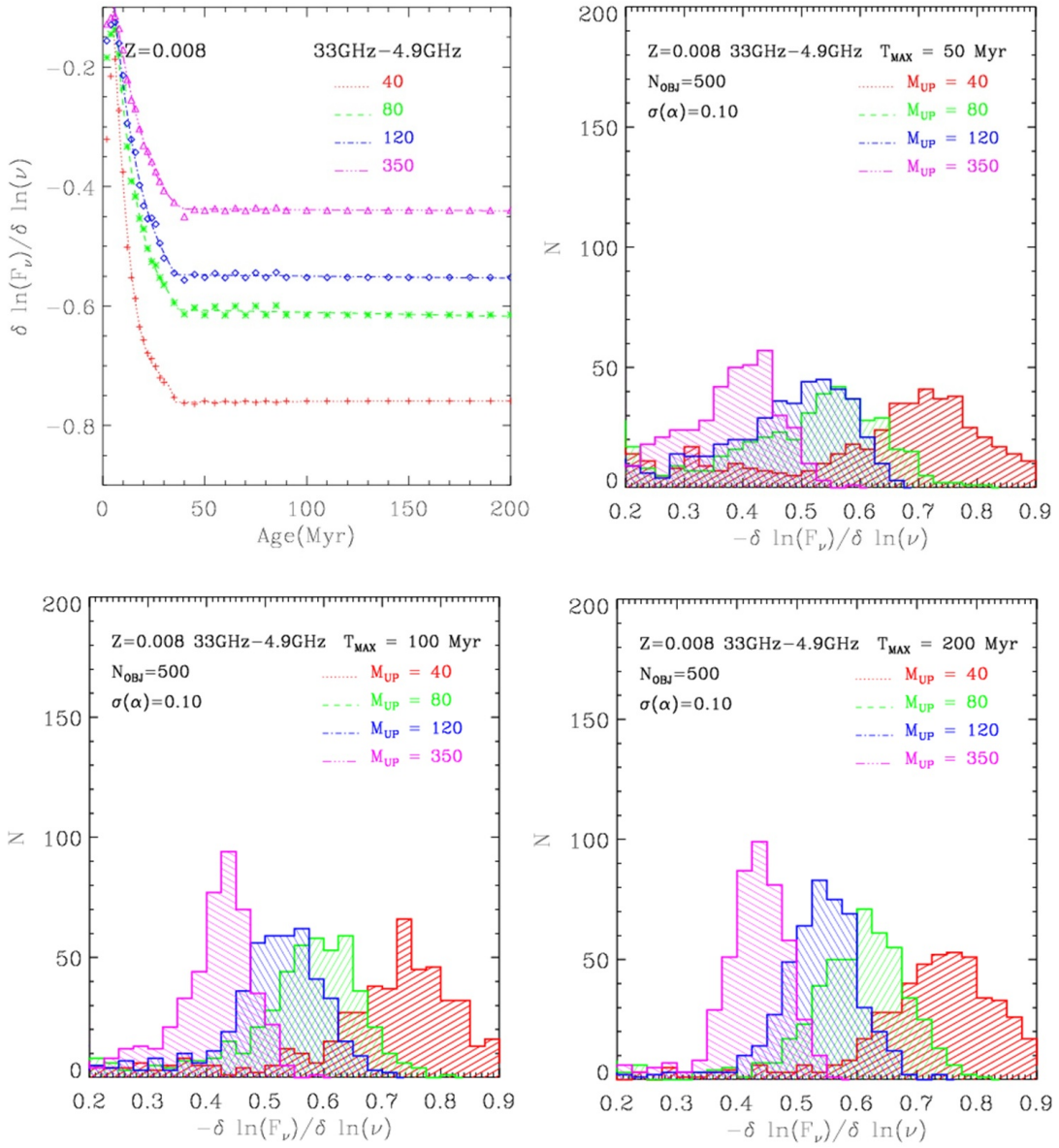

Figure 6.28: Time evolution of the 33GHz−4.9GHz rest frame radio-emission slope for starburst models with Z=0.008 (upper left panel). Simulations of the distribution of the slopes for starburst models of different M_{up} uniformly distributed in age from t=0 to t=T_{MAX}, as indicated in the corresponding labels of the plots. Each histogram is for 500 objects and the standard deviation of the individual slopes is assumed to be 0.1

stars of different mass in such constant SFR galaxy models.

We note that we used a constant metallicity for the starburst, while we know that at high redshifts the constant SFR is accompanied by a global enrichment of the galaxy. May this effect smear out the differences shown in the figure 6.28 ? Though a thorough test should be done to answer this question we stress that in general the metallicity evolves linearly with time. This means that, for example, between Z=0.008 and Z=0.02 we expect about four times the number of objects found in the metallicity range between Z=0.001 and Z=0.004. Since the effect of metallicity is not strong we guess that by considering models where the chemical evolution is taken into account would provide results not much different from those shown here. This is an investigation planned for the next future.

At this point is worth recalling here that this approach is meant to discriminate only between IMF distributions that differ in the mass range above about 8 $M_{\odot}$. Indeed if two IMF distributions differ only in the range below that of massive stars ($M \leq 8\ M_{\odot}$) they will produce the same radio slope. This is because the radio slope probe the relative number of stars more massive than 8 $M_{\odot}$ and not the number ratios between massive stars and low mass stars.

In conclusion, if feasible, the proposed test would be the first direct test on the upper mass range of the IMF across the universe.

Table 6.6: Relative massive stars fractions for different IMF, Chabrier (Chabrier 2003)(CHA), this work (KEN) and the Salpeter one(Salpeter 1955) (SAL). The $MassNormalization$ is the total mass in solar masses of the IMF without a normalization constant. M is the mass integral and N is the number integral.

M_{up}	40 $M_\odot$	80 $M_\odot$	120 $M_\odot$	350 $M_\odot$
$Normalization$				
KEN	3.3195	3.4888	3.5703	3.7374
CHA	0.0754	0.0794	0.0813	0.0855
SAL	5.6107	5.7800	5.8615	6.0286
$M > 1\ M_\odot/M_{Tot}$				
KEN	0.6240	0.6423	0.6504	0.6661
CHA	0.5665	0.5882	0.5981	0.6177
SAL	0.3692	0.3877	0.3962	0.4129
$M > 10\ M_\odot/M_{Tot}$				
KEN	0.1478	0.1891	0.2077	0.2431
CHA	0.1443	0.1870	0.2067	0.2454
SAL	0.0874	0.1142	0.1265	0.1507
$N > 1\ M_\odot/M_{Tot}$				
KEN	0.2216	0.2117	0.2071	0.1981
CHA	0.1937	0.1849	0.1807	0.1722
SAL	0.1311	0.1278	0.1262	0.1228
$N > 1\ M_\odot/N_{KEN}$				
CHA	0.8741	0.8734	0.8725	0.8690
SAL	0.5916	0.6036	0.6091	0.6199
$N > 10\ M_\odot/M_{Tot}$				
KEN	0.0084	0.0089	0.0089	0.0088
CHA	0.0082	0.0087	0.0087	0.0085
SAL	0.0050	0.0054	0.0054	0.0054
$N > 10\ M_\odot/N_{KEN}$				
CHA	0.9693	0.9737	0.9747	0.9736
SAL	0.5916	0.6036	0.6091	0.6199
$N > 20\ M_\odot/M_{Tot}$				
KEN	0.0024	0.0031	0.0033	0.0034
CHA	0.0024	0.0032	0.0033	0.0034
SAL	0.0014	0.0019	0.0020	0.0021
$N > 20\ M_\odot/N_{KEN}$				
CHA	0.9936	1.0020	1.0046	1.0063
SAL	0.5916	0.6036	0.6091	0.6199
$10\ M_\odot > N > 30\ M_\odot/M_{Tot}$				
KEN	0.0112	0.0107	0.0104	0.0100
CHA	0.0107	0.0102	0.0100	0.0095
SAL	0.0066	0.0064	0.0063	0.0062
$10\ M_\odot > N/N_{KEN} > 30\ M_\odot$				
CHA	0.9578	0.9564	0.9551	0.9511
SAL	0.5916	0.6036	0.6091	0.6199

Chapter 7

Star formation rate indicators

7.1 Star formation rates indicators: analytic approximations.

In the previous chapters I described how we obtained a consistent set of SSP integrated spectral energy distributions including emission lines, free-free and non-thermal radio emission. I then used these SSP spectra to predict the intrinsic (i.e. not dust absorbed) and the attenuated SED of starburst models. From these models I can now derive analytical relations providing the SFR as a function of luminosities in different bands. Among such indicators, both the intensity of the recombination lines and that of free-free emission are tightly related to the ionizing photon luminosity coming from the central star clusters. They thus trace the number of massive stars born in the very recent times ($\leq$ 7 Myr) and, for this reason they should be considered, in principle, optimal indicators of the most recent, i.e. ongoing, star formation rate. Similar to these indicators is also the Far-UV emission which is essentially produced by the hottest stars. On the contrary the near UV flux of a composite system may not be strictly associated with the ongoing star formation rate since even objects as old as one Gyr, particularly if they are metal poor, may significantly contribute to this wavelength range. Finally, non-thermal radio emission, which may dominate the radio band around a frequency of a few GHz, is efficiently produced in the age range between $\sim$7 Myr and $\sim$35 Myr. It is also a good indicator of the recent star formation history but its time delay with respect to e.g. emission lines or free-free emission could be comparable to the decay time of an individual starburst episode.

As we have seen the Far UV continuum and optical and sometimes near infrared recombination lines may be affected by dust attenuation. Furthermore, free-free radio emission may suffer from problems arising from the spatial resolution of the telescopes (which could be alleviated in distant objects) and from the fact that it could be hardly disentangled from the synchrotron emission. Thus their use as SFR indicators is always accompanied by a careful definition of the possible biases just discussed. With these caveats in mind I present and discuss in this chapter some analytic approximations that can be used to derive (or predict) the star formation rates of star forming galaxies from their luminosities.

I begin from the intrinsic luminosities because they constitute the reference values and because, in general, one first obtains such intrinsic luminosities from estimates of the attenuation and then transforms

to star formation rates.

An important point that is worth mentioning is that the longer is the time range over which a SSP contribute to a given process that emits in a given spectral band, the more is the time needed for this process to be considered in stationary state and thus to be analyzed with indicators that generally assume this condition to be fulfilled.

Following a common approximation I consider in the followings a stellar system with a star formation rate constant in time, and calculate the corresponding luminosity produced by the aforementioned emission processes.

7.2 The integrated ionizing photon rate at constant star formation

Given that nebular emission depends critically on the ionizing photon luminosity we begin with the calculation of the integrated photon luminosity in a galaxy with constant star formation rate. The integrated ionizing photon rate of a galaxy model at a time t is given by

$$Q(H)^{gal}(t,Z) = \int_0^t Q(H)^{SSP}(t-t',Z)\, SFR(t')dt' \tag{7.1}$$

where $SFR(t')$is the star formation rate at time t' and $Q(H)^{SSP}(t-t',Z)$ is the ionizing photon rate of a SSP of age $t_{ssp} = t - t'$ and given metallicity Z. Using the ionizing spectra already obtained in Section 3.2.1 of Chapter 3 (see Figure 3.3) and a constant SFR of 10 $M_{\odot}yr^{-1}$ we obtain the integrated number of ionizing photons $Q(H)$, shown in Figure 7.1. We recall that our SSP were constructed assuming a two-power law IMF (Kennicutt 1983).

Since $Q(H)$ is dominated by the most massive stars, the number of ionizing photons emitted by a galaxy with constant SFR will initially grow and soon saturate to a constant maximum value, when there is a balance between the newly formed ionizing massive stars and the ones that die. Looking at Figure 3.3 we see that, almost independently from the metallicity, the characteristic time of the saturation is set by the rapid drop of $Q(H)$ for SSP with ages above about 6 Myr. Thus this is the typical time delay for the emission lines as well as for the free-free radio emission to be considered in a stationary state. The effect of M_{up} on $Q(H)$ is a direct consequence of the variation of the $Q(H)$ of the SSPs shown in Figure 3.3. After a time which is of the order of 6 Myr a stellar system with constant SFR produces ionizing photons at a constant rate. In this case there is a tight relation between the SFR and the luminosity of ionizing photons Q(H). After denoting by C_2 the ratio between the SFR and the corresponding Q(H) in the equation below

$$\left(\frac{\mathrm{SFR}}{M_{\odot}yr^{-1}}\right) = C_2 \times \left(\frac{Q(H)}{\mathrm{s}^{-1}}\right) \tag{7.2}$$

we collect in Table 7.1 the values of C_2 obtained with our constant SFR models, for different SSPs parameters. C_2 in this table is the value obtained at the steady saturation value of $Q(H)$.

The values of C_2 in Table 7.1 are shown in Figure 7.2 as a function of Z for various values of M_{up}.

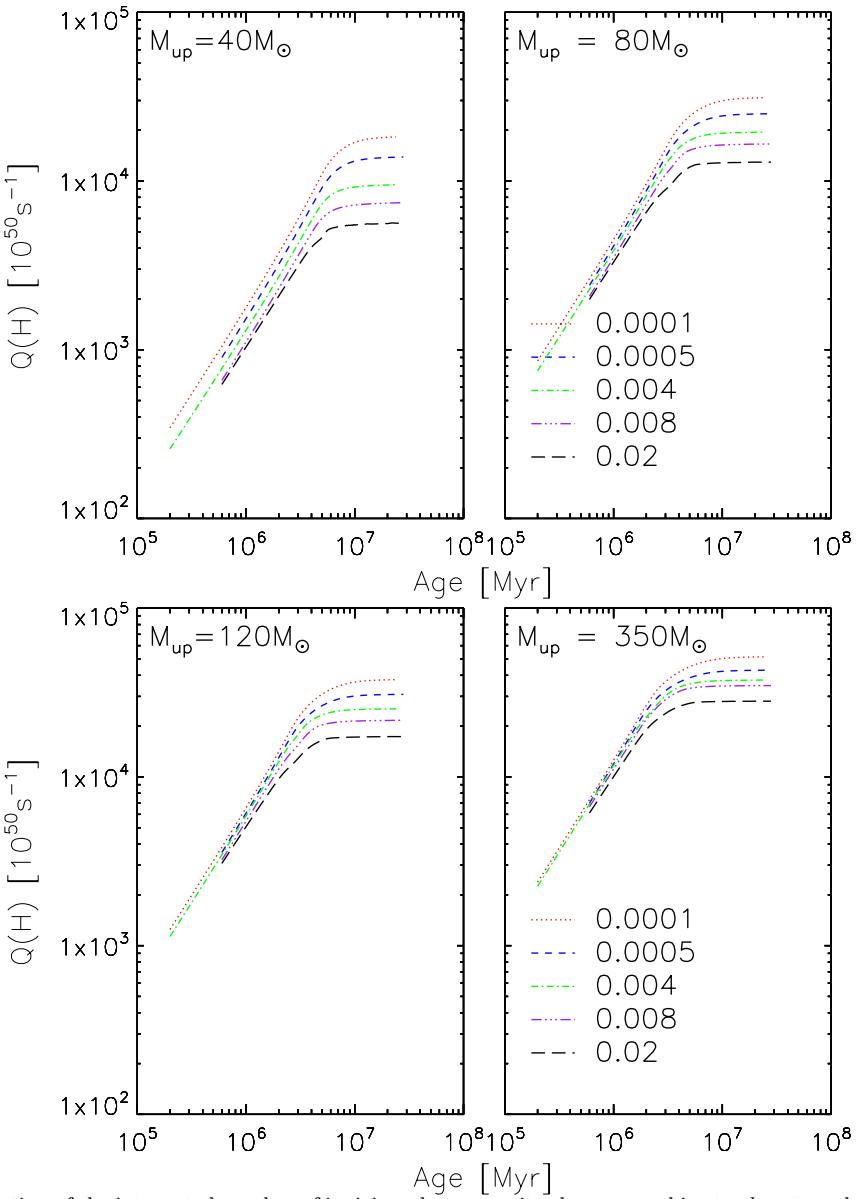

Figure 7.1: Evolution of the integrated number of ionizing photons emitted per second in star-burst models with a constant SFR=10 $M_\odot$/yr. The upper panels are for M_{up} = 40 and 80 $M_\odot$ cases, while the bottom panel for M_{up} = 120 and 350 $M_\odot$. Different line styles represent different metallicities, as indicated.

Table 7.1: Integrated ionization photon luminosity per unit SFR, $Q(H)$/SFR, and the values of the constant $C_2 = SFR/Q(H)$, derived from our starburst models for different metallicities (Z) and upper mass limits.

Z	$\frac{Q(H)/SFR}{\frac{10^{53}/s}{M_\odot/yr}}$	$\frac{\sigma}{\frac{10^{53}/s}{M_\odot/yr}}$	$\frac{C_2}{\frac{M_\odot/yr}{10^{-54}/s}}$
(1)	(2)	(3)	(4)
$M_{up} = 40$			
0.0001	1.740	0.018	5.749
0.0005	1.303	0.012	7.675
0.0040	0.884	0.007	11.31
0.0080	0.679	0.011	14.73
0.0200	0.505	0.035	19.79
$M_{up} = 80$			
0.0001	3.013	0.045	3.319
0.0005	2.415	0.046	4.141
0.0040	1.872	0.023	5.342
0.0080	1.543	0.081	6.482
0.0200	1.201	0.070	8.325
$M_{up} = 120$			
0.0001	3.661	0.055	2.731
0.0005	2.954	0.046	3.385
0.0040	2.394	0.065	4.177
0.0080	2.038	0.081	4.908
0.0200	1.690	0.034	5.918
$M_{up} = 350$			
0.0001	4.863	0.194	2.056
0.0005	4.090	0.144	2.445
0.0040	3.644	0.188	2.744
0.0080	3.384	0.104	2.955
0.0200	2.783	0.065	3.594

Column(1): metallicity. Column(2): production rate of ionizing photons per unit solar mass formed. Column(3): standard deviation of the production rate of ionizing photons per unit solar mass formed. Column(4): calibration constant (C_2) of the SFR-Q(H) relation as given in Equation 7.2.

They can be fitted by a multiple regression relation to provide the following relation between the SFR and the integrated ionizing photon flux -called Q(H) for simplicity- for a constant star forming region of arbitrary Z and M_{up} (in the range tested here):

$$\begin{aligned} \frac{\text{SFR}}{\text{Q(H)}} &= 5.69 \times 10^{-54} \left(\frac{Z}{0.02}\right)^{0.135} \left(\frac{M_{up}}{120}\right)^{-0.42} \times f \\ f &= 10^{0.220/\left(1+120\ \left(\frac{M_{up}}{120}-1/3\right)\right)} \end{aligned} \tag{7.3}$$

For comparison using M_{up}=100 $M_\odot$, as used by Murphy et al. (2012) with the Starburst99 stellar population model with a Kroupa (2001) IMF, we obtain a coefficient of 1.355×10^{53} which is very similar to that derived by Murphy et al. (2012) (1.37×10^{53}).

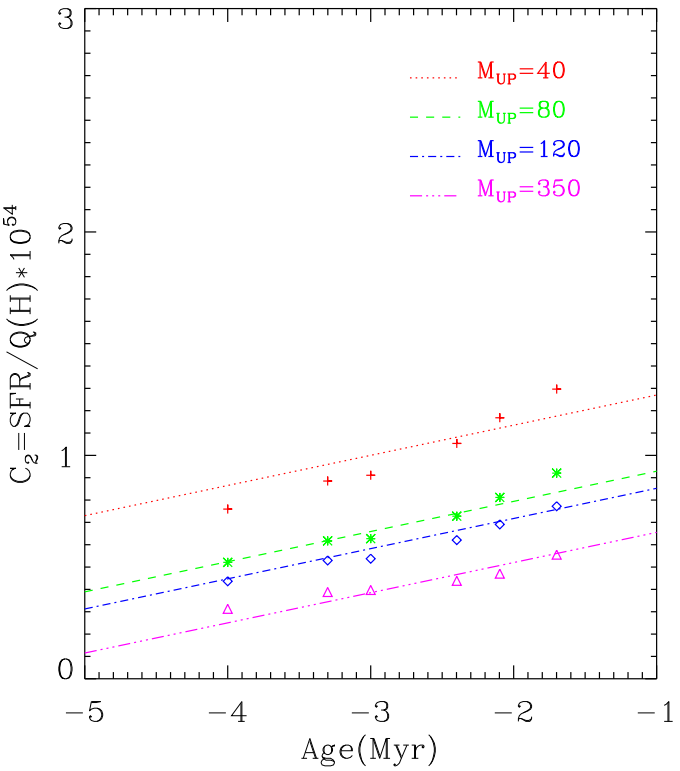

Figure 7.2: Variation of the constant $C_2 = SFR/Q(H)$ (Equation 7.2) with metallicity for different upper mass limits. C_2 is the value averaged over the first 10 Myr of the burst of star formation. Different symbols are used to indicate different values of M_{up} as shown in the figure. A multiple regression fit is given by Equation 7.3

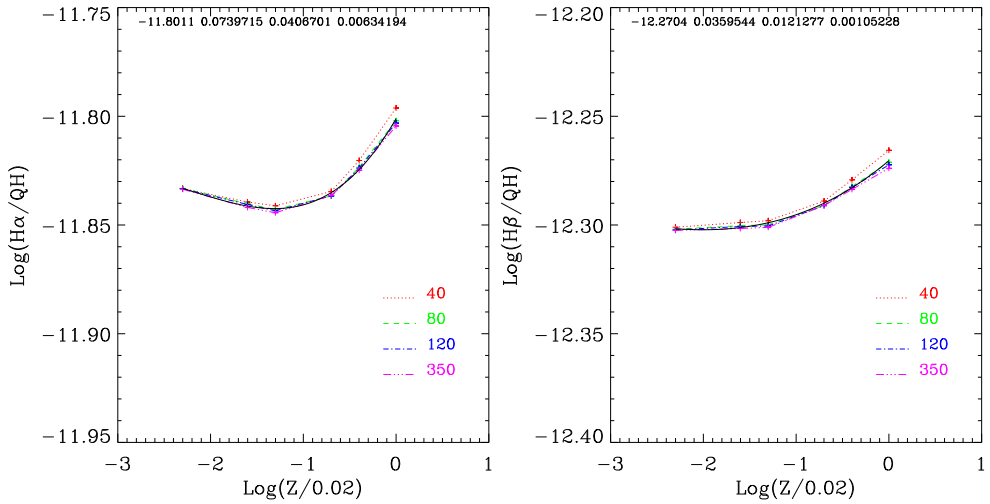

Figure 7.3: Variation of the average ratio $L(H\alpha)$/Q(H) and $L(H\beta)$/Q(H) with metallicity for SSP of different M_{UP} and with age less than 10 Myr. The data are collected in Table 7.2. The black lines are the fitting relations 7.7 and 7.12, respectively.

7.3 SFR – L_{ff} calibration

Eliminating $Q(H)$ in Equation 4.1, using Equation 7.3, we obtain the relation between the SFR and the luminosity of the free-free radio emission for a model with constant star formation rate:

$$\frac{SFR}{M_\odot/yr} = \frac{L_{\rm ff}}{1.7\times10^{27}}\left(\frac{\rm T_e}{10^4{\rm K}}\right)^{-0.45}\left(\frac{\nu}{\rm GHz}\right)^{0.1}\times\left(\frac{Z}{0.02}\right)^{0.12}\left(\frac{M_{up}}{120}\right)^{-0.5} \tag{7.4}$$

By using Equation 4.4 for the T_e in equation 7.4 we have the relation between SFR and free-free continuum luminosity at any frequency and for any value of metallicity and M_{UP} in our SSP library.

We may compare equation 7.4 with the one obtained by Murphy et al. (2012), assuming a Kroupa (Kroupa 2001) IMF with $\rm M_{up} = 100 M_\odot$ and solar metallicity:

$$\frac{\rm SFR}{\rm M_\odot yr^{-1}} = \left(\frac{L_{\rm ff}}{2.17\times10^{27}}\right)\left(\frac{T_e}{10^4{\rm K}}\right)^{-0.45}\left(\frac{\nu}{\rm GHz}\right)^{0.1} \tag{7.5}$$

If, in the Murphy et al. (2012) relation we account that at solar metallicity $\rm T_e$ ∼7400 K, the coefficient at the denominator becomes 1.90×10^{27}. On the other hand if in our equation we account for the lower $\rm M_{up}$ adopted by Murphy, our coefficient becomes 1.88×10^{27}, in very good agreement with that of Murphy et al. (2012).

7.4 SFR -Hα calibration

An equation similar to Equation 4.1 can be obtained for Hα luminosity, by using Equation 5.34 in Osterbrock & Ferland (2006):

$$\frac{L(H\alpha)}{\rm erg\ s^{-1}} = 1.37\times10^{-12}\left(\frac{\rm T_e}{10^4\ K}\right)^{-0.14}\left(\frac{\rm Q(H)}{\rm s^{-1}}\right) \tag{7.6}$$

Since this equation holds for a pure Hydrogen gas we prefer to use our HII region models. We collect all the models younger than 8 Myr and, for each value of the metallicity and M_{UP}, we calculated the average value of the ratios $L(H\alpha)$/Q(H). These ratios are shown in in Table 7.2 and are plotted in the left panel of Figure 7.3. Plus symbols refer to the data with different values of the metallicity and M_{UP} while the lines result from the fit obtained for the different values of the metallicity. In this fit we did not attempt to include the effect introduced by the variation of M_{UP} because, as it may be seen from the figure, it can be neglected. The fitting relation is

$$\mathrm{Log}\frac{\mathrm{L(H\alpha)}}{\mathrm{Q(H)}} = -11.8011 + 0.07397\ \mathrm{Log}\left(\frac{\mathrm{Z}}{0.02}\right) + 0.04067\ \mathrm{Log}\left(\frac{\mathrm{Z}}{0.02}\right)^2 + 0.00634\ \mathrm{Log}\left(\frac{\mathrm{Z}}{0.02}\right)^3 \quad (7.7)$$

The $L(H\alpha)/Q(H)$ ratios shown in Table 7.2 have an average value of $< L(H\alpha)/Q(H) >$=1.481×10^{-12} erg, with a standard deviation of 5.027×10^{-14}. This shows that the dependence on the metallicity is also actually quite small and likely it is smaller than the observational uncertainty of the observational data. We can thus assume that, within a few percent

$$\frac{L(H\alpha)}{\mathrm{erg\ s^{-1}}} = 1.48 \times 10^{-12} \frac{\mathrm{Q(H)}}{\mathrm{s^{-1}}} \quad (7.8)$$

and to a very good approximation we have

$$\frac{L(H\alpha)}{\mathrm{erg\ s^{-1}}} = 2.60 \times 10^{41} \left(\frac{Z}{0.02}\right)^{-0.135} \left(\frac{M_{up}}{120}\right)^{0.42} \frac{SFR}{M_\odot\ yr^{-1}} \quad (7.9)$$

or

$$\frac{SFR}{M_\odot} = 3.84 \times 10^{-42} \left(\frac{Z}{0.02}\right)^{+0.135} \left(\frac{M_{up}}{120}\right)^{-0.42} \frac{L(H\alpha)}{\mathrm{erg\ s^{-1}}} \quad (7.10)$$

The latter calibration is in very good agreement with that of Panuzzo et al. (2003), taking into account that their coefficient, SFR/L(Hα)=6.08 × 10^{-42} must be reduced by the factor 1.39 (see Table 2.1) to account for the larger number of massive stars in our IMF with respect to the Salpeter one adopted by them.

Note that, for purposes of completeness, we show in Table 7.2 also the predicted values of the ratios $Ly\alpha/Q(H)$ though we do not use these ratios in this work.

7.5 SFR − Hβ calibration

In a similar way we may obtain a relation between the Hβ luminosity and the Hydrogen ionising photon luminosity, using Equation 5.34 in Osterbrock & Ferland (2006):

$$\frac{L(H\beta)}{\mathrm{erg\ s^{-1}}} = 4.76 \times 10^{-13} \left(\frac{\mathrm{T_e}}{10^4\ K}\right)^{-0.14} \left(\frac{\mathrm{Q(H)}}{\mathrm{s^{-1}}}\right) \quad (7.11)$$

As in the case of the Hα luminosity we show in Table 7.2 the average values of the ratio $L(H\beta)$/Q(H) obtained by considering our HII region models younger than 8 Myr. These ratios are plotted in the right

Table 7.2: Variation of the ratios $H\alpha/Q(H)$, $H\beta/Q(H)$ and $Ly\alpha/Q(H)$ as a function of metallicities and upper mass limits.

Z	M_{up} $M_\odot$	T_e K	$H\alpha/Q(H)$ $\times 10^{-12}$	$H\beta/Q(H)$ $\times 10^{-13}$	$Ly\alpha/Q(H)$ $\times 10^{-11}$
0.0001	350	24210	1.467	4.983	1.714
0.0001	120	21730	1.468	4.986	1.718
0.0001	80	20530	1.468	4.980	1.719
0.0001	40	17920	1.468	5.000	1.714
0.0005	350	22090	1.439	4.993	1.511
0.0005	120	20350	1.443	5.004	1.524
0.0005	80	19330	1.444	5.008	1.525
0.0005	40	16940	1.447	5.025	1.518
0.0010	350	20510	1.430	4.999	1.430
0.0010	120	19260	1.434	5.007	1.438
0.0010	80	18440	1.436	5.012	1.442
0.0010	40	16370	1.441	5.035	1.443
0.0040	350	15210	1.457	5.116	1.260
0.0040	120	14570	1.457	5.116	1.254
0.0040	80	14180	1.457	5.117	1.244
0.0040	40	13120	1.463	5.141	1.242
0.0080	350	11640	1.497	5.204	1.223
0.0080	120	11370	1.500	5.215	1.221
0.0080	80	11110	1.502	5.221	1.215
0.0080	40	10640	1.512	5.257	1.208
0.0200	350	7663	1.569	5.322	1.213
0.0200	120	7768	1.573	5.342	1.217
0.0200	80	7795	1.577	5.356	1.218
0.0200	40	8081	1.599	5.425	1.221

panel of Figure 7.3. Plus symbols refer to the data with different values of the metallicity and M_{UP} while the lines result from the fit obtained for the different values of the metallicity. Also in this case we did not attempt to include the effect introduced by the variation of M_{UP} because it can be neglected. The fitting relation for Hβ is

$$\mathrm{Log}\frac{\mathrm{L(H}\beta)}{\mathrm{Q(H)}} = -12.2704 + 0.03595\ \mathrm{Log}\left(\frac{\mathrm{Z}}{0.02}\right) + 0.012128\ \mathrm{Log}\left(\frac{\mathrm{Z}}{0.02}\right)^2 + 0.00105\ \mathrm{Log}\left(\frac{\mathrm{Z}}{0.02}\right)^3 \quad (7.12)$$

The $L(H\beta)/Q(H)$ ratios shown in Table 7.2 have an average value of $< L(H\beta)/Q(H) >$=5.120×10^{-013} erg, with a standard deviation of 1.398×10^{-014}. Even in this case the dependence on the metallicity is also small and likely smaller than the uncertainty of the observational data. We can thus assume that, within a few percent

$$\frac{L(H\beta)}{\mathrm{erg\ s^{-1}}} = 5.12 \times 10^{-13} \frac{\mathrm{Q(H)}}{\mathrm{s^{-1}}} \quad (7.13)$$

and to a very good approximation we obtain the following calibartion of the SFR against the Hβ luminosity:

$$\frac{L(H\beta)}{\mathrm{erg\ s^{-1}}} = 9.0 \times 10^{40} \left(\frac{Z}{0.02}\right)^{-0.135} \left(\frac{M_{up}}{120}\right)^{0.42} \frac{SFR}{M_\odot/yr} \quad (7.14)$$

or

$$\frac{SFR}{M_\odot/yr} = 1.1 \times 10^{-41} \left(\frac{Z}{0.02}\right)^{+0.135} \left(\frac{M_{up}}{120}\right)^{-0.42} \frac{L(H\beta)}{\mathrm{erg\ s^{-1}}} \quad (7.15)$$

Equations 7.4, 7.10 and 7.15 are general relations between the SFR and the free-free continuum, the Hα and the Hβ luminosities of star forming regions that includes the dependence on the metallicity of the environment and on the IMF upper mass limit of the stellar populations. They account for the dependence of the number of ionizing photons on the stellar metallicity and M_{up} and on the dependence of gas T_e on the gas metallicity (Equation 4.4). Equations 7.4 shows that if the metallicity of a young stellar population decreases from solar to one tenth solar, the corresponding free-free luminosity increases by about a factor of two. If M_{up} of the population increases by a factor of two the free-free luminosity increases by 50%. The same trend with Z and M_{up} is also noted in the relationships obtained for Hα and Hβ luminosities though their luminosity is somewhat less sensitive to the metallicity than that of the free-free continuum.

7.6 SFR − UV calibrations

Here we show the relation between the SFR and the UV fluxes. We define the FUV and NUV fluxes as:

$$FUV = \nu_{1600} L(1600\text{Å}) \tag{7.16}$$

$$NUV = \nu_{2000} L(2000\text{Å}) \tag{7.17}$$

respectively. We have run constant SFR models at constant metallicity equal to that of the different SSP and we have computed the ratios SFR/FUV and SFR/NUV at different time steps. The results are shown in Figures 7.4 to 7.7. In contrast to what happens for the integrated ionizing photon luminosity of the same models shown in Figure 7.1, the time-scale to reach a stationary situation, characterized by a constant ratio between the SFR and the luminosity, is much longer for the UV fluxes. The ratio declines rapidly and it approaches a constant value only after about 100 Myr. The model values are fitted by polynomial expressions of the kind

$$\begin{aligned} Log\left(\frac{\text{SFR}}{\text{FUV}}\right) &= a_0 + a_1\ t + a_2\ t^2 \qquad t \leq 60\ Myr \\ Log\left(\frac{\text{SFR}}{\text{FUV}}\right) &= b_0 + b_1\ t + b_2\ t^2 \qquad t \geq 60\ Myr \\ Log\left(\frac{\text{SFR}}{\text{FUV}}\right) &= c_0 \qquad\qquad\qquad\ t \geq 100\ Myr \end{aligned} \tag{7.18}$$

and analogous for the NUV band. We adopt two polynomial approximations, one which is valid at young ages where the ratio falls rapidily, and the other that is valid at relatively older ages. The constants of the polynomials, a_0, a_1, a_2, b_0, b_1, b_2 are colected in Tables 7.3 and 7.4 for the case of the FUV and NUV luminosities, respectively. The costant of the last equation, c_0, represents the constant value which approximates the average values above 100 Myr.

At fixed M_{UP}, the variation with metallicity is small. We thus provide also the the average value of c_0 for the different metallicities at each value of M_{UP} (written in the line that indicates the M_{UP} value). Finally at the bottom of each table we also provide the average value of c_0 for the different values of

metallicity and M_{UP} in the table. These values indicate that the accuracy with which the SFR can be estimated without knowledge of Z and M_{UP} is quite good. We remind the reader that this holds only for ages larger than about 100 Myr. At younger ages, in particular below a few tens of Myr, assuming this age independent value could result in an underestimation of the corresponding SFR as large as a factor of two.

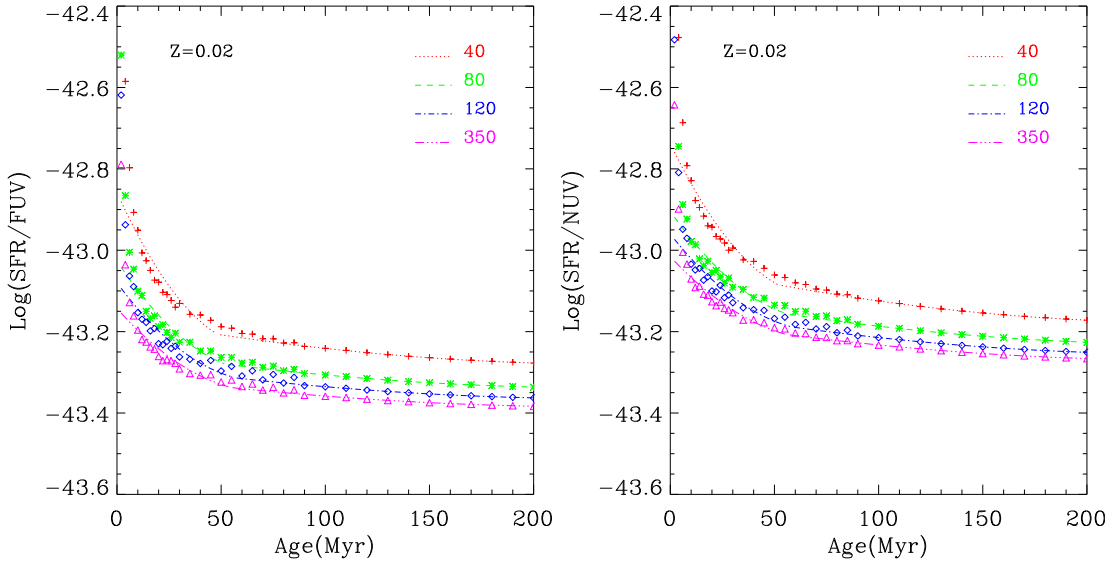

Figure 7.4: Variation of the average ratio SFR/FUV and SFR/NUV with age for SSP of Z=0.02 and different M_{UP} as labelled in the figure. Fitting rleations are in Equation 7.18.

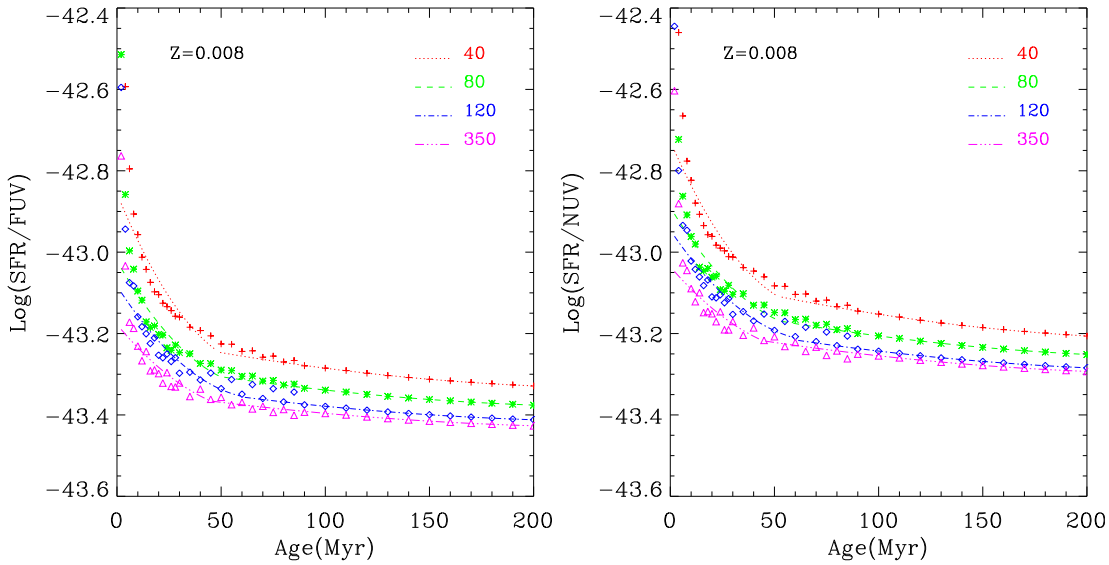

Figure 7.5: Same as 7.4 but for Z=0.008

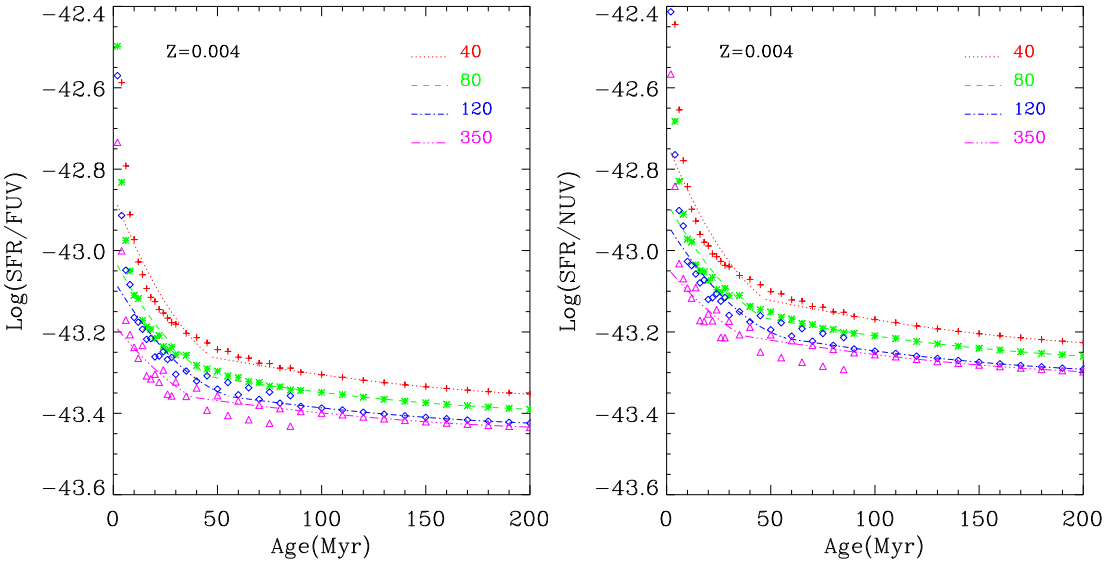

Figure 7.6: Same as 7.4 but for Z=0.004

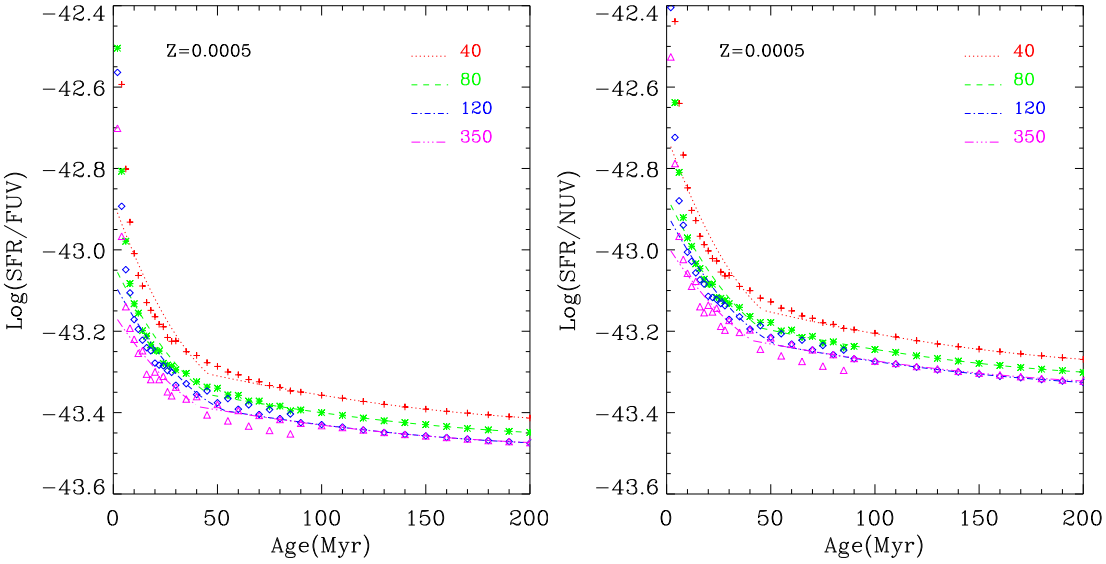

Figure 7.7: Same as 7.4 but for Z=0.0005

Table 7.3: FUV/SFR calibration (Equation 7.18) for different upper mass limits.

		age < 60 Myr			age ≥ 60 Myr		
Z	a_0	a_1	a_2	b_0	b_1	b_2	c_0
SFR/FUV	M_{up}= 40			$< c_0 >$=	-43.364725	±0.055222	
0.00010	-42.83384	-0.01513	1.11988E-004	-43.23158	-0.00147	2.77985E-006	-43.41567
0.00050	-42.88115	-0.01406	1.04742E-004	-43.24968	-0.00133	2.57386E-006	-43.41341
0.00100	-42.87463	-0.01427	1.08613E-004	-43.24732	-0.00126	2.47150E-006	-43.39984
0.00400	-42.86290	-0.01303	9.71259E-005	-43.21183	-0.00116	2.29372E-006	-43.35315
0.00800	-42.85573	-0.01247	9.21757E-005	-43.19760	-0.00110	2.20459E-006	-43.32891
0.02000	-42.85825	-0.01127	8.38875E-005	-43.16438	-0.00097	2.04585E-006	-43.27737
SFR/FUV	M_{up}= 80			$< c_0 >$=	-43.404261	±0.0441	
0.00010	-42.97745	-0.01160	8.40371E-005	-43.27635	-0.00131	2.48204E-006	-43.44009
0.00050	-43.03454	-0.01050	7.65301E-005	-43.30808	-0.00114	2.18316E-006	-43.44855
0.00100	-43.01760	-0.01067	7.79226E-005	-43.30155	-0.00109	2.12877E-006	-43.43412
0.00400	-43.01785	-0.00949	6.91317E-005	-43.26720	-0.00101	1.99946E-006	-43.39027
0.00800	-43.02154	-0.00897	6.51505E-005	-43.26416	-0.00094	1.88565E-006	-43.37608
0.02000	-43.02641	-0.00778	5.57780E-005	-43.24247	-0.00081	1.70796E-006	-43.33646
SFR/FUV	M_{up}= 120			$< c_0 >$=	-43.432073	±0.0418	
0.00010	-43.01444	-0.01073	7.64473E-005	-43.30711	-0.00123	2.31910E-006	-43.45967
0.00050	-43.07832	-0.00959	6.85590E-005	-43.34413	-0.00107	2.08590E-006	-43.47496
0.00100	-43.06581	-0.00962	6.91450E-005	-43.33608	-0.00100	1.96741E-006	-43.45841
0.00400	-43.07097	-0.00858	6.15562E-005	-43.31305	-0.00092	1.81222E-006	-43.42426
0.00800	-43.08318	-0.00791	5.65462E-005	-43.31160	-0.00084	1.69435E-006	-43.41214
0.02000	-43.07988	-0.00690	4.91043E-005	-43.27623	-0.00075	1.58599E-006	-43.36300
SFR/FUV	M_{up}= 350			$< c_0 >$=	-43.438473	±0.031753484	
0.00010	-43.08790	-0.00912	6.49805E-005	-43.30852	-0.00118	2.22504E-006	-43.45593
0.00050	-43.15567	-0.00786	5.54750E-005	-43.34563	-0.00106	2.11078E-006	-43.47366
0.00100	-43.16108	-0.00746	5.25342E-005	-43.33947	-0.00096	1.88678E-006	-43.45667
0.00400	-43.17965	-0.00653	4.64040E-005	-43.33024	-0.00086	1.69668E-006	-43.43409
0.00800	-43.17777	-0.00613	4.34642E-005	-43.33399	-0.00078	1.57088E-006	-43.42692
0.02000	-43.14313	-0.00575	4.03708E-005	-43.30427	-0.00069	1.45803E-006	-43.38357
All Z and M_{up}				$< c_0 >$=	-43.409883	±0.033568930	

Table 7.4: NUV/SFR calibration (Equation 7.18) for different upper mass limits.

	age	<	60	Myr	age	≥	60	Myr
Z	a_0		a_1	a_2	b_0		b_1	b_2	c_0
SFR/NUV	M_{up}=		40		$< c_0 >$=		-43.2332	±0.0388	
0.00010	-42.66225		-0.01520	1.11249E-004	-43.05782		-0.00164	3.06895E-006	-43.26440
0.00050	-42.71838		-0.01412	1.04150E-004	-43.08611		-0.00148	2.82672E-006	-43.26922
0.00100	-42.71805		-0.01437	1.08801E-004	-43.08914		-0.00139	2.66125E-006	-43.26091
0.00400	-42.73472		-0.01250	9.21080E-005	-43.06269		-0.00132	2.53461E-006	-43.22657
0.00800	-42.72735		-0.01172	8.40748E-005	-43.04879		-0.00129	2.51147E-006	-43.20622
0.02000	-42.73786		-0.01061	7.53252E-005	-43.02953		-0.00119	2.40046E-006	-43.17206
SFR/NUV	M_{up}=		80		$< c_0 >$=		-43.2692	±0.0283	
0.00010	-42.80296		-0.01172	8.38474E-005	-43.10032		-0.00147	2.74201E-006	-43.28483
0.00050	-42.86859		-0.01064	7.68319E-005	-43.13720		-0.00133	2.56565E-006	-43.30103
0.00100	-42.85862		-0.01081	7.84202E-005	-43.14157		-0.00121	2.30190E-006	-43.29176
0.00400	-42.88076		-0.00918	6.59875E-005	-43.11588		-0.00116	2.21498E-006	-43.25951
0.00800	-42.88971		-0.00841	5.89768E-005	-43.11743		-0.00110	2.14181E-006	-43.25167
0.02000	-42.90448		-0.00727	4.95115E-005	-43.10730		-0.00099	1.99920E-006	-43.22629
SFR/NUV	M_{up}=		120		$< c_0 >$=		-43.2955	±0.0265	
0.00010	-42.83668		-0.01093	7.68604E-005	-43.12794		-0.00142	2.69643E-006	-43.30364
0.00050	-42.90959		-0.00979	6.94259E-005	-43.17709		-0.00120	2.26607E-006	-43.32606
0.00100	-42.90512		-0.00978	6.97465E-005	-43.17755		-0.00112	2.12431E-006	-43.31604
0.00400	-42.93278		-0.00829	5.86281E-005	-43.16197		-0.00105	2.00264E-006	-43.29187
0.00800	-42.94602		-0.00754	5.20522E-005	-43.16330		-0.00099	1.92870E-006	-43.28448
0.02000	-42.96022		-0.00648	4.38995E-005	-43.14106		-0.00092	1.86004E-006	-43.25116
SFR/NUV	M_{up}=		350		$< c_0 >$=		-43.2982	±0.0189	
0.00010	-42.90943		-0.00936	6.61187E-005	-43.13159		-0.00132	2.44152E-006	-43.29757
0.00050	-42.98632		-0.00807	5.64489E-005	-43.17945		-0.00115	2.17510E-006	-43.32239
0.00100	-43.00187		-0.00758	5.30657E-005	-43.17813		-0.00107	2.04624E-006	-43.31152
0.00400	-43.04048		-0.00620	4.29806E-005	-43.17574		-0.00098	1.87967E-006	-43.29780
0.00800	-43.03581		-0.00589	4.05095E-005	-43.18004		-0.00093	1.80875E-006	-43.29338
0.02000	-43.01579		-0.00546	3.63885E-005	-43.16497		-0.00085	1.71840E-006	-43.26646
All Z and M_{up}					$< c_0 >$=		-43.2740	±0.0302	

7.7 SFR−Bolometric Luminosity calibrations

From the models used for the SFR-FUV calibration relation we derive also the calibration of the SFR with respect to the bolometric luminosity. The time evolution of the SFR/BOL ratio is shown in Figure 7.8, as a function of Z and M_{up}. Like the SFR/UV ratios, also the SFR/BOL ratio converges to a stationary value in a $\sim$ 100 Myr timescale. Though the bolometric luminosity is generally not known, there are methods to derive estimates of the bolometric luminosity, e.g. using the FUV luminosity and the FIR luminosity. In the same way as for the FUV luminosity, we derive a polinomyal approximation that holds for different M_{UP} values and for two different age ranges:

$$\begin{aligned}
\mathrm{Log}\left(\frac{\mathrm{SFR}}{\mathrm{BOL}}\right) &= a_0 + a_1\ t + a_2\ t^2 \qquad t\ \leq\ 60\ Myr \\
\mathrm{Log}\left(\frac{\mathrm{SFR}}{\mathrm{BOL}}\right) &= b_0 + b_1\ t + b_2\ t^2 \qquad t\ \geq\ 60\ Myr \\
\mathrm{Log}\left(\frac{\mathrm{SFR}}{\mathrm{BOL}}\right) &= c_0 \qquad\qquad\qquad\ t\ \geq\ 100\ Myr
\end{aligned} \tag{7.19}$$

where SFR is in $M_\odot$/yr and BOL is the bolometric luminosity of the starburst in erg/s. The coefficients of the polinomial are listed in Table 7.5 which has the same format of Table 7.3.

Table 7.5: BOL/SFR calibration (Equation 7.19) for different upper mass limits.

		age < 60 Myr			age ≥ 60 Myr		
Z	a_0	a_1	a_2	b_0	b_1	b_2	c_0
M_{up}=	40			$< c_0 >$=	-43.677216	±0.046967057	
0.00010	-43.30380	-0.00970	6.86451E-005	-43.53201	-0.00151	2.69748E-006	-43.72715
0.00050	-43.29489	-0.00998	7.15918E-005	-43.53989	-0.00138	2.54224E-006	-43.71393
0.00100	-43.28635	-0.01015	7.43185E-005	-43.54381	-0.00121	2.11147E-006	-43.70234
0.00400	-43.27693	-0.00969	7.00830E-005	-43.52966	-0.00108	1.85582E-006	-43.67146
0.00800	-43.26604	-0.00943	6.85165E-005	-43.50207	-0.00115	2.18838E-006	-43.64547
0.02000	-43.24252	-0.00880	6.33691E-005	-43.47503	-0.00100	1.81272E-006	-43.60294
M_{up}=	80			$< c_0 >$=	-43.741529	±0.044980833	
0.00010	-43.47519	-0.00678	4.67442E-005	-43.64359	-0.00096	1.23937E-006	-43.78697
0.00050	-43.47423	-0.00686	4.77263E-005	-43.62727	-0.00120	2.28246E-006	-43.77728
0.00100	-43.46617	-0.00692	4.81429E-005	-43.62771	-0.00111	2.12658E-006	-43.76505
0.00400	-43.45748	-0.00668	4.71595E-005	-43.61444	-0.00100	1.89880E-006	-43.73780
0.00800	-43.43660	-0.00651	4.57825E-005	-43.60048	-0.00089	1.63501E-006	-43.71456
0.02000	-43.40757	-0.00606	4.24468E-005	-43.56905	-0.00075	1.27726E-006	-43.66751
M_{up}=	120			$< c_0 >$=	-43.778823	±0.045621606	
0.00010	-43.54869	-0.00549	3.60019E-005	-43.67695	-0.00115	2.05714E-006	-43.82461
0.00050	-43.54736	-0.00553	3.70135E-005	-43.69183	-0.00089	1.41315E-006	-43.81218
0.00100	-43.54202	-0.00556	3.73679E-005	-43.68552	-0.00093	1.71302E-006	-43.80461
0.00400	-43.52138	-0.00560	3.81792E-005	-43.66348	-0.00093	1.84915E-006	-43.77595
0.00800	-43.50131	-0.00545	3.69954E-005	-43.65372	-0.00078	1.41702E-006	-43.75345
0.02000	-43.46621	-0.00516	3.52549E-005	-43.60975	-0.00071	1.24572E-006	-43.70214
M_{up}=	350			$< c_0 >$=	-43.819663	±0.049671653	
0.00010	-43.65302	-0.00421	2.78240E-005	-43.74979	-0.00084	1.26055E-006	-43.86727
0.00050	-43.65057	-0.00420	2.78790E-005	-43.73686	-0.00099	1.98449E-006	-43.85584
0.00100	-43.64134	-0.00437	2.94098E-005	-43.74795	-0.00080	1.45758E-006	-43.84985
0.00400	-43.62340	-0.00421	2.88614E-005	-43.72540	-0.00070	1.21211E-006	-43.81623
0.00800	-43.60299	-0.00411	2.75990E-005	-43.70776	-0.00067	1.19781E-006	-43.79379
0.02000	-43.54059	-0.00413	2.75180E-005	-43.64655	-0.00072	1.40478E-006	-43.73500
All Z and M_{up}				$< c_0 >$=	-43.754307	±0.060494393	

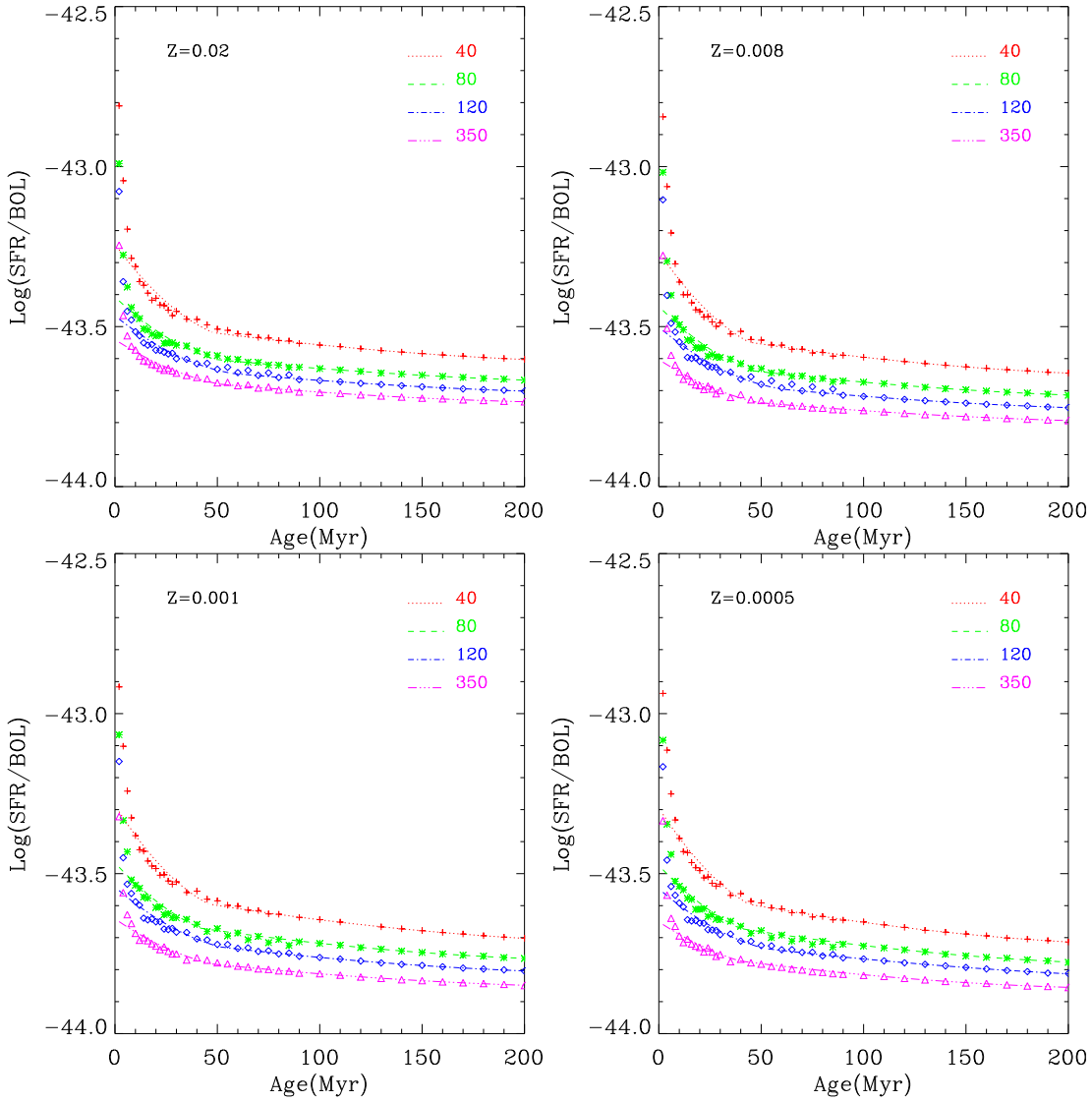

Figure 7.8: Variation of the average ratio SFR/BOL with age for SSP of Z=0.02 and different M_{UP} as labelled in the figure. Fitting relations are in Equation 7.19.

7.8 Star formation rates calibrations for mildly obscured starbursts

7.8.1 Far-UV, Far-Infrared and Bolometric Luminosity of Star Forming Galaxies

We have seen while discussing the attenuation of the star forming regions in NGC6946 (Section 6.3) that at low star formation rates and, in any case when the attenuation is low, the FIR luminosity (between 3 μm and 1000 μm) is not a robust indicator of the star formation rate. Since, instead, the SFR correlates tightly with the bolometric luminosity of the starburst, there have been many attempts in literature to obtain an estimate of this unknown quantity from the observed ones. For example, in absence of attenuation, the bolometric luminosity of a starburst almost coincides with its ultraviolet luminosity. In the case that the starburst is superimposed to an older population this may not be true because, as shown in our fits of the star forming region, a non negligible fraction of the UV luminosity may come from the intermediate age population, especially in the near UV spectral region. What is still strongly correlated with the starburst activity is the luminosity in the far UV, because the intermediate/old population cannot compete with the emission from the young massive stars in this wavelength range (unless the SFR is so low that the contribution from the hot post-AGB stars becomes important). In this section I wish to see if the models that I have computed may help in defining a robust relation that may provide an estimate of the bolometric luminosity of the starbursts, from observed quantities. The problem of deriving the bolometric luminosity of a starburst has been already studied in literature. For example there have been attempts to derive the attenuation in the FUV spectral region from the slope of the UV continuum (Calzetti et al. 1994; Meurer et al. 1999; Reddy et al. 2010, 2012). If the FUV and the FIR luminosities are both known, it is conceivable that a combination of the two quantities could provide a good estimate of the bolometric luminosity, because what is seen in the FIR has been simply taken from the far UV (e.g. Buat et al. 1999). Here we have to discard the first option because, in our star forming regions we cannot determine the UV slope, given that we have already seen that this is affected by the emission of an underlying intermediate age population. However this problem could be much more general than thought, because when the star formation lasts for more than a few tens of Myr, then the near UV begins to be affected by the intermediate age populations, which do not contribute to emission lines, radio emission and far UV. This could be a common situation at high redshifts where the starburst activity could be more prolonged in time than in the local Universe, because of the larger gas reservoirs. Thus we resort to our models to clarify this point. In Figure 7.9 we compare the bolometric, far-UV and far-IR luminosities of all the starburst model we have computed ($\simeq$30000 models). In the upper left panel of Figure 7.9 we plot the FUV luminosity against the bolometric luminosity of the model (L_{BOL}). The bolometric luminosity range corresponds to a range of star formation rates of a fraction to a few solar masses per year, which is a typical value for our star forming regions. The attenuation of the best fit models, already discussed in the previous sections, is not high which also could be a typical condition of young star forming regions at high redshifts. We see from the panel that the FUV luminosity may

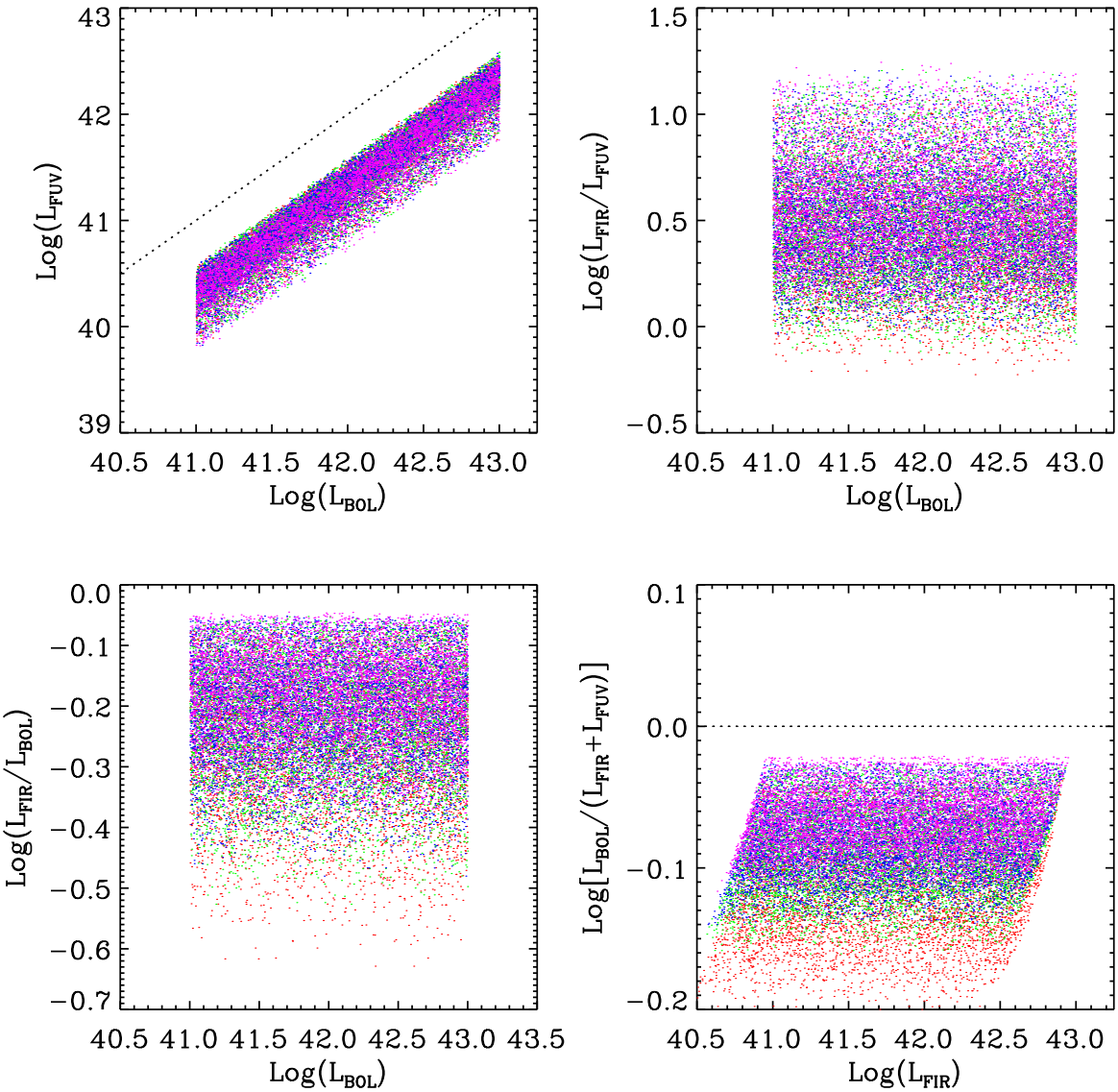

Figure 7.9: Plots of FUV, FIR/FUV, FIR/BOL and BOL/(FIR+FUV) luminosities versus bolometric luminosity for our $\sim$ 30000 starburst models. All luminosities are in erg/s. The FIR luminosity is the 3 to 1000 μm integral of the SED.

change by about one order of magnitude, for a given value of the bolometric luminosity. The largest value the FUV luminosity can attain is about half the bolometric luminosity. In the upper right panel we plot the ratio between the FIR and the FUV luminosities against the bolometric one. Here we see that the highest value of the ratio L_{FIR}/L_{FUV} is near ten while the lowest one is near unity. In the latter case the FIR luminosity is similar to the FUV one and the object is not heavily extinguished. There are also a few models where this ratio is as low as 0.5, indicating that the attenuation is low. At the same time, at the high side, the ratios are not as large as those found in very luminous ar ultra luminous infrared sources, where they can reach values of hundreds and thousands. In summary the attenuation of our models is small to mild. The third plot, in the lower left panel, shows the ratio between the FIR and bolometric luminosities, against the bolometric one. From this plot we see that at maximum the FIR luminosity may be around the 75% of the total one. The minimum ratio, instead, is around 25% though in the majority of the models this ratio is above 50%. We stress here that an attenuation of 50% corresponds to a $\tau \sim 0.7$ which, considering that it should refer to UV wavelengths, is not large. In any case we have all the elements to check whether the bolometric luminosity can be obtained by straightly summing up the FUV and FIR luminosities. This is shown in the fourth panel, in the lower right side of the figure. The panels depict the variation of the ratio $L_{BOL}/(L_{FUV}+L_{FIR})$ against L_{FIR}. In this panel we use the latter luminosity because it is an observable quantity. As can bee seen from the panel, the simple sum $L_{FUV}+L_{FIR}$ is not a bad estimator of the bolometric luminosity, thinking that at maximum it is offset by not more than a factor of 30% in a range of FIR (or bolometric) luminosity of about two order of magnitude. However this consideration refers to a model luminosity and it does not include the possible accuracy with which the FIR and FUV luminosities can be obtained. Furthermore it is not well assessed how the FUV luminosity defined as $\nu L(\nu)$ at λ =1500$\mathring{A}$ may trace the bolometric one in an un-attenuated galaxy. For this reason we have searched for a simple linear combination of the FUV and FIR luminosities that may be possibly improve upon the previous result. By looking at our models we have found that the relation

$$L^o_{BOL} = L_{FIR} + C \times L_{FUV} \tag{7.20}$$

can be an optimal relation to derive the bolometric luminosity This is shown in Figure 7.10. In this figure we plot the ratio between pseudo bolometric luminosity L^o_{BOL}, obtained by combining the FIR and FUV luminosities of the models, and the corresponding model bolometric luminosity, that we know by construction. The figure is divided in two regions by the solid thick line. In the lower region we plot the simple ratio plotted in the lower right panel of Figure 7.9. In this case the pseudo luminosity is obtained by Equation 7.20 by assuming a constant C=1. We note that in this figure the abscissa is the logarithm of the ratio between the FIR and FUV luminosities. The four populated strips are the models computed for different values of M_{UP}. Starting from the bottom we have the models with M_{UP}=40 $M_\odot$ (red points) then those with M_{UP}=80 $M_\odot$ (green points), those with M_{UP}=120 $M_\odot$ (blue points) and finally those with M_{UP}=350 $M_\odot$ (pink points). These models exactly correspond to the ones shown in the previous figure, but the abscissa compress them to the shown areas. It can be seen that the pseudo bolometric luminosity can be within the 30% of the bolometric luminosity of the model, as already discussed. In the

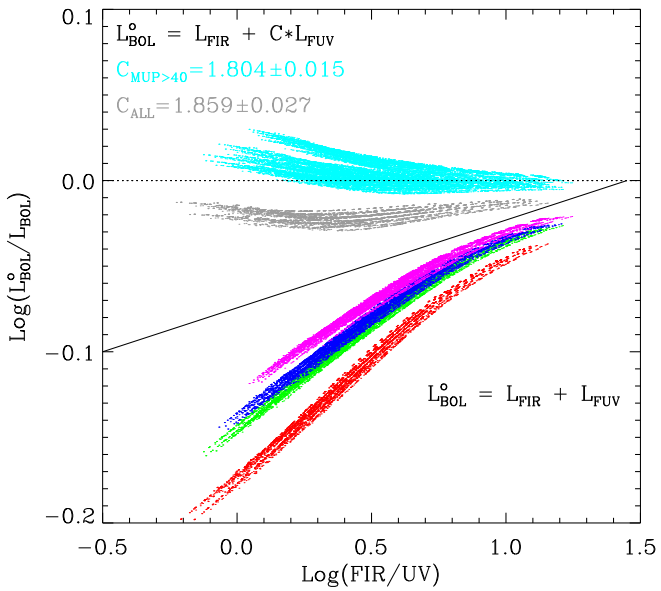

Figure 7.10: Ratio of the pseudo-bolometric luminosity $L^o_{BOL} = L_{FIR} + C \times L_{FUV}$ to the true L_{BOL} versus the FIR to UV luminosity ratio for the same models as in Figure 7.9. The sequences of models below the thick solid black line have $C = 1$, and the different colored strips corresponds to $M_{UP} = 40$ (red), 80 (green), 120 (blue), 350 (pink) $M_\odot$. Above that line, the gray dots are models for all M_{UP} values with $C = 1.859$, the cyan dots are all models with $M_{UP} > 40$ $M_\odot$ with $C = 1.804$. This latter calibration allows to estimate L_{BOL} from observationally assessable luminosities.

second region, on top of the solid thick black line we plot the pseudo luminosity that we have obtained by changing the constant C in order to force a the ratio on the ordinate to have a mean value of 1. Here we have plotted the models with M_{UP}=40 $M_\odot$ in gray and all the other models in cyan. In the models with M_{UP}=40 $M_\odot$ the pseudo-bolometric luminosity is poorly defined also in the case of C=1 (the red strip) and the models remain separated even when we try to force the ratio to 1. If we consider all the models, the value of the constant in Equation 7.20 that forces an average value of 1 is

$$C_{ALL} = 1.859 \qquad \sigma_{ALL} = 0.027 \tag{7.21}$$

where σ_{ALL} is the standard deviation around the average value L^o_{BOL}/L_{BOL}=1, for all the models. If we consider only models with M_{UP} >40 $M_\odot$, then we obtain a slightly different value for the constant,

$$C_{M_{UP}>40} = 1.804 \qquad \sigma_{M_{UP}>40} = 0.015 \tag{7.22}$$

where $\sigma_{M_{UP}>40}$ is the standard deviation for the models with IMF upper mass limit $M_{UP} > 40$ $M_\odot$. We note that in the latter case the standard deviation of the ratios becomes almost half the previous one. Thus our models suggest that, at least for mild attenuated sources, the linear combination of FIR and FUV luminosities indicated in Equation 7.20 should provide an estimate of the bolometric luminosity of the star-burst with an internal accuracy as low as 3%. This level of accuracy does not depend on the underlying upper limit of the IMF (most likely it does not depend on the adopted IMF). This method of deriving the bolometric luminosity of a starburst should be quite independent from the presence of an underlying older stellar population because both the FUV and the FIR luminosities should be dominated by the star formation activity. We recall that our models have been computed for a large number of initial parameters, as listed in Table 6.1. They account for different geometries between dust and stars, different gas fractions in the galaxy and in dense clouds, different stellar escape times from these clouds, different clouds optical depths and different starburst ages. As such, they should reproduce many of the realistic conditions that can be found in nature and thus the calibration obtained by Equation 7.20 should be quite robust. We note another important aspect that is related to Equation 7.20. It is well known that fitting the FUV SED of a star-burst galaxy in the framework of a panchromatic fit is one of the more difficult tasks. Indeed, while the FIR and radio SED can be easily fitted, the panchromatic fit require a more thorough physical information to be provided to the models. We have seen that our galaxies could be easily fitted on one spectral region but the models were off in other spectral regions. If Equation 7.20 is verified to be of general use, then it would be very easy to derive the bolometric luminosity of the starburst and from there a correct estimate of the star formation rate. In other words the panchromatic SED helped us to find a relation of general utility that could be used to skip the difficult task of repeating the fits on large data-sets.

With the pseudo-bolometric luminosity so derived, the SFR can be obtained from Equation 7.19. However again there is an uncertainty introduced by the age of the star forming object.

For example, assuming the constant values for all the metallicities and M_{UP} values in Table 7.5, that is suited for the advanced phases of the starbursts, and the constant C=1.859 in Equation 7.20, we obtain

$$\frac{SFR}{M_{\odot}/yr} = 1.76 \times 10^{-44} \, (L_{FIR} + 1.859 \times L_{FUV}) \tag{7.23}$$

which should provide a good estimate ($\leq$10%) of the star formation rates in star forming mildly obscured galaxies. Of course this value would not be good for our very young objects. For our regions we should instead use the value of BOL/SFR corresponding to very young ages, which is provided by an average of the constant a_0 in Table 7.5. In this case Equation 7.23 becomes

$$\frac{SFR}{M_{\odot}/yr} = 3.2 \times 10^{-44} \, (L_{FIR} + 1.859 \times L_{FUV}) \tag{7.24}$$

and the derived SFR would be about two times the one derived with Equation 7.23, and in agreement with the SFR derived in our young starburst regions. Said in another way, unless one has another way to determine the age of the starburst, adopting Equation 7.23 should provide a good fit for the large majority of the objects. There will be an underestimate of about a factor of two in the case of very young objects. Note that using the FIR alone as an indicator of SFR could be significantly worse than that, because the FIR luminosity could significantly underestimate the bolometric one for a large fraction of the starburst lifetime.

7.8.2 Star formation rates from radio emission

Radio emission escape from the galaxy almost unattenuated. The only source of attenuation could be free-free absorption $\tau_{\rm ff}$ which however decreases rapidly at increasing frequency as given below

$$\tau_{\rm ff} = 3.014 \times 10^{-2} (\frac{T_e}{10^4 K})^{-1.5} (\frac{\nu}{GHz})^{-2} (\frac{EM}{pc \; cm^{-6}}) \; G_{ost}(\nu, T_e) \tag{7.25}$$

where EM is the emission measure given as the integral of $N_e N_i$ along the line-of-sight ($EM = \int_{los} N_e N_i ds$), N_e and N_i = N(HII) + N(HeII) are the local electron and ion densities, respectively. $G_{ost}(\nu, T_e)$ is as given in Equation 4.3.

The star formation rate indicators based on radio observations should thus be relatively safe from the problems of attenuation or from those related to the fact that the FIR luminosity is not representative of the bolometric one. To get these indicators from our models, we plot in Figure 7.11 the calibration constants C(ν)=SFR/F$_\nu$ at ν=1.4, 4.9, 8.5 and 33.0 GHz, in units of M$_\odot$yr^{-1}/10^{-28}erg s^{-1}Hz^{-1}, against the corresponding radio frequencies, for both the star-bursting regions and M100 and for the different cases of M_{up}. A multiple regression that fits all the starburst data as a function of ν and M$_{UP}$ is provided by Equation 7.27.

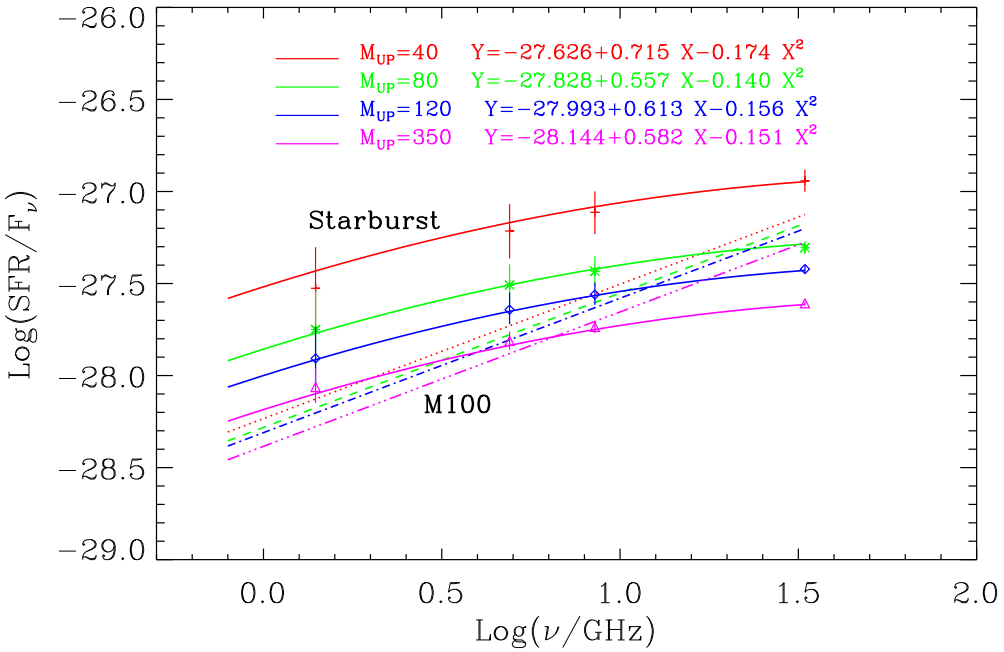

Figure 7.11: Calibration constants C(ν)=SFR/L$_\nu$, in units of M$_\odot$yr^{-1}/10^{-28}erg s^{-1}Hz^{-1}, at ν=1.4, 4.9, 8.5 and 33.0 GHz, for the star-bursting regions (solid lines) and M100 (3-dot-dashed lines). The different cases of M_{up} are coded by different colours as indicated in the labels. The vertical bars show the effect of changing the metallicity in the range of our starburst models. The labels also provide fitting relations for the individual starburst cases.

Concerning the dependence on M_{up}, there is a clear difference between the young starburst and the normal star formation regime in the sense that, in the former case the constant is about a factor of three larger independently from the frequency. Again this effect is due to the young age of the starburst regions coupled with the dependence of the thermal radio emission on M_{up}. Indeed for the normal SFR regime the dependence on M_{up} becomes significant only at high frequencies, where the thermal emission start dominating. From the fits we derive the following general relations between SFR (in $M_{\odot}yr^{-1}$) and radio luminosity (in erg $s^{-1}Hz^{-1}$). For the very young starbursts, we have at any frequency between 1.4 GHz and 33 GHz, to better than 10%:

$$\log(\frac{\mathrm{SFR}}{\mathrm{L}\nu})^{\mathrm{tot}} = -28.00 + 0.613\log(\nu) - 0.156[\log(\nu)]^2 \ - \log(\frac{\mathrm{M_{up}}}{120})(0.7 - 0.65\log(\frac{\mathrm{M_{up}}}{120})]) \tag{7.26}$$

or

$$\log(\frac{\mathrm{SFR}}{\mathrm{L}\nu})^{\mathrm{tot}} = -27.88 + 0.52\log(\nu/1.4) - 0.140[\log(\nu/1.4)]^2 \ - \log(\frac{\mathrm{M_{up}}}{120})(0.7 - 0.65\log(\frac{\mathrm{M_{up}}}{120})]) \tag{7.27}$$

where, in both equations, ν is in GHz.

For M100 and for the evolved starbursts we have for the total radio emission

$$\log(\frac{\mathrm{SFR}}{\mathrm{L}\nu})^{\mathrm{tot}} = 0.73\ \log(\nu) - 0.16\ \log(\frac{\mathrm{M_{up}}}{120}) - 28.31 \tag{7.28}$$

and for the non-thermal radio emission, we have

$$\log(\frac{\mathrm{SFR}}{\mathrm{L}\nu})^{\mathrm{nth}} = 0.58\ \log(\nu) - 0.43\ \log(\frac{\mathrm{M_{up}}}{120}) - 28.33 \tag{7.29}$$

Relations similar to Equations 7.27, 7.28 and 7.29 above were provided by Murphy et al. (2011), assuming Kroupa IMF (with $M_{up} = 100$), solar metallicity and a constant SFR over a timescale of 100 Myr. For the total radio emission

$$\left(\frac{SFR}{L\nu}\right)^{tot}_{Mur} = 10^{-27}\left(2.18\nu^{-0.1}(\frac{T_e}{10^4})^{0.45} + 15.1\nu^{-0.85}\right)^{-1} \tag{7.30}$$

and for non-thermal radio emission

$$\left(\frac{SFR}{L\nu}\right)^{nth}_{Mur} = 10^{-27}(6.64 \times 10^{-29}\nu^{0.85}) \tag{7.31}$$

These relations are in between our relations in 7.27 and 7.28, running only about $\leq$ 20% lower than our one for normal star forming galaxies, below 33 GHz. However at frequencies higher than 33 GHz the difference grows rapidly and at 100 GHz our values are ∼40% and ∼200% higher than that of Murphy et al. (2011) for starburst and normal galaxies, respectively. Interestingly, the relation derived by Schmitt et al. (2006b) with Starburst99, assuming a Salpeter IMF (with $M_{up} = 100$), solar metallicity

and a continuous SFR of 1 M$\odot yr^{-1}$

$$\left(\frac{SFR}{L\nu}\right)^{tot}_{Sch} = 10^{-27}(8.55\nu^{-0.8} + 1.6\nu^{-0.1}) \tag{7.32}$$

agrees well with our relations in 7.27 and 7.28 at frequencies from about 33 GHz to 100 GHz. Above 100 GHz the dust emission contribution becomes dominant.

Chapter 8

Summary and Future Work

The study of the properties of galaxies to possibly map their formation and evolutionary paths is an active research field both from the observational and the theoretical side. Enormous observational efforts are continuously devoted to map the SED of nearby and high-z galaxies over all the wavelength range, by surveying the sky with both ground and space-borne instruments. Surveys in different spectral ranges have uncovered galaxies with drastically different activity levels and energy budgets, symptoms of underlying disparate basic physical properties. It is these basic properties that one aims to uncover in order to get insights on the complex behaviour of mass assembly and recycling in galaxies.

The fundamental tools necessary to analyze and to infer theoretical insights from these data are spectral synthesis models. These models are first of all based on the availability of a complete library of stellar evolution models, that homogeneously cover the range of stellar masses, metallicities, and evolutionary phases that contribute to the integrated SED of a galaxy. From these and a library with a complete coverage of the stellar parameters, the integrated SED of single stellar populations, SSP, can then be computed. SSP SED libraries covering a wide range in age and metallicity are the necessary inputs required to build the integrated spectra of galaxies. The stellar radiation in galaxies interacts with gas and dust of the ISM from the emission sites to the outskirts. Stellar processes such as CCSN explosions combine with the galactic magnetic field to give rise to an important non-thermal radio component. Therefore, to compare the full observed SEDs it is important to account at very least for the main processes producing radiation and affecting the radiation path, i.e. stars, ionized gas nebulae for the main recombination lines and continuum emission, CCSN for the non-thermal radio emission, and the interaction between stellar radiation and dust grains in the ISM.

This thesis has focused on a major revision and extension of the SSP models based on the PARSEC stellar models, to include also the effects of ionized nebulae (line and continuum emission) and of the non-thermal emission due to the explosion of massive stars. Another important aspect, dictated by the different claims on the universality of the IMF, and its possible differences between star bursting galaxies and more quiescent star forming objects, is that we have also considered the dependence of the results

on the upper mass limit of the IMF. The final new SSP libraries are computed for M_{up}= 40, 80, 120 and 350 $M_{\odot}$ and for five different values of metallicities Z= 0.0001, 0.0005, 0.004, 0.008 and 0.02.

These new SSP models are then used in combination with the radiative transfer code GRASIL to include also the stellar extinction by dust and the ensuing IR emission, and therefore to provide a panchromatic UV-to radio SED modelling. We have calibrated and applied this model to observations and discussed the implications and the retrieved information. We have carried out a critical investigation of the effect of Z, M_{up} and star formation regime (star bursting versus normal star forming) on SFR and dust attenuation properties of star forming galaxies. This has allowed us to provide a consistent set of SFR calibrations, that are explicitly dependent on Z and M_{up} and also on the age of the starburst, at wavelengths ranging from UV to radio. The latter parameter is particularly important in the analysis of star-bursting galaxies because, while the age should be a quantity that is derived from the fit, it is important to stress that different SFR indicators prove different characteristic time-scales that only a panchromatic population synthesis tool can put into a coherent picture. For the most common indicators we have also provided their time dependences in form of analytical approximations.

Below we summarize in some details each step of the work performed and the main results of this thesis.

8.1 Summary of the results

Chapter 2 In this Chapter, I focused on the computation of the integrated stellar spectra of SSPs for 5 different metallicities and 4 different IMF upper mass limits.

I have adopted the recently updated Padova stellar evolutionary tracks PARSEC (Bressan et al. 2012), that are widely used by the astronomical community, to obtain a new complete SSP SED library. Among the major changes implemented in PARSEC, of particular mention are the new models of massive stars which supersede the old widely used ones (from Padova) that were computed more than twenty years ago. With respect to other existing more updated stellar evolution models (e.g. Eggenberger et al. 2008; Decressin et al. 2009; Chieffi & Limongi 2013) while it has to be noted that the PARSEC models do not yet account for rotation (that is being implemented), it is important to stress that they provide a homogeneous sets of models over a wide range of metallicities and masses. None of the existing sets of evolutionary tracks have been computed from very low to very massive stars (M_{up}=350 $M_{\odot}$). Even more important, the PARSEC models account in a homogeneous way for the most recent recipes for the mass-loss mechanism, in particular the enhancement arising when the luminosity of the star approaches the Eddington limit.

Among other things, this has important consequences on the range of masses involved in the CCSN explosions that contribute to the non thermal radio emission. The adopted stellar atmospheric spectral library used to assign a stellar SED along each isochrone is the one by Chen et al. (2015), that homogenizes different existing libraries for low, intermediate and massive stars. I discussed the important role played by age, metallicity and IMF on the ionizing photons emitted per unit solar mass of a SSP, as well as the integrated spectra (Figure 2.4).

Chapter 3 In this Chapter, I analyzed and modeled how the integrated stellar spectra of SSPs computed in Chapter 2 are modified by the presence of an ionized medium surrounding a young stellar population. The aim here is that of obtaining a robust estimate of the intensities of the main recombination lines and of the nebular continuum emission, which are relevant in improving the diagnostic capabilities of our population synthesis code. We do not aim instead to perform a detailed analysis of the dependence of a large ensemble of emission lines on the critical parameters of the HII nebulae, nor to generate models suited for the determinations of element abundances or to be used as diagnostics of the ISM conditions.

I used the photoionisation code CLOUDY to model and analyze how the integrated spectra of SSP used as central sources of a nebula are modified by the presence of the surrounding medium ionised by the most massive stars. I computed the intensities of some selected recombination and collisionally excited lines (as listed in Table 3.1) as a function of age of the SSP, again for the same five different metallicities and four different M_{up} mentioned above. The free-free nebular continuum computed by CLOUDY is the source of the thermal radio emission component, for which we accounted for the explicit dependence of the electron temperature on M_{up} and metallicity. Finally, the emission lines and nebular continuum resulting from CLOUDY were self consistently added to the original SSP integrated spectra.

Chapter 4 In this Chapter, I presented our model for the non-thermal radio emission to be included in the SSP, following the work by Bressan et al. (2002), and I discussed the characteristics and behaviour of the thermal and non thermal radio emission in the new SSPs.

For the free-free emission, I was able to show that the electron temperature T_e (usually assumed to have a constant value of 10^4 K in the literature) is a strong function of the metallicity, decreasing by more than a factor of two from 0.0005 $Z_\odot$ to $Z_\odot$ and that the upper mass limit has a much lower impact on T_e. I further provided a fitting relation between T_e, Z and M_{up} which can be used with confidence almost independently of M_{up}.

For the non-thermal part, I followed the model by Bressan et al. (2002), and accounted for the recent advances in the theory of massive stars evolution and supernova explosions. These advances concern the range of masses that goes into producing CCSN explosion and thereby contributing to the synchrotron emission, and have led to heavily revise the standard assumption that all stars above $8M_\odot$ explode as core-collapse supernovae.

The models for massive stars in PARSEC include the most recent findings on the efficiency of mass loss rate. This was previously overestimated by significant factors, leading to pre-supernova masses significantly smaller than those predicted by the most recent calculations. Also, with the most recent models, intermediate mass stars in the 6 $M_\odot$ to 8 $M_\odot$ range do not explode as CCSN, since they evolve toward oxygen-neon super AGB stars. Finally, recent works on CCSN explosion criteria have indicated that the final collapse produces a CCSN only if the initial mass of the star is smaller than about M = 30 $M_\odot$. Stars more massive than this either undergo a failed SN or will enter the pair instability phase, followed by either a complete unbinding of the star or by the collapse to a black hole. The two-fold effect of this distinction between failed and successful SN is that the expected supernovae rate should be smaller (as supported by the cosmic SN rate problem) and that the first SN appears after $\sim$ 7 Myr

from the formation of the star cluster, much later than the case when stars more massive than 8 $M_{\odot}$ are all considered to explode as CCSN. Coincidentally, the free-free emission abruptly fades away at about 7 Myr. The non-thermal emission from SSP lasts up to about 35–38 Myr, depending on the metallicity (Figures 4.8 and 4.9). Finally the non-thermal emission is not sensitive to M_{up} as long as M_{up} is larger than the assumed threshold of $M = 30 M_{\odot}$ for failed SN.

At this stage, the new SSP SED libraries include the stellar component, the HII component, emission lines and nebular continuum including the thermal radio emission, and the non-thermal radio component.

Chapter 5 In this Chapter, I have used our SSP libraries as an input to the radiative transfer model GRASIL in order to account for the interaction of the stellar radiation with dust in the ISM. I have thus extended our modelling also to the IR spectral region. By providing an input star formation history (we used the CHE_EVO code) and our SSP libraries, we have first discussed the effects of some of the main adjustable parameters of GRASIL on the final SED (burst age t_{sb}, escape time of young stars from their birth cloud t_{esc}, radius of the molecular cloud r_{mc}, gas mass fraction f_{gas} and core radius of the cirrus for a King Profile geometry r_{diff}). The next step was to calibrate the non-themal radio emission, and to test the performance of our new panchromatic model to reproduce observed SEDs, including the q-parameter. To these aims I have considered the nearby normal spiral galaxy M100, that has well sampled UV to radio observations available, and fitted its SED separately with M_{up}=40, 80, 120 and 350 $M_{\odot}$. From the best fit SED, I obtained a CSSN rate to non thermal radio luminosity ratio ($E^{NT}_{1.49}$) larger by a factor of 1.4 than the value previously obtained by Bressan et al. (2002). This calibration is our reference value for all subsequent fits. As an indication of a good calibration, our average value of $q_{1.4GHz}$ is 2.40, and the individual values for each case of upper mass limit are in line with the observed value of 2.35 $\pm$ 0.15. It was interesting to see how the various physical properties derived from the best fit models varies with the upper mass limits. For example while the bolometric luminosity is almost unchanged by construction (the fitted SED remain the same), the FIR luminosity increases by about the 14 % from the lower to the larger value of M_{up}. The SFR averaged over the last 100 Myr decreases by a factor of $\sim$ 6 % by increasing M_{up} in the same range.

Chapter 6 In this Chapter I have focused on the performance of our model to reproduce the spectral energy distribution of young star forming regions. These regions represent an interesting workbench for our model because they may represent typical conditions that can be found in the early phases of galaxy evolution.

After examining the literature for the best suited candidates with a well sampled UV-radio SED and at least one of the recombination emission line, I adopted the star-bursting regions of the well studied nearby (6.8 Mpc) galaxy NGC 6946 as our work bench. These regions, with a typical size of $\sim$0.8 kpc, have been extensively studied and show a large thermal over non-thermal radio emission ratios.

To model these regions, I generated a large library of more than 30000 starburst models by varying six GRASIL main adjustable parameters for each case of M_{up}. For all cases of M_{up}, I was able to reproduce the far-UV attenuation, the attenuation in the Hα line, the emission in the mid- and far-infrared and

the intensity and slope of the emission at radio frequencies. All best fit SEDs are characterised by a flatter radio slope and a higher q-parameter (ranging from $\sim$ 2.4 to$\sim$ 2.7) than is the case in a normal star forming galaxy. From these best fit models, it is possible to derive a wide range of galaxy properties but in this work I concentrated on the SFR and dust attenuation properties. I presented and discussed separately the resulting best fit SEDs (Figures 6.3 to 6.19) of the nine star bursting regions of NGC 6946, which were all fairly well reproduced by using any of the four IMF upper mass limits, and all with the same calibration constant value for the non-thermal component fixed in Chapter 5.

I also investigated the attenuation curves of the galaxies studied in this work, in particular their dependence on the galaxy type, i.e. starburst vs. normal regime, and also the effects of using different M_{up}. From our attenuation curves (Figures 6.4 to 6.20), we saw that, while in the steady star forming galaxy M100, the attenuation in the recombination lines Hα and Hβ is significantly higher than that in the surrounding continuum, by a factor of 4 on average, this is not true for the star bursting regions where this factor is not larger than 1.3. The fact that, in starburst galaxies, the attenuation in the lines is significantly larger than that in the surrounding continuum is well known and it is a manifestation that young stars are more dust enshrouded than older stars. Instead the fact that in normal star forming galaxies this effect is even larger is at first glance suprising. However it can be easily explained by thinking that, on one side the attenuation in the line must be similar to that in the far-UV, because the originating radiation comes from the same physical sites, rich in young star forming regions. On the other, the contribution of the old and much less extinguished populations in the optical continuum is relatively more important in normal star forming galaxies than in star-bursting galaxies (and even more so if the regions are very young) and thus the difference between the attenuation at Hα and in the nearby continuum is larger in normal galaxies.

The relative attenuation of star-bursts is very similar for the different M_{up} cases, in spite of the different properties of the models used in each case of M_{up}. Furthermore, the attenuation curves of the modelled star-bursting regions of NGC 6946 have R_V values that are roughly twice that of the Calzetti et al. (2000) curve. This also reflects the effects of the age-dependent attenuation. I also provided relations between the attenuation at 1600 A and the ratio, FIR/F$_{1600}$ which can be relevant at high-z in estimating the intrinsic FUV flux (hence the SFR using the SFR-FUV calibration discussed in Chapter 7).

The star forming regions of NGC6946, being young and dominated by free-free emission, are also a possible site to check for the effects of the upper mass limit of the IMF. I this searched for a direct way to determine the IMF upper mass limit from our best fit SED models to these regions. In doing so, I investigated the evolution of the radio emission slope (in particular between 33 GHz - 1.4 GHz) against starburst age and I considered also much older burst ages (up to 200 Myr) than those of the star forming regions in NGC6946 studied in this work (<20 Myr).

I found the interesting trend that at ages younger than $\sim$ 30Myr, this slope is more dependent from the age than from M_{up}. This means that, at these young ages, the possibility to discriminate the best M$_{up}$ from the best fits is challenged by a significant degeneracy between M_{up} and the age of the burst. This is what we find for the star bursting regions studied in this work, i.e. that all regions can be well

fitted by models computed with different values of M_{up}. Of course the derived parameters, as the average SFR and the corresponding SFR indicators show a strong dependence on M_{up}, contrary to the case of M100. This may be explained by considering that in M100 the star formation has reached the stationary condition where as many stars enter the evolutionary phase that characterize a given SFR indicator, as those that exit this phase. Thus in the case of M100 the radio emission is dominated by non-thermal emission (even at 33 GHz) and this component does not depend on M_{up}. At the same time the FIR emission has important contribution from stars less massive than M_{up} and this also may allow for an accommodation of different M_{up} values in the fit. Indeed the only case that is really excluded in the fit of M100 is that computed with M_{up}=350 $M_{\odot}$ because it produces an evident excess of thermal radio emission.

Coming back to the radio slope, we see that above $\sim$ 30Myr it becomes constant and shows a significant dependence on M_{up}. This the radio slope method to check for the upper mass limit of the IMF should work in star-burst regions characterized by an almost constant SFR continuing for more than about a few tens of Myr. Actually, such continuous starbursting regions with ages above $\sim$ 30Myr are difficult to be found in the local universe. Instead, the early phases of galaxy evolution at high-z redshift should be excellent sites to find prolonged burst of star formation (e.g. up to 1Gyr, Tacconi et al. 2010; Mancuso et al. 2016, 2017; Lapi et al. 2017a) due to the large gas fractions. Motivated by this finding I searched in literature for radio data on high redshift star forming galaxies and I have found that the radio slope was already measured in a sample of about 50 sub-millimetre galaxies (Thomson et al. 2014). The radio slopes in the rest-frame frequency interval between 1.4GHz and 610 MHz are found to range between -1.4 to about 0 (Figure 6.26) with a clear peak at $<\alpha>=<\delta ln(F_{\nu})/\delta ln(\nu)>=-0.79\pm$ 0.06 and a typical standard deviation for the individual objects of $\sigma = 0.15$. A simple preliminary comparison with the predicted value for our models, (Figure 6.27) indicates that these sub-millimeter galaxies are consistent with a family of objects drawn from models with a Kennicutt IMF with M_{up} $\sim$100, which is very similar to the Chabrier (2003) IMF. This very preliminary result is extremely important in view of the important debate on the universality of the IMF, and in particular on very recent evidence (Romano et al. 2017) that in star-burst galaxies a top-heavy IMF should be preferred.

To check the ability of our models to distinguish between the different M_{up} using the radio slope as a strong signature of the differences, I also ran a simple simulation where starburst models are assigned an age uniformly distributed from zero to maximum ages ranging from 50 to 200 Myr, assuming an gaussian error with $\sigma = 0.1$ for the individual objects. The histograms of the distributions of radio slopes for 500 objects drawn from models with different M_{up} (different panels in Figure 6.28) show that the different values of M_{up} give rise to different families of models with slopes that peak at different values. This effect becomes more pronounced as the maximum ages increases. If this test is feasible, it would be the first direct test, to the best of our knowledge, on the upper range of the IMF across the universe. In this context, our model will be extremely relevant in interpreting the results of the forth-coming SKA telescope which will provide us with unprecedented sensitivity, observations at high-redshift, where we expect to find galaxies that have maintained a burst with a $\sim$ 1 Gyr timescale, and at very high redshifts where the first galaxies formed.

Chapter 7 In this Chapter we have provided analytical relations for the SFR as a function of observed luminosities in different bands, each band having its own caveats and different timescales of the involved physical processes. We stress the effects of possible differences in the typical timescales of the different SFR indicators should be kept into account when using these relations. Furthermore, the differences in the star formation rate (SFR) estimated by different authors in the literature are mainly ascribed to differences in the input physics of the stellar evolutionary model, atmosphere model and the adopted IMF. These differences are often neglected when applying these relations, despite the importance of the SFR calibrations in high-redshift studies where we encounter systems with a wide range of metallicities and possibly upper mass limits different from those in the local universe.

We provided two sets of SFR calibrations that can be used to convert attenuation-corrected and dust-unaffected luminosities at various bands (UV - radio) to SFR estimates. The first are analytical relations, all functions of M_{up} and metallicity, obtained from our SSPs and relate SFR with intrinsic UV-optical luminosities (in the absence of dust) while the second are obtained from the best fit model SEDs (and from our starburst models library in some cases) of the galaxies studied in this work: the extranuclear star-bursting regions of NGC 6946 with sub-solar metallicity and the normal star-forming galaxy M100 with near-solar metallicity.

We first provide relations, all as a function of M_{up} and metallicity, between SFR and luminosities at thermal radio, and at the intrinsic Hα, Hβ, FUV (1600$\sim$A) and NUV (2000$\sim$A) bands. For the FUV and NUV with a much longer saturation timescale than the radio and recombination lines, we provided calibrations in two age bins for these bands only, one at $\leq$ 60 Myr and the other above $\geq$60 Myr. Additionally, we provided a SFR - bolometric luminosity relation at the above mentioned age bins. This is particularly useful in young systems which are not strongly attenuated and where the FIR alone is only a fraction of the bolometric luminosity. In addition to the SFR-radio calibrations, we also provided, both for the normal star forming galaxy M100 and for the NGC6946 star bursting regions, a single relation that can be used at frequencies between 1.4 - 33 GHz. These relations were remarkably in good agreement with those of Murphy et al. (2011).

The presence of dust introduces modifications to the SED through attenuation in the UV-optical wavelengths and re-emission in the infra-red. We have stressed that the use of the FIR luminosity (L_{FIR}) as a star formation indicator depends on the level of attenuation. At low attenuation, it becomes unreliable, but the bolometric luminosity (L_{BOL}) gets closer to the observed FUV luminosity L_{FUV} (at $\lambda = 1600\ A$). A robust relation that may provide an estimate of L_{BOL} of the starbursts from observed quantities would be extremely useful in this context. To this aim, we utilised our starburst model library to study the variation of L_{FUV} and L_{FIR} with L_{BOL} (Figure 7.9).

The L_{FIR}/L_{FUV} log ratio ranges from $\sim$ 1 to 10 showing that the the attenuation of our models is small to mild. With the aim of using the sum $L_{FIR}+L_{FUV}$ as an estimator of the bolometric luminosity, we provided a fitting relation between L_{BOL}, L_{FIR} and L_{FUV} with an offset not greater than 30% in a range of FIR (or bolometric) luminosity of about two orders of magnitude. The proportionality constant in this relation can be used either for all the four M_{up} values or for M_{up} above $40M_{\odot}$ with the standard deviation of the latter case (1.5%) almost twice that of the former case (2.7%). We remind that there is

an uncertainty introduced by the age of the star forming objects when the above relations are used to estimate the bolometric luminosity and in turn the SFR. As an example, the difference in calibrations obtained using the relations we provided for advanced starbursts and that obtained using relations for very young objects amounts to a factor of ~ 2. Nevertheless, this factor could be significantly worse than that if FIR is used alone as an indicator of SFR because the FIR luminosity could significantly underestimate the bolometric one for a large fraction of the starburst lifetime. Furthermore, such relations could be used to derive a statistical SFR estimate for a sample of objects which are a priori known to populate an entire range of ages.

8.2 Future Work

While being already a thorough update of our population synthesis tools, the work I have been doing is still far from being complete. I will try in the followings to outline three possible areas of improvement where I have already started to work on.

8.2.1 Extending the data sample for calibration

The results presented in this thesis (in particular those concerning star formation and dust attenuation properties) have been obtained from a panchromatic analysis of only a few galaxies, the normal star-forming galaxy M100 that has been used to calibrate the model for non thermal radio emission, and the star-bursting regions of NGC6946, that have been used to check the overall performance in the star-burst regime. To increase the significance of our results and the confidence of the model I am currently extending our investigation to a large sample of nearby galaxy. For this purpose, I concentrate on the SIRTF Nearby Galaxy Survey (SINGS) Kennicutt et al. (2003) which is a comprehensive infrared imaging (at infrared, visible, and ultra- violet wavelengths) and spectroscopic survey of 75 nearby galaxies with distances less than ≤ 30 Mpc. Dale et al. (2007, 2012) published UV-to-radio broad-bands SEDs for the SINGS galaxies. The listed data comprises the FUV($1500\mathring{A}$) and NUV ($2300\mathring{A}$) filters of GALEX Gil de Paz et al. (2007), 2MASS data for J, H, and Ks Jarrett et al. (2003), IRAC and MIPS data for the filters centred on 3.6, 4.5, 5.8, 8.0, 24, 70, and $160\mu m$ Dale et al. (2005). I already complemented the radio data of Dale et al. (2007) with that of Tabatabaei et al. (2017) who provided multi- wavelength observations at 1.4 GHz, 4.8 GHz, 8.5 GHz, and 10.5 GHz for the KINGFISH (Key Insights on Nearby Galaxies; a Far-Infrared Survey with Herschel) sample of nearby galaxies (Kennicutt et al. 2011). For the final sample selection I also require the presence of the FUV flux, the Hα measurement and at least one photometric observation in the radio band. This criterium is required to ensure that we may fully exploit our panchromatic synthesis tool. I found that 50 out of the full 75 galaxies meet the above criterion. In Figure 8.1, we show the morphological type and metallicity as given by Kennicutt et al. (2003) for the full sample and in Table 8.1 we list their basic properties.

No	Galaxy	Type	Distance (Mpc)	M_B (mag)	(Hα + [NII]) log ergs cm^{-2}s^{-1}	[NII]/Hα	12+log(O/H) (Average)	L(Hα) (log ergs s^{-1})
(1)	(2)	(3)	(4)	(5)	(6)	(7)	(8)	(9)
1	NGC0024	SAc	7.3 ±2.3	-17.31 ±0.69	-11.87 ±0.04	0.37 ±0.03	8.6 ±0.2	39.82
2	NGC0337	SBd	22.4 ±2.3	-20.09 ±0.24	-11.43 ±0.03	0.23 ± . . .	8.51 ±0.06	41.33
3	NGC0584	E4	20.1 ±1.9	-19.92 ±0.22	. . .	. . .	8.75 . . .	. . .
4	NGC0628	SAc	7.3 ±1.4	-19.6 ±0.43	-10.84 ±0.04	0.34 ±0.05	8.69 ±0.01	40.87
5	NGC0855	E	9.73 ±0.76	-17.01 ±0.2	-12.23 ±0.04	0.19 ±0.01	8.55 ±0.09	39.83
6	NGC0925	SABd	9.12 ±0.17	-19.24 ±0.11	-11.1 ±0.7	0.2 ±0.07	8.52 ±0.01	40.89
7	NGC1097	SBb	17.1 ±2.3	-21.21 ±0.31	-10.95 ± . . .	0.69 ±0.41	8.78 ±0.01	41.18
8	NGC1266	SB0pec	30.0±2.3	-18.89 ±0.19	. . .	. . .	8.59 . . .	40.17[d]
9	NGC1291	SB0_a	10.8 ±2.3	-20.64 ±0.47	. . .	. . .	8.86 . . .	40.55[a]
10	NGC1316	SAB0	21.5 ±1.7	-22.49 ±0.2	. . .	. . .	9.15 . . .	. . .
11	NGC1377	S0	25.0 ±2.3	-18.85 ±0.22	. . .	. . .	8.59 . . .	39.03[d]
12	NGC1404	E1	20.8 ±1.7	-20.73 ±0.21	. . .	. . .	8.88 . . .	. . .
13	NGC1482	SA0pec	23.2 ±2.3	-18.76 ±0.24	-11.8 ±0.05	0.69 ±0.01	8.53 ±0.1	40.59
14	NGC1512	SBab	11.8 ±2.3	-19.32 ±0.43	-11.66 ±0.1	0.34 ±0.2	8.84 ±0.08	40.47
15	NGC1566	SABbc	20.4 ±2.3	-21.45 ±0.26	-10.88 ±0.08	0.62 ±0.06	8.99 . . .	41.49
16	NGC1705	SA0pec	5.1 ±0.6	-15.65 ±0.27	-11.5 ±0.02	0.09 ± . . .	8.12 ±0.05	40.05
17	NGC2403	SABcd	3.13 ±0.14	-18.93 ±0.14	-10.25 ±0.04	0.22 ±0.05	8.57 ±0.01	40.81
18	HoII	Im	3.39 ±0.2	-16.71 ±0.16	-11.27 ±0.04	0.12 ±0.07	7.93 ±0.12	39.91
19	M81DWA	I	3.55 ±0.26	-11.7 ±0.19	. . .	. . .	7.49 . . .	35.9[a]
20	DDO053	Im	3.56 ±0.25	-13.61 ±0.18	-12.43 ±0.12	0.02 ±0.01	7.8 ±0.1	38.83
21	NGC2798	SBapec	26.2 ±2.3	-18.97 ±0.22	-11.84 ±0.06	0.36 ±0.08	8.69 ±0.05	40.97
22	NGC2841	SAb	14.1 ±1.5	-20.67 ±0.25	-11.64 ±0.22	0.61 ±0.08	8.88 ±0.02	40.42
23	NGC2915	I0	3.78 ±0.45	-15.85 ±0.28	-11.95 ±0.05	0.14 ±0.01	8.11 ±0.1	39.31
24	HoI	IABm	3.84 ±0.46	-14.94 ±0.28	-12.44 ±0.05	0.08 ±0.08	7.82 ±0.09	38.87
25	NGC2976	SAcpec	3.56 ±0.38	-17.16 ±0.25	-11.19 ±0.06	0.36 ±0.01	8.67 ±0.04	39.89
26	NGC3049	SBab	23.9 ±2.3	-18.71 ±0.23	-11.93 ±0.07	0.4 ±0.01	8.82 ±0.01	40.77
27	NGC3031	SAab	3.55 ±0.13	-20.22 ±0.13	-10.32 ±0.05	0.55 ±0.08	8.7 ±0.01	40.61
28	NGC3034	I0	3.89 ±0.25	-19.36 ±0.17	. . .	. . .	8.82 ±0.02	41.07[a]
29	HoIX	Im	3.7 ±0.7	-13.98 ±0.42	-13.07 ±0.14	0.04 ±0.02	8.56 ±0.08	38.22
30	M81DWB	Im	5.3 ±1.3	-14.21 ±0.54	-12.86 ±0.05	0.05 ±0.03	8.01 ±0.11	38.74
31	NGC3190	SAapec	26.4 ±1.3	-20.4 ±0.15	-12.68 ±0.05	1.53 ±0.2	8.82 . . .	40.24
32	NGC3184	SABcd	11.1 ±1.9	-19.87 ±0.38	-11.12 ±0.05	0.52 ±0.05	8.83 ±0.01	40.82
33	NGC3198	SBc	13.68 ±0.5	-19.71 ±0.13	-11.4 ±0.04	0.3 ±0.02	8.62 ±0.02	40.89
34	IC2574	SABm	4.02 ±0.41	-16.9 ±0.24	-11.23 ±0.07	0.05 ±0.02	8.05 ±0.12	40.13
35	NGC3265	E	23.2 ±2.3	-18.39 ±0.24	-12.28 ±0.07	0.53 ±0.01	8.63 ±0.1	40.29
36	Mrk33	Impec	22.9 ±2.3	-17.85 ±0.24	-11.7 ±0.01	0.27 ± . . .	8.63 ±0.02	41.05
37	NGC3351	SBb	9.33 ±0.39	-19.38 ±0.14	-11.24 ±0.08	0.65 ±0.03	8.9 ±0.01	40.41
38	NGC3521	SABbc	10.1 ±2.3	-20.65 ±0.5	-10.85 ±0.04	0.56 ±0.01	8.7 ±0.02	40.97
39	NGC3621	SAd	6.55 ±0.18	-19.5 ±0.12	-10.55 ±0.04	0.4 ±0.07	8.53 ±0.01	41.03
40	NGC3627	SABb	9.38 ±0.35	-20.45 ±0.13	-10.74 ±0.05	0.55 ±0.05	8.66 ±0.17	41.03
41	NGC3773	SA0	11.9 ±2.3	-16.81 ±0.43	-11.99 ±0.07	0.23 ± . . .	8.68 ±0.03	40.22
42	NGC3938	SAc	13.4 ±2.3	-19.84 ±0.39	-11.25 ± . . .	0.42 ±0.25	8.74 . . .	40.94
43	NGC4125	E6pec	23.9 ±2.8	-21.26 ±0.27	. . .	. . .	8.95 . . .	. . .
44	NGC4236	SBdm	4.45 ±0.45	-18.0 ±0.24	. . .	. . .	8.45 . . .	40.34[a]
45	NGC4254	SAc	16.5 ±0.6	-20.85 ±0.13	-10.89 ±0.04	0.45 ± . . .	8.79 ±0.01	41.46
46	NGC4321	SABbc	14.32 ±0.46	-20.81 ±0.12	-11.06 ±0.07	0.43 ±0.01	8.84 ±0.02	41.18
47	NGC4450	SAab	16.5 ±0.6	-20.24 ±0.13	-12.21 ±0.04	0.51 ±0.31	8.8 . . .	40.09
48	NGC4536	SABbc	14.45 ±0.27	-19.75 ±0.11	-11.38 ±0.03	0.45 ±0.09	8.6 ±0.06	40.85
49	NGC4552	E	15.92 ±0.81	-20.33 ±0.15	. . .	. . .	8.81 . . .	. . .
50	NGC4559	SABcd	10.3 ±2.3	-19.69 ±0.5	-10.97 ±0.05	0.28 ±0.15	8.55 ±0.01	41.08
51	NGC4569	SABab	16.5 ±0.6	-21.03 ±0.13	-11.53 ±0.22	0.99 ±0.06	8.92 . . .	38.98
52	NGC4579	SABb	16.5 ±0.6	-20.79 ±0.13	-11.48 ±0.01	0.62 ±0.37	8.88 . . .	40.71
53	NGC4594	SAa	9.33 ±0.34	-20.76 ±0.13	. . .	. . .	8.88 . . .	. . .
54	NGC4625	SABmpe	9.2 ±2.3	-16.8 ±0.55	-12.03 ±0.06	0.52 ±0.01	8.7 ±0.12	39.74
55	NGC4631	SBd	7.62 ±0.14	-19.73 ±0.11	-10.55 ±0.06	0.28 ±0.06	8.43 ±0.1	41.24
56	NGC4725	SABabp	11.91 ±0.33	-20.42 ±0.12	. . .	. . .	8.73 ±0.1	41.36[b]
57	NGC4736	SAab	5.2 ±0.43	-19.89 ±0.21	-10.72 ±0.06	0.71 ±0.01	8.66 ±0.03	40.34
58	DDO154	IBm	4.3 ±0.89	-14.43 ±0.46	-12.76 ±0.05	0.05 ±0.03	7.78 ±0.07	38.66
59	NGC4826	SAab	7.48 ±0.69	-20.25 ±0.22	-11.15 ±0.11	0.72 ±0.02	8.87 ±0.07	40.22
60	DDO165	Im	4.57 ±0.4	-15.59 ±0.21	-12.91 ±0.1	0.08 ±0.05	7.84 ±0.08	38.54
61	NGC5033	SAc	14.8 ±2.3	-20.12 ±0.35	-11.23 ±0.09	0.48 ±0.29	8.66 ±0.02	41.0
62	NGC5055	SAbc	7.8 ±2.3	-20.23 ±0.65	-10.8 ±0.07	0.49 ±0.02	8.77 ±0.02	40.87
63	NGC5194	SABbcp	7.62 ±0.35	-20.63 ±0.14	-10.45 ±0.04	0.59 ±0.01	8.86 ±0.01	41.1
64	NGC5195	SB0pec	7.62 ±0.35	-19.43 ±0.14	. . .	. . .	8.67 . . .	39.79[a]
65	Tol89	SBdm	16.7 ±2.3	-19.1 ±0.32	-11.79 ± . . .	0.26 ±0.16	8.52 ±0.05	40.7
66	NGC5408	IBm	4.81 ±0.38	-16.57 ±0.2	-11.33 ±0.02	0.06 ±0.03	8.02 ±0.08	40.18
67	NGC5474	SAcdp	6.8 ±1.7	-17.69 ±0.55	-11.65 ±0.03	0.22 ±0.13	8.57 ±0.18	40.08
68	NGC5713	SABbcp	29.4 ±2.3	-20.53 ±0.2	-11.63 ± . . .	0.55 ± . . .	8.64 ±0.04	41.13
69	NGC5866	S0	15.42 ±0.85	-20.2 ±0.16	. . .	. . .	8.8 . . .	. . .
70	IC4710	SBm	9.0 ±2.3	-18.03 ±0.56	. . .	. . .	8.46 . . .	. . .
71	NGC6822	IBm	0.47 ±0.05	-14.99 ±0.25	-10.54 ±0.04	0.05 ±0.03	8.4 ±0.16	38.95
72	NGC6946	SABcd	6.8 ±1.7	-21.04 ±0.55	-10.42 ±0.06	0.45 ±0.09	8.73 ±0.02	41.16
73	NGC7331	SAb	14.52 ±0.6	-21.05 ±0.13	-11.07 ±0.03	0.61 ±0.04	8.68 ±0.02	41.02
74	NGC7552	SBab	21.0 ±2.3	-20.44 ±0.26	. . .	. . .	8.76 ±0.02	39.88[c]
75	NGC7793	SAd	3.91 ±0.43	-18.4 ±0.26	-10.6 ±0.08	0.31 ±0.07	8.6 ±0.01	40.59

Table 8.1: Basic properties of the galaxy sample.

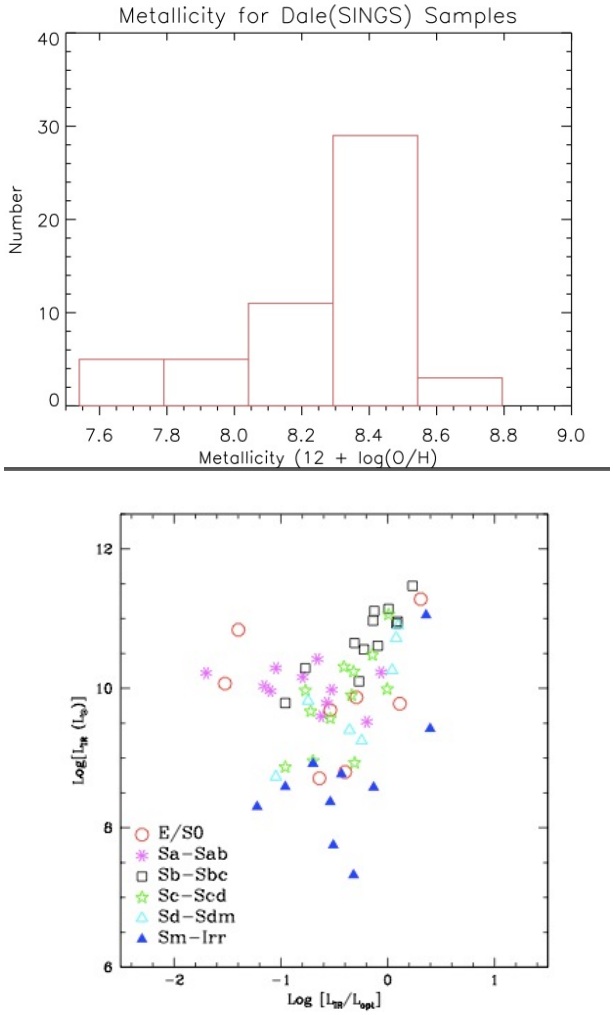

Figure 8.1: Metallicity distribution (Top) and Morphological types (Bottom) of the 75 SINGS sample

The entries in Table 8.1 are organized as follows Column (1): The index number. Column (2): Galaxy name. Column (3): Morphological type from Moustakas et al. (2010). Column (4): Distance taken from Moustakas et al. (2010).Column (5): Absolute B-band magnitude relative to vega taken from Moustakas et al. (2010).Column (6): Integrated Hα + [NII] emission-line flux with the uncertainty in units of log ergs cm^{-2} s^{-1} from Kennicutt et al. (2009).Column (7): [NII]$\lambda\lambda$6548, 6583/Hα ratio from Kennicutt et al. (2009). Column (8): Global nebular oxygen abundances derived by Moustakas et al. (2010) using two different methods (KK05 and PT05) as described briefly in the text. According to Moustakas et al. (2010), the difference between the two metallicity values obtained by the two methods is due to an as yet unidentified systematic zero-point offset, and that the true oxygen abundance should lie somewhere in between these values. We thus adopt the average of the two values as our oxygen abundances. Entries without uncertainties are sources without spectroscopy measurements and their metallicity were approximated by the authors using the B-band luminosity-metallicity (L-Z) relation given by their equations 9 and 10. Column (9): Integrated Hα luminosity in units of log ergs s^{-1}. Kennicutt et al. (2009) presented integrated Hα + [NII] emission-line flux for 58 of our 75 SINGS sample. We first subtracted the [NII] contamination from the Hα flux using the [NII]/Hα ratio given in column (7). Then we corrected this flux for Galactic foreground extinction using the relation by Moustakas et al. (2006) adopting the Hα/Hβ ratio given in Table 1 of Kennicutt et al. (2009). No correction was made for the extinction within and between individual galaxies. The final integrated Hα luminosity was then derived using the distance given in column (4). For the remaining 27 sources, we searched the literature and obtained the integrated Hα emission-line flux (corrected for [NII] contamination) for 19 sources, in order of preference from a: Kennicutt et al. (2008), b:Leroy et al. (2012), c:Schmitt et al. (2006a) and d:Moustakas et al. (2006).

8.2.2 Investigating the radio slope of high redshift galaxies

One of the results I have obtained in this work concerns the possible use of the radio slope to identify the kind of the IMF. I have shown that while it would be difficult for a single object to use the radio slope for this purpose, I predict that for a population of objects probing the first hundred Myr of galaxy evolution, the expected slope should peak around a value which does depend on the relative proportion of between free-free and non-thermal emission. Such populations can be perhaps detected at high redshifts. For example, the new South African MeerKAT radio telescope, a precursor to the Square Kilometre Array (SKA), is already performing deep continuum observations of the earliest radio galaxies and in its first light image showed more than 1300 galaxies in the distant Universe, compared to the about 70 previously known in the same location. It is important to better define the evolution of the slope of such galaxies and this is possible with our synthesis code because we may provide it with the physical conditions that best represent the environments of the early evolutionary phases. Furthermore, while in this thesis we have limited our interest to the case of the upper mass limit of the IMF and constant SFR, we should consider other possibilities, like a variation of the slopes and more complex descriptions of the star formation history. We should also perform more realistic simulations, by taking into considerations the observed galaxy samples, i.e. the galaxy number densities and corresponding redshift distributions

(when available), and the accuracy of their measurement, that in our preliminary simulations have been only guessed.

8.2.3 Improving the fitting algorithm

The number of the physical parameters that we may investigate with our model can easily lead to an exceedingly large number of models to be managed. Only for exploring the range of parameters shown in Table 6.1 we needed to calculate more than 30000 star-burst models. With our code, other important parameters can be tested, like for example the kind of dust, perhaps following a dust formation process that should be included in the chemical evolution code using the general recipes of e.g. Nanni et al. (2014, 2013) and that could provide different dust species for the early phases of galaxy evolution. New comprehensive stellar spectral libraries will be available in the next future that include different elemental partitions (alpha-enhanced or, better to say, Iron-depressed), possible effects of rotation and a sound treatment of the effects of binary interaction in stellar evolution. From the observational side, new data may come in other spectral windows. All these new parameters and observational data will require further fine tuning of the solutions which might better developed with some automatic fitting algorithms (e.g. da Cunha et al. 2010, 2015).

Bibliography

Abbott, B. P., Abbott, R., Abbott, T. D., et al. 2016, Physical Review Letters, 116, 241102

Aerts, C. 2015, Astronomische Nachrichten, 336, 477

Alexandroff, R. M., Heckman, T. M., Borthakur, S., Overzier, R., & Leitherer, C. 2015, ApJ, 810, 104

Allard, F., Hauschildt, P. H., Alexander, D. R., & Starrfield, S. 1997, ARA&A, 35, 137

Andrews, B. H., Weinberg, D. H., Schönrich, R., & Johnson, J. A. 2017, ApJ, 835, 224

Arimoto, N. 1996, in Astronomical Society of the Pacific Conference Series, Vol. 98, From Stars to Galaxies: the Impact of Stellar Physics on Galaxy Evolution, ed. C. Leitherer, U. Fritze-von-Alvensleben, & J. Huchra, 287

Arimoto, N., & Yoshii, Y. 1987, A&A, 173, 23

Asplund, M., Grevesse, N., & Sauval, A. J. 2005, in Astronomical Society of the Pacific Conference Series, Vol. 336, Cosmic Abundances as Records of Stellar Evolution and Nucleosynthesis, ed. T. G. Barnes, III & F. N. Bash, 25

Asplund, M., Grevesse, N., Sauval, A. J., & Scott, P. 2009, ARA&A, 47, 481

Baade, W. 1944, ApJ, 100, 137

Baes, M., Davies, J. I., Dejonghe, H., et al. 2003, MNRAS, 343, 1081

Bailyn, C. D. 1995, ARA&A, 33, 133

Baraffe, I., Chabrier, G., Allard, F., & Hauschildt, P. H. 1998, A&A, 337, 403

Bergvall, N., Zackrisson, E., Andersson, B.-G., et al. 2006, A&A, 448, 513

Berkhuijsen, E. M. 1984, A&A, 140, 431

Bertelli, G., Bressan, A., Chiosi, C., Fagotto, F., & Nasi, E. 1994, A&AS, 106

Bertelli, G., Girardi, L., Marigo, P., & Nasi, E. 2008, A&A, 484, 815

Bica, E., & Alloin, D. 1986, A&A, 162, 21

Borthakur, S., Heckman, T. M., Leitherer, C., & Overzier, R. A. 2014, Science, 346, 216

Bowen, I. S. 1928, ApJ, 67

Bressan, A., Granato, G. L., & Silva, L. 1998, A&A, 332, 135

Bressan, A., Marigo, P., Girardi, L., et al. 2012, MNRAS, 427, 127

Bressan, A., Silva, L., & Granato, G. L. 2002, A&A, 392, 377

Brown, T. M., Ferguson, H. C., Smith, E., et al. 2005, AJ, 130, 1693

Buat, V., Donas, J., Milliard, B., & Xu, C. 1999, A&A, 352, 371

Buat, V., & Xu, C. 1996, A&A, 306, 61

Buzzoni, A. 1989, ApJS, 71, 817

Caffau, E., Ludwig, H.-G., Steffen, M., Freytag, B., & Bonifacio, P. 2011, Sol. Phys., 268, 255

Calura, F., Pozzi, F., Cresci, G., et al. 2017, MNRAS, 465, 54

Calzetti, D., Armus, L., Bohlin, R. C., et al. 2000, ApJ, 533, 682

Calzetti, D., Kinney, A. L., & Storchi-Bergmann, T. 1994, ApJ, 429, 582

Calzetti, D., Kennicutt, R. C., Engelbracht, C. W., et al. 2007, ApJ, 666, 870

Cardelli, J. A., Clayton, G. C., & Mathis, J. S. 1989, ApJ, 345, 245

Castelli, F., & Kurucz, R. L. 2004, ArXiv Astrophysics e-prints, astro-ph/0405087

Cenarro, A. J., Peletier, R. F., Sánchez-Blázquez, P., et al. 2007, MNRAS, 374, 664

Chabrier, G. 2003, PASP, 115, 763

Chabrier, G., & Baraffe, I. 1997, A&A, 327, 1039

Charlot, S., & Bruzual, A. G. 1991, ApJ, 367, 126

Charlot, S., & Fall, S. M. 2000, ApJ, 539, 718

Chary, R., & Elbaz, D. 2001, ApJ, 556, 562

Chen, Y., Bressan, A., Girardi, L., et al. 2015, MNRAS, 452, 1068

Chen, Y., Girardi, L., Bressan, A., et al. 2014, MNRAS, 444, 2525

Chen, Y., Trager, S., Peletier, R., & Lançon, A. 2011, in Journal of Physics Conference Series, Vol. 328, Journal of Physics

Conference Series, 012023
Chieffi, A., & Limongi, M. 2013, ApJ, 764, 21
Chiosi, C., Bertelli, G., & Bressan, A. 1988, A&A, 196, 84
Coelho, P., Bruzual, G., Charlot, S., et al. 2007, MNRAS, 382, 498
Condon, J. J. 1992, ARA&A, 30, 575
Condon, J. J., Anderson, M. L., & Helou, G. 1991, ApJ, 376, 95
Condon, J. J., & Ransom, S. M. 2016, Essential Radio Astronomy (Princeton University Press)
Condon, J. J., & Yin, Q. F. 1990, ApJ, 357, 97
Conroy, C., & van Dokkum, P. 2012a, ApJ, 747, 69
Conroy, C., & van Dokkum, P. G. 2012b, ApJ, 760, 71
Cordier, D., Pietrinferni, A., Cassisi, S., & Salaris, M. 2007, AJ, 133, 468
Cyburt, R. H., Amthor, A. M., Ferguson, R., et al. 2010, ApJS, 189, 240
da Cunha, E., Charlot, S., & Elbaz, D. 2008, MNRAS, 388, 1595
da Cunha, E., Eminian, C., Charlot, S., & Blaizot, J. 2010, MNRAS, 403, 1894
da Cunha, E., Walter, F., Smail, I. R., et al. 2015, ApJ, 806, 110
Dale, D. A., & Helou, G. 2002, ApJ, 576, 159
Dale, D. A., Helou, G., Contursi, A., Silbermann, N. A., & Kolhatkar, S. 2001, ApJ, 549, 215
Dale, D. A., Bendo, G. J., Engelbracht, C. W., et al. 2005, ApJ, 633, 857
Dale, D. A., Gil de Paz, A., Gordon, K. D., et al. 2007, ApJ, 655, 863
Dale, D. A., Aniano, G., Engelbracht, C. W., et al. 2012, ApJ, 745, 95
de Jager, C., Nieuwenhuijzen, H., & van der Hucht, K. A. 1988, A&AS, 72, 259
de Mink, S. E. 2010, PhD thesis, Utrecht University
de Mink, S. E., Langer, N., Izzard, R. G., Sana, H., & de Koter, A. 2013, ApJ, 764, 166
Decressin, T., Charbonnel, C., Siess, L., et al. 2009, A&A, 505, 727
Devriendt, J. E. G., Guiderdoni, B., & Sadat, R. 1999, A&A, 350, 381
Dotter, A. 2016, ApJS, 222, 8
Draine, B. T. 2011, Physics of the Interstellar and Intergalactic Medium (Princeton University Press)
Draine, B. T., & Lee, H. M. 1984, ApJ, 285, 89
Draine, B. T., Dale, D. A., Bendo, G., et al. 2007, ApJ, 663, 866
Edmunds, M. G. 2001, MNRAS, 328, 223
Edvardsson, B., Andersen, J., Gustafsson, B., et al. 1993, A&A, 275, 101
Eggen, O. J., Lynden-Bell, D., & Sandage, A. R. 1962, ApJ, 136, 748
Eggenberger, P., Carrier, F., Mathis, S., & Miglio, A. 2008, Journal of Physics: Conference Series, 118, 012021
Eldridge, J. J., McClelland, L. A. S., Xiao, L., Stanway, E. R., & Bray, J. 2015, in Wolf-Rayet Stars: Proceedings of an International Workshop held in Potsdam, Germany, 1-5 June 2015. Edited by Wolf-Rainer Hamann, Andreas Sander, Helge Todt. Universitätsverlag Potsdam, 2015., p.177-182, ed. W.-R. Hamann, A. Sander, & H. Todt, 177
Ercolano, B., Barlow, M. J., Storey, P. J., & Liu, X.-W. 2003, MNRAS, 340, 1136
Ertl, T., Janka, H.-T., Woosley, S. E., Sukhbold, T., & Ugliano, M. 2015, ArXiv e-prints, arXiv:1503.07522 [astro-ph.SR]
Ferland, G. 1996, Hazy: A Brief Introduction to CLOUDY (Univ. of Kentucky Physics Department Internal Report)
Ferland, G. J., Porter, R. L., van Hoof, P. A. M., et al. 2013, Rev. Mexicana Astron. Astrofis., 49, 137
Ferraro, F. R., Sabbi, E., Gratton, R., et al. 2006, ApJ, 647, L53
Fryer, C. L., Belczynski, K., Wiktorowicz, G., et al. 2012, ApJ, 749, 91
Galliano, F., Madden, S. C., Jones, A. P., et al. 2003, A&A, 407, 159
Gil de Paz, A., Boissier, S., Madore, B. F., et al. 2007, ApJS, 173, 185
Girardi, L., Bertelli, G., Bressan, A., et al. 2002, A&A, 391, 195
Girardi, L., Bressan, A., Bertelli, G., & Chiosi, C. 2000, A&AS, 141, 371
Gordon, K. D., Misselt, K. A., Witt, A. N., & Clayton, G. C. 2001, ApJ, 551, 269
Gräfener, G., & Hamann, W.-R. 2008, A&A, 482, 945
Granato, G. L., Lacey, C. G., Silva, L., et al. 2000, ApJ, 542, 710
Gregg, M. D., Silva, D., Rayner, J., et al. 2004, in Bulletin of the American Astronomical Society, Vol. 36, American Astronomical Society Meeting Abstracts, 1496
Grevesse, N., & Sauval, A. J. 1998, Space Sci. Rev., 85, 161
Groves, B., Dopita, M. A., Sutherland, R. S., et al. 2008, ApJS, 176, 438
Gutkin, J., Charlot, S., & Bruzual, G. 2016, MNRAS, 462, 1757
Hauschildt, P. H., Baron, E., & Allard, F. 1997, ApJ, 483, 390
Heckman, T. M., Borthakur, S., Overzier, R., et al. 2011, ApJ, 730, 5
Heger, A., Fryer, C. L., Woosley, S. E., Langer, N., & Hartmann, D. H. 2003, ApJ, 591, 288
Heger, A., & Woosley, S. E. 2002, ApJ, 567, 532

Helou, G., Khan, I. R., Malek, L., & Boehmer, L. 1988, ApJS, 68, 151
Helou, G., Soifer, B. T., & Rowan-Robinson, M. 1985, ApJ, 298, L7
Henry, R. B. C., & Worthey, G. 1999, PASP, 111, 919
Horiuchi, S., Beacom, J. F., Kochanek, C. S., et al. 2011, ApJ, 738, 154
Horiuchi, S., Nakamura, K., Takiwaki, T., Kotake, K., & Tanaka, M. 2014, MNRAS, 445, L99
Huang, S.-S., & Struve, O. 1954, Annales d'Astrophysique, 17, 85
Humphreys, R. M., & Davidson, K. 1979, ApJ, 232, 409
Hurley, J. R., Pols, O. R., & Tout, C. A. 2000, MNRAS, 315, 543
Ibar, E., Ivison, R. J., Best, P. N., et al. 2010, MNRAS, 401, L53
Inoue, A. K. 2003, PASJ, 55, 901
Irwin, A. W. 2012, FreeEOS: Equation of State for stellar interiors calculations, Astrophysics Source Code Library, ascl:1211.002
Issa, M. R., MacLaren, I., & Wolfendale, A. W. 1990, A&A, 236, 237
Iwata, I., Inoue, A. K., Matsuda, Y., et al. 2009, ApJ, 692, 1287
Izotov, Y. I., Orlitová, I., Schaerer, D., et al. 2016, Nature, 529, 178
Janka, H.-T. 2012, Annual Review of Nuclear and Particle Science, 62, 407
Jarrett, T. H., Chester, T., Cutri, R., Schneider, S. E., & Huchra, J. P. 2003, AJ, 125, 525
Kallman, T. 1999, XSTAR: A program for calculating conditions and spectra of photoionized gases, Astrophysics Source Code Library, ascl:9910.008
Kennicutt, Jr., R. C. 1983, ApJ, 272, 54
Kennicutt, Jr., R. C. 1998, ARA&A, 36, 189
Kennicutt, Jr., R. C., Lee, J. C., Funes, José G., S. J., Sakai, S., & Akiyama, S. 2008, ApJS, 178, 247
Kennicutt, Jr., R. C., Armus, L., Bendo, G., et al. 2003, PASP, 115, 928
Kennicutt, Jr., R. C., Hao, C.-N., Calzetti, D., et al. 2009, ApJ, 703, 1672
Kennicutt, R. C., Calzetti, D., Aniano, G., et al. 2011, PASP, 123, 1347
Koeppen, J., & Arimoto, N. 1990, A&A, 240, 22
Kroupa, P. 2001, MNRAS, 322, 231
Kurucz, R. L. 1992, in IAU Symposium, Vol. 149, The Stellar Populations of Galaxies, ed. B. Barbuy & A. Renzini, 225
Kurucz, R. L. 1993, in Astronomical Society of the Pacific Conference Series, Vol. 44, IAU Colloq. 138: Peculiar versus Normal Phenomena in A-type and Related Stars, ed. M. M. Dworetsky, F. Castelli, & R. Faraggiana, 87
Kurucz, R. L. 2005, Memorie della Societa Astronomica Italiana Supplementi, 8, 86
Kurucz, R. L. 2011, Canadian Journal of Physics, 89, 417
Lacey, C. G., Baugh, C. M., Frenk, C. S., et al. 2016, MNRAS, 462, 3854
Lagache, G., Dole, H., & Puget, J.-L. 2003, MNRAS, 338, 555
Lançon, A., Hauschildt, P. H., Ladjal, D., & Mouhcine, M. 2007, A&A, 468, 205
Laor, A., & Draine, B. T. 1993, ApJ, 402, 441
Lapi, A., Mancuso, C., Bressan, A., & Danese, L. 2017a, ArXiv e-prints, arXiv:1708.07643
Lapi, A., Mancuso, C., Celotti, A., & Danese, L. 2017b, ApJ, 835, 37
Larson, R. B., & Tinsley, B. M. 1978, ApJ, 219, 46
Lawton, B., Gordon, K. D., Babler, B., et al. 2010, ApJ, 716, 453
Le Borgne, J.-F., Bruzual, G., Pelló, R., et al. 2003, A&A, 402, 433
Lee, Y.-W., Demarque, P., & Zinn, R. 1994, ApJ, 423, 248
Leitherer, C., Ekström, S., Meynet, G., et al. 2014, ApJS, 212, 14
Leitherer, C., Schaerer, D., Goldader, J. D., et al. 1999, ApJS, 123, 3
Leroy, A. K., Bigiel, F., de Blok, W. J. G., et al. 2012, AJ, 144, 3
Li, A., & Draine, B. T. 2001, ApJ, 554, 778
Li, Y., Calzetti, D., Kennicutt, R. C., et al. 2010, ApJ, 725, 677
Li, Z., & Han, Z. 2007, ArXiv e-prints, arXiv:0712.1859
Lisenfeld, U., & Ferrara, A. 1998, The Astrophysical Journal, 496, 145
López-Sánchez, Á. R., Dopita, M. A., Kewley, L. J., et al. 2012, MNRAS, 426, 2630
Maeder, A., , & Meynet, G. 2000, Annual Review of Astronomy and Astrophysics, 38, 143
Maeder, A., & Meynet, G. 1988, A&AS, 76, 411
Maeder, A., & Meynet, G. 2003, A&A, 411, 543
Mancuso, C., Lapi, A., Shi, J., et al. 2016, ApJ, 823, 128
Mancuso, C., Lapi, A., Prandoni, I., et al. 2017, ApJ, 842, 95
Maraston, C. 1998, MNRAS, 300, 872
Maraston, C. 2005, MNRAS, 362, 799
Maraston, C., Daddi, E., Renzini, A., et al. 2006, ApJ, 652, 85
Marigo, P., & Aringer, B. 2009, A&A, 508, 1539

Marigo, P., Bressan, A., Nanni, A., Girardi, L., & Pumo, M. L. 2013, MNRAS, 434, 488
Marigo, P., Girardi, L., Bressan, A., et al. 2008, A&A, 482, 883
Martins, L. P., González Delgado, R. M., Leitherer, C., Cerviño, M., & Hauschildt, P. 2005, MNRAS, 358, 49
Matteucci, F., & Francois, P. 1989, MNRAS, 239, 885
Matteucci, F., & Tornambe, A. 1987, A&A, 185, 51
McCrea, W. H. 1964, MNRAS, 128, 147
Melbourne, J., Williams, B. F., Dalcanton, J. J., et al. 2012, ApJ, 748, 47
Meurer, G. R., Heckman, T. M., & Calzetti, D. 1999, ApJ, 521, 64
Meynet, G., & Maeder, A. 1997, A&A, 321, 465
Mezger, P. G., & Henderson, A. P. 1967, ApJ, 147, 471
Moustakas, J., Kennicutt, Jr., R. C., & Tremonti, C. A. 2006, ApJ, 642, 775
Moustakas, J., Kennicutt, Jr., R. C., Tremonti, C. A., et al. 2010, ApJS, 190, 233
Murphy, E. J., Helou, G., Condon, J. J., et al. 2010, ApJ, 709, L108
Murphy, E. J., Condon, J. J., Schinnerer, E., et al. 2011, ApJ, 737, 67
Murphy, E. J., Bremseth, J., Mason, B. S., et al. 2012, ApJ, 761, 97
Nanni, A., Bressan, A., Marigo, P., & Girardi, L. 2013, MNRAS, 434, 2390
Nanni, A., Bressan, A., Marigo, P., & Girardi, L. 2014, MNRAS, 438, 2328
Nestor, D. B., Shapley, A. E., Kornei, K. A., Steidel, C. C., & Siana, B. 2013, ApJ, 765, 47
Nomoto, K. 1984, in Astrophysics and Space Science Library, Vol. 109, Stellar Nucleosynthesis, ed. C. Chiosi & A. Renzini, 239
Nomoto, K., Kamiya, Y., & Nakasato, N. 2013, in IAU Symposium, Vol. 281, Binary Paths to Type Ia Supernovae Explosions, ed. R. Di Stefano, M. Orio, & M. Moe, 253
Nugis, T., & Lamers, H. J. G. L. M. 2000, A&A, 360, 227
O'Connor, E., & Ott, C. D. 2011, ApJ, 730, 70
Oster, L. 1961, Reviews of Modern Physics, 33, 525
Osterbrock, D. E. 1989, Astrophysics of gaseous nebulae and active galactic nuclei (University Science Books, Mill Valley, CA)
Osterbrock, D. E., & Ferland, G. J. 2006, Astrophysics of gaseous nebulae and active galactic nuclei (University Science Books)
Panuzzo, P., Bressan, A., Granato, G. L., Silva, L., & Danese, L. 2003, A&A, 409, 99
Panuzzo, P., Granato, G. L., Buat, V., et al. 2007, MNRAS, 375, 640
Papovich, C., Labbé, I., Glazebrook, K., et al. 2016a, Nature Astronomy, 1, 0003
Papovich, C., Labbé, I., Glazebrook, K., et al. 2016b, Nature Astronomy, 1, 0003
Pauldrach, A., Puls, J., & Kudritzki, R. P. 1986, A&A, 164, 86
Pietrinferni, A., Cassisi, S., Salaris, M., & Castelli, F. 2004, ApJ, 612, 168
Pilyugin, L. S., Grebel, E. K., Zinchenko, I. A., & Kniazev, A. Y. 2014, AJ, 148, 134
Popescu, C. C., Misiriotis, A., Kylafis, N. D., Tuffs, R. J., & Fischera, J. 2000, A&A, 362, 138
Prugniel, P., & Soubiran, C. 2001, A&A, 369, 1048
Rayner, J. T., Cushing, M. C., & Vacca, W. D. 2009, ApJS, 185, 289
Reddy, N. A., Erb, D. K., Pettini, M., Steidel, C. C., & Shapley, A. E. 2010, ApJ, 712, 1070
Reddy, N., Dickinson, M., Elbaz, D., et al. 2012, ApJ, 744, 154
Renzini, A. 1981, Annales de Physique, 6, 87
Renzini, A., & Fusi Pecci, F. 1988, ARA&A, 26, 199
Rich, R. M. 1988, AJ, 95, 828
Rich, R. M., Sosin, C., Djorgovski, S. G., et al. 1997, ApJ, 484, L25
Rickard, L. J., & Harvey, P. M. 1984, AJ, 89, 1520
Robertson, B. E., Ellis, R. S., Dunlop, J. S., McLure, R. J., & Stark, D. P. 2010, Nature, 468, 49
Romano, D., Matteucci, F., Zhang, Z.-Y., Papadopoulos, P. P., & Ivison, R. J. 2017, MNRAS, 470, 401
Rosa-González, D., Schmitt, H. R., Terlevich, E., & Terlevich, R. 2007, ApJ, 654, 226
Rowan-Robinson, M., & Crawford, J. 1989, MNRAS, 238, 523
Rubele, S., Girardi, L., Kerber, L., et al. 2015, MNRAS, 449, 639
Rubin, R. H. 1968a, ApJ, 154, 391
Rubin, R. H. 1968b, ApJ, 153, 761
Salpeter, E. E. 1955, ApJ, 121, 161
Sánchez-Blázquez, P., Peletier, R. F., Jiménez-Vicente, J., et al. 2006, MNRAS, 371, 703
Sandage, A. R. 1953, AJ, 58, 61
Sander, A., Shenar, T., Hainich, R., et al. 2015, A&A, 577, A13
Scalo, J. M. 1986, Fund. Cosmic Phys., 11, 1
Schmitt, H. R., Calzetti, D., Armus, L., et al. 2006a, ApJS, 164, 52
Schmitt, H. R., Calzetti, D., Armus, L., et al. 2006b, ApJ, 643, 173
Searle, L., Sargent, W. L. W., & Bagnuolo, W. G. 1973, ApJ, 179, 427

Shapley, H. 1918, ApJ, 48
Sharma, M., Theuns, T., Frenk, C., et al. 2016, MNRAS, 458, L94
Siebenmorgen, R., & Krügel, E. 2007, A&A, 461, 445
Siess, L. 2007, A&A, 476, 893
Silva, F. 1999, ModeModel the SED of dust galaxies and Applications (PhD Thesis) (International School for Advanced Studies, Trieste, Italy)
Silva, L., Bressan, A., Granato, G. L., & Panuzzo, P. 2002, in Astrophysics and Space Science Library, Vol. 274, New Quests in Stellar Astrophysics: the Link Between Stars and Cosmology, ed. M. Chávez, A. Bressan, A. Buzzoni, & D. Mayya, 175
Silva, L., Granato, G. L., Bressan, A., & Danese, L. 1998, ApJ, 509, 103
Silva, L., Schurer, A., Granato, G. L., et al. 2011, MNRAS, 410, 2043
Slemer, A., Marigo, P., Piatti, D., et al. 2017, MNRAS, 465, 4817
Smartt, S. J. 2009, ARA&A, 47, 63
Spera, M., & Mapelli, M. 2017, MNRAS, 470, 4739
Spera, M., Mapelli, M., & Bressan, A. 2015, MNRAS, 451, 4086
Sukhbold, T., & Woosley, S. E. 2014, ApJ, 783, 10
Sutherland, R. S., & Dopita, M. A. 1993, ApJS, 88, 253
Sweigart, A. V. 1987, ApJS, 65, 95
Tabatabaei, F. S., Schinnerer, E., Krause, M., et al. 2017, The Astrophysical Journal, 836, 185
Tacconi, L. J., Genzel, R., Smail, I., et al. 2008, ApJ, 680, 246
Tacconi, L. J., Genzel, R., Neri, R., et al. 2010, Nature, 463, 781
Tang, J., Bressan, A., Rosenfield, P., et al. 2014, MNRAS, 445, 4287
Tang, J., Bressan, A., Slemer, A., et al. 2016, MNRAS, 455, 3393
Terlevich, R., Melnick, J., Masegosa, J., Moles, M., & Copetti, M. V. F. 1991, A&AS, 91, 285
Thomson, A. P., Ivison, R. J., Simpson, J. M., et al. 2014, MNRAS, 442, 577
Tinsley, B. M. 1968, ApJ, 151, 547
Tinsley, B. M. 1972, A&A, 20, 383
Tinsley, B. M. 1973, ApJ, 186, 35
Tinsley, B. M. 1980, Fund. Cosmic Phys., 5, 287
Ugliano, M., Janka, H.-T., Marek, A., & Arcones, A. 2012, ApJ, 757, 69
Valdes, F., Gupta, R., Rose, J. A., Singh, H. P., & Bell, D. J. 2004, ApJS, 152, 251
van der Kruit, P. C. 1971, A&A, 15, 110
van der Kruit, P. C. 1973, A&A, 29, 263
van Dokkum, P. G., & Conroy, C. 2012, ApJ, 760, 70
Vanzella, E., Giavalisco, M., Inoue, A. K., et al. 2010, ApJ, 725, 1011
Vazdekis, A. 2008, in Astronomical Society of the Pacific Conference Series, Vol. 390, Pathways Through an Eclectic Universe, ed. J. H. Knapen, T. J. Mahoney, & A. Vazdekis, 255
Vazdekis, A., & Arimoto, N. 1999, ApJ, 525, 144
Vega, O., Clemens, M. S., Bressan, A., et al. 2008, A&A, 484, 631
Vega, O., Silva, L., Panuzzo, P., et al. 2005, MNRAS, 364, 1286
Vink, J. S., de Koter, A., & Lamers, H. J. G. L. M. 2000, A&A, 362, 295
Vink, J. S., de Koter, A., & Lamers, H. J. G. L. M. 2001, A&A, 369, 574
Vink, J. S., Muijres, L. E., Anthonisse, B., et al. 2011, A&A, 531, A132
Westera, P., Lejeune, T., Buser, R., Cuisinier, F., & Bruzual, G. 2002, A&A, 381, 524
Whitford, A. E. 1978, ApJ, 226, 777
Whitford, A. E., & Rich, R. M. 1983, ApJ, 274, 723
Wofford, A., Charlot, S., Bruzual, G., et al. 2016, MNRAS, 457, 4296
Woosley, S. E. 2017, ApJ, 836, 244
Worthey, G. 1994, ApJS, 95, 107
Worthey, G. 1999, in Astronomical Society of the Pacific Conference Series, Vol. 192, Spectrophotometric Dating of Stars and Galaxies, ed. I. Hubeny, S. Heap, & R. Cornett, 283
Worthey, G., Faber, S. M., & Gonzalez, J. J. 1992, ApJ, 398, 69
Xin, Y., & Deng, L. 2005, ApJ, 619, 824
Young, J. S., Xie, S., Kenney, J. D. P., & Rice, W. L. 1989, ApJS, 70, 699
Zhang, F., Han, Z., Li, L., & Hurley, J. R. 2004, A&A, 415, 117
Zhang, F., Han, Z., Li, L., & Hurley, J. R. 2005, MNRAS, 357, 1088
Zhu, Y.-N., Wu, H., Cao, C., & Li, H.-N. 2008, ApJ, 686, 155
Zubko, V., Dwek, E., & Arendt, R. G. 2004, ApJS, 152, 211